Copper battery for heat to power conversion and energy storage

Sunny Isaïe MAYE

EPFL

■ École
polytechnique
fédérale
de Lausanne

2020

À Guillaume Fartaria…

En souvenir de nos premiers pas en chimie…

Acknowledgements

This thesis would have been a very different challenge altogether without the incredible support of many people who have shared with me some of their time and advice over the past four years.

First, I would like to thank my advisor, Professor Hubert Girault, for his welcome to LEPA, starting with my master's project, and for giving me the opportunity to work on my PhD in the academic environment of the laboratory. I appreciated his ability to gather a stimulating LEPA team and the pleasant atmosphere thus created. I am grateful to him for having given me the possibility to collaborate with scientific experts, obtain access to the EPFL facilities and to attend conferences and workshops. Above all, I would like to thank him for his constant encouragement and trust.

I had the wonderful opportunity to collaborate with Dr Pekka Peljo, my co-supervisor. I am thankful to him for having asked me four years ago to be part of his project on the Cu redox flow battery. The time I spent working with him in the laboratory, developing the cell setup and discussing electrochemistry was one of the most exciting and motivating periods of my time at EPFL. I consider myself very lucky to have been taught by him: he has so many skills in electrochemistry and such a natural ability to improve and imagine systems. I am indeed honoured to have worked with him over these past four years in Sion.

I would like to acknowledge the contribution of the jury members of my PhD oral defense: Professor Christos Comninellis, Dr. Peter Fischer, Dr. Léonard Berlouis and the jury president Professor Marinella Mazzanti. I appreciate the time they spent reading and analysing the thesis. Their questions, comments and suggestions led to a very fruitful and stimulating discussion about batteries and heat conversion.

Among my colleagues at LEPA, I am especially grateful to Dr. Véronique Amstutz, Dr. Heron Vrubel and Dr. Andreas Lesch for their help and support during my studies. They taught me how to conduct academic research, how to use and maintain almost all the machines available in the laboratory as well as helping me develop setups (RFB and metal corrosion system). I also need to mention and thank Prof. Jose Antonio Manzanares from Valencia University, who improved significantly the thermodynamic description of our Cu RFB system. For assistance regarding analytical platforms at EPFL, I would like to thank Dr. Pascal Mieville (NMR), Dr. Mounir Mensi (XPS), Dr. Pascal Schouwink (XRD) and Dr. Emad Oveisi (CIME-SEM).

Beside my main project, I had the opportunity to study different aspects of electrochemistry and to collaborate with Dr. Lucie Rivier, Dr. Solène Gentil, Ms. Imene Atek, Dr. Alberto Battistel, Dr. Evgeny Smirnov and Mr. Danick Reynard. Thank you for all the discussions and the moments we shared together in and out of the lab. I am thankful to all the LEPA members for the agreeable atmosphere and everything they shared with me (Géraldine, Milica, Yingdi, Natalia, Alexandra, Justine, Justyna, Dominika, Sorour, Elena, Astrid, Mik, Victor, Yorick, Grégoire, Alejandro, Jonnathan, Terumasa, Patrick, Vimanshu and all the others). I hope I was also able to give back at least a small part of what I received at LEPA.

Résumé

Une importante partie de la production d'électricité provient de la conversion de chaleur. En effet, les centrales électriques brûlent généralement des carburants comme le gaz naturel, le charbon ou emploie la fission nucléaire pour produire de l'énergie thermique qui peut se transformer en électricité grâce à un cycle thermodynamique et au travail mécanique d'une turbine. Cependant, avec ces méthodes, de hauts rendements ne sont atteints qu'avec des températures élevées selon la théorie prédite par Carnot. De grandes quantités de chaleur de récupération à basse températures ne sont pas converties en électricité et sont habituellement simplement perdues. En conséquent, il y a ici une opportunité d'améliorer la conversion d'énergie thermique en électricité en récupérant les pertes de chaleur.

Ces chaleurs à basses températures (en dessous de 200°C) sont disponibles en grandes quantités par l'intermédiaire des pertes de chaleur industrielles, mais aussi par le biais des énergies renouvelables comme l'énergie solaire thermique et l'énergie géothermique. Etant donné que les énergies renouvelables sont utilisables seulement par intermittence durant certaines périodes de la journée ou selon la saison, il devient particulièrement intéressant de pouvoir les stocker afin de pouvoir les distribuer et consommer de manières plus efficaces. Néanmoins, la production d'électricité à partir de ces chaleurs à basses températures est un défi conséquent pour les technologies existantes. Les piles rechargeables thermiquement permettent la conversion et le stockage de l'énergie thermique en électricité, mais elles ne peuvent atteindre que de faibles voltages et de basses puissances de sortie.

Pour ce travail de thèse, nous présentons une batterie à flux rechargeable thermiquement qui utilise la complexation du cuivre avec l'acétonitrile dans un électrolyte non-aqueux et qui est capable de fournir un voltage de plus de 1V. Par distillation de l'acétonitrile, le complexe de Cu(I) et acétonitrile devient instable et réactif, ce qui permet la formation de cuivre métallique et de Cu(II) dans une solution de propylène carbonate, chargeant ainsi la batterie. Avec ce procédé, nous avons démontré une production d'électricité avec une densité de puissance de 200 $W \cdot m^{-2}$ et nous avons estimé une efficacité du system complet entre 5 et 14%. Ces résultats démontrent la faisabilité de ce concept pour produire et stocker de l'électricité à partir de pertes de chaleurs à basses températures.

Keywords: conversion de l'énergie thermique à basses températures en électricité, batterie à flux rechargeable thermiquement, cuivre, acétonitrile, cycle thermodynamique, électrochimie.

Abstract

An important part of the electricity production relies on heat conversion. Indeed power plants burn fuels like natural gas, coal or use nuclear fission to produce heat that can be transformed into electricity through a thermodynamic cycle and the mechanical work of a turbine. However, with such methods, high efficiencies are only reached with high temperatures according to the Carnot theory. Large amounts of waste heat or low-temperature heat are not converted into electrical power during these processes and are usually simply not exploited. Therefore, there is an opportunity to improve the way in which the heat is used and especially for electricity production, if waste heat can be recovered.

Low-grade heat (below 200 ℃) is available in vast quantities from industry, but also from renewable sources such as solar thermal or geothermal energy. As renewable energies are often available intermittently during specific time of the day or according to the season, the storage of the low-temperature heat coming from these sources is particularly interesting for a more efficient distribution and consumption. However, production of electric power from these heat sources is challenging with existing technologies. Thermally regenerative batteries allow both the conversion and the storage of thermal energy into electric power, but they suffer from low operation voltages and low output powers.

Here, we propose a thermally regenerative flow battery based on copper complexation with acetonitrile in non-aqueous solutions operating at voltages above 1V. Cu(I) complex can be destabilized by removal of acetonitrile by distillation, leading to production of solid copper and Cu(II) in a solution of propylene carbonate, thereby charging the battery. With this reaction, we demonstrate the electricity production at power densities up to 200 $W \cdot m^{-2}$, and estimate the theoretical efficiency of the full system between 5-14%. The results demonstrate a proof-of-concept for producing and storing electricity from low-quality heat.

Keywords: waste heat to power conversion and storage, thermally regenerative redox flow battery, copper, acetonitrile, thermodynamic cycle, electrochemistry.

List of abbreviations

ACN	acetonitrile
BSE	backscattered electron
CE	counter electrode
CHP	combined heat and power
CV	cyclic voltammetry
EDX	energy dispersive X-ray spectroscopy
EIS	electrochemical impedance spectroscopy
DSC	differential scanning calorimetry
LSV	linear sweep voltammetry
MD	membrane distillation
MED	multiple effect distillation
NP	nanoparticle
OHE	osmotic heat engine
ORC	organic Rankine cycle
PC	propylene carbonate
PRO	pressure retarded osmosis
RE	reference electrode
RDE	rotating disk electrode
RFB	redox flow battery
SE	secondary electron
SEM	scanning electron microscopy
SGP	salinity gradient power
TEA	tetraethylammonium
TEM	transmission electron microscopy
WE	working electrode
XPS	X-ray photoelectron spectroscopy
XRD	X-ray diffraction

List of symbols

A	absorbance or electroactive surface area	m^2
c	molar concentration	$mol \cdot L^{-1}$
C_M	concentration of the metal M	$mol \cdot L^{-1}$
$C_{M^{n+}}$	concentration of the metallic ions M^{n+}	$mol \cdot L^{-1}$
$C_{M^{n+}}^*$	bulk concentration of the metallic ions M^{n+}	$mol \cdot L^{-1}$
C^0	standard concentration	$mol \cdot L^{-1}$
C_p	thermal capacity	$J \cdot K^{-1}$
D	diffusion coefficient	$m^2 \cdot s^{-1}$
$D_{M^{n+}}$	diffusion coefficient of metallic ions M^{n+}	$m^2 \cdot s^{-1}$
$E(t)$	electrode potential	V
E_{eq}	equilibrium potential	V
E_i	initial potential	V
$E_{1/2}$	half-wave potential	V
E^0	standard potential	V
$E^{0'}$	formal potential	V
F	Faraday's constant	96485 C
ΔH_{vap}	enthalpy of vaporisation	$J \cdot mol^{-1}$
i	correction factor for osmotic pressure Eq.3	-
i	electric current	A
i_k	kinetic controlled current	A
$i_{l,a}$	anodic limiting current	A
k_a	anodic rate constant	$m \cdot s^{-1}$
k_b	cathodic rate constant	$m \cdot s^{-1}$
k^0	standard heterogeneous rate constant	$m \cdot s^{-1}$
k_B	Boltzmann constant	$1.38066 \cdot 10^{-23} \ J \cdot K^{-1}$
m, m_s	mass, sample mass	g
n	number of electron	-
p	pressure	Pa, bar, atm
P	power	W
Q	electric charge or heat	C or J
$\dot{Q}$	heat flow	W
r_H	hydrodynamic radius	m

R	universal gas constant	8.31451 J·K^{-1}·mol^{-1}
t	time	s
T	temperature	K
W	work	J
Z_{Im}	imaginary component of impedance	Ω
Z_{Re}	real component of impedance	Ω
α	charge transfer coefficient	-
$\beta, 1-\alpha$	charge transfer coefficient	-
η	efficiency	-
η	dynamic viscosity	Pa·s
η	dimensionless overvoltage	-
Δ_o	crystal field splitting energy	cm^{-1}
λ	wavelength	nm
σ	dimentionless scan rate	-
v	potential scan rate	V·s^{-1}
v_n	vibration n	cm^{-1}
χ	dimensionless current parameter	-
ψ	charge transfer parameter	-
Ψ	dimensionless current	-
ω	dimensionless kinetic rate parameter	-
ω	rotation rate	rpm, s^{-1}

Content

Chapter VI:

Cu redox flow battery for heat to power conversion and energy storage

Chapter VII: Conclusions and outlook

Chapter I   Introduction

The aim of this thesis is to propose, develop and characterize a system, which is able to convert and store thermal energy under chemical energy at low temperatures (<200°C) inside an energy storage device, such as an electrochemical cell.

1.   Heat to power conversion

Current electricity production still relies strongly on the conversion of heat *via* the mechanical work of a turbine, but this approach cannot be used efficiently at temperatures below 200 °C to satisfy the the Carnot efficicency (Eq. 1.1). Here, a new approach is based on thermo-electrochemical systems to convert low-grade heat first into a chemical energy, which can then in turn be converted on demand into electricity through an electrochemical reaction. To illustrate this principle, a copper based battery is studied. This model system is especially effective for using low quality heat below 160 °C to produce and store electricity. The battery can be charged and discharged as a conventional battery, but it can also be charged by a thermo-chemical reaction. This thermal charge process is predicted to have a maximum theoretical efficiency of *ca.* 10-14%. This is similar to efficiencies reported for mechanical heat to power methods like the organic Rankine cycle or the Kalina cycle, and significantly higher than for standard thermoelectric devices. The main advantage of the system, however, is its ability to store the energy in the battery, where it is available on demand.

The thermal charging process can be integrated with any heat source of *ca.* 140-160°C or more, including waste heat from industrial processes and power plants, but also geothermal sources and even heat from standard solar thermal collectors. More generally, the project will formulate the thermodynamic concepts of thermo-electrochemical systems.

According to the International Energy Agency (IEA), there is an opportunity to improve the way how the heat is used and especially for electricity production. From an IEA report, around 65% of the primary energy, which is consumed for power generation, is lost during the conversion, transmission and distribution (Fig. 1.1). One of the solutions, proposed by IEA, is the combined heat and power (CHP). CHP uses simultaneously heat and power from the same energy source, at or near the place of consumption.[1] With CHP, the low or middle-grade heats, which are not used for the electricity production and usually released in the environment (cooling tower), could be transferred to water for district heating of industries and habitations such as hotels, campuses or residential buildings. This CHP system should be able to save 20% energy, compared to the most efficient separated production of power and heat.[2] Although CHP is a nice way to lower heat losses, the technology behind is the same than for common power plants and does not provide solutions for the heat to power conversion of low-temperature waste heat. Additionally, higher energy efficiency of the power plants can be achieve (around 53%) if the integration of a cycle using the low-temperature is introduced.[3,4]
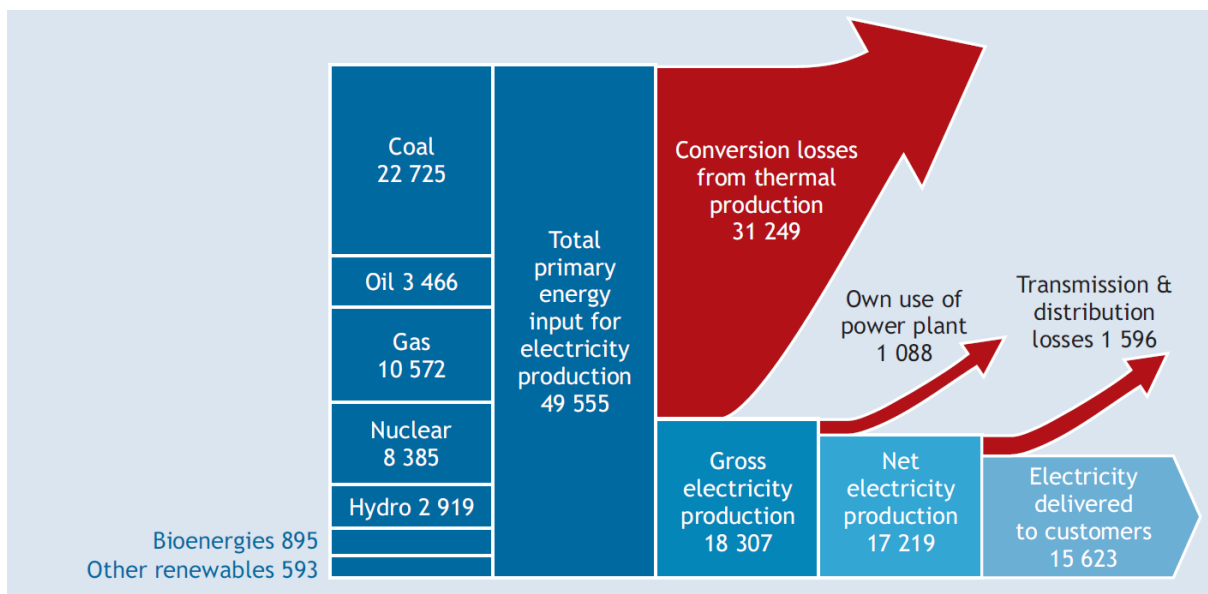
Figure 1.1. Energy flows (TWh) in the global electricity system.[1]

Waste heat from industries are not the only sources of low and middle-grade heat. For example, geothermal sources and solar thermal collectors are able to provide low quality heat (< 150°C). With the treatment of all these kinds of thermal energy, several advantages and benefits are possible. The efficiency of industries production could be increased with utilization of large waste heat quantities, which have a very low economic value. The environmental impacts of low-temperature heat will be decreased by its consumption for conversion. Electrical power from geothermal and solar sources will not increase the emissions of carbon dioxide.

If proven successful, thermo-electrochemical electricity generation could become a game-changer technology in electricity generation, with the possibility to replace or complement conventional steam engines and gas turbines. This would be also beneficial for the Swiss Energy Strategy 2050, aiming to improve the energy efficiency and enhance integration of renewable energy production into the grid.

1.1. Heat engines

1.1.1. Rankine and Kalina cycle

Nowadays, a large part of the electrical energy is currently produced through the conversion of heat into mechanical work. A well-known theoretical model of heat engine is described by the Carnot cycle. In this system, four reversible transformations occur. First, the heat input (Q_{in}) is transferred to the system by contact with a thermostat at high temperature (T_h). Then, the system cools from T_h to T_c *via* an adiabatic expansion of the fluid before releasing heat to the cold thermostat. After the adiabatic compression, the system reaches its initial state at T_h. At the end, the modification of the pressure and volume during the cycling allows the production of a mechanical work (W) by a piston. Heat engine efficiencies can be compared with the Carnot theoretical efficiency:[5]

$$\eta_{Carnot} = \frac{W}{Q_{in}} = 1 - \frac{T_c}{T_h} \qquad 1.1$$

However, during the conversion of heat inside steam turbine power plants, the Carnot cycle is not corresponding to the different transformations of the fluid. Another thermodynamic process, called the Rankine cycle, gives a better understanding of the transformations, which occurs in coal, gas, geothermal and nuclear power plants.[6]
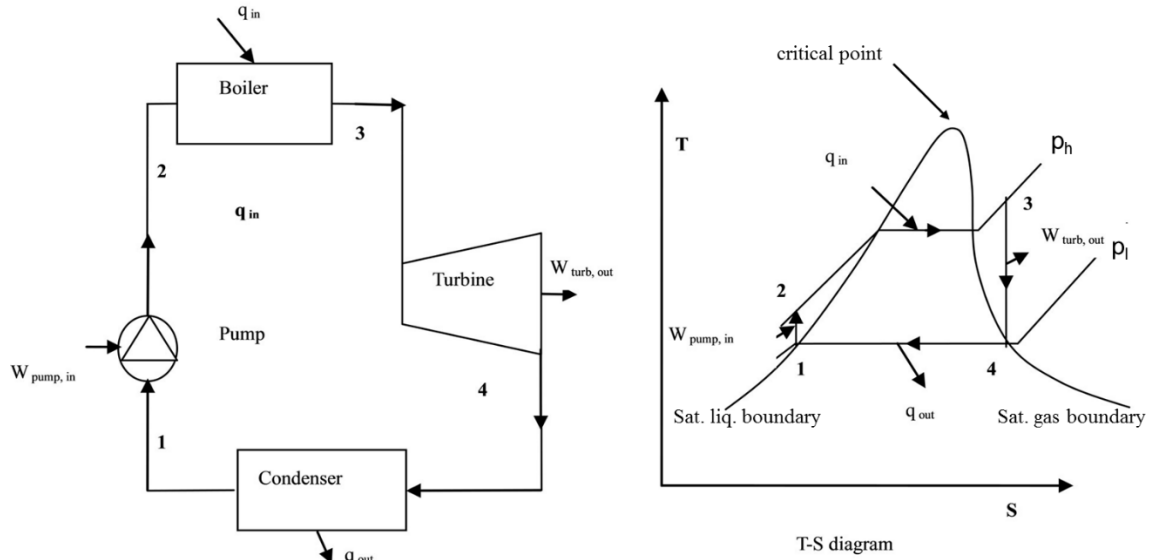
Figure 1.2. a) Process flow diagram of a Rankine cycle and b) T-S diagram of the same cycle with superheating of stream.[6]

All transformations in a Rankine cycle can be analysed and compared with the Carnot cycle (Fig. 1.2):

- 1-2: Isentropic compression of the liquid fluid (usually water[7]) is performed by a pump. Here, the difference with the Carnot cycle comes from the work input, which is needed to pump the liquid from the low (p_l) to high pressure (p_h).

- 2-3: Inside the boiler, heat exchange allows the heating of the liquid and its evaporation. In Figure 1.2b, the stream is even additionally heated (superheating) to get dry vapour. By comparison with the Carnot cycle, the heat input is done at constant pressure (p_h) and the temperature is changing due to the heating of the liquid to its boiling point. Another difference is the phase transition of the fluid in the system.

- 3-4: Through a gas turbine, the stream of dry vapour induces a power generation by its isentropic pressure expansion and decrease of its temperature.

- 4-1: At constant pressure (p_l), the wet vapour is transformed into a liquid inside the condenser.

The final efficiency for the ideal Rankine cycle is lower than that of the theoretical Carnot cycle because the work of the pump (W_{pump}) has to be taken into account:[8]

$$\eta_{Rankine} = \frac{W_{out} - W_{pump}}{Q_{in}} \qquad 1.2$$

However, Equation 1.2 is still an ideal efficiency, which does not include irreversible transformations. Indeed, in practice, entropy formation can be created *via* pressure losses in the boiler, condenser and pipes, but also during the compression in the pump and gas expansion in the turbine.[8] In addition, heat losses are occurring and decrease the final power generation. To improve the efficiency, the difference of temperature and pressure can be increased, if the heat source and the pump allows it.[9] But it is not sufficient enough, if these two parameters are modified, the pump and turbine should be able to handle such conditions. In case of an increase of pressure by the pump, which is coupled with an increase of the boiling temperature, the efficiency should be higher. Nevertheless, the moisture content of the vapour phase is also increased and it is known that humidity affects badly gas turbine.[10] By consequence, superheating and reheated Rankine cycle, which increase vapour temperature and counterbalance the moisture content of the vapour, can improve the efficiency without enhancement of the turbine deterioration.[11]

It seems that the traditional Rankine cycle is the most appropriate method to extract power from heat, with efficiencies around 35% for a temperature range between 300 and 550°C.[12] Due to the Carnot efficiency, the yield drops for heats at low temperatures. Consequently, low-grade heats are simply not exploited as they probably could be. Indeed, some techniques are already known for the use of low-temperature heat (organic Rankine cycle, Kalina cycle…). Unfortunately, for the moment, only small amounts of low-grade heat ($< 200°C$) are involved in electricity production, due to the lack of specific power plants at the industrial scale.

A typical steam turbine is efficient enough for temperatures above 300°C. Alternative approaches have been developed to fulfil the requirements for the use of waste heat. A heat-to-power converter, which has the same principle as the steam Rankine cycle, is the organic Rankine cycle (ORC). In this system, water is exchanged with organic fluids because of their physical properties (Table 1.1). Organic fluids usually have a lower boiling temperature than water.

Consequently, organic vapour stream can be produced with low and medium-grade heat (80°C to 300°C).[13] On the other side, ORC has to deal with the flammability and toxicity of the fluid. The energy efficiency of the ORC is between 5 and 20%.[14] However, ORC still has several advantages over the traditional Rankine cycle. With a low boiling point, the ORC needs less thermal energy for the heating and evaporation of the fluids. During evaporation, lower pressures and temperatures are required. In the turbine, the gas expansion ends in the vapour region, meaning that no liquid suspension should be present. Hence, no superheating is needed to keep the vapour dry and the turbine has less risks to suffer from erosion. Another consequence of the low pressure inside the turbine is the use of a cheaper simple stage turbine.[15]

Table 1.1. Summary of fluids properties comparison in Rankine and organic Rankine cycle.[16]

	Steam Rankine cycle	**Organic Rankine cycle**
Fluid	Water	Organic compound
Critical pressure	High	Low
Critical temperature	High	Low
Boiling point	High	Low
Condensing pressure	Low	Acceptable
Specific heat	High	Low
Viscosity	Low	Relatively high
Flammability	No	Yes and depends on fluid
Toxicity	No	Yes
Environmental impact	No	High and depends on fluid
Availability	Available	Supply problem
Cost	Cheap	more expensive

The optimization of the organic liquid has a crucial importance. Many articles try to characterize different organic compounds to estimate the most suitable for ORC.[13,15,17] For example, in the hydrocarbon family, isobutane is already used for geothermal power plants in Reno (NV, USA) and seems to provide the best efficiency among the different organic fluids, which were tested.[18,19] Nowadays, ORC is the most common thermodynamic cycle for the conversion of waste heat.

Another possibility for the conversion of low-temperature heat was developed in the 80s by Dr. Alexander Kalina. The Kalina cycle works with a working fluid containing a mixture of ammonia and water. An ideal fraction of ammonia in the liquid phase is around 70 wt% for geothermal sources with low and middle-grade heat.[20,21] In this system, the boiling temperature and the applied high-pressure can be tuned according to the temperature of the heat source, by changing the concentration of ammonia in the working fluid.[22–24]

In Figure 1.3, the process flow diagram shows the different steps of the working fluid during the production of power. The main operations are the compression of the ammonia solution by the pump (1-2), the preheating in the recuperator (2-3), the heat transfer for the evaporation of the ammonia-water mixture in the evaporator (3-5), the separation of the vapour and liquid, the expansion of the gas in the turbine to a lower pressure and the electricity production (6-7), mixing and cooling of the low pressure gas with the liquid in the recuperator and condenser.
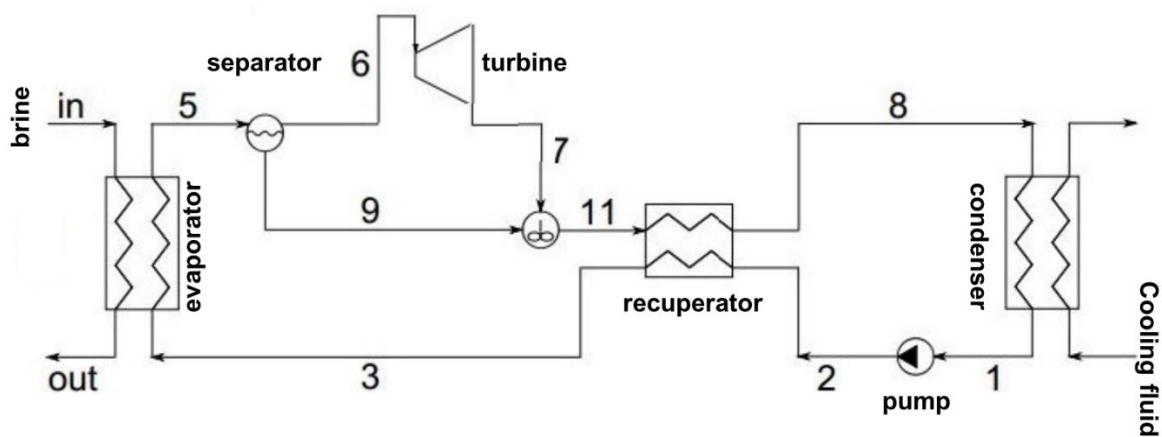
Figure 1.3. Process flow diagram of a simple Kalina cycle.[25]

The energy efficiency of the Kalina cycle can theoretically reach 45-52% and is around 20% more energetically efficient than the organic Rankine cycle for the same temperatures.[26] In Table 1.2, some power plants, which are using waste heat and geothermal source with a Kalina cycle, are presented.

Table 1.2. Examples of Kalina cycle in power plants around the world.[27]

Project name/location	Heat source	Electrical output	Start up
Canoga park (Demo), USA	515 °C exhaust gas of gas turbine, later solar centaur gas turbine	3 MW, later 6.5 MW	1992–1996
Fukuoka city, Japan	Waste heat from incineration plant	5 MW	1999
Kashima steel works, Japan	98 °C water, waste heat of production	3.1 MW	1999
Husavik, Iceland	Geothermal brine at 124 °C	2 MW	2000
Unterhaching, Germany	Geothermal	3.4 MW	2007

Another type of system using low-temperature heat is the salinity gradient power (SGP) engine, which works with the osmotic energy.[28] This energy comes from the mixing between solutions with different concentrations of a salt. For example, the work, that can be extracted when 1 m³ of river water is crossing a semi-permeable membrane to dilute a seawater draw solution, reaches approximately 0.75 kWh.[29] For an ideal solution, the osmotic pressure equation gives a nice indication about the minimal pressure, that needs to be applied to the highly concentred side of the semi-permeable membrane in a way to avoid dilution (*i* is the Van't Hoff factor, *T* temperature in Kelvin, *R* universal gas constant and *c* the molar concentration):

$$\pi = icRT \qquad\qquad 1.3$$

In Figure 1.4, a schematic diagram of the osmotic heat engine (OHE) is shown with a pressure-retarded osmosis (PRO) for the SGP unit. In the PRO part, diffusion of the working liquid (*e.g.* water) occurs through the membrane and provokes a dilution and a compression of the salty draw solution. The draw solution is split for the power generation, with a liquid expansion in the hydroturbine, and for the pressurizing of the draw solution, with the pressure

exchanger. At the end, the solutions have to be regenerated by heat. The regeneration unit can be operated by solvent or salt extraction.
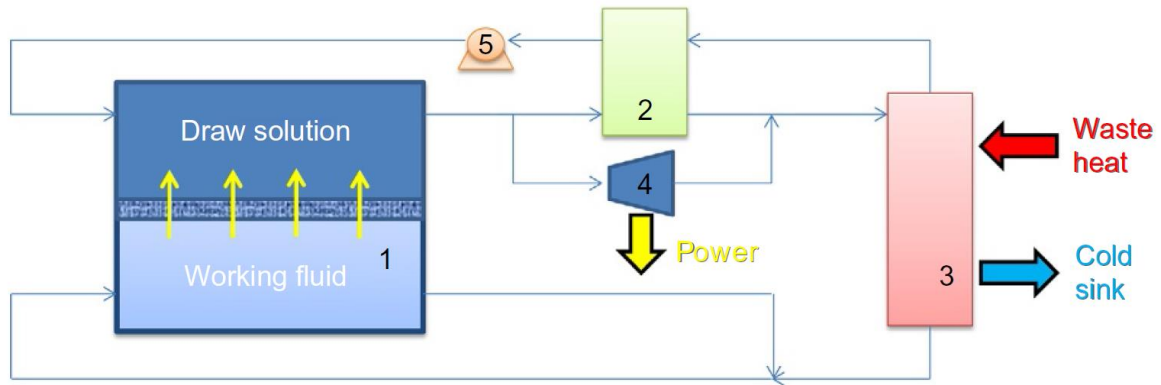
Figure 1.4. Simplified process flow diagram of an osmotic heat engine with (1) PRO unit, (2) pressure exchanger, (3) regeneration unit, (4) hydroturbine and (5) booster pump.[30]

Solvent extraction can be done by evaporative processes like multiple effect distillation (MED). With MED, heat is used to evaporate liquid in a first unit and this vapour is the driving steam for the evaporation of liquid in the other chambers with decreasing pressures.[31] Membrane distillation (MD) is also a technique for the solvent extraction.[32] In Figure 1.5, MD operates by difference of vapour pressures between the hot water and the channel for condensation. A hydrophobic membrane prevents the liquid water to go back into the hot liquid. At the end, fresh water and a more concentrate solution are recovered in parallel. Salt extraction by heat is also possible with thermolytic salts ($(NH_4)_2CO_3$), which are forming a gas with low-temperature heat and replace the distillation of the solvent.[33,34] However, the thermal efficiency of membrane distillation is much better even if it remains quite low at 10%.[30]
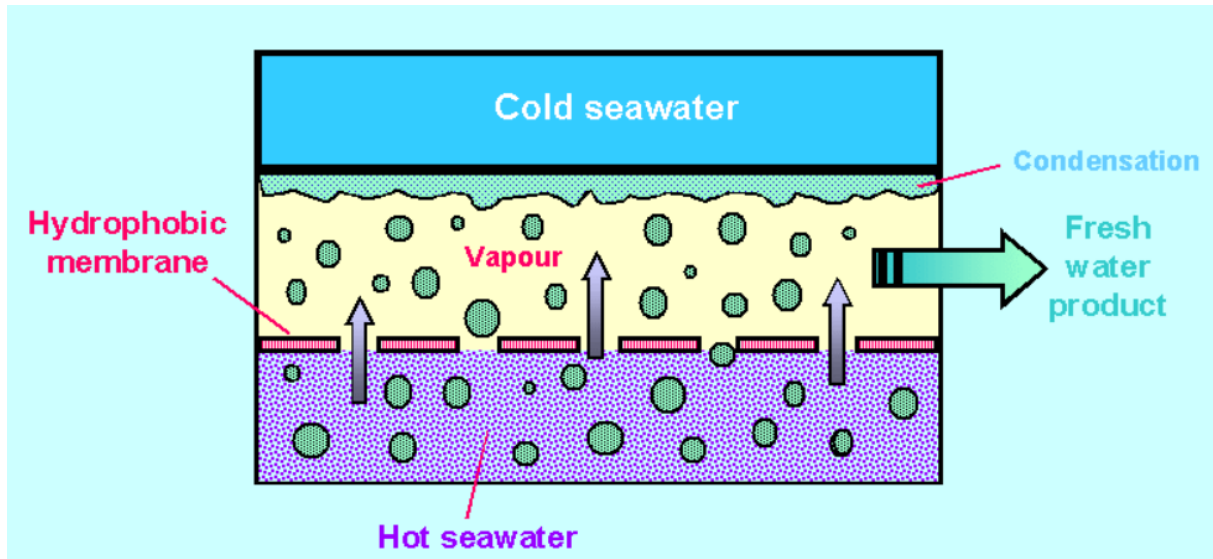
Figure 1.5. Schematic representation of membrane distillation.[35]

Other heat engines can be used for the heat to power generation of low-temperature heat: for examples the Maloney-Robertson cycle (which has similarities with Kalina cycle, because it also uses aqueous solution of ammonia as working fluid)[36], solar-powered Stirling engine[37], combined cycles (*e.g* Brayton cycle with Rankine cycle)[38], carbon carrier cycles.[39]

Additionally, some technologies are promising such as the thermoelectric devices. Generation of electricity directly from a temperature differential is achieved in the thermoelectric systems by specific semiconductors (Fig. 1.6).[40] This phenomenon is called the Seebeck effect. A typical set-up is made from one p-type and one n-type semi-conductor with an electrical connection in series and a thermal connection in parallel between the heat source and the heat sink.[41] The main problem with thermoelectric devices is their high thermal conductivity, which decreases the Seebeck effect and the temperature gradient between the heat and cooling sources.[42] To exceed this problem, a material with high electric conductivity and low thermal conductivity should be used. However, these conductivities are usually high in metal or low in glass, plastic and ceramics.[43] An interesting material, called semi-metallic polymers, is able to have a high Seebeck value and a low thermal conductivity.[44] This type of material is a good candidate for an enhancement of the low efficiency in thermoelectric systems (around 1-5%).[45]
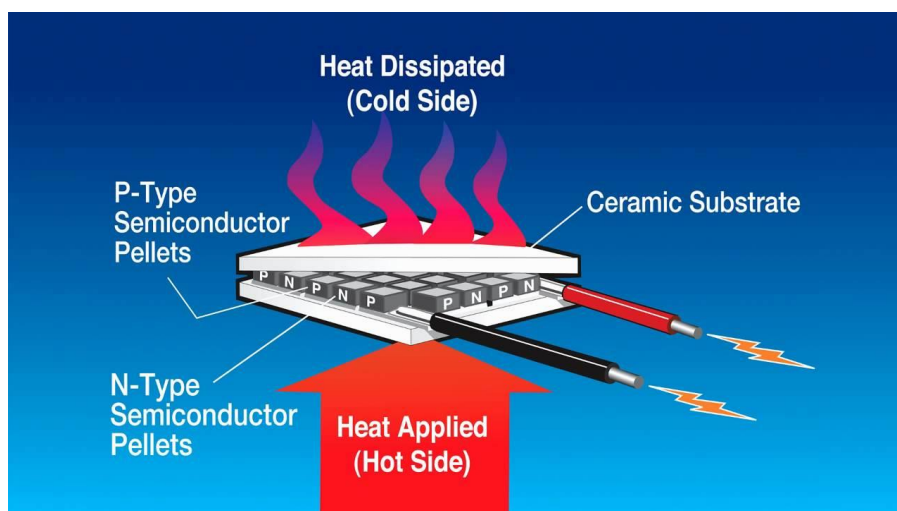
Figure 1.6. Schematic representation of a thermoelectric generator (Tellurex.com).

2.   Energy storage in battery

As potentially large amounts of low-temperature heats are available from industries and renewable energy sources (solar and geothermal sources), it could be interesting to be able to store this thermal energy like electricity inside a battery. However for such an application, the thermal energy cannot be simply store inside an isolated tank filled with water (or other liquids), which acts as a heat carrier. This low-grade heat needs to interact with reactants and to induce a chemical reaction, which produces compounds that can be used as electroactive species inside an electrochemical cell. In the following sections, the energy storage device and the chemistry applied for the thermal energy conversion are described.

2.1.   Redox flow battery

Regarding the storage of electricity, elelctrochemical systems are particularly interesting because they can reach high energy density and can be modulated according to the need of the users. Consequently, batteries seem to be the ideal candidate to deal with the surplus of production in the electrical network, which happens frequently when there is a lower demand than the projected one. Since these excesses of available energy might be lost in the grid, the storage will optimize the electricity production and allows compensating the period when lack of power occurs. This ability to regulate the demand and the availability of the resources are of great interest regarding intermittent renewable energies. Indeed, the electricity from wind or solar sources are not produced constantly and have peaks of production depending the weather, the time of the day or year and others environmental apsects. Furthermore, theses peaks of production do not always fit in time with the moment of the need for power. Thus, the implementation on large scale of electrochemical devices should be economically advantageous and environmentaly with a better use of the ressources.

For such purposes, a wide interest has been devoted to redox flow batteries (RFBs), which can have a large flexibity between the energy and the power capacity by using external retention tanks for the electrolyte.[46–48] In RFBs, the energy and the power capacity are independant from each other, as the energy capacity depends on the volume of the redox electrolyte and the power capacity on the dimensions, numbers and organization of the electrochemical cells. According to the needs, the RFB can be adjusted and sized.

RFBs have been widely described in many reviews.[47,49–51] Here, in Fig. 1.7, a scheme of the RFB technology is represented with one electrochemical cell with the positive and negative electrode. As it is mentioned in its name, RBFs can charge large volumes of redox electrolyte by pumping the solution from external tanks to the cell. The positive and negative electrolytes are separated by a membrane, which avoids also the contact between both electrodes. During the charging step, an electrical current or a voltage potential is applied to induce the reduction of the redox active molecule of the (−) side ($M^x \rightarrow M^{x-1}$) and the oxidation of the redox species on the (+) side ($N^y \rightarrow N^{y+1}$). As one electron is gained for the reduction from the oxidation in the other side, this charge transfer needs to be equilibrate by the migration of ions from the supporting electrolyte (S^-, S^+) through the membrane. Depending on the current and

time of the electrolysis, the redox species reach a certain state of charge according to the con-centrentration and volume of the electrolyte (*e.g.* SOC = 50% if half of the redox species are charged). After the charging step, the electrolyte is stored in separated containers to prevent from self-discharge until electricity is required.
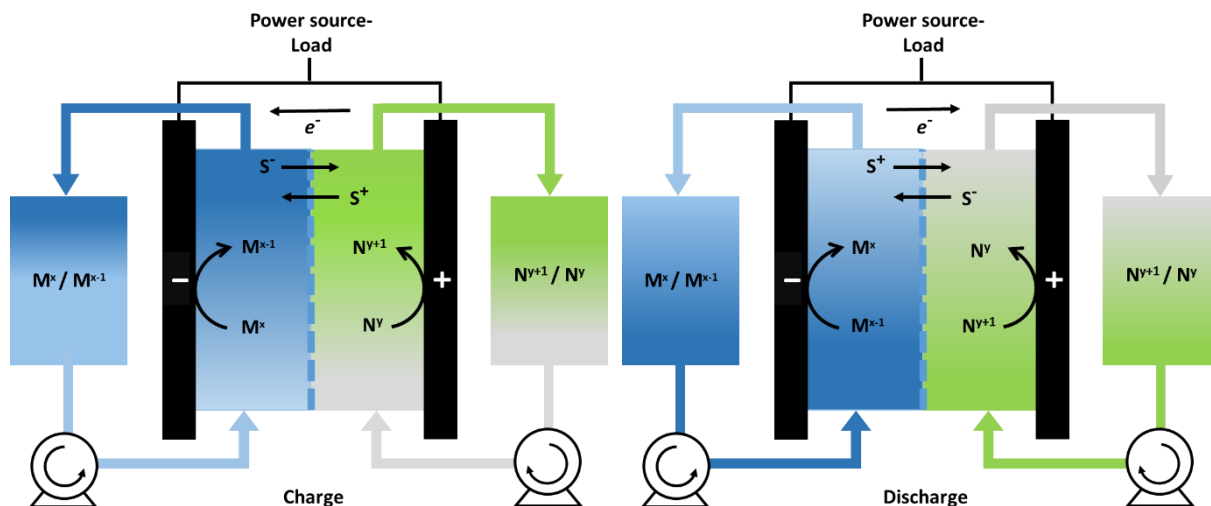
Figure 1.7. Schematic representation of RFB with the electrical charge (on the left) and discharge (on the right).

When the charged electrolytes are circulating again in the electrochemical cell, they will spontenaously react in the opposite way as during the charging step (discharge in Fig. 1.7) and oxidation occurs on the negative side and reduction on the positive one. Finally, the initial redox active ions (M^x, N^y) are regenerated and can be charged again. The ability of RFBs to perrform multiple charge/discharge cycles allows a great flexibility to store energy during rel-atively short or long time depending on the application.

In the RFB set-up, a critical component is the membrane. The role of the membrane is to separate to two half-cells by preventing the diffusion and mixing of the electroactive species on both sides of the battery. However, the separator needs also to keep the electroneutrality of both electrolytes. In the same time, the membrane avoids the electrodes to be in contact and to shortcut the electrical circuit. The ideal membrane should fullfill the following criteria:[52]

- High ionic conductivity of the supporting electrolyte to balance the electron migration during the charge and discharge of the cell: the charge carriers need to preserve the

electroneutrality of the full circuit. Bad conductivity will induce ohmic resistance and therefore heating effects. This will affect drastically the voltage and energy efficency of the RFB.

- High ionic selectivity to avoid the migration, crossover and mixing of the redox mediators: if the charged mediators can cross the membrane, the coulombic efficiency will drop because of the self-discharge by contact between the two sides.

- Chemical stability: with high content of corrosive acids or the use of organic solvents, the separator needs to stay stable in these harsh environments. Additonally the presence of oxidative or reducing compounds can enhance the deterioration of the membrane.

- Mechanical stability: as usually the cells are compressed and the circulating electrolyte can have a high pressure, the mechanical strength of the membrane has to resist to the pressure applied.

- Long life time: for long term cycling, the membrane needs to stay stable and therefore needs to be chemically and mechanically resistant to the RFB specific conditons

Three main types of membranes can be listed for RFB application: anionic, cationic, and porous (or non-ionic) membranes.[52,53] Anionic exchange membrane are selective to anions and are particularly interesting to limit the crossover of positively charged redox mediators, which are present in the electrolyte compostion. Event if the selectivity is high for this type of separator, their conductivity and chemical stability can be relatively poor. To improve the chemical resitance, they are commonly reinforced with a layer of polymer such as polyethylene (FAP-330-PE from Fumatech), perfluoroalkoxy alkanes (FAPQ-3100-PFA from Fumatech) or polyether ether ketone (FAB-130-PEEK from Fumatech). Already, few commercial membranes such as Selemion (AGC Engineering Co.), Neosepta AHA (Astom), FAP (Fumatech, BWT group), AMI-7001 (Membrane international Inc.) have been tested.[53–56]

Cationic membranes are broadly applied in RFB because of their high conductivity for protons. The most common cationic exchange membrane is the Nafion (from Dupont), which is a polymer close to hydrophibic polytetrafluoroethylene (PTFE) with additional sulfonic acid

groups. This $-SO_3^-$ function forms channels in the Nafion structure that can be hydrated and where proton hoping can occur.[57,58] As many RFBs are based on an aqueous and acidic electrolyte, the protons can easily cross the membrane and induce a low resistance throught the membrane, which is advantageous regarding the voltage and energy efficicencies of the battery. However, the membrane may also be permeable to the cations from the redox mediator and can lower the coulombic efficiency. Different methods were done to improve the selectivity of cationic membranes by filling the pore to with inorganic materials (SiO_2)[59–61] or by imitating the Nafion with another sulfonated polymer.[62]

Porous membranes are a cheaper alternative to ionic membranes and have pores in the micrometer scale. A commercially available porous membrane that is used for RFB applications is the Daramic.[63] The crossover throught the pores are relatively consequent and the Daramic is usually modified by pore-filling with ion exchange resins and crosslinkers.[52,64,65] Modified nanofiltration membranes with SiO_2 are also proposed as porous separator and show promising performance to lower the price of the membrane.[66,67]

Another key element of the RFB is the electrode. The choice of the electrodes is mainly influenced by the electrolyte composition, which is targeted. The final electrodes of the RFB need to fullfill several conditions to allow a high performance of the cell:[68]

- High reactivity with the redox mediatior: the electron transfer at the electrode should only be limited by the diffusion of the redox species and not be by the kinetics at the heterogenous interface between the electrolyte and electrode. Therefore, the redox couple at the electrode should observe a reversible or quasi-reversible electrochemical behaviour. If an irreversible electron transfer process occurs at the electrode, the energy efficiency of the battery will be affected with losses of voltage to induce the slow electron transfer.

- No reactivity with the supporting electrolyte and solvent: to avoid the degradation of the electrolyte and to control the eletrochemistry inside the electrolyte, only the redox mediator has to react on the electrode. If the deterioration of the electrolyte occurs at the electrode, the side-products might interfere with the conductivity of the solution and with the electrochemistry at the heterogenous interface of the electrode.

- As for the membrane, the electrodes should be mechanically and chemically stable for a given electrolyte content. The degradation of the electrode might poison the electrolyte and decrease or modifiy its active surface area. The electrodes should also be resistant to highly oxidative or reductive conditions that can be encountered during the charge, discharge and resting storage modes.

- High active surface area is preferred to increase the proportion and probability of electrochemical reaction when the electrolyte is flowing inside the cell. When the reaction sites are maximized, the electrical current that can be applied or recover can reach higher values. It usually implies the use of porous electrodes that can be compressed in the battery.

The electrodes for RFB applications are often based on carbon material such as C-felt, which are very porous with a high active surface.[69] Even if the reversibility of the chemical reaction is not always optimal, its porosity, prize and compressibility still make these electrodes attractive with some treatments of their surface for enhancing the reactivity.[70–72] When a solid metal is depositied on the electrode during the charge of the battery (Fe, Cu), the metal cannot be stored in the external tank and the RFB loses its ability to decoupled the volume of charge species with the cell dimensions. To overpass this limitation, suspension of solid particles, on which the metal can be plated, have been tested to store the charged species in the external tanks. Theses conductive particles in suspension form an electrical conductive network and this type of electrode are called slurry electrodes.[73–75]

There is a large variety of electrolyte composition for the RFB and they are commonly classified between aqueous and organic electrolytes. The choice of the redox mediator will determine the cell voltage according the potential of the negative and positive redox reaction. The solvent will set a limit for the concentrations of the supporting electrolyte and redox active species. Consquently, the ionic conductivity and power energy density of the RFB relies on the solubility of the salts in the circulating solution.

In the aqueous solvent, the supporting electrolyte is mainly an acid with a concentration of 1 to 5 M (H_2SO_4, HCl). The most commerciliased RFB is the all-vanadium RFB (V^{3+}/V^{2+}, VO_2^+/VO^{2+}).[76,77] With the vanadium battery, different mediators for the positive side have been investigated like iron (V^{3+}/V^{2+}, Fe^{3+}/Fe^{2+})[78,79], cerium (V^{3+}/V^{2+}, Ce^{4+}/Ce^{3+})[80], manganese

$(V^{3+}/ V^{2+}, Mn^{3+}/ Mn^{2+})^{81}$ and polyhalides $(V^{3+}/ V^{2+}, BrCl_2^-/ Br^-)^{50,82}$. On the negative side vanadium seems to be the ideal candidate because the reduced and charge mediator stays as an ion (V^{2+}) and is not a metallic solid like Fe, Pb, Zn (zinc-bromine RFB[83]).

Organic redox flow batteries can refer to a RFB with an organic solvent and/or organic mediator for the composition of the electrolyte. These types of RFB have been developed to improve the potential window of the battery cycling[84] and to target new redox mediators, which are not accessible in aqueous phases (mainly metal ligand complexes).[54,84–87] Ruthenium, vanadium, chromium, manganese, nickel, iron, cobalt and uranium complexes have been tested in acetonitrile or propylene carbonate solvents with tetraethylammonium tetrafluoroborate (TEABF$_4$) or 1-ethyl-3-methylimidazolium hexafluorophosphate (EMIPF$_6$) as charge carriers.[52] Ru,[88] V,[89] Cr[87] and Mn[85] are complexed with acetylacetonate (acac) and Ru[90], Ni, Fe with tris(2,2'-bipyridine) ligand (bpy)[55,84]. For most of theses batteries, the electrolyte is the same in the fully discharge state on both sides of the cell. During the charging step, the oxidized complex is kept in the (+)-tank and the reduced one in the (−)-tank. This is useful for rebalancing the volume of the electrode after a discharge and this should avoid huge losses of capacity of the battery. RFBs based on Li-battery are also considered as organic RFBs with their organic solvent composition.[91]

All-organic RFB (organic solvent and redox meditor) are also tested to improve the solubilty of the redox mediator that can be quiet low with metal-ligand complexes. The targeted redox mediator molecules for the negative electrolyte can be viologen[92,93], anthraquinone[94–96], aloxazine[97] and N-methylphthalimide (on (−)-side).[98] On the (+)-side, 2,2,6,6,-teramethyl-1-piperidinylxy (TEMPO) is the most commun organic compound for RFB.[92,93,98] Some organic polymer mediator are also tested in aqueous electrolytes for safety reason.[92]

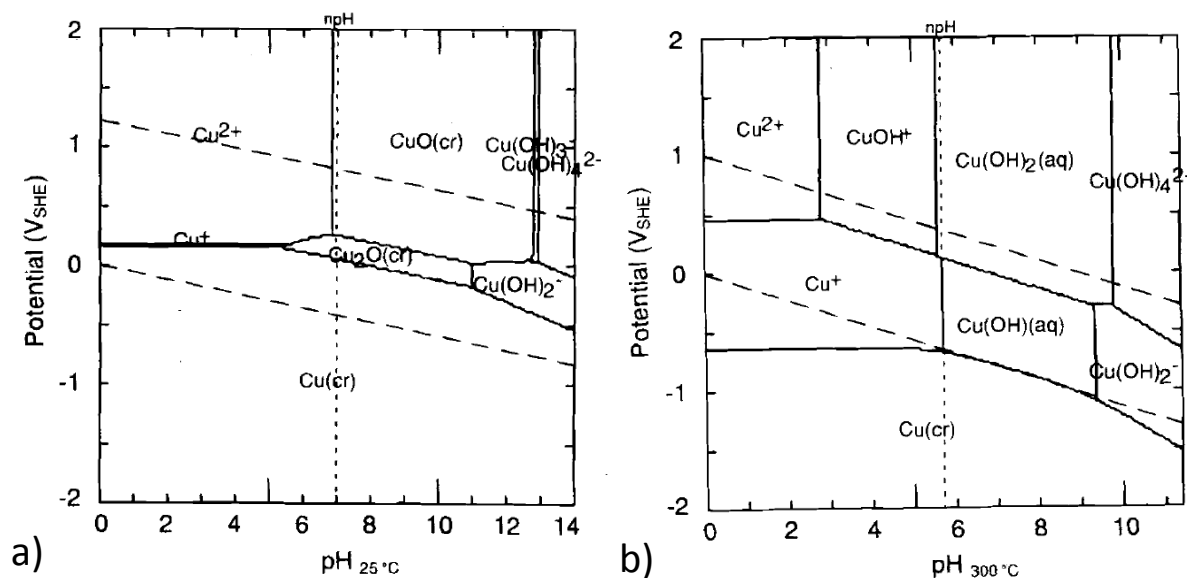## 2.2.   Copper redox flow battery

For this project, the goal is to work on a thermo-electrical system, which is able to store energy from electrical power or a thermal source. For that purpose, an all-copper redox flow battery (RBF) is investigated. Different Cu RFB have been described by using different solvents such as acetonitrile,[99] acetonitrile-water mixtures,[100] hydrochloric acid solutions,[101]

copper-containing ionic liquid[102,103] and deep eutectic solvents.[104] One of the first Cu secondary battery was built by Kratochvil and Betty with two redox couples Cu/CuClO$_4$ and Cu-ClO$_4$/Cu(ClO$_4$)$_2$ in a pure acetonitrile (ACN) solution. This battery developed a potential of 1.35 V and shows a good stabilization of Cu(I) in ACN.[99] However, perchlorates are explosive with copper at high temperatures, and so they are not suitable for thermally regenerative systems. Additionally, Parker *et al.* demonstrated a process, where segregated copper from roasted concentrates and ores was leached with a Cu(II) acetonitrile-water solution, followed by thermal disproportionation of Cu(I) from this solution to recover metallic Cu and the Cu(II) containing leaching solution.[105] It means that Cu(I) can be heated to give back metallic Cu, but also Cu(II), as Cu(I) is disproportionated. If Cu and Cu(II) are considered as electroactive species, Cu oxidation at the anode and Cu(II) reduction at the cathode can produce electric current and regenerate Cu(I). Then, the Cu(I) solution can be recycled and can again undergo a redox reaction induced by heat. The idea to couple the thermal charge by the Cu(I) disproportionation and to store Cu(II) and Cu in a electrochemical cell was previously proposed in an aqueous acetonitrile solvent by P. Peljo *et al.*[100]

In this RFB, Cu(I) needs to remain stable in solution after the discharge for the cycling of the battery. However, Cu(I) ions are not really stable in aqueous media.[106–108] They can disproportionate to Cu(II) ions and Cu particles. From the Pourbaix diagram of copper in aqueous solution (Fig. 1.8a), the area of Cu(I) stability is almost non present at 25°C.[109] It was also reported that the potential of the Cu RFB was decreasing with larger concentrations of water inside the solvent.[100]

One solution to have a stable Cu(I) in aqueous solution seems to heat it. From the Pourbaix diagram of copper (Fig. 1.8b), the potential window of Cu(I) stability is not negligible at high temperatures and in acidic conditions.[109] However, working at such high temperatures is not practical with aqueous solutions. By considering the Hard Soft Acid Base rule, Cu(I) is soft with a good π-donor character (comparing to Cu(II)) and acetonitrile is a solvent with π-acceptor characteristics. With a boiling point close to 82°C,[110] ACN seems to be an ideal complexing agent for the solubilisation of Cu(I) and for the disproportion of Cu(I) by its evaporation with waste heat.

Figure 1.8. Pourbaix diagram of copper in an aqueous solution at a) 25°C and b) 300°C.[109]

For the synthesis of the electroactive species, which is targeted for the Cu redox flow battery, a Cu(I) complex needs to be produced. The reducing ability of metallic Cu on Cu (II) in acetonitrile is known since 1923, when Morgan used this method for the preparation of cuprous chloride or bromide-mono(acetonitrile) complexes.[111]

In this work, the goal is to develop the concept of P. Peljo *et al.* in a purely organic solvent made of acetonitrile (for Cu(I) stabilization) and propylene carbonate (as a working liquid). By removing water from the system, higher potentials, higher power generations and a better heat conversion performance are expected for the heat to power all Cu-RFB. Indeed, if a solvent can be found with a high boiling point and no azeotropic properites with ACN, the heat required will be only assigned to the ACN distillation for the Cu(I) disproportionation. Propylene carbonate (PC) is chosen here as the co-solvent of acetonitrile because of its high boiling point and previous application in electrochemical storage systems (organic RFBs, lithium batteries). With this organic molecule, only the ACN will be distillated as the ACN and PC do not form an azeotropic liquid mixture.

The projected cycling process of the Cu RFB is described in Fig. 1.9. with a thermal charge from solar heat collectors:
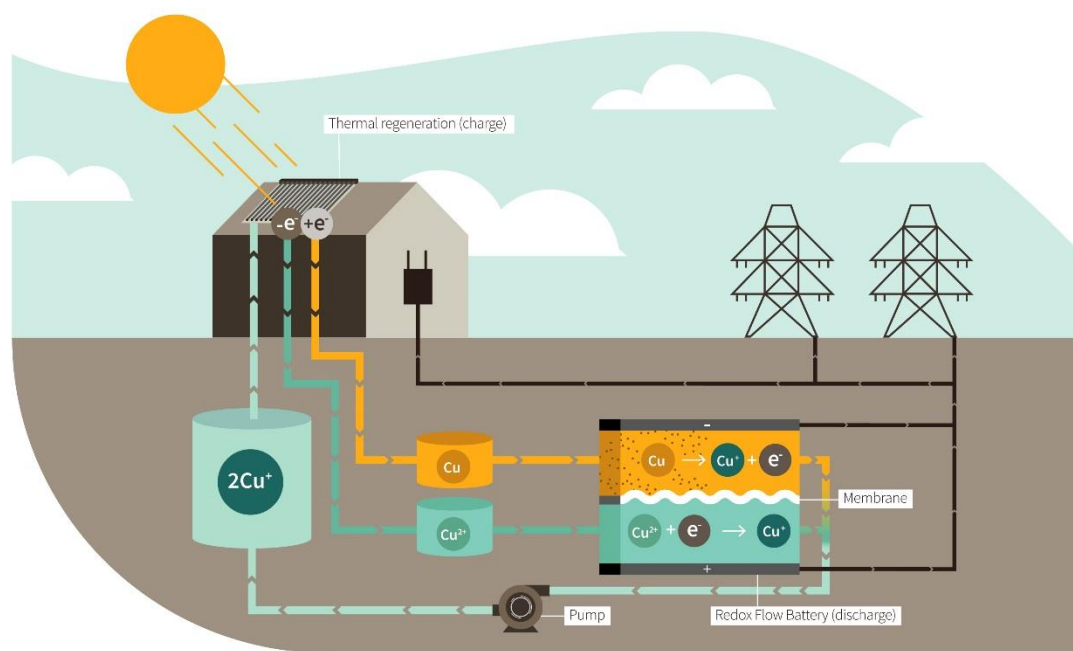
Figure 1.9. Schematic diagram for thermo-electrochemical copper battery.

3. Scope of the present work

This thesis work covers three main topics: (i) the electrochemistry of the Cu(I)/Cu(0) and Cu(II)/Cu(I) redox couples in acetonitrile and propylene carbonate, (ii) the thermodynamic of the Cu(I) disproportionation reaction induced by heat and the characterization of the vapour-liquid equilibrium for mixtures of acetonitrile and propylene carbonate, and (iii) the development of the Cu redox flow battery, which is able to be charged electrically and thermally.

In this first chapter, the heat conversion to electricity was presented and the technology of the redox flow battery is described, especially regarding the integration of Cu-based electrolyte and the coupling of the thermal charge with the electrical discharge in energy storage devices.

Chapter 2 gives an electrochemical characterization of the Cu(II)/Cu(I) in the organic solvent mixture containing acetonitrile and propylene carbonate. The influences of the temperature and of the propylene carbonate content are investigated for the cell potential, the diffusion and the kinetic parameters. With the temperature effect, the activation energies of the diffusion and electron transfer at the electrode are determined according to the PC content in solution.

Chapter 3 is devoted to the study of the $Cu(CH_3CN)_4^+$ deposition on Cu electrode. The simulations and fittings of the linear sweep voltammetry are calculated from an algorithm, which is applicable in the case of an instantaneous nucleation of a univalent ion on the same metal. The diffusion and kinetic parameters are fitted and simlulated with three equation derived from the main algorithm.

Chapter 4 is dedicated to the thermodynamic anaylsis of the Cu(I), acetonitrile and propylene carbonate electrolyte. The thermoanalytical technique used is the differential scanning calorimetry and this method allows determing precisely different thermodynamic parameters that are essential for the estimation of the energy efficiency of the thermal energy conversion to electrical power.

Chapter 5 is devoted to the development and optimization of the redox flow battery system. This section highlights the importance of the distance between electrodes in the cell

and the need to have a membrane, which is as ionically conductive as possible. Different modifications of the negative electrode are presented to deal with the cost and deterioration of the usual Cu foam electrode. An automatized set-up for the synthesis of Cu NPs demonstrates the ability to produce Cu slurry for battery applications.

Chapter 6 finally demonstrates the feasibility to couple thermal charging step with a redox flow battery to obtain an electrical power output. The performances of the heat to electricity conversion in the Cu flow cell reach efficiencies rarely obtained for a system, which can store the energy and is limited by the Carnot cycle efficiency

Chapter 7 summarizes the main results of the previous chapters and opens the discussion for further improvments for a potential scale-up of the Cu battery system to target industrial waste heat.

4. References

1. International Energy Agency (IEA). Combined heat and power: evaluating the benefits of greater global investment. (2008).

2. Martens, A. The energetic feasibility of CHP compared to the separate production of heat and power. *Applied Thermal Engineering* **18**, 935–946 (1998).

3. Hisazumi, Y., Yamasaki, Y. & Sugiyama, S. Proposal for a high efficiency LNG power-generation system utilizing waste heat from the combined cycle1Published in co-operation with the Japanese Society of Energy Resources.1. *Applied Energy* **60**, 169–182 (1998).

4. Shi, X. & Che, D. A combined power cycle utilizing low-temperature waste heat and LNG cold energy. *Energy Conversion and Management* **50**, 567–575 (2009).

5. Infelta, P. & Graetzel, M. *Thermodynamique: Principes et Applications*. (BrownWalker Press, 2006).

6. Reddy, V. S., Kaushik, S. C., Tyagi, S. K. & Panwar, N. An Approach to Analyse Energy and Exergy Analysis of Thermal Power Plants: A Review. *Smart Grid and Renewable Energy* **01**, 143–152 (2010).

7. Badr, O., Probert, S. D. & O'Callaghan, P. Rankine cycles for steam power-plants. *Applied Energy* **36**, 191–231 (1990).

8. Vetter, C., Wiemer, H.-J. & Kuhn, D. Comparison of sub- and supercritical Organic Rankine Cycles for power generation from low-temperature/low-enthalpy geothermal wells, considering specific net power output and efficiency. *Applied Thermal Engineering* **51**, 871–879 (2013).

9. Dincer, I. & Al-Muslim, H. Thermodynamic analysis of reheat cycle steam power plants. *Int. J. Energy Res.* **25**, 727–739 (2001).

10. Kurz, R. & Brun, K. Degradation in Gas Turbine Systems. *J. Eng. Gas Turbines Power* **123**, 70–77 (2000).

11. Roy, J. P., Mishra, M. K. & Misra, A. Performance analysis of an Organic Rankine Cycle with superheating under different heat source temperature conditions. *Applied Energy* **88**, 2995–3004 (2011).

12. Goswami, D. Y. & Kreith, F. *Energy Conversion*. (CRC Press, 2007).

13. Bao, J. & Zhao, L. A review of working fluid and expander selections for organic Rankine cycle. *Renewable and Sustainable Energy Reviews* **24**, 325–342 (2013).

14. Little, A. B. & Garimella, S. Comparative assessment of alternative cycles for waste heat recovery and upgrade. *Energy* **36**, 4492–4504 (2011).

15. Wali, E. Optimum working fluids for solar powered Rankine cycle cooling of buildings. *Solar Energy* **25**, 235–241 (1980).

16. Tchanche, B. F., Lambrinos, Gr., Frangoudakis, A. & Papadakis, G. Low-grade heat conversion into power using organic Rankine cycles – A review of various applications. *Renewable and Sustainable Energy Reviews* **15**, 3963–3979 (2011).

17. Papadopoulos, A. I., Stijepovic, M. & Linke, P. On the systematic design and selection of optimal working fluids for Organic Rankine Cycles. *Applied Thermal Engineering* **30**, 760–769 (2010).

18. Kanoglu, M. & Bolatturk, A. Performance and parametric investigation of a binary geothermal power plant by exergy. *Renewable Energy* **33**, 2366–2374 (2008).

19. Kanoğlu, M. & Çengel, Y. A. Improving the Performance of an Existing Air-Cooled Binary Geothermal Power Plant: A Case Study. *J. Energy Resour. Technol* **121**, 196–202 (1999).

20. Wall, G., Chuang, C.-C. & Ishida, M. Exergy study of the Kalina cycle. *Analysis and design of energy systems: analysis of industrial processes* **10**, 73–77 (1989).

21. Marston, C. H. & Hyre, M. Gas Turbine Bottoming Cycles: Triple-Pressure Steam Versus Kalina. *J. Eng. Gas Turbines Power* **117**, 10–15 (1995).

22. Kalina, A. I. Generation of Energy by Means of a Working Fluid, and Regeneration of a Working Fluid. (1982).

23. Kalina, A. I. Combined-Cycle System With Novel Bottoming Cycle. *J. Eng. Gas Turbines Power* **106**, 737–742 (1984).

24. Kalina, A. I. Combined Cycle and Waste Heat Recovery Power Systems Based on a Novel Thermodynamic Energy Cycle Utilizing Low-Temperature Heat for Power Generation. V001T02A003 (1983).

25. Saadatfar, B., Fakhrai, R. & Fransson, T. Thermodynamic vapor cycles for converting low-to medium-grade heat to power: a state-of-the-art review and future research pathways. *J Macro Trends Energy Sustain* **2**, (2014).

26. Jurgen, R. K. The promise of the Kalina cycle: Using an ammonia-water mixture, the Kalina steam cycle may permit thermal-mechanical-electrical energy conversion efficiencies of 45 percent. *IEEE Spectrum* **23**, 68–70 (1986).

27. Ogriseck, S. Integration of Kalina cycle in a combined heat and power plant, a case study. *Applied Thermal Engineering* **29**, 2843–2848 (2009).

28. Achilli, A., Cath, T. Y. & Childress, A. E. Power generation with pressure retarded osmosis: An experimental and theoretical investigation. *Journal of Membrane Science* **343**, 42–52 (2009).

29. Yip, N. Y. & Elimelech, M. Thermodynamic and Energy Efficiency Analysis of Power Generation from Natural Salinity Gradients by Pressure Retarded Osmosis. *Environ. Sci. Technol.* **46**, 5230–5239 (2012).

30. Tamburini, A., Cipollina, A., Papapetrou, M., Piacentino, A. & Micale, G. 7 - Salinity gradient engines. in *Sustainable Energy from Salinity Gradients* 219–256 (Woodhead Publishing, 2016).

31. Cipollina, A., Micale, G. & Rizzuti, L. *Seawater Desalination: Conventional and Renewable Energy Processes*. (Springer Science & Business Media, 2009).

32. Lawson, K. W. & Lloyd, D. R. Membrane distillation. *Journal of Membrane Science* **124**, 1–25 (1997).

33. McGinnis, R. L., McCutcheon, J. R. & Elimelech, M. A novel ammonia–carbon dioxide osmotic heat engine for power generation. *Journal of Membrane Science* **305**, 13–19 (2007).

34. Ranck, J. P. A preliminary technical and economic investigation of sea water demineralization by ion-exchange for calcium and bicarbonate ions and their subsequent removal by thermal decomposition (1). *Desalination* **6**, 75–85 (1969).

35. Figure078d. http://www.separationprocesses.com/Distillation/Fig078d.htm.

36. Maloney Jr, J. D. & Robertson, R. C. *Thermodynamic study of ammonia-water heat power cycles*. http://oai.dtic.mil/oai/oai?verb=getRecord&metadataPrefix=html&identifier=ADA297656 (1953).

37. Kongtragool, B. & Wongwises, S. A review of solar-powered Stirling engines and low temperature differential Stirling engines. *Renewable and Sustainable Energy Reviews* **7**, 131–154 (2003).

38. Akbari, A. D. & Mahmoudi, S. M. S. Thermoeconomic analysis & optimization of the combined supercritical CO2 (carbon dioxide) recompression Brayton/organic Rankine cycle. *Energy* **78**, 501–512 (2014).

39. Öström, T. & Karthäuser, J. Method for conversion of low temperature heat to electricity and cooling, and system therefore. (2012).

40. Hamid Elsheikh, M. *et al.* A review on thermoelectric renewable energy: Principle parameters that affect their performance. *Renewable and Sustainable Energy Reviews* **30**, 337–355 (2014).

41. Nolas, G. S., Morelli, D. T. & Tritt, T. M. Skutterudites: A phonon-glass-electron crystal approach to advanced thermoelectric energy conversion applications. *Annual Review of Materials Science* **29**, 89–116 (1999).

42. Bian, Z. & Shakouri, A. Enhanced solid-state thermionic emission in nonplanar heterostructures. *Applied physics letters* **88**, 012102 (2006).

43. Snyder, G. J. & Toberer, E. S. Complex thermoelectric materials. *Nature materials* **7**, 105–114 (2008).

44. Bubnova, O. *et al.* Semi-metallic polymers. *Nat Mater* **13**, 190–194 (2014).

45. Champier, D. Thermoelectric generators: A review of applications. *Energy Conversion and Management* **140**, 167–181 (2017).

46. Nguyen, T. & Savinell, R. F. Flow Batteries. *Electrochem. Soc. Interface* **19**, 54–56 (2010).

47. Alotto, P., Guarnieri, M. & Moro, F. Redox flow batteries for the storage of renewable energy: A review. *Renewable and Sustainable Energy Reviews* **29**, 325–335 (2014).

48. Noack, J., Roznyatovskaya, N., Herr, T. & Fischer, P. The Chemistry of Redox-Flow Batteries. *Angewandte Chemie International Edition* **54**, 9776–9809 (2015).

49. Skyllas-Kazacos, M., Chakrabarti, M. H., Hajimolana, S. A., Mjalli, F. S. & Saleem, M. Progress in Flow Battery Research and Development. *J. Electrochem. Soc.* **158**, R55–R79 (2011).

50. Weber, A. Z. *et al.* Redox flow batteries: a review. *J Appl Electrochem* **41**, 1137 (2011).

51. Perry, M. L. & Weber, A. Z. Advanced Redox-Flow Batteries: A Perspective. *J. Electrochem. Soc.* **163**, A5064–A5067 (2016).

52. Shin, S.-H., Yun, S.-H. & Moon, S.-H. A review of current developments in non-aqueous redox flow batteries: characterization of their membranes for design perspective. *RSC Advances* **3**, 9095–9116 (2013).

53. Schwenzer, B. *et al.* Membrane Development for Vanadium Redox Flow Batteries. *ChemSusChem* **4**, 1388–1406 (2011).

54. Liu, Q., Sleightholme, A. E. S., Shinkle, A. A., Li, Y. & Thompson, L. T. Non-aqueous vanadium acetylacetonate electrolyte for redox flow batteries. *Electrochemistry Communications* **11**, 2312–2315 (2009).

55. Mun, J. *et al.* Non-Aqueous Redox Flow Batteries with Nickel and Iron Tris(2,2′-bipyridine) Complex Electrolyte. *Electrochem. Solid-State Lett.* **15**, A80–A82 (2012).

56. Chakrabarti, M. H., Dryfe, R. A. W. & Roberts, E. P. L. Evaluation of electrolytes for redox flow battery applications. *Electrochimica Acta* **52**, 2189–2195 (2007).

57. Yan, L., Zhu, S., Ji, X. & Lu, W. Proton Hopping in Phosphoric Acid Solvated Nafion Membrane: A Molecular Simulation Study. *J. Phys. Chem. B* **111**, 6357–6363 (2007).

58. Devanathan, R. *et al.* Atomistic Simulation of Water Percolation and Proton Hopping in Nafion Fuel Cell Membrane. *J. Phys. Chem. B* **114**, 13681–13690 (2010).

59. Miyake, N., Wainright, J. S. & Savinell, R. F. Evaluation of a Sol-Gel Derived Nafion/Silica Hybrid Membrane for Proton Electrolyte Membrane Fuel Cell Applications: I. Proton Conductivity and Water Content. *J. Electrochem. Soc.* **148**, A898–A904 (2001).

60. Mahreni, A., Mohamad, A. B., Kadhum, A. A. H., Daud, W. R. W. & Iyuke, S. E. Nafion/silicon oxide/phosphotungstic acid nanocomposite membrane with enhanced proton conductivity. *Journal of Membrane Science* **327**, 32–40 (2009).

61. Zhang, B. *et al.* Enhanced proton conductivity of Nafion nanohybrid membrane incorporated with phosphonic acid functionalized graphene oxide at elevated temperature and low humidity. *Journal of Membrane Science* **518**, 243–253 (2016).

62. Kim, S. *et al.* Cycling performance and efficiency of sulfonated poly(sulfone) membranes in vanadium redox flow batteries. *Electrochemistry Communications* **12**, 1650–1653 (2010).

63. Wei, X. *et al.* Microporous separators for Fe/V redox flow batteries. *Journal of Power Sources* **218**, 39–45 (2012).

64. Mohammadi, T. & Skyllas-Kazacos, M. Characterisation of novel composite membrane for redox flow battery applications. *Journal of Membrane Science* **98**, 77–87 (1995).

65. Haddadi-asl, V. & Mohammadi, T. Effect of Processing Methods and Conditions on Properties of Conductive Carbon-Polyolefins Composite. *Iranian Polymer Journal* **5**, 153–164 (1996).

66. Zhang, H., Zhang, H., Li, X., Mai, Z. & Wei, W. Silica modified nanofiltration membranes with improved selectivity for redox flow battery application. *Energy & Environmental Science* **5**, 6299–6303 (2012).

67. Zhang, H., Zhang, H., Li, X., Mai, Z. & Zhang, J. Nanofiltration (NF) membranes: the next generation separators for all vanadium redox flow batteries (VRBs)? *Energy & Environmental Science* **4**, 1676–1679 (2011).

68. Amstutz, V. Redox flow battery and indirect water electrolysis. *Infoscience* https://infoscience.epfl.ch/record/213651 (2015) doi:10.5075/epfl-thesis-6813.

69. Kim, K. J., Kim, Y.-J., Kim, J.-H. & Park, M.-S. The effects of surface modification on carbon felt electrodes for use in vanadium redox flow batteries. *Materials Chemistry and Physics* **131**, 547–553 (2011).

70. Li, X., Huang, K., Liu, S., Tan, N. & Chen, L. Characteristics of graphite felt electrode electrochemically oxidized for vanadium redox battery application. *Transactions of Nonferrous Metals Society of China* **17**, 195–199 (2007).

71. Sun, B. & Skyllas-Kazakos, M. Chemical modification and electrochemical behaviour of graphite fibre in acidic vanadium solution. *Electrochimica Acta* **36**, 513–517 (1991).

72. Sun, B. & Skyllas-Kazacos, M. Modification of graphite electrode materials for vanadium redox flow battery application—I. Thermal treatment. *Electrochimica Acta* **37**, 1253–1260 (1992).

73. Petek, T. J., Hoyt, N. C., Savinell, R. F. & Wainright, J. S. Slurry electrodes for iron plating in an all-iron flow battery. *Journal of Power Sources* **294**, 620–626 (2015).

74. Petek, T. J., Hoyt, N. C., Savinell, R. F. & Wainright, J. S. Characterizing slurry electrodes using electrochemical impedance spectroscopy. *Journal of the Electrochemical Society* **163**, A5001–A5009 (2016).

75. Yan, W. *et al.* All-polymer particulate slurry batteries. *Nat Commun* **10**, 1–11 (2019).

76. Rychcik, M. & Skyllas-Kazacos, M. Characteristics of a new all-vanadium redox flow battery. *Journal of Power Sources* **22**, 59–67 (1988).

77. Skyllas-Kazacos, M., Rychcik, M., Robins, R. G., Fane, A. G. & Green, M. A. New all-vanadium redox flow cell. *Journal of the Electrochemical Society* **133**, 1057 (1986).

78. Wang, W. *et al.* A New Fe/V Redox Flow Battery Using a Sulfuric/Chloric Mixed-Acid Supporting Electrolyte. *Advanced Energy Materials* **2**, 487–493 (2012).

79. Wang, W. *et al.* A new redox flow battery using Fe/V redox couples in chloride supporting electrolyte. *Energy & Environmental Science* **4**, 4068–4073 (2011).

80. Liu, Y., Xia, X. & Liu, H. Studies on cerium (Ce4+/Ce3+)–vanadium(V2+/V3+) redox flow cell—cyclic voltammogram response of Ce4+/Ce3+ redox couple in H2SO4 solution. *Journal of Power Sources* **130**, 299–305 (2004).

81. Xue, F.-Q., Wang, Y.-L., Wang, W.-H. & Wang, X.-D. Investigation on the electrode process of the Mn(II)/Mn(III) couple in redox flow battery. *Electrochimica Acta* **53**, 6636–6642 (2008).

82. Skyllas-Kazacos, M. Novel vanadium chloride/polyhalide redox flow battery. *Journal of Power Sources* **124**, 299–302 (2003).

83. Ponce de León, C., Frías-Ferrer, A., González-García, J., Szánto, D. A. & Walsh, F. C. Redox flow cells for energy conversion. *Journal of Power Sources* **160**, 716–732 (2006).

84. Kim, J.-H. *et al.* Development of metal-based electrodes for non-aqueous redox flow batteries. *Electrochemistry Communications* **13**, 997–1000 (2011).

85. Sleightholme, A. E. S. *et al.* Non-aqueous manganese acetylacetonate electrolyte for redox flow batteries. *Journal of Power Sources* **196**, 5742–5745 (2011).

86. Yamamura, T., Shiokawa, Y., Yamana, H. & Moriyama, H. Electrochemical investigation of uranium β-diketonates for all-uranium redox flow battery. *Electrochimica Acta* **48**, 43–50 (2002).

87. Liu, Q. *et al.* Non-aqueous chromium acetylacetonate electrolyte for redox flow batteries. *Electrochemistry Communications* **12**, 1634–1637 (2010).

88. Chakrabarti, M. H., Roberts, E. P. L., Bae, C. & Saleem, M. Ruthenium based redox flow battery for solar energy storage. *Energy Conversion and Management* **52**, 2501–2508 (2011).

89. Shinkle, A. A., Sleightholme, A. E. S., Griffith, L. D., Thompson, L. T. & Monroe, C. W. Degradation mechanisms in the non-aqueous vanadium acetylacetonate redox flow battery. *Journal of Power Sources* **206**, 490–496 (2012).

90. Matsuda, Y. *et al.* A rechargeable redox battery utilizing ruthenium complexes with non-aqueous organic electrolyte. *J Appl Electrochem* **18**, 909–914 (1988).

91. Brushett, F. R., Vaughey, J. T. & Jansen, A. N. An All-Organic Non-aqueous Lithium-Ion Redox Flow Battery. *Advanced Energy Materials* **2**, 1390–1396 (2012).

92. Janoschka, T. *et al.* An aqueous, polymer-based redox-flow battery using non-corrosive, safe, and low-cost materials. *Nature* **527**, 78–81 (2015).

93. Liu, T., Wei, X., Nie, Z., Sprenkle, V. & Wang, W. A Total Organic Aqueous Redox Flow Battery Employing a Low Cost and Sustainable Methyl Viologen Anolyte and 4-HO-TEMPO Catholyte. *Advanced Energy Materials* **6**, 1501449 (2016).

94. Huskinson, B. *et al.* A metal-free organic–inorganic aqueous flow battery. *Nature* **505**, 195–198 (2014).

95. Huskinson, B., Marshak, M., Gerhardt, M. & Aziz, M. J. Cycling of a Quinone-Bromide Flow Battery for Large-Scale Electrochemical Energy Storage. *ECS Transactions* (2014) doi:10.1149/06137.0027ecst.

96.   Lin, K. *et al.* Alkaline quinone flow battery. *Science* **349**, 1529–1532 (2015).

97.   Lin, K. *et al.* A redox-flow battery with an alloxazine-based organic electrolyte. *Nat Energy* **1**, 1–8 (2016).

98.   Li, Z. *et al.* Electrochemical Properties of an All-Organic Redox Flow Battery Using 2,2,6,6-Tetramethyl-1-Piperidinyloxy and N-Methylphthalimide. *Electrochem. Solid-State Lett.* **14**, A171–A173 (2011).

99.   Kratochvil, B. & Betty, K. R. A Secondary Battery Based on the Copper(II)-(I) and (I)-(0) Couples in Acetonitrile. *J. Electrochem. Soc.* **121**, 851–854 (1974).

100.   Peljo, P., Lloyd, D., Doan, N., Majaneva, M. & Kontturi, K. Towards a thermally regenerative all-copper redox flow battery. *Phys. Chem. Chem. Phys.* **16**, 2831–2835 (2014).

101.   Leung, P. *et al.* Evaluation of electrode materials for all-copper hybrid flow batteries. *Journal of Power Sources* **310**, 1–11 (2016).

102.   Schaltin, S. *et al.* Towards an all-copper redox flow battery based on a copper-containing ionic liquid. *Chem. Commun.* **52**, 414–417 (2016).

103.   Li, Y. *et al.* A non-aqueous all-copper redox flow battery with highly soluble active species. *Electrochimica Acta* **236**, 116–121 (2017).

104.   Lloyd, D., Vainikka, T. & Kontturi, K. The development of an all copper hybrid redox flow battery using deep eutectic solvents. *Electrochimica Acta* **100**, 18–23 (2013).

105.   Parker, A. J., Muir, D. M., Smart, Y. C. & Avraamides, J. An application of acetonitrile leaching and disproportionation. *Hydrometallurgy* **7**, 213–233 (1981).

106.   Raymond C. Bott, †, Graham A. Bowmaker, *, Carol A. Davis, †, Gregory A. Hope, * & Jones‡, B. E. Crystal Structure of [Cu4(tu)7](SO4)2]·H2O and Vibrational Spectroscopic Studies of Some Copper(I) Thiourea Complexes. http://pubs.acs.org/doi/abs/10.1021/ic970910q (1998).

107.   Rizvi, M. A. Complexation modulated redox behavior of transition metal systems (review). *Russ J Gen Chem* **85**, 959–973 (2015).

108.   Rizvi, M. A., Akhoon, S. A., Maqsood, S. R. & Peerzada, G. M. Synergistic effect of perchlorate ions and acetonitrile medium explored for extension in copper redoximetry. *J Anal Chem* **70**, 633–638 (2015).

109.   Beverskog, B. & Puigdomenech, I. Revised Pourbaix Diagrams for Copper at 25 to 300°C. *J. Electrochem. Soc.* **144**, 3476–3483 (1997).

110.   Di Cave, S. & Mazzarotta, B. Isobaric vapor-liquid equilibria for the binary systems formed by acetonitrile and aromatic hydrocarbons. *J. Chem. Eng. Data* **36**, 293–297 (1991).

111.   Morgan, H. H. CCCXLII.—Preparation and stability of cuprous nitrate and other cuprous salts in presence of nitriles. *J. Chem. Soc., Trans.* **123**, 2901–2907 (1923).

Chapter II

Cu^{2+}/Cu$^+$ electrochemistry in acetonitrile and propylene carbonate mixtures

Based on the submitted paper,

Electrochemistry of Cu(II)/Cu(I) in acetonitrile and propylene carbonate,

S. Maye, H. H. Girault & P. Peljo,

Abstract

In this Chapter II, the objective is to understand the electrochemistry of the positive side of the all-Cu redox flow battery. Therefore, the redox mechanism of the Cu^{2+}/Cu$^+$ couple is described for different solvent compositions with acetonitrile (ACN) and propylene carbonate (PC). The diffusion of the redox species and the kinetic of the electron transfer at the working electrode are investigated and compared with the variation of the PC content in the Cu(I)-ACN solution. Furthermore, the influence of the temperature on the Cu(I)-ACN-PC system is characterized and allows the calculation of the activation energies for the diffusion and kinetic parameters. With the redox potential depending on the temperature, the Gibbs energy, the entropy and the enthalpy of the electron transfer reactions have been determined for the Cu^{2+}/Cu$^+$ redox couple.

Cyclic voltammetry (CV) and linear sweep voltammetry (LSV) are the main electrochemical techniques that are utilized in this chapter for the determination of the diffusion coefficients (D), heterogeneous rate constants (k^0) and charge transfer coefficients (α). During the data analysis, the calculation of the diffusion coefficient is based on the Randles-Sevcik equation with CV or on the Levich equation with LSV at rotating disk electrode (RDE). The values of the heterogeneous rate constant are extracted from CV with the Nicholson method for quasi-reversible system and with the Koutecký-Levich equation for LSV at RDE. The general trends are in good agreement with previous works; the kinetics and diffusion are faster with higher temperatures and when small ratios of PC are introduced in the solvent composition.

1.   Introduction

The interest for the study of the Cu^{2+}/Cu^+ redox couple results from the idea of Peljo *et al.* to build an energy storage system based on the thermodynamics and electrochemistry of copper.[1] The thermally regenerative all-copper redox flow battery described in this paper uses low temperature heat sources to charge the battery and to store energy under a chemical form. This heat to chemical energy conversion was previously applied by A.J. Parker *et al.* to purify copper.[2] In their work, Parker *et al.* demonstrated a process, where segregated copper from roasted concentrates and ores were leached with a Cu^{2+} containing acetonitrile-water solution to form Cu^+ complex stabilized by ACN. This method relies on the comproportionation of Cu with Cu^{2+} to $2Cu^+$ in ACN and is followed by the thermal disproportionation of Cu^+ from this solution to recover pure metallic Cu particles and the Cu^{2+} containing leaching solution.[3] It means that Cu^+ solutions can be heated to remove the complexing ACN to destabilize the Cu^+ and give back metallic Cu, but also Cu^{2+}, as Cu^+ is disproportionated during the distillation of the ACN.[4,5] If Cu and Cu^{2+} are considered as electroactive species, Cu oxidation at the anode and Cu^{2+} reduction at the cathode can produce electric current and regenerate Cu^+. Then, the Cu^+ solution can be recycled and then again undergoes a redox reaction induced by heat (distillation of ACN). The cycling process of the proposed Cu RFB is described in Scheme 2.1. The originality of this approach is to couple these processes of RFB and thermal recycling of the metallic Cu and Cu^{2+} with the Cu^+ ion.

Different Cu RFBs have been studied using different solvents such as acetonitrile [6], acetonitrile-water mixtures [1], hydrochloric acid solutions [7], copper-containing ionic liquids [8]

and deep eutectic solvents [9]. One of the first Cu secondary battery was built by Kratochvil and Betty with two redox couples $Cu/CuClO_4$ and $CuClO_4/Cu(ClO_4)_2$ in a pure acetonitrile (ACN) solution [6]. This battery developed a potential of 1.35 V and shows the strong stabilization of Cu^+ in ACN [6]. However, perchlorates are explosive with copper at high temperatures, making this approach unsuitable for scale-up if the thermal process of A. J. Parker is applied during the charge of the battery.
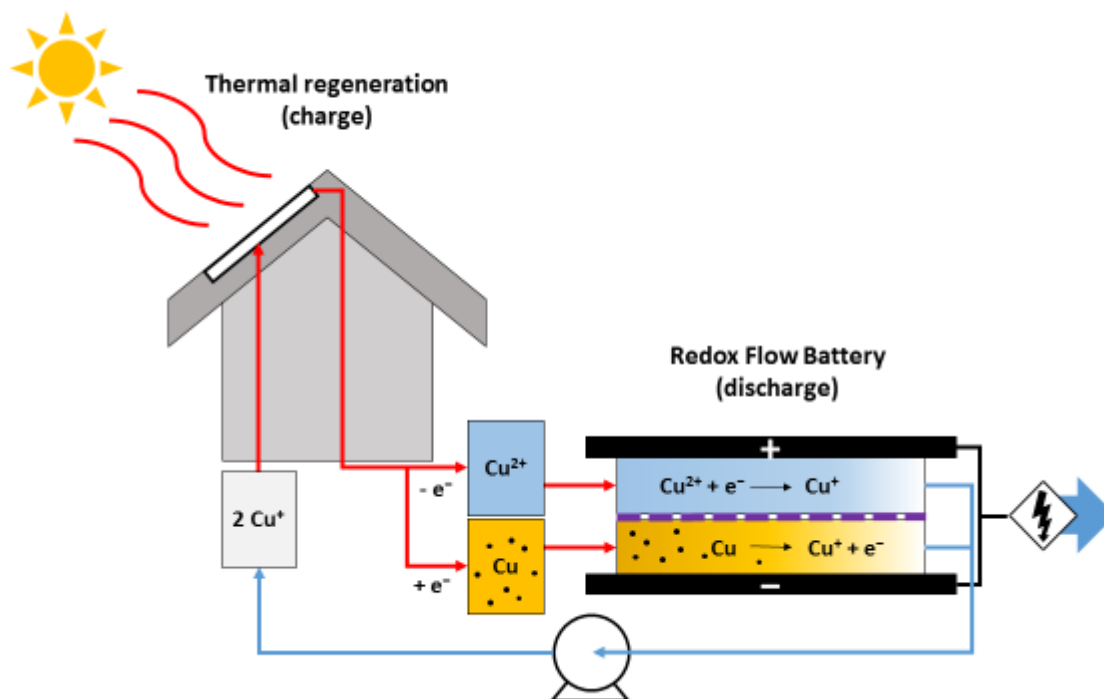
Scheme 2.1. Full representation of the all-Cu redox flow battery coupled with thermal treatment of the Cu(I) as a charging process.

In the RFB, Cu^+ needs to remain stable in solution after the discharge for the cycling of the battery. However, Cu^+ ions are not really stable in aqueous media [10–12], as they readily disproportionate to Cu^{2+} ions and metallic Cu. From the Pourbaix diagram of copper in aqueous solution, the area of Cu^+ stability is almost absent at 25°C [13]. Consequently, ACN is chosen to stabilize Cu^+, because it is known to complex well with Cu^+ [14,15] and because the boiling point of ACN is relatively low (82°C).[16] As ACN is evaporated during the regeneration of Cu and Cu^{2+}, a co-solvent, which will not undergo a physical change, is required. Water was proposed earlier, but it was reported that the voltage of the Cu RFB decreases with larger concentrations of water inside the solvent [1]. Propylene carbonate (PC) is selected here for its high boiling point (242°C) and for its high dielectric constant. It is for similar reasons that PC was also tested in some electrolytes for Li batteries.[17–19]

Considering a Cu-ACN-PC battery with heat to power conversion, the characterization of the electrochemistry needs to be described to check the limits that will be faced and the feasibility of such a system. The electrochemistry of the Cu^+/Cu in ACN has been already studied by Atek *et al.* [20] and will be described in the following chapter. The main focus of this chapter is dedicated to the electron transfer in the Cu^{2+}/Cu^+ redox couple. Already few papers have described the electrochemistry of Cu^+ in pure ACN,[21] in water [22–24], in ACN-water mixtures[25] and in ionic liquids.[26] However, no complete studies are available from our knowledge for the description of the electrochemistry of Cu in ACN-PC solvent mixtures. In this chapter the kinetics, mass transfer and thermodynamics parameters for the electron transfer at a working electrode are studied and characterized.

2.   Theory

2.1.   Mass transport and kinetics with potential sweep methods

During the recording of a CV, the potential at the working electrode changes with time, cycling between an initial potential (E_i) and a final one (E_f). For potential sweep methods (LSV and CV), the speed of the measurement is determined by the scan rate (v in $V \cdot s^{-1}$). Equations 2.1 and 2.2 describe the evolution of the potential with time from a low to high potential (Eq. 2.1) and from a high to a low potential (Eq. 2.2). In the case of LSV, the potential scanning is applied only in one way for either oxidation or reduction of the electroactive species:

$$E(t) = E_i + vt \tag{2.1}$$

$$E(t) = E_f - vt \tag{2.2}$$

At a WE, the potential of the electrode is given by the Nernst equation (Eq. 2.3), when the redox reaction is at equilibrium:

$$E_{eq} = E^0 + \frac{RT}{nF}\ln\left(\frac{a_o}{a_r}\right) = E^{0\prime} + \frac{RT}{nF}\ln\left(\frac{C_o^*}{C_r^*}\right) \tag{2.3}$$

with E_{eq} as the equilibrium potential at the working electrode in V, E^0 the standard potential and $E^{0\prime}$ the formal redox potential of the compound in V.

For a reversible system, the change of potential induces a modification of the ratio between the concentration of the oxidized (C_o) and reduced (C_r) form of the redox species. As a response to the applied potential, the redox species, which are at the WE surface, are oxidized

or reduced. Equation 2.8 describes the current of a reversible system according to the dimensionless current $\chi(\sigma t)$. This equation is calculated from the partial differential equations (Eq. 2.4 and 2.5), which are the Fick's second law of diffusion for the oxidized and reduced species:

$$\frac{\partial C_o(x,t)}{\partial t} = D_o \frac{\partial^2 C_o(x,t)}{\partial x^2} \qquad\qquad 2.4$$

$$\frac{\partial C_r(x,t)}{\partial t} = D_r \frac{\partial^2 C_r(x,t)}{\partial x^2} \qquad\qquad 2.5$$

The initial and boundary conditions are the following:

$$t = 0, \qquad C_r(x,0) = C^*_{Cu^+} \qquad\qquad C_o(x,0) = C^*_{Cu^{2+}} = 0 \qquad\qquad 2.6$$

$$x \to \infty, \qquad C_r(\infty,t) = C^*_{Cu^+} \qquad\qquad C_o(\infty,t) = 0 \qquad\qquad 2.7$$

$$i = nFAC^*_r\sqrt{\pi D_r \sigma} \cdot \chi(\sigma t) \qquad\qquad \sigma = \frac{nFv}{RT} \qquad\qquad 2.8$$

This approach is valid in the presence of sufficient amount of supporting electrolyte, so that almost no mass transport of the oxidized and reduced species takes place by migration. The dimensionless current for reversible system, $\chi(\sigma t)$ depends on the time and indicates the link between the current and potential. The $\pi^{0.5}\chi(\sigma t)$ values were calculated by different methods (numerical[27], series solution[28,29], partially analytical[30,31] and others[32,33]). Equation 2.9 is called the Randles-Sevcik equation, which gives the current of the LSV or CV peak and corresponds to Equation 2.8 for the maximum value of $\pi^{0.5}\chi(\sigma t)$ at 0.4463[28,34]. According to the Randles-Sevcik equation for reversible systems, the peak current I_p is proportional to the square root of the rate scan. This effect can be explained by the diffusion at the working electrode. If the scan rate is slow, the diffusion layer can grow around the electrode and less redox species can reach the WE to create an electric current. The opposite happens for a fast scan rate: the diffusion layer has no time to grow and more analytes can flow rapidly to be oxidized or reduced due to a large concentration gradient between the bulk and electrode surface.

$$I_p = 0.4463\, nFAC\sqrt{\frac{nFvD}{RT}} \qquad\qquad 2.9$$

In the case of quasi-reversible redox reactions, the kinetics parameters (k^0, k_a, k_c, α) influence the current response during the potential scan. The kinetics of the electron transfer

cannot be neglected because this step is not fast enough. Consequently, the boundary conditions are not the same. The current at a WE can be described first at equilibrium by the Butler-Volmer type equation (2.10). This equation is obtained from the anodic rate constant (k_a) for the oxidation of the reduced species at the WE interface and from the cathodic rate constant (k_c) for the reduction of the oxidized species at the WE interface (Eq. 2.11 and 2.12). By applying equations 2.1 - 2.3 to the equation 2.10, the current as the function of time can be solved numerically. [35]

$$x \to 0, \qquad \frac{I(t)}{nFA} = D_r \left[\frac{\partial C_r(x,t)}{\partial x} \right]_{x=0} = k_a C_r(0,t) - k_c C_o(0,t) \qquad \text{2.10}$$

$$k_c = k^0 \exp(-\alpha f(E - E^{0\prime})) \qquad \text{2.11}$$

$$k_a = k^0 \exp\left((1-\alpha)f(E - E^{0\prime})\right) \qquad \text{2.12}$$

Sometimes these rate constants can be defined differently, by substituting $\alpha = 1 - \beta$. [36,37]

The quasi-reversible behaviour of electron transfer at the electrode was first described by Matsuda & Ayabe for a system, which stands between a fully reversible (Nernstian) and totally irreversible reaction. For this type of redox reactions, the limitations do not come only from the diffusion but also from the kinetics of the electron transfer for the anodic and cathodic response. To classify the three categories of reactivity, they defined a reversibility factor, Λ, which can additionally be used with α for the determination of the peak shape parameters (i_p, E_p, $E_{p/2}$): [30,35]

$$\Lambda = \frac{k^0}{\left(\pi D_o^{1-\alpha} D_r^\alpha \frac{nF}{RT} v \right)^{0.5}} \qquad \text{2.13}$$

Reversible: $\qquad \Lambda \geq 15$

Quasi-reversible: $\qquad 15 \geq \Lambda \geq 10^{-2(1+\alpha)}$

Irreversible: $\qquad \Lambda \leq 10^{-2(1+\alpha)}$

The influence of the electron transfer kinetics on the CV potential peak separation for quasi-reversible systems was highlighted by Nicholson, who defined the charge parameter ψ, which is similar to the reversibility factor of Matsuda & Ayabe (Eq. 2.13). In this theory, the modification of the peak separation should indicate a particular kinetics of the redox species at

the electrode. With simulated CV, Nicholson showed that a larger peak separation is observed with small ψ and k^0 indicating a more irreversible charge transfer. For the determination of the heterogeneous rate constant k^0, the so-called method of Nicholson can be applied. In this method, the potential peak separation corresponds to a specific value of the dimensionless kinetic parameter ψ (Table 2.1). The working function, which describes the relation between ΔE_p and ψ, was numerically calculated by Nicholson [38]. From the following equation, the heterogeneous rate constant k^0 can be found with its corresponding ψ [27,38] :

$$\psi = \Lambda \pi^{-0.5} = \frac{\left(\frac{D_r}{D_o}\right)^{\frac{\alpha}{2}} k^0}{\sqrt{\pi D_r f \nu}} \qquad 2.14$$

In Eq. 2.14, the effect of the scan rate on the peak separation can be extrapolated. With higher ν, a smaller ψ is predicted and consequently a bigger peak separation on the CV. However, the scan rate is not influencing the kinetics and so it is common to record multiple CVs at different scan rates to have a good estimation of k^0. To be able to use the Nicholson method, the ohmic drop absolutely needs to be compensated. Indeed, the ohmic resistance has the same signature on CV than k^0 and provokes an increase of the peak separation especially at high scan rates. In non-aqueous solvents, the compensation of some residual internal resistance can be particularly difficult to achieve.

Table 2.1: Evolution of the peak potential separation with the kinetic parameter

ψ	ΔE_p / mV
20	61
7	63
6	64
5	65
4	66
3	68
2	72
1	84
0.75	92
0.5	105
0.35	121
0.25	141
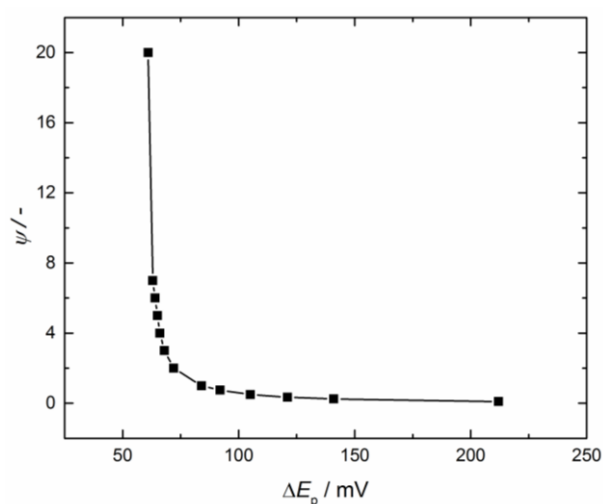
Figure 2.1. Evolution of the kinetic parameter, ψ, with the peak potential separation.

2.2. Mass transport and kinetics with RDE

The rotating disk electrode is an electrochemical technique that involves a rotational motion of the electrode regarding the electrolyte. In such an experiment, a forced and controlled convection of the solution is induced to the electrode and bring the redox active species at the bulk concentration until a distance of the boundary layer, δ, from the electrode. Between δ and the electrode surface, a diffusion process occurs that gives the name of diffusion layer thickness to δ (Eq. 2.17). During linear sweep voltammetry at a rotating disk electrode, the equation 2.15, known as the Levich equation[39], describes the anodic limiting current ($i_{l,a}$) and the equation 2.16 shows the mass transfer coefficient:

$$i_{l,a} = 0.62nFAD_r^{2/3}\omega^{1/2}v^{-1/6} \qquad\qquad 2.15$$

$$m_r = \frac{D_r}{\delta_r} = 0.62D_r^{2/3}\omega^{1/2}v^{-1/6} \qquad\qquad 2.16$$

$$\delta_r = 1.61D_r^{1/3}\omega^{-1/2}v^{1/6} \qquad\qquad 2.17$$

This limiting current is totally governed by the mass-transfer, which depends on the viscosity v, diffusion coefficient D_r and on the angular frequency of rotation ω. Consequently, D_r can be calculated from the limiting current as long as the other parameters are known (ω, v...).

For a general definition of a current response during a LSV, the Koutecký-Levich equation combines $i_{l,a}$ with the kinetic current i_K, which arises under purely kinetic controlled conditions:

$$i_K = FAk_a(E)C_R^* \qquad\qquad 2.18$$

$$k_a(E) = k^0 \exp\left[(1-\alpha)f\left(E - E^{0'}\right)\right] \qquad\qquad 2.19$$

$$\frac{1}{i} = \frac{1}{i_{l,a}} + \frac{1}{i_K} = \frac{1}{0.62nFAD_R^{2/3}\omega^{1/2}v^{-1/6}C_R^*} + \frac{1}{i_K} \qquad\qquad 2.20$$

By recording data at various angular speeds, it is possible to build Koutecký-Levich plots (1/i *vs.* $\omega^{-1/2}$), that can be used to extract i_K at the intercept and D_r from the slope. As the kinetic current is defined in the Butler-Volmer equation, the kinetic parameters can be calculated by using the Tafel behavior of the current under kinetic control, which means to

consider the current for potential at the beginning of the oxidation current, where diffusion can be neglected.

$$i_K = i_0[e^{(1-\alpha)f\eta} - e^{-\alpha f\eta}] \qquad\qquad 2.21$$

$$i_K = i_0 e^{(1-\alpha)f\eta} \qquad\qquad 2.22$$

3.   Material and methods

3.1.   Chemicals

All solvents and chemicals were used as received without further purification and were stored in a glove box under nitrogen. The solvents were acetonitrile (ACN, CH_3CN, extra dry over molecular sieves, 99.9%, from Acros) and propylene carbonate (PC, $C_4H_6O_3$, anhydrous, 99.7%, from Sigma-Aldrich). The supporting electrolyte was tetraethylammonuim tetrafluoroborate (TEABF$_4$, 99%, from ABCR) and the electroactive species tetrakis(acetonitrile)copper(I) tetrafluoroborate was either commercial, ([Cu(CH_3CN)$_4$]BF$_4$, > 98%, from TCi), or prepared by comproportionation reactions.[14,15] For the synthesis of [Cu(CH_3CN)$_4$]BF$_4$, copper(II) tetrafluoroborate hydrate (Cu(BF$_4$)$_2$·xH$_2$O, from Sigma-Aldrich), acetonitrile (ACN, CH_3CN, from Merck) and copper wire (dia. 1 mm, $\geq$ 99.99%, from GoodFellow) were of analytical grade and were used as received. The comproportionation reaction occurs in a Schlenk line filled with nitrogen. The Cu⁺ complex with ACN is dried overnight under vacuum and stored in a nitrogen-filled glove box.

3.2.   Electrochemical measurements

Electrochemical analyses were obtained with a Metrohm Autolab model PGSTAT302N potentiostat. Cyclic voltammetry (CV), chronopotentiometry (CP) and electrochemical impedance spectroscopy (EIS) were performed inside a three-electrode set-up with a Pt wire as counter electrode (CE) and a Pt disk working electrode (WE, dia. 2 mm). The reference electrode (RE) was made with a Cu wire (dia. 1 mm, $\geq$ 99.99%, GoodFellow) inside the solution containing 0.1 M TEABF$_4$ and 0.01 M [Cu(ACN)$_4$]BF$_4$ in ACN-PC mixtures. Diffusion coefficients and rate constants were determined from CV at different temperatures (between 25-70°C). For linear sweep voltammetry (LSV) measurements, a three-electrode cell

was built with a Pt rotating disk electrode (RDE) serving as a WE. CE, RE and electrolyte solutions are similar as for the other electrochemical measurements.

All potentials are expressed *vs.* the Cu wire in the solution of the given concentration of $[Cu(CH_3CN)_4]BF_4$. Hence, the potential of the Cu reference in equilibrium with 10mM Cu(I) solution in acetonitrile on the "non-aqueous standard copper electrode" scale (SCuE), *i.e. vs.* Cu(I) solution with the activity of 1 in equilibrium with Cu in acetonitrile is assumed to follow the Nernst equation considering the $\gamma Cu^+=1$, *i.e.* the potential of the reference is -0.118 V *vs.* SCuE in acetonitrile. To establish the relation with the ferrocene (Fc) scale recommended by IUPAC, the potential of the Fc^+/Fc couple *vs.* Cu/10mM Cu(I) in ACN was measured as 0.69 $\pm$ 0.01 V, *i.e.* the potential of the reference electrode used is -0.69 V *vs.* Fc^+/Fc.

For the determination of the diffusion coefficient of Cu^{2+}, which is needed for the calculation of the heterogeneous rate constant with the Nicholson method, an electrolysis is performed inside a H-cell with a ACN solution of 0.1 M $[Cu(CH_3CN)_4]BF_4$ with 0.3 M $TEABF_4$ as supporting electrolyte. The reticulated vitreous carbon (RVC) WE on the positive side produces the Cu^{2+} solution and, on the negative RVC CE, metallic Cu is plated with the reduction of Cu^+. The SCuE is used as the RE on the positive side to set the Cu^+ oxidation at 1.4 - 1.5 V and the separation between both half-cells is realized with glass wool (Fig. 2.2). The final Cu^{2+} solution is diluted to reach a concentration of 10 mM for electrochemical analysis.

All experiments were performed under the inert N_2 atmosphere of a glovebox (or under an anaerobic atmosphere with a flow of nitrogen inside the set-up) and by applying a positive feedback *iR* compensation.

3.3.   UV-vis and Raman analysis

UV-vis spectroscopy was carried out with a ChemStation for UV-visible spectroscopy (Agilent Technologies, USA).

Raman spectra were measured at room temperature by an inVia Raman Microscope (Renishaw, UK) with a pulsed excitation line of 532 (Nd-YAG laser) or 633 nm (helium-neon laser). Liquid samples and the air sensitive $[Cu(CH_3CN)_4]BF_4$ powder were analysed inside a sealed UV-vis cuvette.
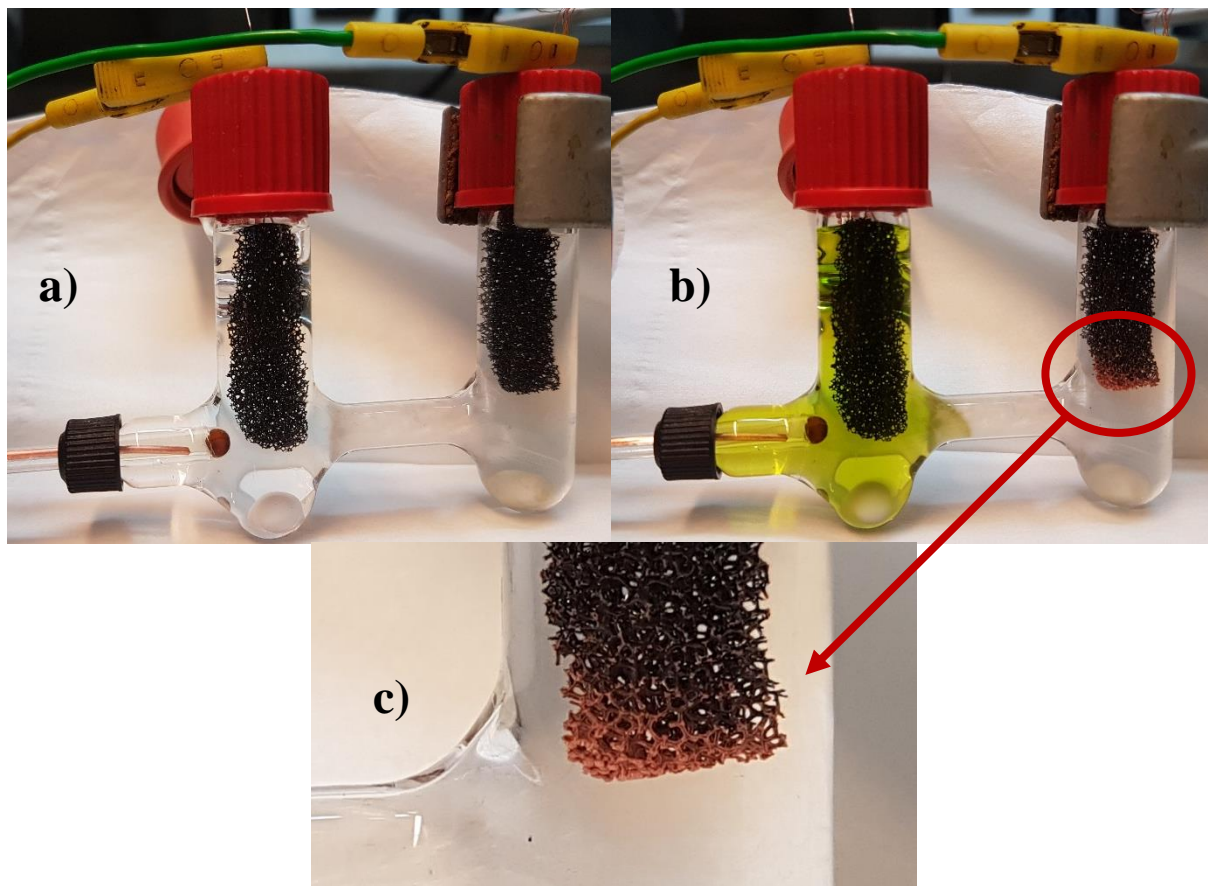
**Figure 2.2.** a) Image of H-cell set-up at t_0 for the electrolysis of Cu^+ with an ACN solution of 0.1 M [Cu(CH₃CN)₄]BF₄ with 0.3 M TEABF₄ as supporting electrolyte. Both electrodes are made of reticulated vitreous carbon (RVC) and the RE is a 10mM Cu^+/Cu electrode. b) Images of the H-cell after full Cu^+ conversion in green Cu^{2+} solution on the positive side and c) in metallic Cu on the negative RVC electrode.

4. Synthesis and characterization of [Cu(CH₃CN)₄]⁺

For the synthesis of the electroactive species, which is targeted for the Cu redox flow battery and for the electrochemical analysis of this chapter, a Cu(I) complex needs to be produced. A well-known synthesis of Cu(I) complex is achieved in ACN, which plays the role of solvent and ligand, during the comproportionation of Cu and Cu(II).[40,15,41] The reaction described below occurs with a constant heating around the boiling point of ACN under inert atmosphere (N₂).

$$Cu + Cu^{2+} + 8\ CH_3CN \underset{\text{Under } N_2}{\overset{\text{Reflux 83 °C}}{\rightleftharpoons}} 2\ Cu(CH_3CN)_4^+$$
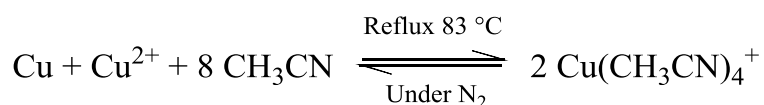
This reflux coupled to the Schlenk line is maintained until the blue solution containing Cu(II) changes to a totally transparent and uncolored phase. If the concentration of Cu(II) in the starting solution is high enough, some Cu(I) complexes can precipitate before removing the solvent. To separate the excess of copper, the solution is filtered inside the glovebox to avoid contact of the sensitive Cu(I) with the moisture coming from ambient air. During the last step, the Cu(I) complex is isolated by evaporating ACN overnight under vacuum. The final aspect of the Cu(I) product is a white and shiny crystalline powder. According to the amount of metallic Cu, which reacts, and the quantity of produced Cu(I), the yield is calculated and reaches 97%. For a long-term storage, the Cu(I) powder is kept inside a glovebox. The amount of water in the starting molecule $Cu(BF_4)_2 \cdot xH_2O$ has been determined, as the yield, from the metallic Cu quantity, and is found to be between 6 and 7.

For this inorganic synthesis, two different counter anions of the starting Cu(II) ion have been tested (BF_4^- and SO_4^{2-}) and it leads to the formation of [Cu(CH₃CN)₄]BF₄ (1) and [Cu(CH₃CN)₄]₂SO₄ (2). According to the solubility of SO_4^{2-}, complex (2) is less miscible in organic media. Therefore, molecule (1) is the chemical species that will be integrated in the battery and is analyzed electrochemically in this chapter.

In a way to confirm the complete conversion of Cu(II) during the comproportionation, UV-vis spectroscopy of the final Cu(I) powder is compared with Cu(II). In Figure 2.3a, the spectrum of $Cu(BF_4)_2$ in water shows the characteristic peak of Cu(II) with a maximum of absorbance around 810 nm.[42] In ACN, this peak is shifted to smaller wavelength and appears

around 760 nm. In both solvent, Cu(II) solution looks blue due to the presence of water in the $Cu(BF_4)_2 \cdot xH_2O$ molecule. However, the wavelength change for the maximal absorption comes from the exchange of water from the Cu(II) solvation shell with ACN. As expected in the case of successful reaction, no trace of Cu(II) appears in the 20 mM $[Cu(CH_3CN)_4]BF_4$ solution of ACN. It is easy to compare the UV-vis spectra of Cu(I) and Cu(II), because Cu(I) electronic configuration $[Ar]4s^0 3d^{10}$ cannot undergo absorption of light in the UV-vis range. Indeed, Cu(I) d orbital, which is completely full with 10 electrons, is not able to promote an electron with UV-vis light (Fig. 2.3b). In consequence, regardless the ligand and symmetry of the complex, no peak should be recorded for any Cu(I) solution.
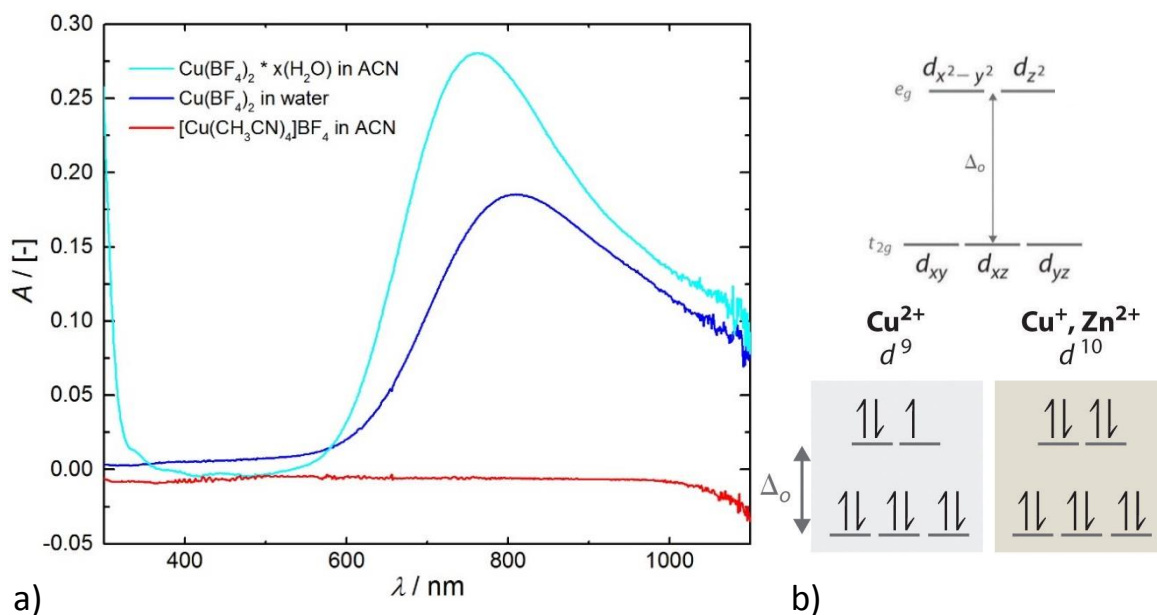
Figure 2.3. a) UV-vis spectra for $[Cu(CH_3CN)_4]BF_4$ in ACN (red), $Cu(BF_4)_2$ in ACN (light blue) and water (blue); b) electronic configuration of Cu(I) and Cu(II) d orbital in an octahedral conformation according to crystal field theory[43].

Between water and ACN, Cu(II) absorbance peak is changing respectively from 810 to 760 nm, meaning that Cu(II) needs more energy for the electron transitions when it is solvated with ACN (Δ_o becomes bigger). This modification can be explained by the crystal field theory, which describes the loss of degeneracy among d or f orbitals for transition metals during their coordination with ligands.[44] By changing some of the water ligands from $Cu(BF_4)_2 \cdot xH_2O$ with ACN, two effects are influencing the Cu(II) ions electronic configuration $[Ar]4s^0 3d^9$. First the ligand ability to increase or decrease the splitting energy Δ_o needs to be considered.

Secondly Δ_o can also be influenced by Cu(II) coordination geometry, which can be affected by the ligand nature. From literature, solvated Cu(II) ions forms distorted octahedral structure along their z-axis in water as well as in ACN.[41,45,46] These results are in agreement with the Jahn-Taller theory, which describes, by applying group theory, the instability of degenerate electronic states for non-linear molecules.[47] For the Cu(II) case, a strong Jahn-Taller distortion is observed in water and ACN, because of the odd electrons number in the e_g orbitals, which are oriented in the z-direction.[44] Therefore, the main influence on the difference of Δ_o between water and ACN complexes with Cu(II) comes from the stronger field formed by ACN, which increases Δ_o. This tendency for ACN to induce a larger Δ_o than water is also reported in the spectrochemical series.[44]

As ACN belongs to the C_{3v} group and contains 6 atoms, it can be calculated, according to the group theory, that this molecule has 12 vibrations modes. Among them, 8 modes coming from 4 doubly degenerated vibrations, arising from the E class, should appear at only 4 different wavelengths ν_5, ν_6, ν_7 and ν_8. The other 4 fundamental vibration modes ν_1, ν_2, ν_3 and ν_4 belong to the symmetric A_1 class.[48] All of them should be Raman and IR active.[49]
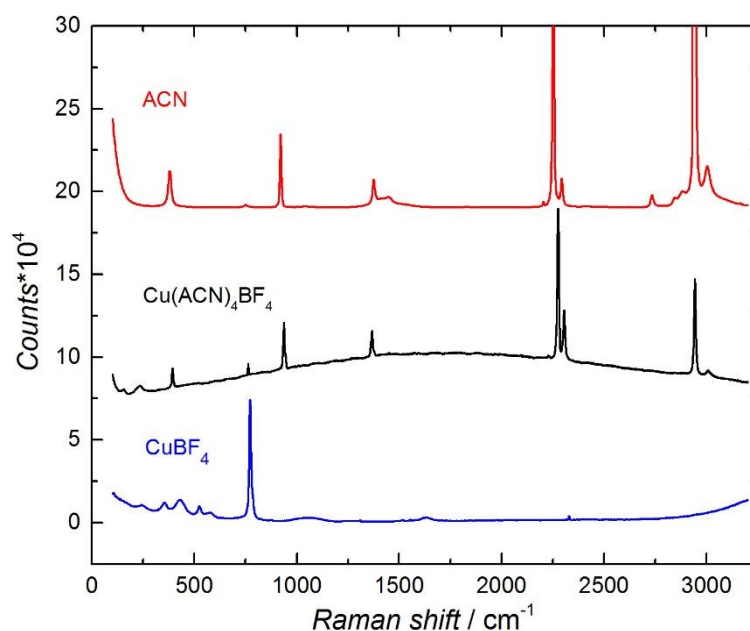
Figure 2.4. Raman spectra of liquid ACN (red), solid [Cu(CH₃CN)₄]BF₄ powder (black) and solid Cu(BF₄)₂ powder (blue).

In Figure 2.4, Raman spectra of liquid ACN and solid $Cu(BF_4)_2$ are compared with ACN, which is coordinated with Cu(I) as the solid $[Cu(CH3CN)_4]BF_4$ salt. Raman spectroscopy is obtained by the inelastic (anti-)Stokes scattering of an exciting light inside a molecule and gives it vibration levels.[48] A summary of the liquid ACN vibrations and ACN vibrations as a ligand is given in Table 2.2. The experimental Raman shifts of the different vibrational states are in good agreement with previous publications, which also help to attribute the mode, class and assignment of vibrations to the Raman shifts.[50–53] By analysing the similarities of the fingerprints between liquid CH_3CN and $[Cu(CH_3CN)_4]BF_4$, 9 peaks are in the same range of energy. Seven of them correspond to the fundamental modes vibrations and ν_7, which is of really low intensity in ACN, doesn't appear in the Cu(I) complex. ACN vibration energies vary from 0.1 to 5.4% between the two samples (Table 2.2). This effect was explained and predicted by Dimitrova with simulations of ACN-cation interactions.[54] Vibrations need higher energies to occur in the complexed ACN, because Cu(I) interaction with the lone pair of nitrogen rigidifies the C−C≡N body. Indeed, this is also visible by the fact that the only vibrations, which show a smaller energy in the complex, are the one involving the CH_3 non-coordinated part of ACN (ν_3 and ν_6, see Table 2.2). Another explanation for the ACN small variation of peak can be the different physical states of both samples (liquid ACN and Cu(I) powder). In Cu(I) crystalline powder, the symmetry of the molecule as well as the symmetry of the crystal lattice need to be considered, because lattice vibrations could also influence the Raman spectrum.[55]

In Figure 2.4, $Cu(BF_4)_2$ spectrum contains the four vibrations modes of BF_4^- anion with energies of 765 (mode A_1), 355 (mode E), 525 and 1060 cm^{-1}.[56–58] Another vibration at 244 cm^{-1} correspond probably to a Cu-F vibration.[58] The same vibration is found at lower Raman shift 235 cm^{-1} for $[Cu(CH_3CN)_4]BF_4$ due the weaker interaction of Cu(I) with BF_4^-. Except the ACN and BF_4^- peaks, $[Cu(CH_3CN)_4]BF_4$ Raman spectra has one specific signal coming from Cu(I) interaction with ACN at 156 cm^{-1}. It is not surprising to find metal transition complexes with metal-ligand vibrations at low Raman shift.[59,60]

Table 2.2. Raman shifts for liquid ACN and coordinated ACN with Cu(I) in [Cu(CH₃CN)₄]BF₄.

Mode [50–53]	Class [50–53]	Assignment [50–53]	Raman shift / cm⁻¹		
			CH_3CN (liq.)	[Cu(CH₃CN)₄]BF₄	Δ / %
ν_8	E	C−C≡N bending	381	394	3.41
$2\nu_8$	A_1 + E		750	763	1.73
ν_4	A_1	C−C stretching	921	938	1.85
ν_7	E	CH_3 rocking	1043		
ν_3	A_1	CH_3 deformation	1376	1363	- 0.94
$\nu_7 + \nu_8$			1415		
ν_6	E	CH_3 deformation	1447	1369	- 5.39
$2\nu_4 + \nu_8$			2205		
ν_2	A_1	C≡N stretching	2251	2276	1.11
$\nu_3 + \nu_4$			2294	2306	0.52
$2\nu_3$	A_1		2735		
$\nu_3 + \nu_6$			2846		
$2\nu_6$			2882		
ν_1	A_1	Sym C−H stret.	2941	2944	0.10
ν_5	E	Asym C−H stret.	3004	3009	0.17

5.   Results and discussion

5.1.   Temperature and solvent effects

The three different oxidation states of Cu in ACN are shown in Fig. 2.5. As ACN is stabilizing the Cu^+ ions, a relatively large window of potential appears for this copper oxidation state. The Cu^+ reduction in Cu is observed at 0.0 ± 0.02 V (*vs.* Cu^+/Cu) with a characteristic deposition peak, which is followed by the faradic process of Cu stripping from the WE. A pre-deposition peak of Cu^+ on the Pt WE surface can also be detected around 0.2 V (*vs.* Cu^+/Cu). The Cu^+ oxidation in Cu^{2+} appears at a half-wave potential of 1.36 ± 0.01 V (*vs.* Cu^+/Cu) with a quasi-reversible peak shape. From the difference of potential between these two redox couples, the stability window of Cu^+ can be approximated to 1.36 V for a 10 mM Cu^+ solution in pure ACN.

Upon addition of some ferrocene, a third redox couple is detected on the CV curve in Fig. 2.5a. The peak with the half-wave potential at 0.69 ± 0.01 V (*vs.* Cu^+/Cu) is induced by the ferrocene/ferrocenium couple. The potential of this redox active compound is commonly used as a reference for electrochemistry in organic media. The CV curve of Cu^+ is also plotted in Figure 2.5b in function of the Fc^+/Fc potential on the second *x*-axis. In the literature, the Fc^+/Fc potential in ACN with 0.1 M n-tetrabutylammonium hexafluorophosphate is reported at 0.99 V (*vs.* Ag/AgCl (0.1 M n-tetrabutylammonium chloride in ACN)) with a peak separation of 87 mV.[61] Here ΔE_p has a comparable value of 84 mV in ACN with 0.1 M TEABF₄. According to Eq. 2.14 and Table 2.1, $\psi = 1$ and $\Lambda = 1.77$, therefore if the boundaries of Matsuda &Ayabe are followed, the redox reaction of Fc^+/Fc is under the quasi-reversible regime in ACN (0.1 M TEABF₄).

Table 2.3. Summary of the $E_{1/2}$ of Cu^+/Cu and Cu^{2+}/ Cu^+ with different references.

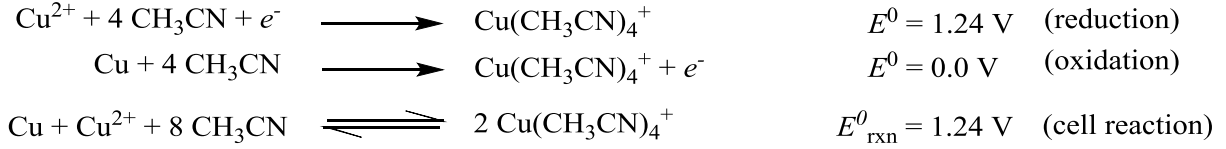| Redox couple	$E_{1/2}$ / V			
	(*vs.* SCuE)	(*vs.* 10 mM Cu^+/Cu)	(*vs.* Fc^+/Fc)	(*vs.* Ag/AgCl)
Cu^+/Cu	− 0.118	0.00	− 0.69	0.30
Cu^{2+}/ Cu	1.242	1.36	0.68	1.67
Fc^+/Fc	0.572	0.69	0.00	0.99
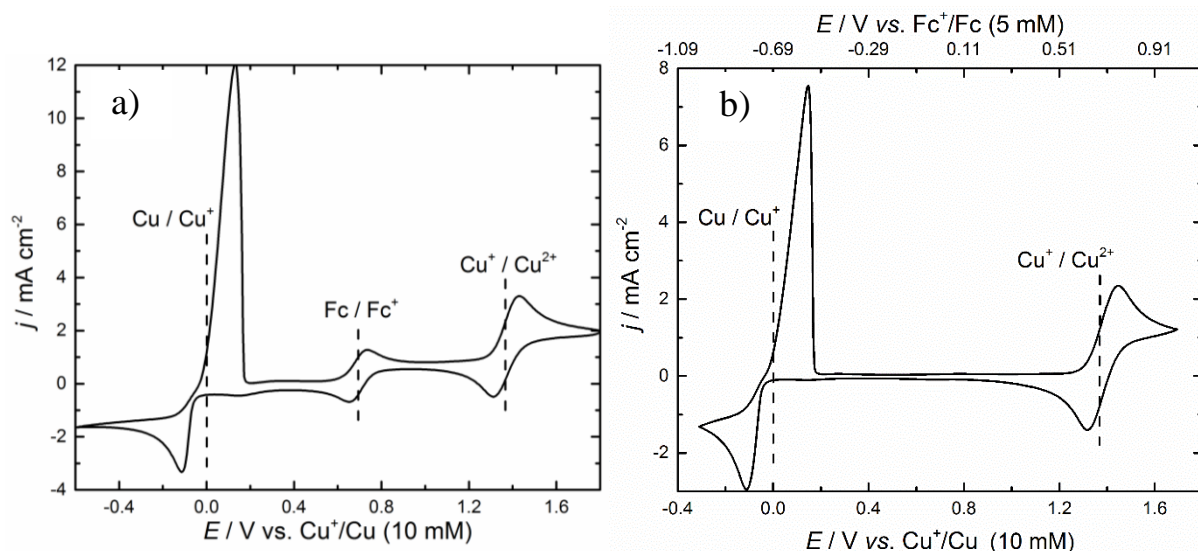
Figure 2.5. a) CV curve of Cu(I) oxidation and reduction peaks with the reference redox couple Fc⁺/Fc (5 mM) on Pt disc electrode from 10 mM of tetrakis(acetonitrile)copper(I) tetrafluoroborate in ACN at a scan rate of 100 mV/s. b) CV curve of Cu(I) oxidation and reduction peaks on Pt disc electrode from 10 mM of tetrakis(acetonitrile)copper(I) tetrafluoroborate in ACN at a scan rate of 100 mV/s.

The effect of the temperature on the redox potential of the Cu^{2+}/Cu^+ is shown in the CVs of Fig. 2.6a. A shift of approximatively +55 mV is observed between the Cu^{2+}/Cu^+ half-wave potential at 25 and 70°C. The dashed CV at 40°C in Fig. 2.6a shows a particular shape, which is assigned to the undesired effect of increased natural convection due to the heating of the solution. With the influence of temperature, various thermodynamics quantities (E_{rxn}, ΔH^0, ΔS^0, ΔG^0, K_{rxn}) can be obtained from the following equations (2.23-2.27). It is particularly interesting to consider the evolution of the potentials with temperature if a battery is pictured with the Cu^+/Cu couple on the negative side and the Cu^{2+}/Cu^+ on the positive side [6,8,9,62–65]. In this case, the electromotive force (emf) of the battery is represented by the standard emf potential of the cell reaction E^0_{rxn}. For the standard potential of the Cu^+ reduction ($E^0_{Cu(I)/Cu}$), the assumption regarding the activity of solid is applied to the Nernst equation with $a_{Cu} = 1$ (Eq. 2.23). As the concentration of Cu^+ of 10 mM was used in the experiments, the potential of the reference electrode can be estimated as -0.118 V *vs.* SCuE, assuming negligible activity effects. The electrochemical discharge comproportionation reaction of the cell is given here with a predicated E^0_{rxn} of 1.24 V and induced the formation of two Cu^+ from Cu^{2+} reduction ($E^0 = 1.24$ V vs. SCuE for a standard 1 M Cu^+ solution at 25°C) and Cu oxidation ($E^0 = 0$V *vs.* SCuE for a standard 1 M Cu^+ solution at 25°C) (Cu | Cu⁺ || Cu⁺ | Cu²⁺):

$$Cu^{2+} + 4\ CH_3CN + e^- \longrightarrow Cu(CH_3CN)_4^+ \qquad\qquad E^0 = 1.24\ V \quad \text{(reduction)}$$

$$Cu + 4\ CH_3CN \longrightarrow Cu(CH_3CN)_4^+ + e^- \qquad\qquad E^0 = 0.0\ V \quad \text{(oxidation)}$$

$$Cu + Cu^{2+} + 8\ CH_3CN \rightleftharpoons 2\ Cu(CH_3CN)_4^+ \qquad\qquad E^0_{rxn} = 1.24\ V \quad \text{(cell reaction)}$$

The $E^0_{Cu(II)/Cu(I)}$ is approximated to the experimental value $E_{1/2}$ of the CVs in Fig. 2.6a (Eq. 2.24). With an increase of the temperature to 50°C, the cell voltage reaches 1.26 V (*vs.* Cu/Cu⁺). Indeed, a small gain of voltage can be expected in the electrochemical cell by working with higher temperatures.

$$E = E^0_{Cu(I)/Cu} + \frac{RT}{F}\ln\left(\frac{a_{Cu(I)}}{a_{Cu}}\right) = E^{0\prime}_{Cu(I)/Cu} + \frac{RT}{F}\ln\left(\frac{C_{Cu(I)}}{C^0}\right) = 0.00\ V\ (vs.\ Cu^+/Cu) \qquad 2.23$$

$$E^0_{Cu(II)/Cu(I)} \approx E_{1/2} \qquad\qquad\qquad 2.24$$

$$\Delta E^0 = E^0_{rxn} = E^0_{Cu(II)/Cu(I)} - E^0_{Cu(I)/Cu} \qquad\qquad\qquad 2.25$$

$$\Delta G^0 = -nFE^0_{rxn} = \Delta H^0 - T\Delta S^0 \qquad\qquad\qquad 2.26$$

From the difference of standard potentials in Eq. 2.25, the Gibbs energy of the Cu and Cu^{2+} comproportionation to Cu^+ can also be calculated with Eq. 2.26. In Fig. 2.6b, the experimental trend that ΔG^0 and E^0_{rxn} follow with various temperatures is nicely illustrated. A linear evolution of ΔG^0 and E^0_{rxn} with temperature is observed and is explained by Eq. 2.26. The linearity of ΔG^0 allows the calculation of thermodynamics constant for the formation of Cu^+ with Cu and Cu^{2+}, assuming that ΔH^0 and ΔS^0 are independent of the temperature. The standard entropy ΔS^0 of the cell reaction is derived from the slope of the linear fit applied to ΔG^0 shift with temperature and reaches $78.6 \pm 6.9\ J \cdot mol^{-1} \cdot K^{-1}$. By using the intercept of the same linear fit, the enthalpy of the overall discharge reaction ΔH^0 is calculated as -97.2 ± 3.3 $kJ \cdot mol^{-1}$. These results show that the Cu^+ generation during the battery discharge is spontaneous, exergonic, and thermodynamically more spontaneous with higher temperatures.
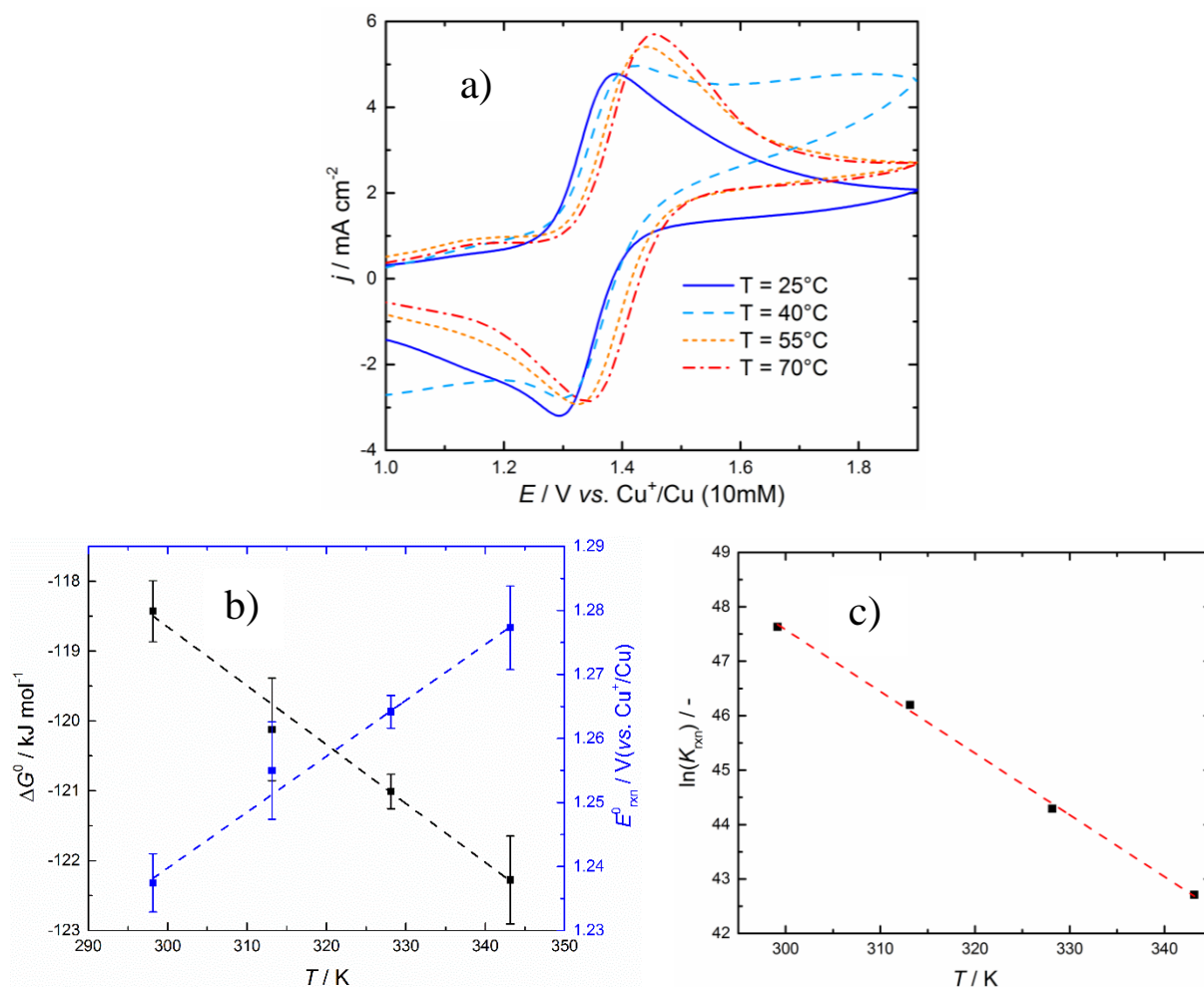
Figure 2.6. CVs of [Cu(CH₃CN)₄]BF₄ (10 mM) in ACN solutions (0.1 M TEABF₄) at 298.15 K. All scan rates are set at 100 mV·s⁻¹. a) CV showing the general electrochemical behavior of Cu⁺ in ACN at different temperatures (25, 40, 55, 70°C) for Cu⁺ in ACN. c) ΔG^0 and E^0_{rxn} evolution with temperature and linear fitting (dashed line), and c) natural logarithm of the equilibrium reaction constant in function of T

In Table 2.4, the thermochemistry of various electrochemical cells is presented and can be compared with the cell potential (1.24 V) of a Cu battery that can be expected from the electrochemistry of Cu⁺ in ACN. Regarding the cell voltage, the Cu-ACN system has a similar voltage than most of the overall reaction dealing with one electron transfer (except the Li-ion battery that has a much higher cell reaction potential, Table 2.4). The overall cell reactions are shown in the spontaneous direction of the discharge in Table 2.4 and therefore the amount of released Gibbs energy of the cell is, as expected always negative in that case. Higher Gibbs energies are obtained when the full cell reaction implies more than one electron (H₂ fuel cell, Zn, Pb, Ni batteries) or when the cell voltage is fundamentally higher (Li-ion battery) (Eq. 2.26). The entropy values are fluctuating the most between the reported data in literature and

between the different chemistries. In Table 2.4, ΔS^0 is mainly negative and leads to a less spontaneous cell reaction with higher temperature. Based on this observation, the discharge should be done at low temperatures to increase the output energy of the system and increase the energy efficiency. A thermally enhanced electrochemical cycle has been done by D. Reynard *et al*. for a V redox flow battery (V RFB) with a heating step (60°C) during the charge and a cooling one (20°C) during the discharge. This use of a different temperature between the charge and discharge shows an increase of energy efficiency of 9%. [66] It is possible the combine this type of thermodynamic cycle to an electrochemical system that have a negative ΔS^0. In the case of the Cu^+ battery, the discharge should be applied at high temperature according to the positive value of the ΔS^0. Two main explanations are exposed to explain the negative sign of the ΔS^0 for the Cu^+ formation:

- The change of physical state between the metallic solid Cu to the complexed and solubilized Cu^+ in ACN,
- The modification of the coordination sphere in ACN between the Cu^{2+} that forms a distorted octahedral complex and Cu^+ with a tetrahedral shape.[41,45,46] The release of two CH_3CN molecules from the Cu(II) complex during reduction.

Table 2.4. Cell potential and thermochemical data for different energy storage systems.

Battery	Overall cell reaction	n_e	E^0_{cell} / V	ΔG^0 / kJ mol^{-1}	ΔH^0 / kJ mol^{-1}	ΔS^0 / J K^{-1}mol^{-1}
H$_2$ fuel cell [67–69]	$2H_2(g) + O_2(g) \rightarrow 2H_2O(l)$	4	1.23	−474	−571	−327
Li-ion battery [70]	$LiCoO_2 \rightarrow (1-x)Li + Li_xCoO_2$	1	3.83	−370	−382	−41
Alkaline [67,71]	$Zn(s) + 2MnO_2(s) \rightarrow ZnO(s) + Mn_2O_3(s)$	2	1.43	−271.4	−269.5	6.4
Zn /Ag$_2$O [67,71]	$Zn(s) + Ag_2O(s) \rightarrow ZnO(s) + 2Ag(s)$	2	1.59	−307.1	−317.2	−34.2
NiCd [71–73]	$Cd(s) + 2NiOOH(s) + 2H_2O(l) \rightarrow$ $Cd(OH)_2(s) + 2 Ni(OH)_2(s)$	2	1.30	−250.3	−282.6	−53.5
NiMH [67,71–74]	$NiOOH(s) + MH \rightarrow Ni(OH)_2(s) + M$	1	1.35	−130.3	−130.2	0.3
Lead-acid [67,71]	$Pb(s) + PbO_2(s) + 2H^+ + 2HSO_4^- \rightarrow$ $2PbSO_4(s) + 2H_2O(l)$	2	1.92	− 370.9	−359.6	40.0
V RFB [75–80]	$V^{2+} + VO_2^+ + 2H^+ \rightarrow V^{3+} + VO^{2+} + H_2O(l)$	1	1.24 to 1.34 1.32 [b]	−120 to −130 −138 [b]	−156 to −190 [c] −162 [c]	−120 to −230 −83.3 [b]
Fe-V RFB [75–77,80]	$Fe^{3+} + V^{2+} \rightarrow Fe^{2+} + V^{3+}$	1	1.02 to 1.10 0.73 [b]	−110 or −99 −70 [b]	−80 or −108 [c] −99.5 [c]	100 or −31 −100 [b]
Fe-Cr RFB [76,77,80,81]	$Fe^{3+} + Cr^{2+} \rightarrow Fe^{2+} + Cr^{3+}$	1	1.18 to 1.2 0.98 [b]	−120 −95 [b]	−118 or −127 [c] −114 [c]	7 or −22 −66 [b]
Cu(CH$_3$CN)$^+$ (this work)	$Cu^{2+} + Cu(s) + 8 CH_3CN(l) \rightarrow 2Cu(CH_3CN)^+$	1	1.24	−120	−97.2	78.6

[a] For x=1. According to reference [70], the entropy of the Li-ion cell changes significantly with the amount of inserted Li in the Li$_x$CoO$_2$. [b] From reference [80]. [c] Calculated values with Eq. 2.26.

Not only has the temperature an effect on the electrochemistry, but also the solvent composition influences the electron transfer process. In the case of interest, the ratio between the ACN and PC content in solution changes the potential and shape of the CV. In Fig. 2.7a, the potential of the Cu^+ oxidation is lowered with increasing content of PC. Additionally, the peak separation between the oxidation and reduction peak becomes larger with less ACN and, in this quasi-reversible redox reaction, the system becomes more irreversible and with a slower kinetics (more data will be shown in Section 4.3). When just a bit of PC is introduced, another shape modification of the CV appears already with only 30% PC: a second peak/hill seems to occur after the first oxidation or reduction. This second phenomena can be probably explained by a non-faradic process linked with a change of the Cu ion complexation with ACN following the first faradic peak. This observation again suggests that the Cu^{2+} forms a complex with 6 ACN ligands instead of 4 for the Cu^+. Also regarding the current of the CVs, the capacitance of the electrical double layer seems to be more important with less available ACN at the electrode interface.

The absence of ACN in the solution avoids the stabilization of the Cu^+ ions and almost no differences of potential are detected between the Cu^{2+}/Cu^+ and Cu^+/Cu when Cu^+ is added in the solution. Without some little additional ACN in the solvent, the Cu^+ oxidation is irreversible. In Fig.2.7b, a predominance diagram is shown for the considered ACN organic system. In this graph, the ACN vol% replaces the acidity of the usual Pourbaix diagram and highlight the decrease of Cu^+ electrochemical window with the diminution of the coordinating ACN concentration.
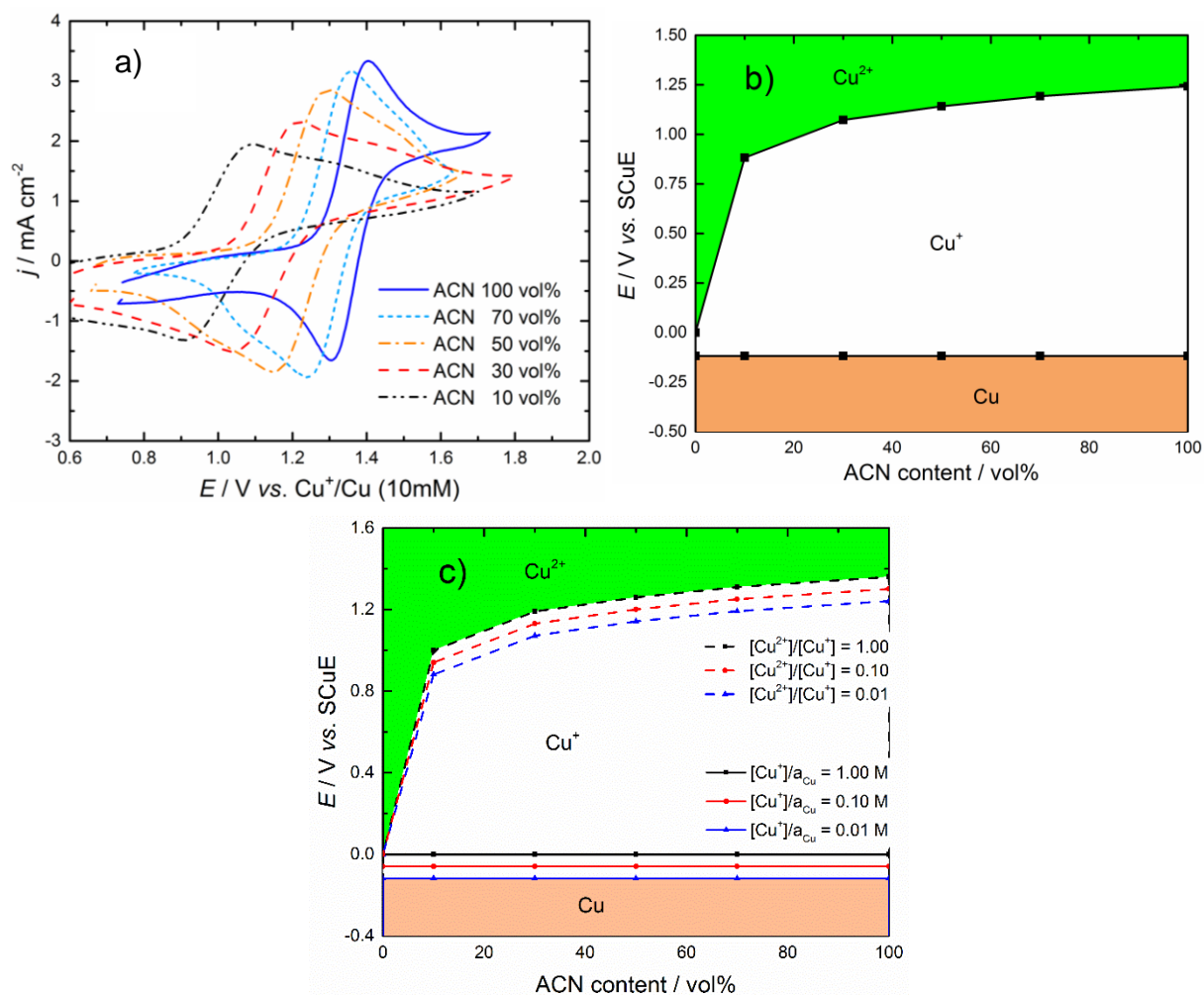
Figure 2.7. The ACN-PC mixtures from 10 to 100 vol% ACN contains [Cu(CH₃CN)₄]BF₄ (10 mM) and TEABF₄ (0.1 M). a) CVs at 100 mVs⁻¹ and 298K showing the effect of the solvent composition on the electrochemical potential of Cu^{2+}/Cu^+ redox couple. b) Predominance diagram for ACN-PC organic solution with the evolution of Cu^{2+}/Cu^+ standard potential in function of the ACN content in PC solution. c) Predominance diagram for ACN-PC organic solution with the evolution of Cu^{2+}/Cu^+ standard potential in function of the ACN content in PC solution for different concentration of Cu^+ and Cu^{2+}/Cu^+ ratios of concentration.

5.2.   Analysis of LSV at RDE

The full CV in Fig. 2.8a is measured on a rotating disk electrode (RDE); the *i*-curve shows the limiting current for the Cu$^+$ oxidation above 1.6 V (*vs.* Cu/Cu$^+$) and the Cu$^+$ reduction under –0.2 V. The Cu oxidation current shows a particular shape with three peaks arising from the stripping under the constant convection of the experiment. To describe the kinetics and diffusion parameters at the WE for the electron transfer between Cu$^+$ and Cu^{2+}, LSVs are recorded with a RDE at different rotational speeds (500 to 3000 rpm, in Fig. 2.8b).
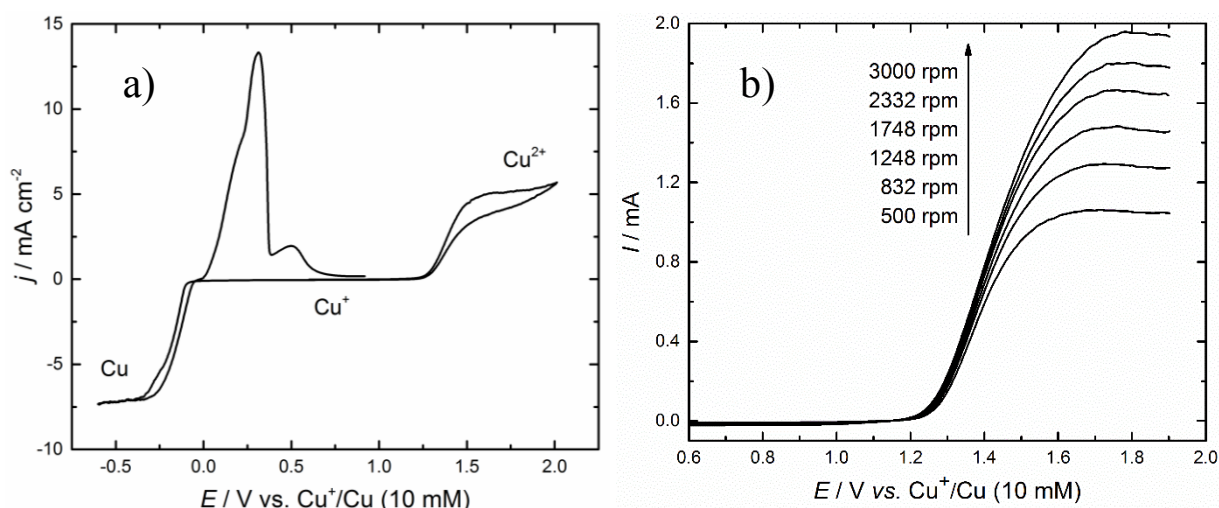
Figure 2.8. RDE experiment with ACN solution, Cu(CH$_3$CN)$_4$]BF$_4$ (10 mM) and TEABF$_4$ (0.1 M).Scan rate at 50 mV s^{-1} a) Full CV at 500 rpm, b) LSVs at various rotation rates for the Cu$^+$ oxidation.

With these other sets of electrochemical data, $E_{1/2}$ appears at 1.38 ± 0.01 V (*vs.* Cu/Cu$^+$) and then shifts to higher value compared to the one from the CVs. As the current is governed by the Koutecký-Levich equation during a LSV at a RDE and because the limiting current is defined by the Levich equation (see Eq. 2.15 and 2.20), the higher angular speeds (ω) increase the anodic limiting current ($i_{l,a}$) intensity (Fig. 2.8b). The Levich relation between $i_{l,a}$ and ω allows the calculation of the diffusion coefficient with the slope of the Koutecký-Levich fit, $D_{Cu+} = 1.56 ± 0.14 \cdot 10^{-5}$ cm$^2 \cdot$s^{-1}. From the Koutecký-Levich plot in Fig. 2.9a, the current with no mass-transfer (i_k) can be extracted at the intercept of the linear regression for different potentials. This plot shows that i_k becomes more important with higher voltage and starts to be constant when voltage for the limiting current are reached. In Fig. 2.9b, the evolution of ln(i_k) indicates also that i_k does not follow the Tafel behavior and starts to be influenced by diffusion control from

1.5 V. With this observation, the choice of the potential that need to be used to determine the kinetics parameter is crucial, especially if a pure and meaningful i_k, that is only controlled by the kinetic at the electrode is targeted. The potential window, which is considered here, is located at the beginning of the oxidation current increase between 1.25 and 1.35 V (*vs.* Cu/Cu$^+$).
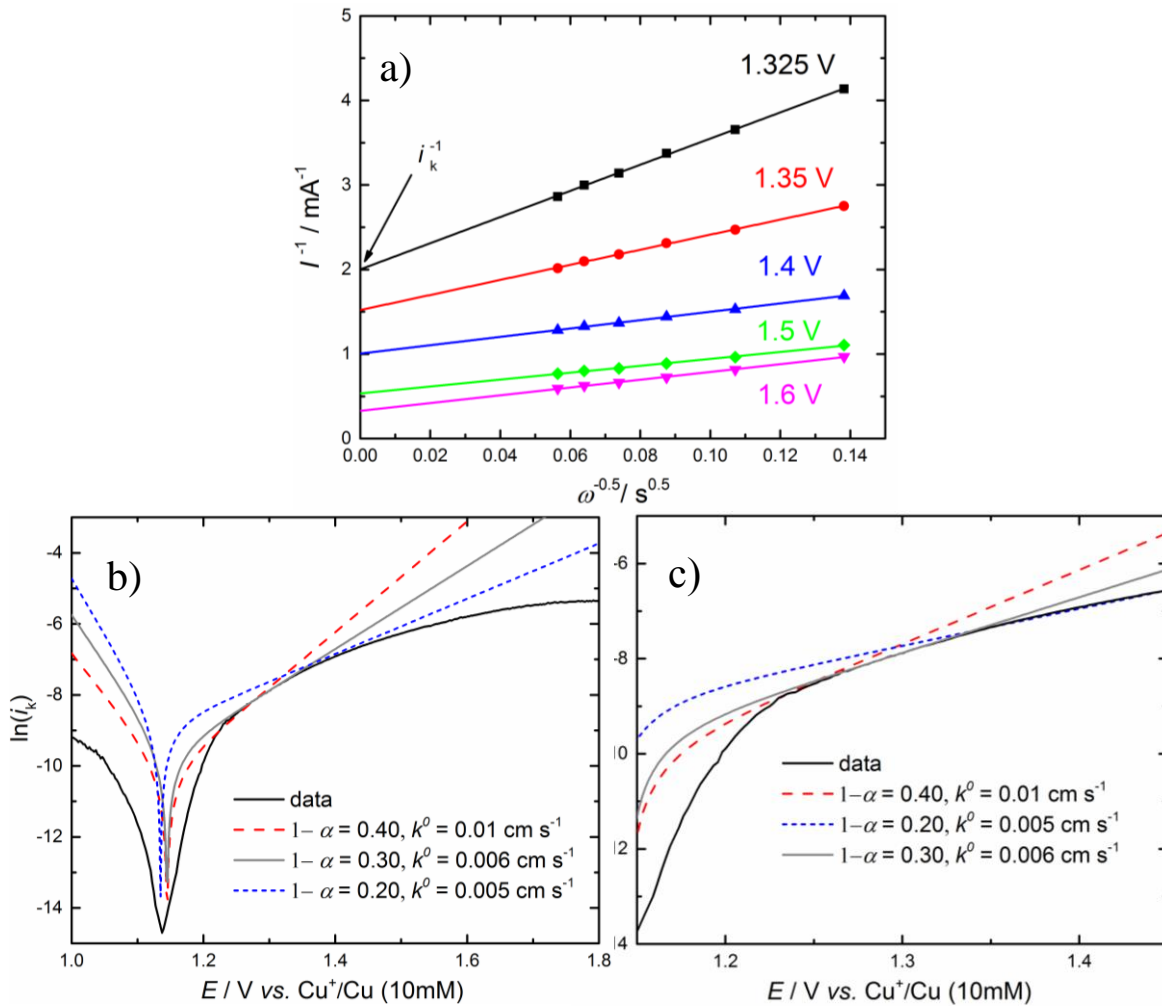
Figure 2.9. a) Koutecký-Levich plot at E = 1.325, 1.35, 1.4, 1.5 and 1.6 V (*vs.* Cu/Cu$^+$). c) Tafel-type plots for the measured data and for the simulations with E^0 = 1.38 V (*vs.* Cu/Cu$^+$), [Cu$^+$]$_0$ = 10 mM and [Cu^{2+}]$_0$ = 5 · 10^{-4} mM.

The Tafel-type plots in Fig. 2.9b-c show the evolution of the $\ln(i_k)$ with the potential, which determines the values of the charge transfer coefficient (α) and of the heterogeneous rate constant (k^0). The simulated curves are calculated with the Eqs 2.18-2.20-2.22. According to Eq. 2.22, the slope of $\ln(i_k)$ *vs.* E is defined by (1-αf) and α can be determined. The α values, which are calculated from the experimental data, give an averaged value of 0.7 ± 0.02. From

the different simulation curves that are visible in the Fig. 2.9b-c, α seems to be comprised between 0.6 and 0.8. A more detailed graph of the influence of α on the Tafel slope is presented in Fig. 2.9c and the focus is concentrated on the potential window, which is mainly controlled by kinetics (1.2 to 1.4 V). As expected from Eq. 2.22, the slope decreases at higher α values and the simulated Tafel curve with $\alpha = 0.7$ fits the best the current at the selected potential 1.25-1.35 V. Regarding k^{0}, the simulated curves predict an interval between 5 to $10 \cdot 10^{-3}$ cm·s^{-1} and the calculation from Eqs. 2.18-2.19 gives a mean number of $6.22 \pm 0.13 \cdot 10^{-3}$ cm·s^{-1} for the standard rate constant. At the end, the simulation curve containing the calculated parameters is plotted in Fig. 2.9b-c with a gray line and stands between the two simulations with the limit values of α and k^{0}.

4.3. Activation energies for the diffusion and kinetics of Cu^{+} oxidation

For a more complete electrochemical analysis of the Cu-ACN-PC system, CVs at different temperatures are recorded for several Cu^{+} solutions of ACN-PC mixtures. The amount of PC was varied from 0 to 90 vol%. Pure PC resulted in a poor electrochemical behaviour of Cu^{+}. In these conditions, the low amount of ACN is not enough to stabilize the Cu^{+} within a convenient potential window and the peak signals for the Cu/Cu^{+} and Cu^{+}/Cu^{2+} overlap. In Fig. 2.7, the effect of the solvent composition has been clearly described. By increasing the ratios of PC, the potential of the Cu^{+} oxidation is decreasing *versus* the Cu^{+}/Cu reference. This shift of approximately -0.4 V between the 100 and 10 vol% ACN solution confirms the stabilization effect of the ACN around the Cu^{+} cations.

In the case of reversible reactions, the peak potentials for the oxidation and reduction do not change with scan rate and the difference of potential between these two peaks should be $59/n$ mV for n, the number of electrons during the transfer at the electrode. An isosbestic point is also obtained for I = 0 A. In Fig. 2.10, it is not the case because Cu(I)/Cu(II) couple has a quasi-reversible behaviour and the peak separation of the oxidation and reduction peak is following the prediction of Nicholson with an increasing separation at higher scan rates. Eq. 2.9 is used in this work to calculate the apparent diffusion coefficient D from the slope of the linear regression, which is fitting the evolution of the anodic peak current with the square root

of the scan rate. As the system is quasi-reversible, Eq. 2.9 is strictly not valid, but is used here to evaluate the apparent diffusion coefficient.
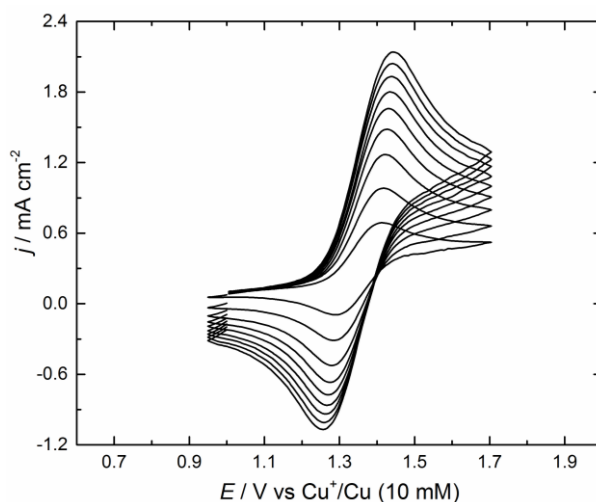

Figure 2.10. CV experiment with ACN solution, Cu(CH₃CN)₄]BF₄ (10 mM) and TEABF₄ (0.1 M). Scan rate at 10-200 mV·s⁻¹.

From the evolution of the apparent diffusion coefficient in Fig. 2.11a, higher temperatures and ACN contents induce a larger diffusion coefficient. This trend is not surprising if the Brownian motion and the Stokes-Einstein equation are considered to explain the effect of these two parameters. While the Einstein relation describes the linearity between D and T, the Stokes-Einsten equation shows the inversed relation of D compared to the viscosity of the medium. As the viscosity of PC is higher than the ACN, the diffusion of Cu^+ is faster in a solvent with lower PC concentrations. The viscosity of ACN-PC solution does not evolve linearly with the PC ratios (cf. Annexes), and the viscosity of the 50 vol% (or 60.5 %(w/w) PC) solution is only 33 % of the pure PC solution. This trend can be partially observed with the larger difference of D between the 50, 30 and 10 ACN vol% solutions, compared to the 100, 70 and 50 % ACN electrolytes, which have a diffusion closer to each other. The influence of low D can be also observed on the CVs in Fig. 2.7a with the decrease of the peak current density for the electrolyte with higher viscosity. This corresponds to the definition of the peak current for CV given by the Randles-Sevcik equation, which states that I_p is proportional to $D^{0.5}$.

According to Fig. 2.11c, the standard rate constant of the Cu^+ oxidation follows the same trend with the temperature and PC content as the diffusion coefficient. One explanation

is that the electron transfer is coupled with a change of the solvation shell around the Cu cation going from a tetrahedral 4-coordinated Cu^+ complex to a probable elongated octahedral 6-coordinated Cu^{2+} complex with ACN. This structural change linked to the redox reaction needs the presence of ACN at the WE to allow a reversible process. In Fig. 2.7a, the CVs with lower ACN content have larger peak separation, which is the sign of a less reversible process according to the Nicholson & Shain theory for quasi-reversible systems.[27,38] As a positive feedback ohmic drop compensation is used when recording these CVs, the peak separation is only assigned to the diminution of the standard rate constant. Consequently, the redox reaction goes from a quasi-reversible to a more irreversible state of kinetics with high PC concentrations.
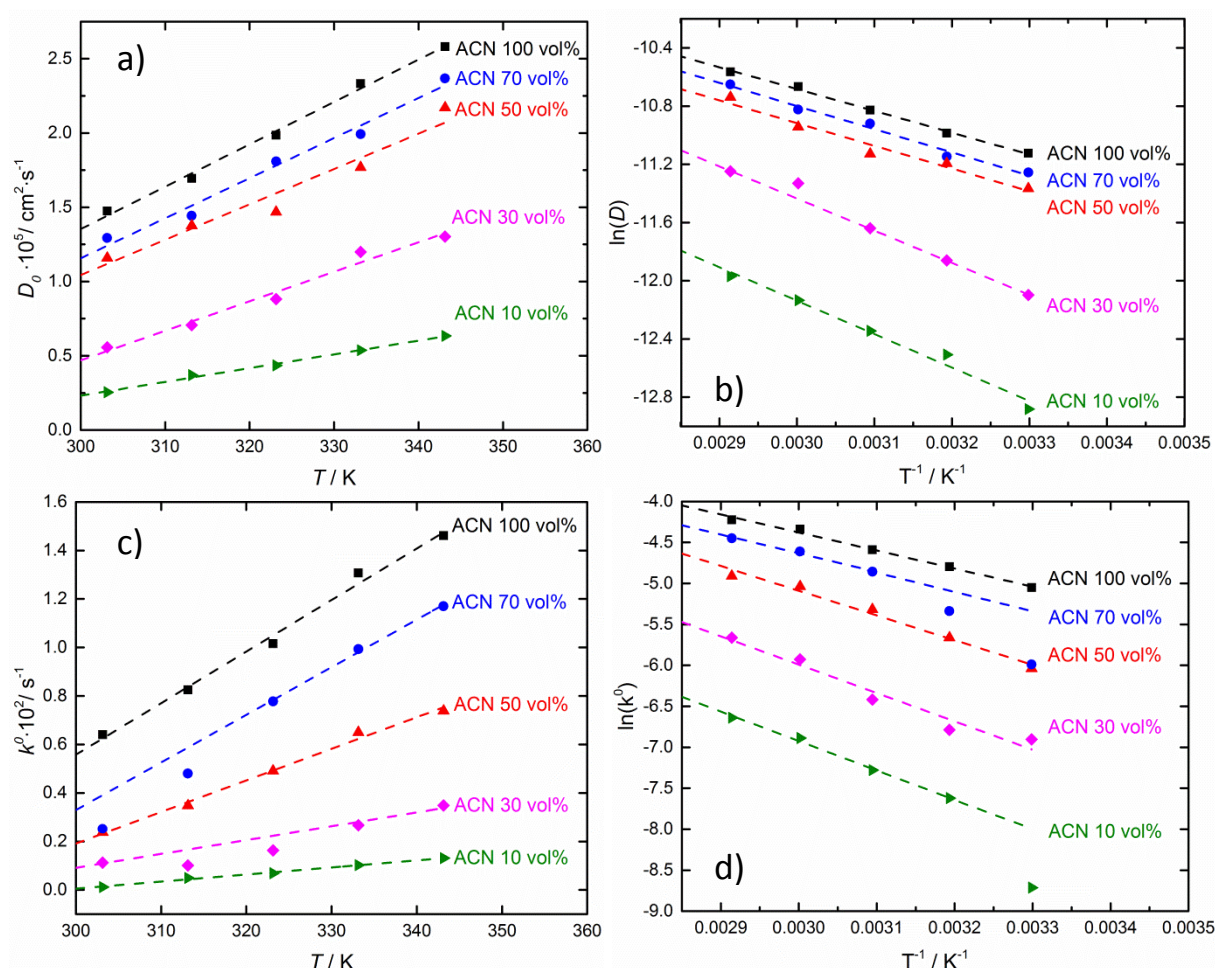
Figure 2.11. a) D in function of the temperature (30 to 70 °C) for solutions with different concentrations of PC in ACN and an electrolyte with $[Cu(CH_3CN)_4]BF_4$ (10 mM) and $TEABF_4$ (0.1 M). b) Arrhenius plot of D for different concentrations of PC in ACN. c) k^0 in function of the temperature (30 to 70 °C) for the same electrolytes. d) Arrhenius plot of k^0 for different concentrations of PC in ACN.

During the calculation of k^0, one approximation is done when Eq. 2.14 is applied to the dimensionless kinetic parameter ψ deduced from the peak separation; the ratio between $D_{Cu(I)}$ and $D_{Cu(II)}$ is considered as constant with the temperature change. The different ratios for the diffusion coefficients of both oxidation states are given in the Annexes with the values of $D_{Cu(II)}$ in the ACN-PC solutions calculated with the Randles-Sevcik equation Eq. 2.9.

A comparison between the kinetic parameters and the literature is shown in Table 2.5. The diffusion coefficient measured in this work corresponds reasonably well to the value reported in literature for ACN, with a slightly lower value [21]. With the difference of viscosity between water and ACN, a higher D is obtained in ACN electrolytes. For k^0, the calculated parameters stand in the middle of the various orders of magnitude that are presented (from 0.18 to $18 \cdot 10^{-3}$ cm·s⁻¹). However, in all the cases, a quasi-reversible kinetic is described. It seems also that the transition state is more symmetrical in aqueous solutions, with α around 0.5, than in organic solvent with 0.3.

Table 2.5. Summary of kinetic parameters in several electrolytes for the Cu(I) oxidation and depositon at 25°C.

Authors	Methods	Conditions	$D \cdot 10^5$ / cm² s⁻¹	$k^0 \cdot 10^3$ / cm s⁻¹	α	
R. Bessette and J. Olver [21]	CA	Cu(I) in ACN, TEAClO₄ 0.1 M	1.64	–	–	
I. D. MacLeod *et al.* [25]	CP, CV	Cu(I) in ACN-H₂O, H₂SO₄ 0.12 M	1.34	0.18	_	
P. Kiekens *et al.* [22]	RDEa RDEb	Cu(I) in H₂O, KCl 0.5 M	1.20	4.6 18	0.49	0.58
B.Stepnik-Swiatek and J. Malyszko [23,24]	RDE	Cu(I) in H₂O, Ca(ClO₄)₂ 1M	1.30	0.27	0.56	
D. Lloyd *et al.* [26]	CV, CA, IS	CuCl₃²⁻ 0.04 M in ethaline	0.027	0.95	0.25	
I. Atek *et al.*[20]	LSV and computation	Cu(I) deposition on Cu WE in ACN, TEABF₄ 0.1 M	1.75	0.03	0.8	
This work	RDE CV	Cu(I) in ACN, TEABF₄ 0.1 M Cu(I) in ACN, TEABF₄ 0.1 M	1.56 ± 0.14 1.48 ± 0.33	6.22 ± 0.13 6.40 ± 0.07	0.7 ± 0.02	

CA: chronoamperometry, CP: chronopotentiometry, CV: cyclic voltammetry, RDE: rotating disk electrode, IS: impedance spectroscopy

With the evolution of D and k^0 as a function of the temperature, the Arrhenius relations for both parameters are plotted in Fig. 2.11b and 2.11d. From the linear fittings, the activation energies for the diffusion and the electron transfer are calculated and reported in Table 2.6. The activation energies E_a for the diffusion and the kinetics increase linearly with the temperature,

and the activation energies are larger for high PC contents. The solutions with ACN 100, 70 and 50 vol% have similar properties regarding the activation energy of the diffusion coefficient. By comparison, the activation energy for k^0 evolves more monotonically with the increase of the PC ratio.

It is difficult to compare all these results with the relevant literature, as there is no published or available studies (from our knowledge). However, E_a for D and k^0 have been reported for the oxidation of Cu^+ in ethaline (mixture of ethylene glycol and choline chloride considered as a deep eutectic solvent) and reach respectively 27.7 and 39 kJ·mol⁻¹ [26]. For this deep eutectic solvent with a viscosity around 15 times higher than the PC, the higher activation energy seems logical for the diffusion. According to Parson's handbook, ions (like Cs^+, Na^+…) have an activation energy for the diffusion in aqueous solution around 16-18 kJ·mol⁻¹ [82]. This indicates that the range that is found for the Cu^+ diffusion activation energy in ACN is reasonable. The presence of ACN lowers the activation energy for k^0.

Table 2.6. Activation energies for the diffusion of the electroactive molecule and its electron transfer at the WE surface.

[ACN] in PC vol%	E_a / kJ·mol⁻¹	
	from $D_{Cu(I)}$	from k^0
100	12.5 ± 0.4	18.3 ± 1.0
70	13.2 ± 0.9	21.2 ± 1.8
50	13.8 ± 2.3	25.1 ± 2.0
30	18.4 ± 1.4	27.7 ± 3.4
10	19.1 ± 1.6	29.8 ± 1.5

6.   Conclusion

With the Randles-Sevcik and Nicholson methods, cyclic voltammetry and rotating disk electrode allow the calculation of Cu^+ and Cu^{2+} diffusion coefficient D and the heterogeneous rate constant k^0 in several ACN-PC mixtures and at different temperatures. Both D and k^0 of the Cu(II)/Cu(I) couple increase with a higher acetonitrile content, and at higher temperatures. The energy activation for the diffusion and the kinetics increase with PC content.

The viscosity of the PC-ACN mixtures and the complexation of Cu ions with ACN are the major factors that guide, respectively, the difference in the diffusion coefficient for the Cu cations and the modification in the kinetics of the electron transfer. The presence of the ACN in the Cu(II)/Cu(I) quasi-reversible one electron system is essential to keep a stable potential window for the +1 oxidation state of the Cu ion. The reversibility of the Cu(II)/Cu(I) electrochemical reaction is dependent of the ACN ligand and the absence of this molecule leads to an irreversible electron transfer with no formation of the Cu(I) after its oxidation.

A battery based on the Cu^+ electrochemistry in ACN and PC is expected to reach a voltage of 1.24 in standard condition with a solvent with pure ACN and 1.0 V when the solvent concentration has 90%(V/V) PC. From CVs recorded at different temperatures, the standard entropy and enthalpy during the $Cu + Cu^{2+}$ comproportionation were evaluated with ΔS^0 and ΔH^0 at respectively, $78.6 \pm 6.9 \ \text{J·mol}^{-1}\text{·K}^{-1}$ and $-95.6 \pm 2.9 \ \text{kJ·mol}^{-1}$. These results confirm the spontaneous and exothermic behavior of the cell discharge to recycle Cu^+ from Cu and Cu^{2+}.

7. References

1. Peljo, P., Lloyd, D., Doan, N., Majaneva, M. & Kontturi, K. Towards a thermally regenerative all-copper redox flow battery. *Phys. Chem. Chem. Phys.* **16**, 2831–2835 (2014).

2. Parker, A. J., Muir, D. M., Smart, Y. C. & Avraamides, J. An application of acetonitrile leaching and disproportionation. *Hydrometallurgy* **7**, 213–233 (1981).

3. Parker, A., Muir, D. M. & Waghorne, W. E. Solvation of ions—some applications. in *Proc R Aust Chem Inst* vol. 39 163–170 (1972).

4. Parker, A. J. *et al.* Compositions containing copper salts, their methods of production and the recovery and purification of copper. *British patent* **1381666**, (1975).

5. Muir, D. M. & Parker, A. J. Low energy processes for the production of pure copper from crude copper, copper sulphate and chalcopyrite by use of aqueous acetonitrile. in *Advances in Extractive Metallurgy* 191–196 (IMM London, 1977).

6. Kratochvil, B. & Betty, K. R. A Secondary Battery Based on the Copper(II)-(I) and (I)-(0) Couples in Acetonitrile. *J. Electrochem. Soc.* **121**, 851–854 (1974).

7. Leung, P. *et al.* Evaluation of electrode materials for all-copper hybrid flow batteries. *Journal of Power Sources* **310**, 1–11 (2016).

8. Schaltin, S. *et al.* Towards an all-copper redox flow battery based on a copper-containing ionic liquid. *Chem. Commun.* **52**, 414–417 (2016).

9. Lloyd, D., Vainikka, T. & Kontturi, K. The development of an all copper hybrid redox flow battery using deep eutectic solvents. *Electrochimica Acta* **100**, 18–23 (2013).

10. Raymond C. Bott, †, Graham A. Bowmaker, *, Carol A. Davis, †, Gregory A. Hope, * & Jones‡, B. E. Crystal Structure of [Cu4(tu)7](SO4)2]·H2O and Vibrational Spectroscopic Studies of Some Copper(I) Thiourea Complexes. http://pubs.acs.org/doi/abs/10.1021/ic970910q (1998).

11. Rizvi, M. A. Complexation modulated redox behavior of transition metal systems (review). *Russ J Gen Chem* **85**, 959–973 (2015).

12. Rizvi, M. A., Akhoon, S. A., Maqsood, S. R. & Peerzada, G. M. Synergistic effect of perchlorate ions and acetonitrile medium explored for extension in copper redoximetry. *J Anal Chem* **70**, 633–638 (2015).

13. Beverskog, B. & Puigdomenech, I. Revised Pourbaix Diagrams for Copper at 25 to 300°C. *J. Electrochem. Soc.* **144**, 3476–3483 (1997).

14. Morgan, H. H. CCCXLII.—Preparation and stability of cuprous nitrate and other cuprous salts in presence of nitriles. *J. Chem. Soc., Trans.* **123**, 2901–2907 (1923).

15. Kubas, G. J., Monzyk, B. & Crumbliss, A. L. Tetrakis(Acetonitrile)Copper(I) Hexafluorophosphate. in *Inorganic Syntheses* (ed. Shriver, D. F.) 90–92 (John Wiley & Sons, Inc., 1979).

16. Haynes, W. M. *CRC Handbook of Chemistry and Physics, 95th Edition*. (CRC Press, 2014).

17. Tobishima, S.-I. & Yamaji, A. Ethylene carbonate—propylene carbonate mixed electrolytes for lithium batteries. *Electrochimica Acta* **29**, 267–271 (1984).

18. Aurbach, D., Daroux, M. L., Faguy, P. W. & Yeager, E. Identification of Surface Films Formed on Lithium in Propylene Carbonate Solutions. *J. Electrochem. Soc.* **134**, 1611–1620 (1987).

19. Marom, R., Francis Amalraj, S., Leifer, N., Jacob, D. & Aurbach, D. A review of advanced and practical lithium battery materials. *Journal of Materials Chemistry* **21**, 9938–9954 (2011).

20. Atek, I., Maye, S., Girault, H. H., Affoune, A. M. & Peljo, P. Semi-analytical modelling of linear scan voltammetric responses for soluble-insoluble system: The case of metal deposition. *Journal of Electroanalytical Chemistry* **818**, 35–43 (2018).

21. Bessette, R. R. & Olver, J. W. Measurement of diffusion coefficients for the reduction of copper(I) and (II) in acetonitrile. *Journal of Electroanalytical Chemistry and Interfacial Electrochemistry* **21**, 525–529 (1969).

22. Kiekens, P., Verbeeck, R. M. H. & Temmerman, E. A kinetic study of the Cu(II)/Cu(I) system in Cl⁻ media at the glassy carbon electrode. *Mikrochim Acta* **76**, 29–36 (1981).

23. Stepnik-Swiatek, B. & Malyszko, J. Determination of diffusion coefficients of Cu(I) ions in concentrated perchlorate solutions. *Monatsh Chem* **113**, 715–718 (1982).

24. Stępnik-Świątek, B. & Małyszko, J. Kinetics of the Cu2+/Cu+ electrode reaction at gold in concentrated aqueous Ca(ClO4)2 solutions. *Journal of Electroanalytical Chemistry and Interfacial Electrochemistry* **292**, 175–185 (1990).

25. Macleod, I. D., Parker, A. J. & Singh, P. Electrochemistry of copper in aqueous acetonitrile. *J Solution Chem* **10**, 757–774 (1981).

26. Lloyd, D., Vainikka, T., Murtomäki, L., Kontturi, K. & Ahlberg, E. The kinetics of the Cu2+/Cu+ redox couple in deep eutectic solvents. *Electrochimica Acta* **56**, 4942–4948 (2011).

27. Nicholson, R. S. & Shain, I. Theory of stationary electrode polarography single scan and cyclic methods applied to reversible, irreversible, and kinetic systems. *Analytical Chemistry* **36**, 706–723 (1964).

28. Sevcik, A. Oscillographic polarography with periodical triangular voltage. *Collection of Czechoslovak Chemical Communications* **13**, 349–377 (1948).

29. Reinmuth, W. H. Nernst-controlled Currents in Hanging-drop Polarography. *Journal of the American Chemical Society* **79**, 6358–6360 (1957).

30. Matsuda, H. & Ayabe, Y. Zur Theorie der Randles-Sevčikschen Kathodenstrahl-Polarographie. *Zeitschrift für Elektrochemie, Berichte der Bunsengesellschaft für physikalische Chemie* **59**, 494–503 (1955).

31. Gokhshtein, Y. P. *Dokl. Akad. Nauk SSSR* **126**, 598 (1959).

32. Ramamurthy, A. C. & Rangarajan, S. K. A Gaussian quadrature analysis of linear sweep voltammetry. *Electrochimica Acta* **26**, 111–115 (1981).

33. Myland, J. C. & Oldham, K. B. An analytical expression for the current-voltage relationship during reversible cyclic voltammetry. *Journal of Electroanalytical Chemistry and Interfacial Electrochemistry* **153**, 43–54 (1983).

34. Randles, J. E. B. A cathode ray polarograph. Part II.—The current-voltage curves. *Trans. Faraday Soc.* **44**, 327–338 (1948).

35. Allen J. Bard & Larry R. Faulkner. *Electrochemical Methods: Fundamentals and Applications, 2nd Edition - Allen J. Bard, Larry R. Faulkner.*

36. Vetter, K. J. *Electrochemical kinetics: theoretical and experimental aspects.* (Academic Press, 1967).

37. Erdey-Gruz, T. & Grúz, T. *Kinetics of electrode processes.* (Wiley-Interscience Budapest, 1972).

38. Nicholson, R. S. Theory and Application of Cyclic Voltammetry for Measurement of Electrode Reaction Kinetics. *Anal. Chem.* **37**, 1351–1355 (1965).

39. Levich, V. G. Physicochemical Hydrodynamics. *Prentice-Hall, Englewood Cliffs, NJ* (1962).

40. Hathaway, B. J., Holah, D. G. & Underhill, A. E. 468. The preparation and properties of some bivalent transition-metal tetrafluoroborate–methyl cyanide complexes. *J. Chem. Soc.* 2444–2448 (1962) doi:10.1039/JR9620002444.

41. Persson, I., Penner-Hahn, J. E. & Hodgson, K. O. An EXAFS spectroscopic study of solvates of copper(I) and copper(II) in acetonitrile, dimethyl sulfoxide, pyridine, and tetrahydrothiophene solutions and a large-angle x-ray scattering study of the copper(II) acetonitrile solvate in solution. *Inorganic Chemistry* **32**, 2497–2501 (1993).

42. Dodi, G., Hritcu, D., Lisa, G. & Popa, M. I. Core–shell magnetic chitosan particles functionalized by grafting: Synthesis and characterization. *Chemical Engineering Journal* **203**, 130–141 (2012).

43. Crystal Field Theory. http://2012books.lardbucket.org/books/principles-of-general-chemistry-v1.0/s27-05-crystal-field-theory.html.

44. Xile Hu. Coordination Chemistry EPFL course. (2012).

45. Nagy, L. *et al.* The local structures of Cu(II) and Zn(II) complexes of hyaluronate. *Journal of Inorganic Biochemistry* **72**, 49–55 (1998).

46. Ohtaki, H., Yamaguchi, T. & Maeda, M. X-Ray Diffraction Studies of the Structures of Hydrated Divalent Transition-Metal Ions in Aqueous Solution. *BCSJ* **49**, 701–708 (1976).

47. Jahn, H. A. & Teller, E. Stability of Polyatomic Molecules in Degenerate Electronic States. I. Orbital Degeneracy. *Proceedings of the Royal Society of London A: Mathematical, Physical and Engineering Sciences* **161**, 220–235 (1937).

48. Walton, P. H. *Beginning Group Theory for Chemistry.* (OUP Oxford, 1998).

49. Sathyanarayana, D. N. *Vibrational Spectroscopy: Theory and Applications*. (New Age International, 2015).

50. Neelakantan, P. Raman spectrum of acetonitrile. *Proc. Indian Acad. Sci.* **60**, 422–424 (1964).

51. Evans, J. C. & Bernstein, H. J. Intensity in the Raman effect: IV. Raman intensity some rules and frequency assignments for CH$_3$CN, CD$_3$CN, CH$_3$CCl$_3$, and CD$_3$CCl$_3$. *Can. J. Chem.* **33**, 1746–1755 (1955).

52. Sadlej, J. Interpretation of the i.r. and Raman spectrum of acetonitrile solutions of electrolytes in the CN stretching region. *Spectrochimica Acta Part A: Molecular Spectroscopy* **35**, 681–684 (1979).

53. Shimanouchi, T. Tables of Molecular Vibrational Frequencies Consolidated Volume I. 1–160 (1972).

54. Dimitrova, Y. Vibrational frequencies and infrared intensities of acetonitrile coordinated with metal cations: an ab initio study. *Journal of Molecular Structure: THEOCHEM* **343**, 25–30 (1995).

55. Sasic, S. *Pharmaceutical Applications of Raman Spectroscopy*. (John Wiley & Sons, 2008).

56. Lozinšek, M. *et al.* Syntheses, crystal structures and Raman spectra of Ba(BF$_4$)(PF$_6$), Ba(BF$_4$)(AsF$_6$) and Ba$_2$(BF$_4$)$_2$(AsF$_6$)(H$_3$F$_4$); the first examples of metal salts containing simultaneously tetrahedral BF$_4^-$ and octahedral AF$_6^-$ anions. *Journal of Solid State Chemistry* **182**, 2897–2903 (2009).

57. Sequeira, C. & Santos, D. *Polymer Electrolytes: Fundamentals and Applications*. (Elsevier, 2010).

58. Addison, C. C. *Inorganic Chemistry of the Main-Group Elements*. (Royal Society of Chemistry, 1976).

59. Suffren, Y., Rollet, F.-G. & Reber, C. Raman spectroscopy of transition metal complexes: molecular vibrational frequencies, phase transitions, isomers, and electronic structures. *Comments on Inorganic Chemistry* **32**, 246–276 (2011).

60. Pavel, I. *et al.* Vibrational behavior of transition metal cupferronato complexes. Raman and SERS studies on nickel(II) cupferronato complexes. *Vibrational Spectroscopy* **23**, 71–76 (2000).

61. Tsierkezos, N. G. Cyclic Voltammetric Studies of Ferrocene in Nonaqueous Solvents in the Temperature Range from 248.15 to 298.15 K. *J Solution Chem* **36**, 289–302 (2007).

62. Peljo, P., Lloyd, D., Doan, N., Majaneva, M. & Kontturi, K. Towards a thermally regenerative all-copper redox flow battery. *Phys. Chem. Chem. Phys.* **16**, 2831–2835 (2014).

63. Li, Y. *et al.* A non-aqueous all-copper redox flow battery with highly soluble active species. *Electrochimica Acta* **236**, 116–121 (2017).

64. Lloyd, D., Magdalena, E., Sanz, L., Murtomäki, L. & Kontturi, K. Preparation of a cost-effective, scalable and energy efficient all-copper redox flow battery. *Journal of Power Sources* **292**, 87–94 (2015).

65. Sanz, L., Lloyd, D., Magdalena, E., Palma, J. & Kontturi, K. Description and performance of a novel aqueous all-copper redox flow battery. *Journal of Power Sources* **268**, 121–128 (2014).

66. Reynard, D., Dennison, C. R., Battistel, A. & Girault, H. H. Efficiency improvement of an all-vanadium redox flow battery by harvesting low-grade heat. *Journal of Power Sources* **390**, 30–37 (2018).

67. Wagman, D. D., Evans, W. H., Parker, V. B., Schumm, R. H. & Halow, I. *The NBS Tables of Chemical Thermodynamic Properties. Selected Values for Inorganic and C1 and C2 Organic Substances in SI Units,*. https://apps.dtic.mil/docs/citations/ADD095481 (1982).

68. Chase, M. W. NIST-JANAF Themochemical Tables, Fourth Edition. *J. Phys. Chem. Ref. Data, Monograph 9* 1–1951 (1998).

69. Cox, J. D., Wagman, D. D. & Medvedev, V. A. CODATA Key Values for Thermodynamics. 1 (1984).

70. Reynier, Y. *et al.* Entropy of Li intercalation in Li x CoO 2. *Physical Review B* **70**, (2004).

71. Noll, R. J. & Hughes, J. M. Heat Evolution and Electrical Work of Batteries as a Function of Discharge Rate: Spontaneous and Reversible Processes and Maximum Work. *Journal of Chemical Education* **95**, 852–857 (2018).

72. Macdonald, D. D. & Challingsworth, M. L. Thermodynamics of Nickel-Cadmium and Nickel-Hydrogen Batteries. *J. Electrochem. Soc.* **140**, 606–609 (1993).

73. Tatsumi, K. *et al.* Atomic structures and energetics of LaNi 5 − H solid solution and hydrides. *Physical Review B* **64**, (2001).

74. Linden, D. & Reddy, T. B. Handbook of Batteries 3rd edition. *TRD: McGraw-Hill* (2002).

75. Pourbaix, M. Atlas of Electrochemical Equilibria in Aqueous Solutions. *NACA* (1984).

76. Bard, A. J., Parsons, R. & Jordan, J. Standard potentials in aqueous solution. (1985).

77. Bratsch, S. G. Standard Electrode Potentials and Temperature Coefficients in Water at 298.15 K. *Journal of Physical and Chemical Reference Data* **18**, 1–21 (1989).

78. Heintz, A. & Illenberger, C. Thermodynamics of Vanadium Redox Flow Batteries - Electrochemical and Calorimetric Investigations. *Berichte der Bunsengesellschaft für physikalische Chemie* **102**, 1401–1409 (1998).

79. Hepler, L. G., Hill, J. O. & Worsley, I. G. Thermochemistry and oxidation potentials of vanadium, niobium, and tantalum. *Chemical Reviews* **71**, 127–137 (1971).

80. Hudak, N. S. Practical thermodynamic quantities for aqueous vanadium- and iron-based flow batteries. *Journal of Power Sources* **269**, 962–974 (2014).

81. Latimer, W. M. *Oxidation states of the elements and their potentials in aqueous solutions.* (Prentice-Hall Incorporated, 1938).

82. Roger Parsons. *Handbook of Electrochemical Constants*. (Academic Press, 1959).

83. Moumouzias, G., Panopoulos, D. K. & Ritzoulis, G. Excess properties of the binary liquid system propylene carbonate + acetonitrile. *J. Chem. Eng. Data* **36**, 20–23 (1991).

8. Annexes

8.1. RDE experiments in ACN solution, Cu(CH₃CN)₄]BF₄ (10 mM) and TEABF₄ (0.1 M). LSVs for the Cu⁺ oxidation at 50 mV s⁻¹ and various rotation rates (500, 832, 1248, 1748, 2332, 3000 rpm) with the corresponding Koutecký-Levich plot for potential with limiting current for the diffusion coefficient calculation.
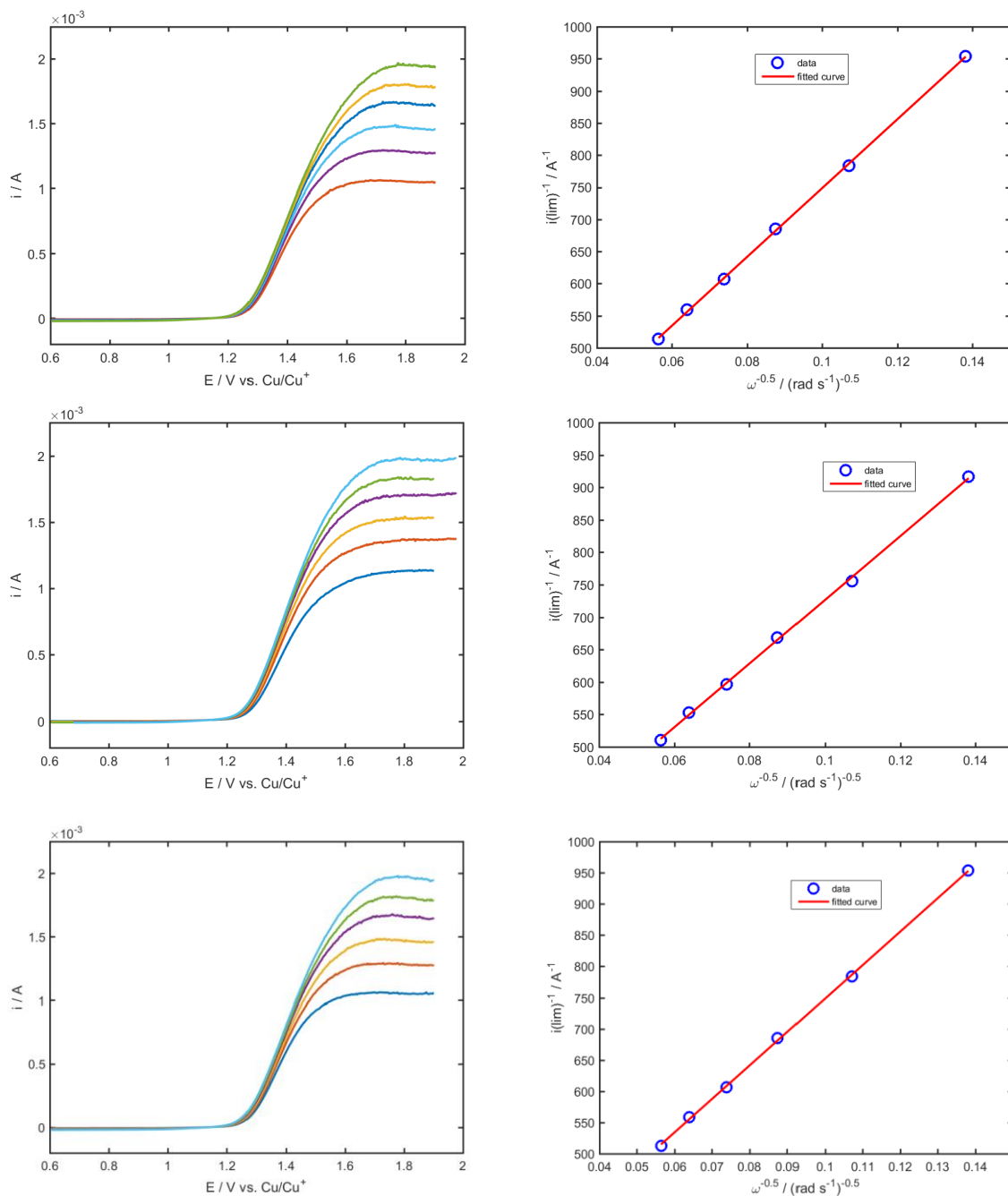
8.2. Viscosity of ACN-PC mixtures and comparison with values in literature. [83]
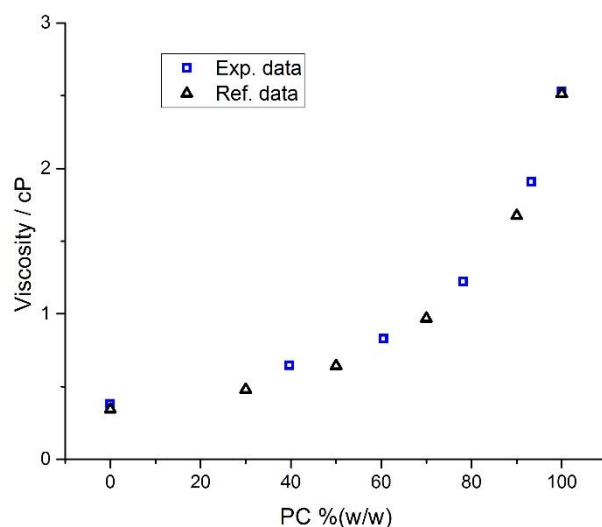
8.3. Diffusion coefficients for the Cu(II) oxidation state and the ratios of $D_{Cu(I)}$:$D_{Cu(II)}$ for the different solvent compositions of the ACN-PC system (Cu(CH₃CN)₄]BF₄ (10 mM) and TEABF₄ (0.1 M)). Detailed CVs at different scan rates for the determination of the Cu(II) diffusion coefficient starting between 1.4-1.5 V *vs.* Cu⁺/Cu (10 mM) in the reduction scanning direction to lower potential. The corresponding plots of the current peak i_p versus the square root of the scan rate is added with the linear regression.
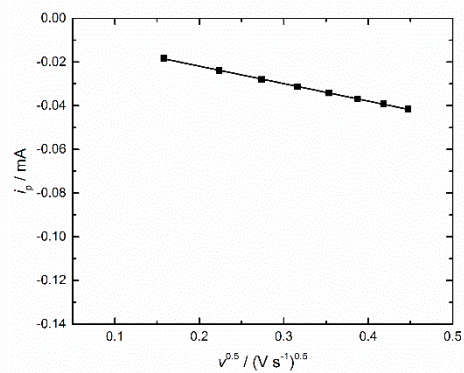
ACN 100 vol%

ACN 70 vol%
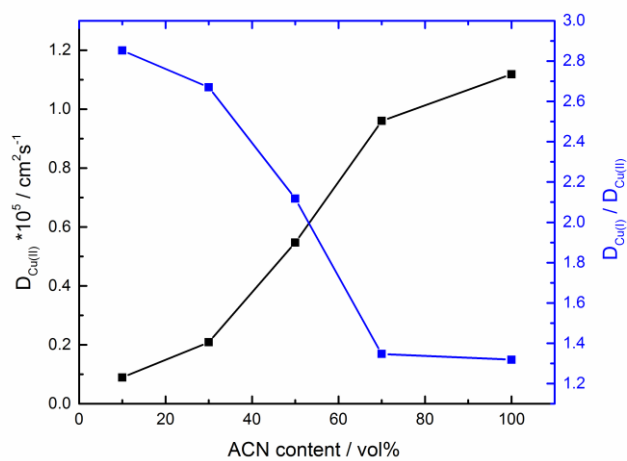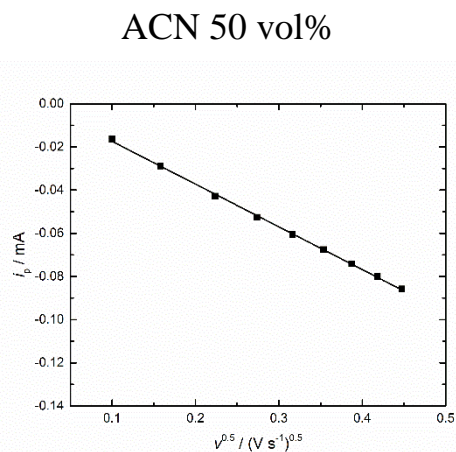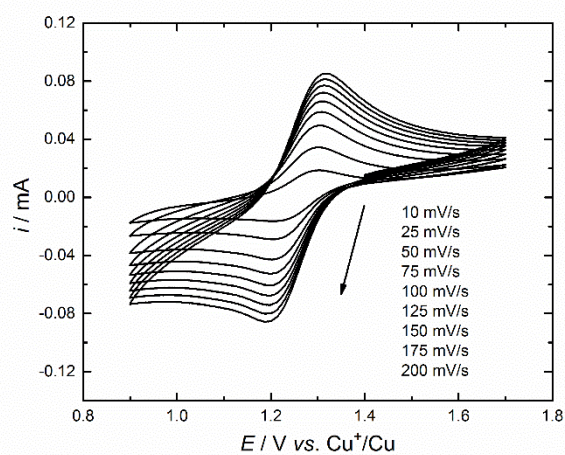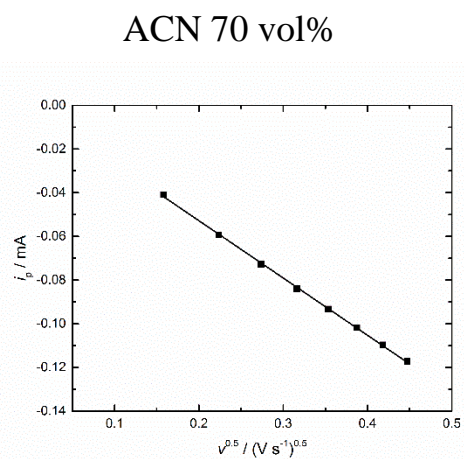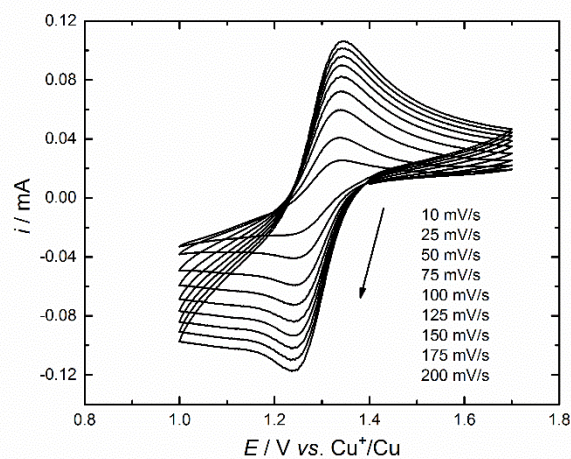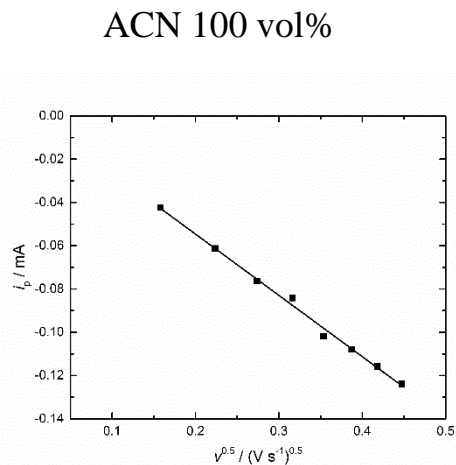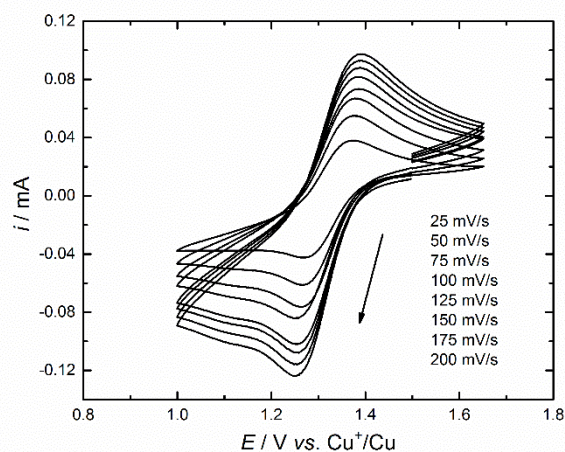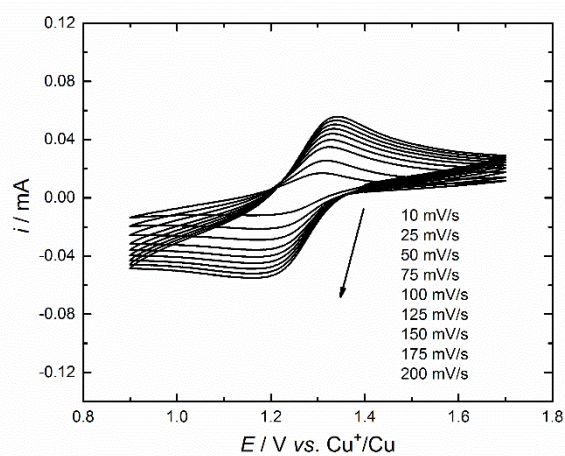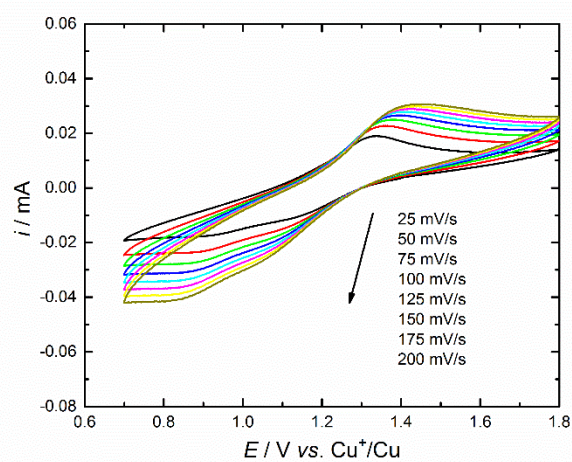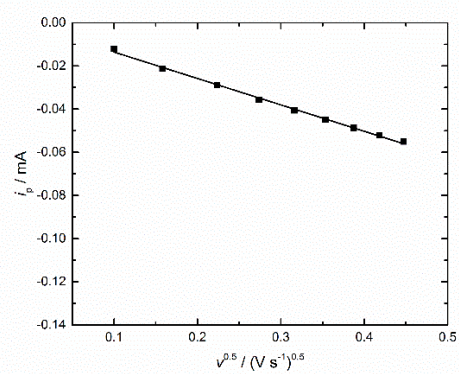
ACN 50 vol%

8.4. Diffusion coefficients for the Cu(I) oxidation state at various temperatures and in different solvent compositions of the ACN-PC system (Cu(CH$_3$CN)$_4$]BF$_4$ (10 mM) and TEABF$_4$ (0.1 M)). Detailed CVs at different scan rates for the determination of the Cu(I) diffusion coefficient starting between 0.5-0.7 V *vs.* Cu⁺/Cu (10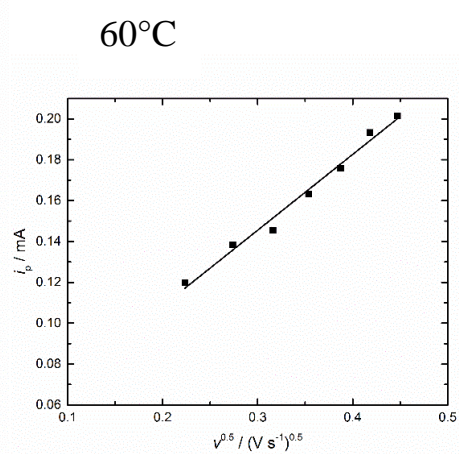 mM) in the oxidation scanning direction to higher potentials. The corresponding plots of the current peak i_p versus the square root of the scan rate is added with the linear regression.

8.4.1. CVs for ACN 100 vol%
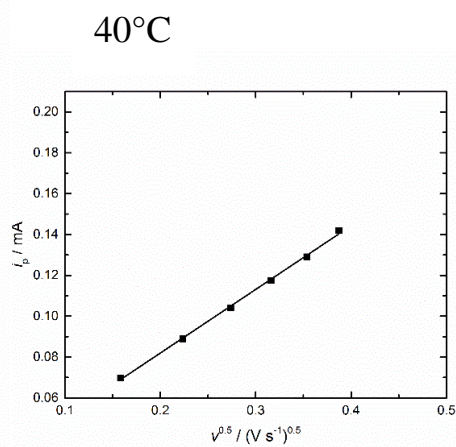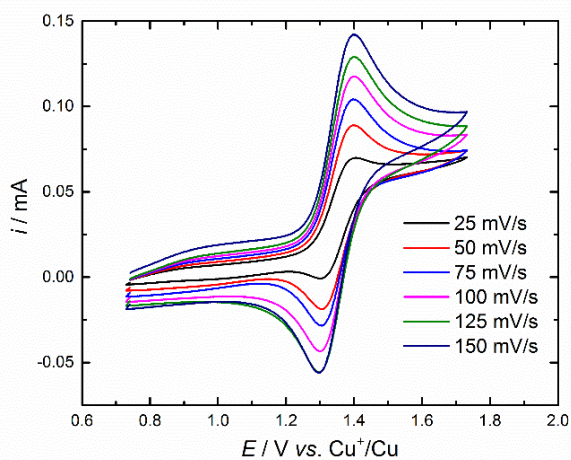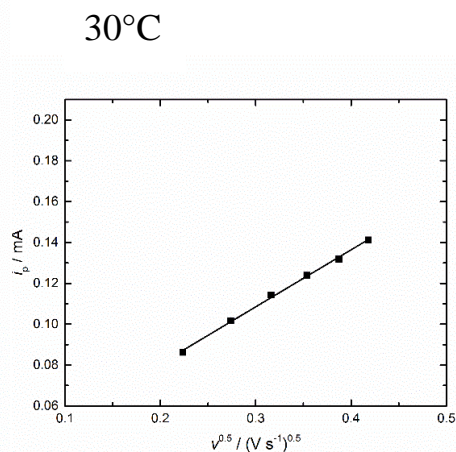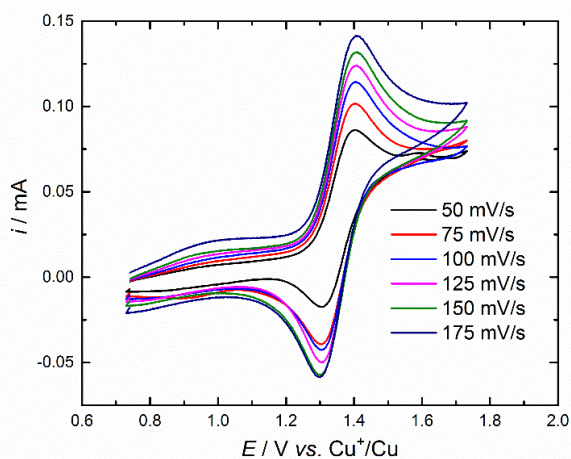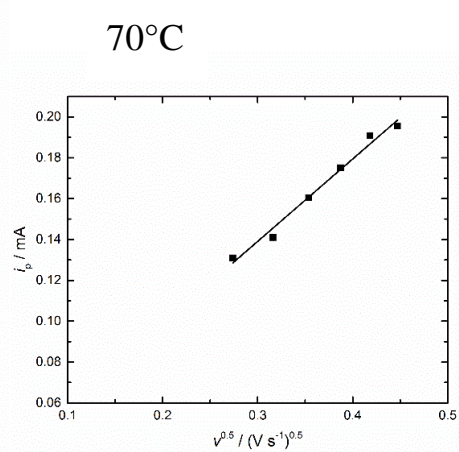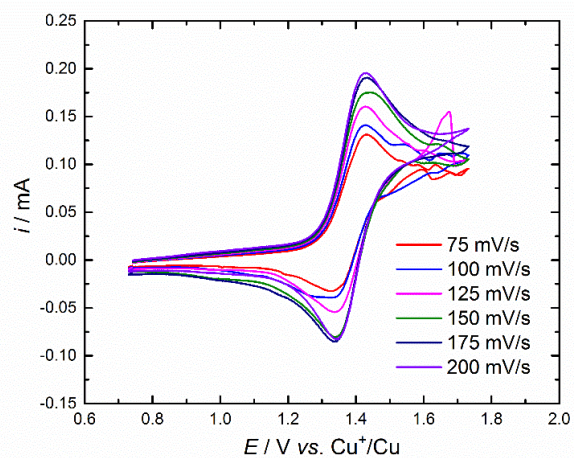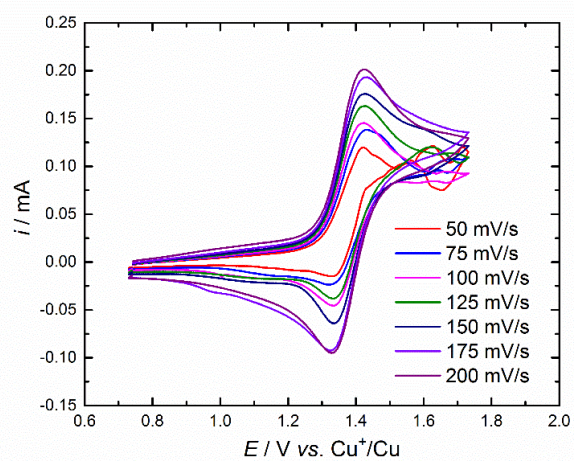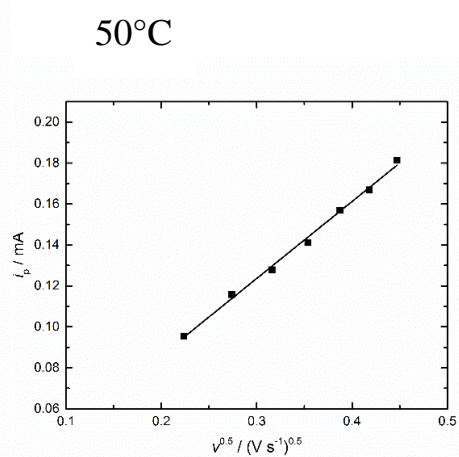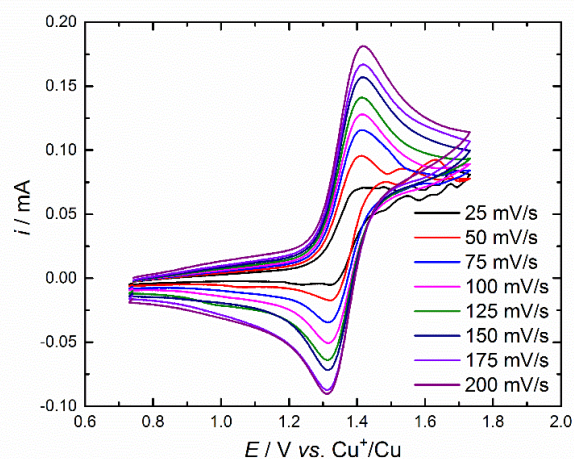
8.4.2. CVs for ACN 70 vol%
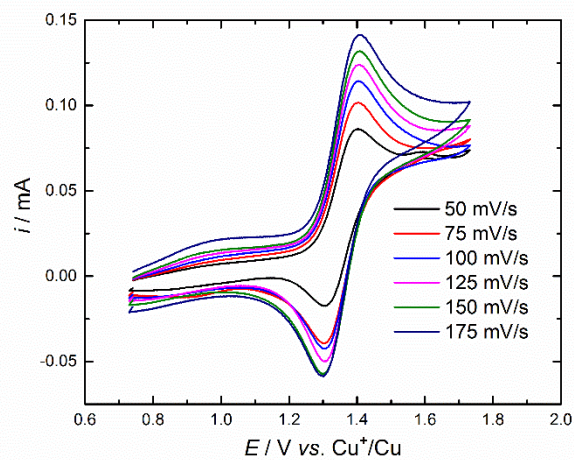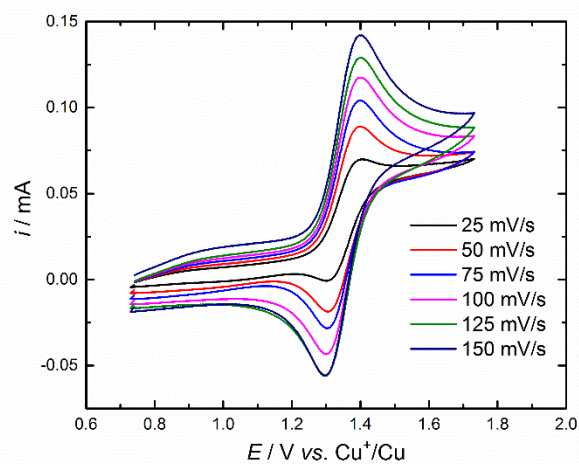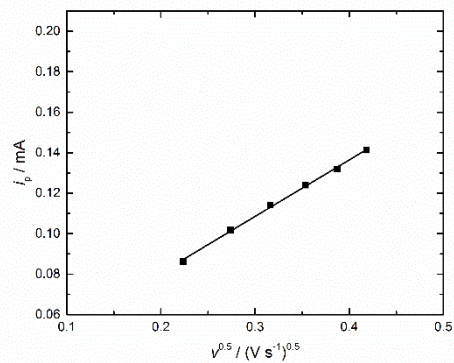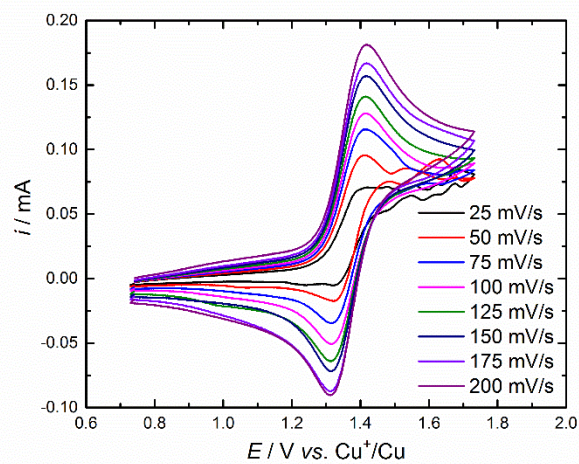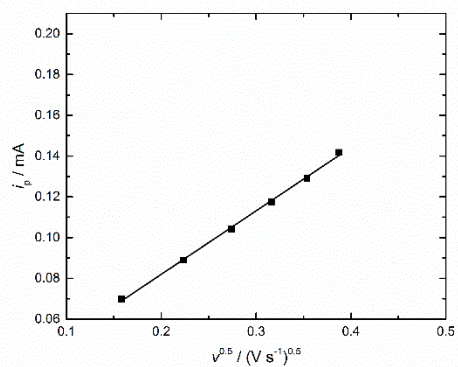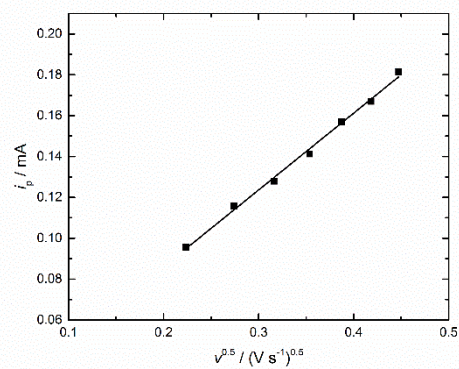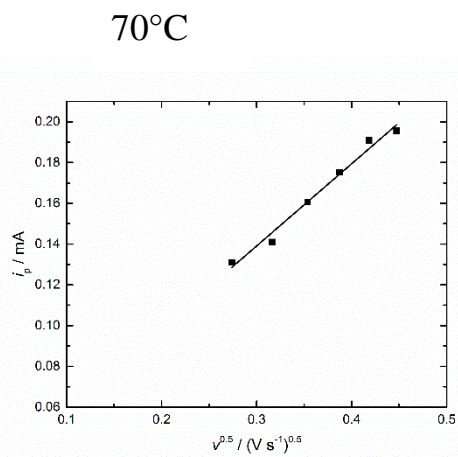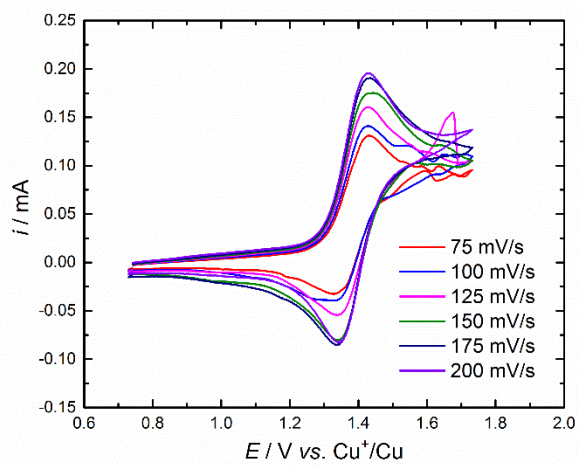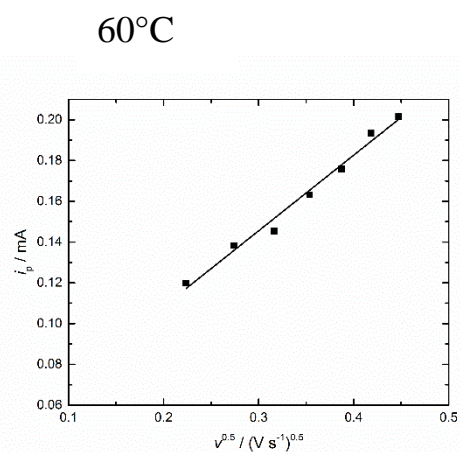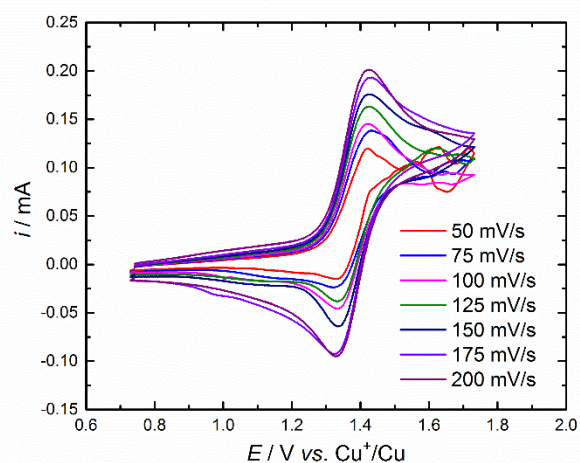
8.4.3. CVs for ACN 50 vol%

60°C

70°C
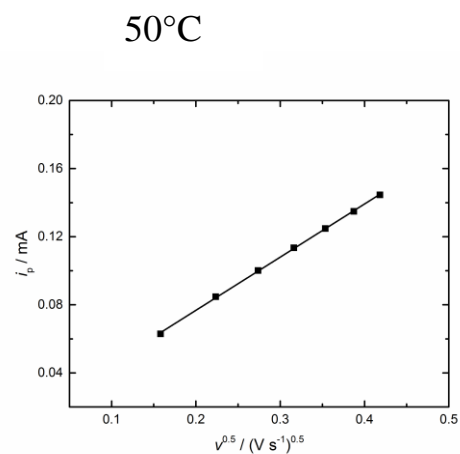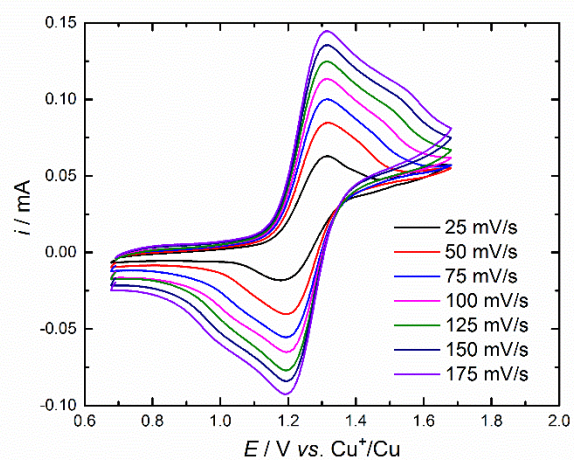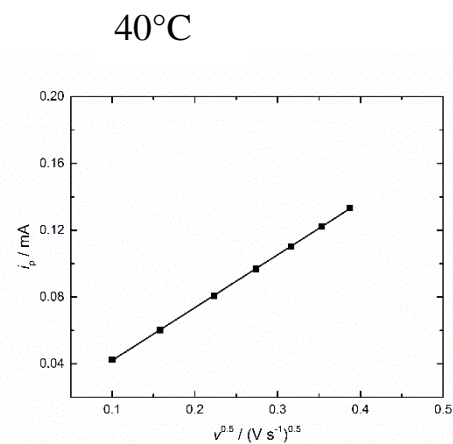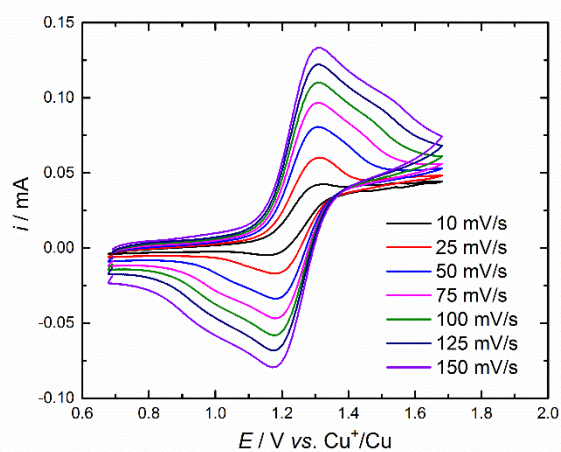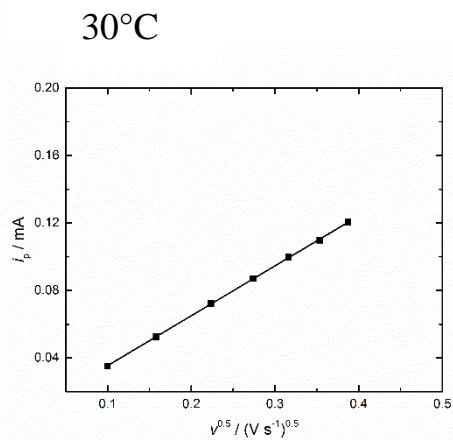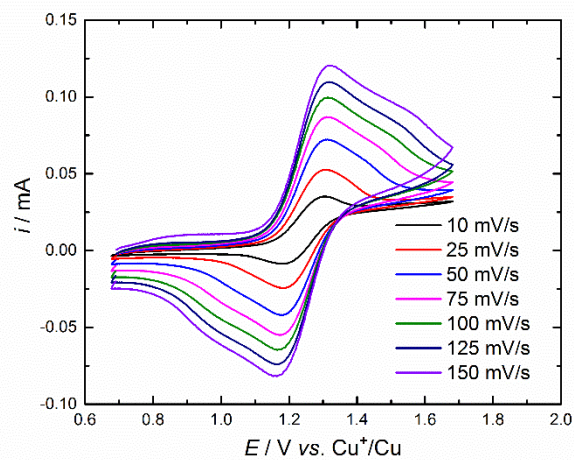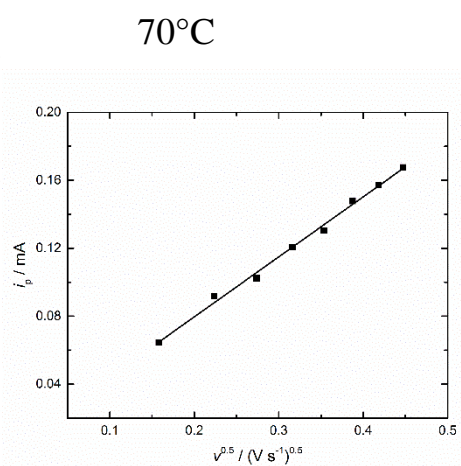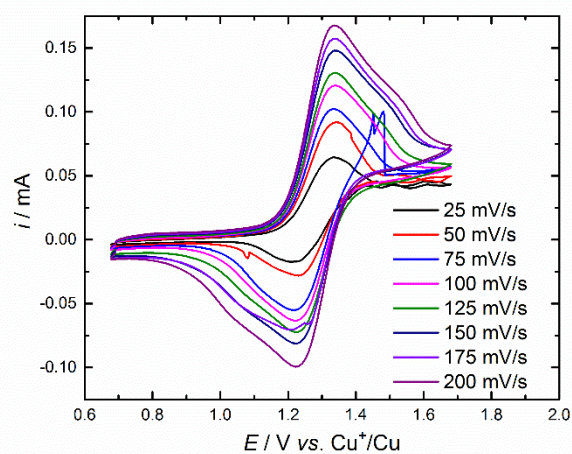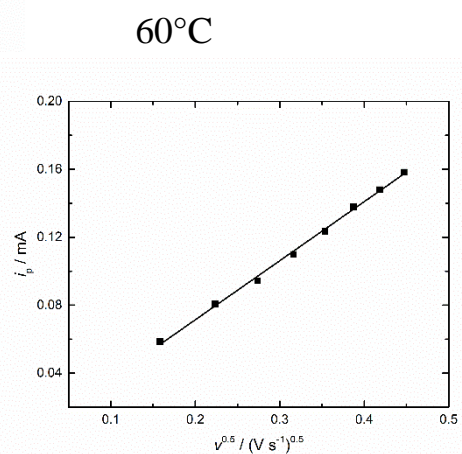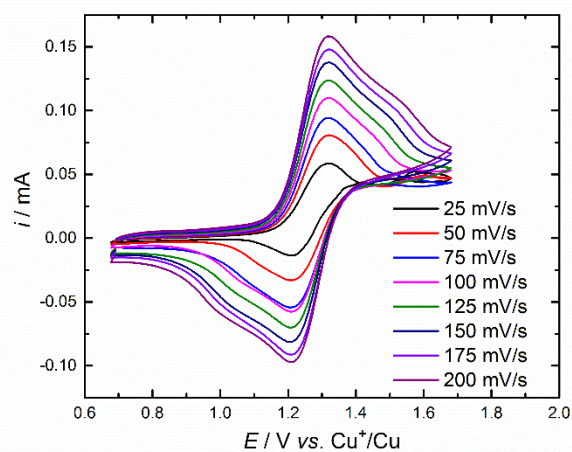
8.4.4. CVs for ACN 30 vol%

30°C

40°C

50°C
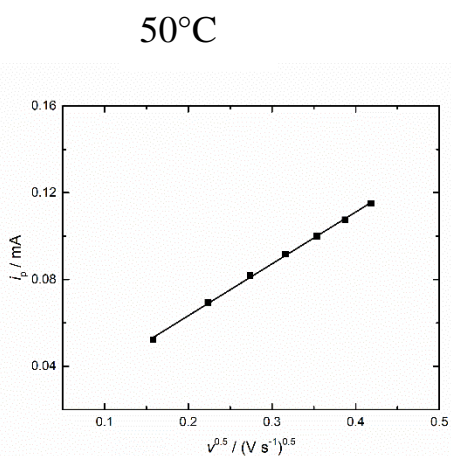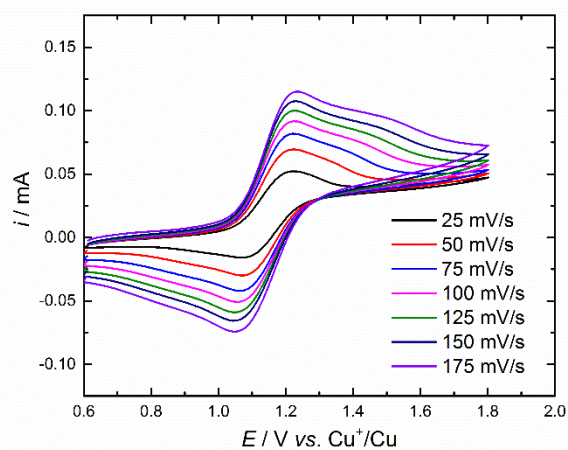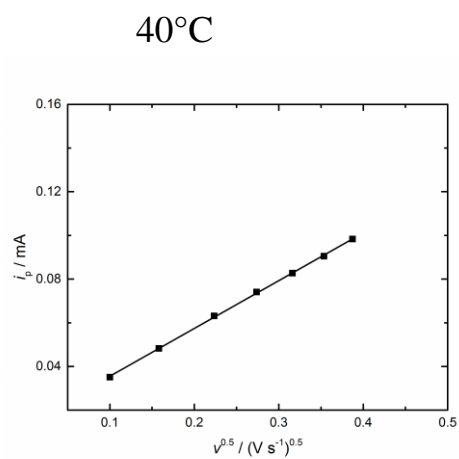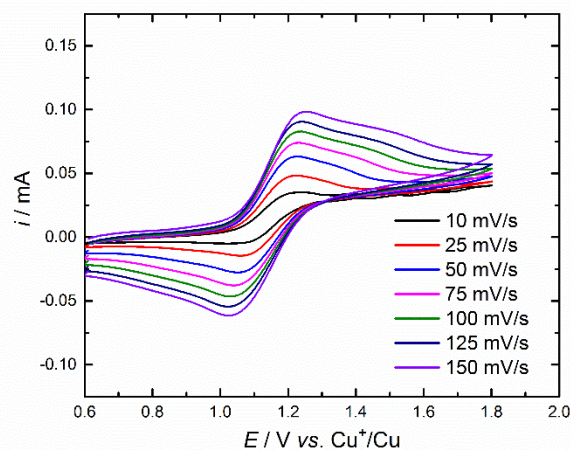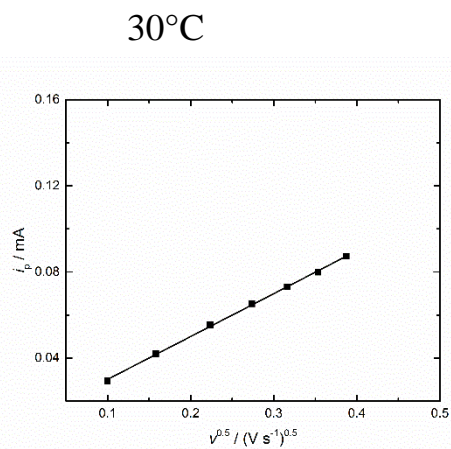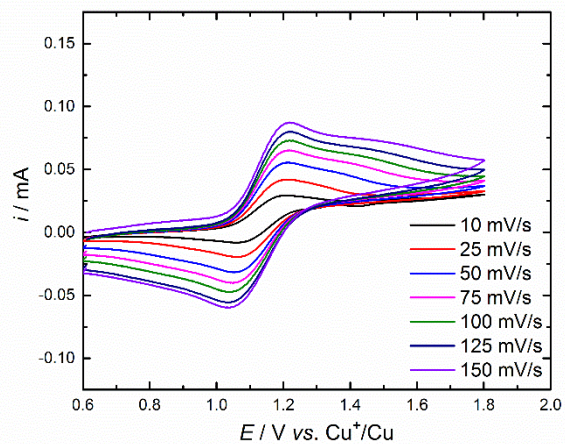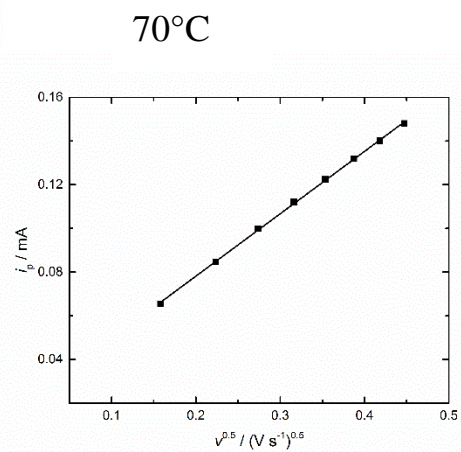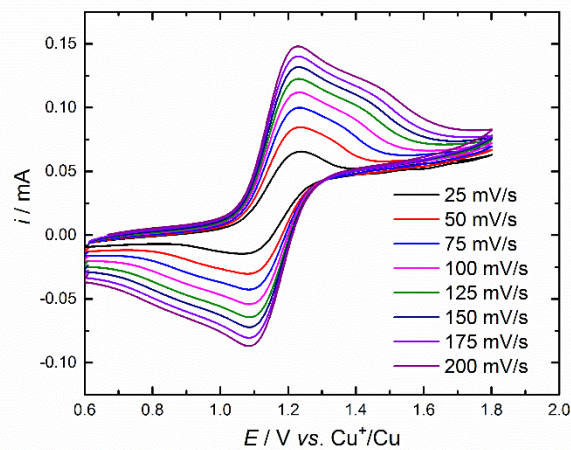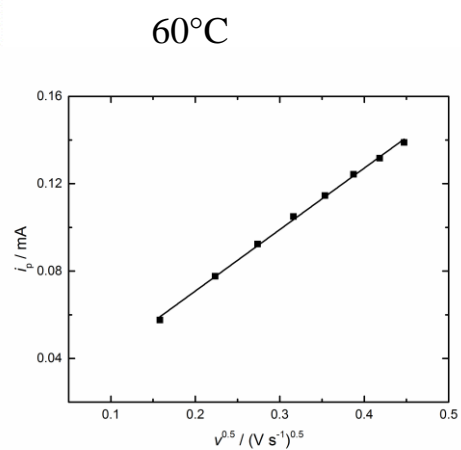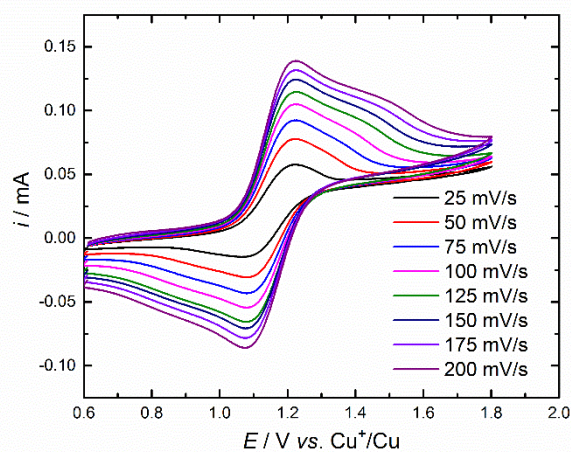
8.4.5. CVs for ACN 10 vol%
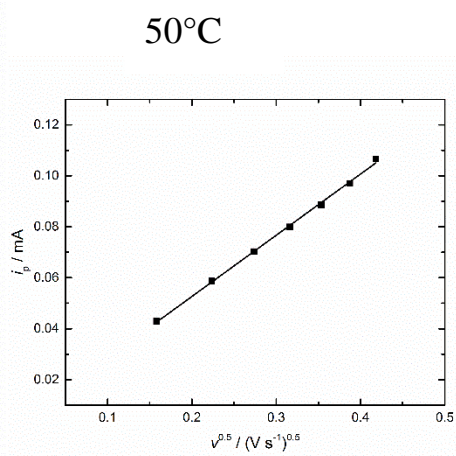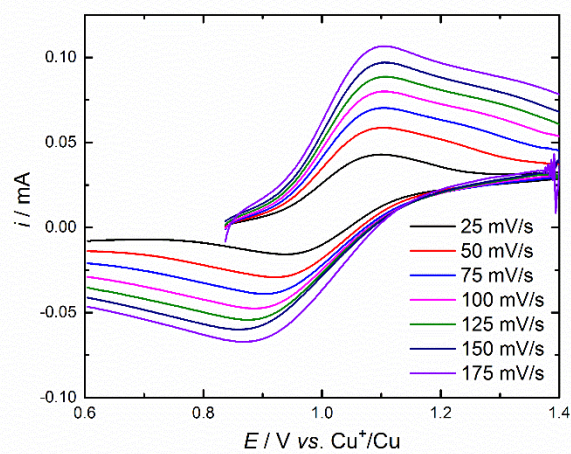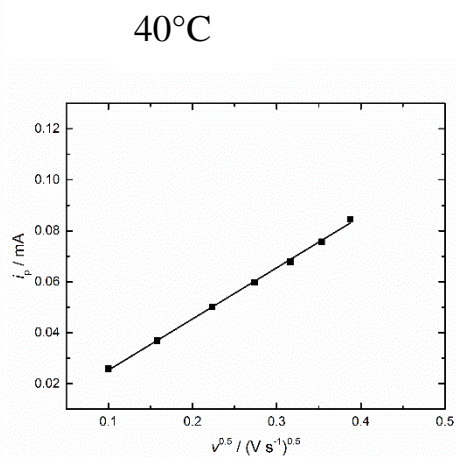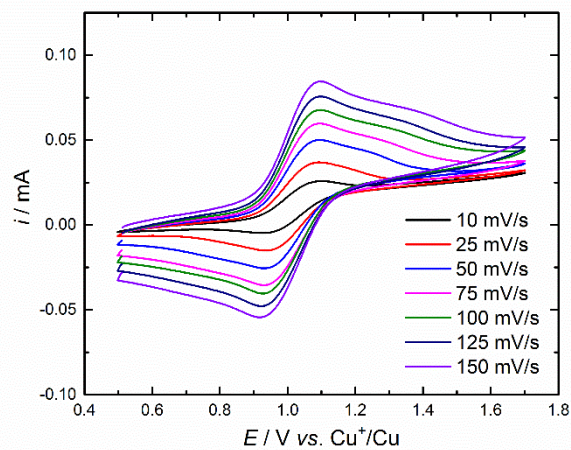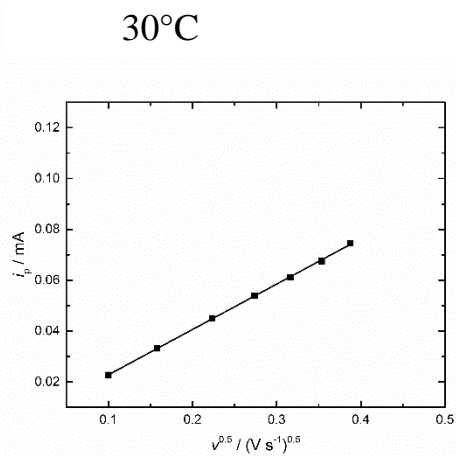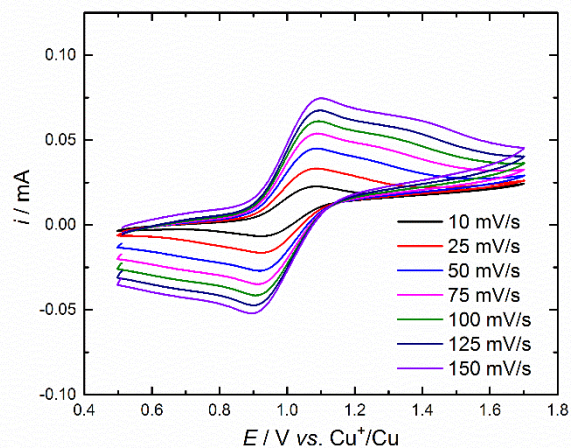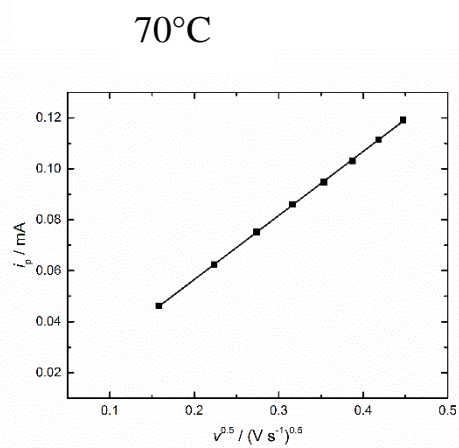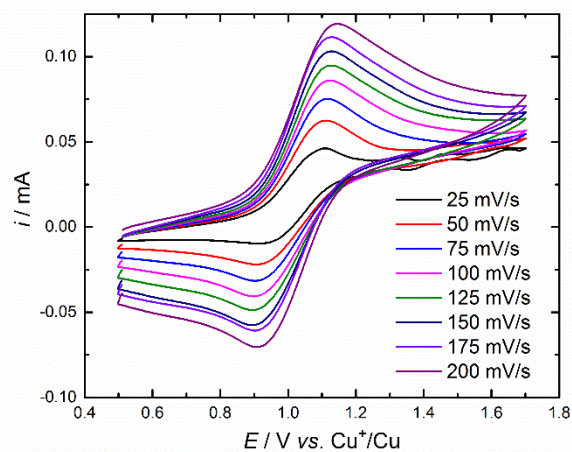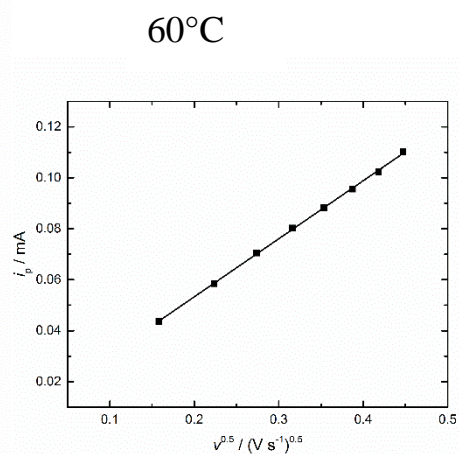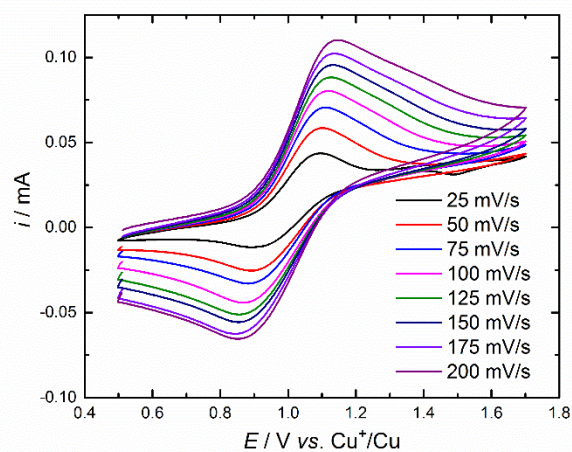
Chapter III

Cu deposition on Cu electrode from Cu⁺ reduction in acetonitrile

Based on the published paper, [1]

Semi-analytical modelling of linear scan voltammetric responses for soluble-insoluble system: The case of metal deposition.

J. Electroanal. Chem. **818**, 35–43 (2018).

I. Atek, S. Maye, H. H. Girault, A. M. Affoune & P. Peljo.

This chapter is a short summary of the more important results from the mentioned paper, which studies the voltammetric response for soluble-insoluble systems. The case of interest is here Cu deposition from Cu^+ salt.

---

[1] According to the Algerian rules, only the first author is allowed to include the paper in the thesis. Therefore, only a short summary of the paper is given here instead of the full paper.

1. Working curves for linear sweep voltammetric responses for soluble-insoluble system

The general theory for voltammetry of soluble-soluble system is well established, and quantitative kinetic information is routinely extracted from the analysis of the experimental results, as described in Chapter 2. But until recently, the general theoretical models describing linear sweep voltammetry (LSV) response for soluble-insoluble systems such as one-step electrodeposition reactions under quasi-reversible condition were absent. We have demonstrated a generalized model for one–step electrodeposition process, for a case where instantaneous nucleation takes place, such as metal deposition on same metal. Consequently, the working curves developed in this work are not suitable when progressive nucleation or supplementary overpotentials are needed during the deposition, for example, when a progressive 3D nucleation occurs,[1,2] as this can drastically change the shape of the LSV response.[1]

Simulated voltammograms were obtained over a wide range of both the dimensionless rate constants and charge transfer coefficients were used to generate working curves to allow easier analysis of the voltammetric data. A summary of the differences between the soluble-soluble and soluble-insoluble systems is given in this section. For soluble-insoluble system the Nernst equation (Eq. 3.1), when the redox reaction is at equilibrium is:

$$E_{eq} = E^0 + \frac{RT}{nF} \ln\left(\frac{a_{M^{n+}}}{a_M} \right) = E^{0'} + \frac{RT}{nF} \ln\left(\frac{C^*_{M^{n+}}}{C^0} \right) \tag{3.1}$$

where $a_M = 1$ for pure metal and $a_{M^{n+}} = \gamma_{M^{n+}} \dfrac{C^*_{M^{n+}}}{C^0}$ are respectively the activity of the metal and the corresponding cation. Unlike for soluble-soluble systems, the change of potential induces a modification of only the concentration of the metal ion in solution ($C_{M^{n+}}$), while the activity of the pure metal is 1 as long as there is any metal left at the electrode. Equation 3.5 describes the current of a reversible system according to the dimensionless current $\chi(\sigma t)$. This equation is calculated from the partial differential equation (Eq. 3.2), which is the Fick's second law of diffusion for the metal ion in solution:

$$\frac{\partial C_{M^{n+}}(x,t)}{\partial t} = D_o \frac{\partial^2 C_{M^{n+}}(x,t)}{\partial x^2} \tag{3.2}$$

The initial and boundary conditions are the following:

$$t = 0, \qquad C_{M^{n+}}(x, 0) = C^*_{M^{n+}} \tag{3.3}$$

$$x \to \infty, \qquad C_{M^{n+}}(\infty, 0) = C^*_{M^{n+}} \tag{3.4}$$

$$i = nFAC^*_{M^{n+}} \sqrt{\pi D_r \sigma} \cdot \chi(\sigma t) \qquad\qquad \sigma = \frac{nFv}{RT} \tag{3.5}$$

This approach is valid in the presence of sufficient amount of supporting electrolyte, so that almost no mass transport of the oxidized and reduced species takes place by migration. The dimensionless current for reversible system, $\chi(\sigma t)$ depends on the time and indicates the link between the current and potential. The $\pi^{0.5}\chi(\sigma t)$ values were calculated numerically by Atek et al. and by others. Equation 3.6 is called the Randles-Sevcik equation for soluble-insoluble system, which gives the current of the LSV or CV peak and corresponds to Equation 3.8 for the maximum value of $\pi^{0.5}\chi(\sigma t)$ at 0.6105[3,4]. Note that the coefficient is different from what is presented in Chapter 2. As for soluble-soluble system, the peak current I_p is proportional to the square root of the rate scan.

$$I_p = 0.6105 nFAC^*_{M^{n+}} (D_{M^{n+}})^{1/2} \left(\frac{nFv}{RT}\right)^{1/2} \tag{3.6}$$

Like for soluble-soluble systems, the kinetics parameters (k^0, k_a, k_c, α) influence the current response during the potential scan for the quasi-reversible redox reactions. The current at a WE can be described by the Butler-Volmer type equation (3.7), but with some differences for the soluble-soluble system. as the concentration of the metal c_M in the Buttler-Volmer type equations can be expressed as $C_M = a_M C^0 = C^0$ assuming that the activity coefficient of the metal is 1.

$$x = 0, \qquad \frac{I(t)}{nFA} = -D_r \left[\frac{\partial C_{M^{n+}}(x, t)}{\partial x}\right]_{x=0} = k_a C^0 - k_c C_{M^{n+}}(0, t) \tag{3.7}$$

$$k_c = k^0 \exp(-\alpha nf(E - E^{0'})) \tag{3.8}$$

$$k_a = k^0 \exp\left((1 - \alpha)nf(E - E^{0'})\right) \tag{3.9}$$

Atek *et al.* have constructed three kinetic curves for single electron transfer process, showing quantitatively the coupling effects of the dimensionless kinetic rate (ω) and the electron transfer coefficient α on LSV responses. The dimensionless heterogeneous rate constant was defined as described by Krulic *et al.* [5]:

$$\omega = \frac{k^0}{\theta^\alpha \left(\pi D \dfrac{nF}{RT} v \right)^{1/2}} \tag{3.10}$$

where D is the diffusion coefficient of the metal ion, v is the scan rate and θ is expressed as:

$$\theta = \exp(\frac{nF}{RT}) \left[E_i - E^0 \right] = C^*_{M^{n+}} / C^0 \tag{3.11}$$

where $C^*_{M^{n+}}$ is the concentration of the metal ion M^{n+} in the bulk and E_i is the initial potential.

The values of ω in the working curves were varied from 10^6 to 10^{-6} while the values of α was varied from 0.2 to 0.8. Fig. 3.1, 3.2 and 3.3 show the peak current ratio $\Psi_p / (\Psi_p)_{rev}$ and the half peak width, $\Delta\Phi_{p/2} = \dfrac{nF}{RT}(E_p - E_{p/2})$ and the cathodic peak postion η_p, $\eta_p = \dfrac{nF}{RT}(E_p - E_{eq})$ as a function of $\log(\omega)$ for different values of α.
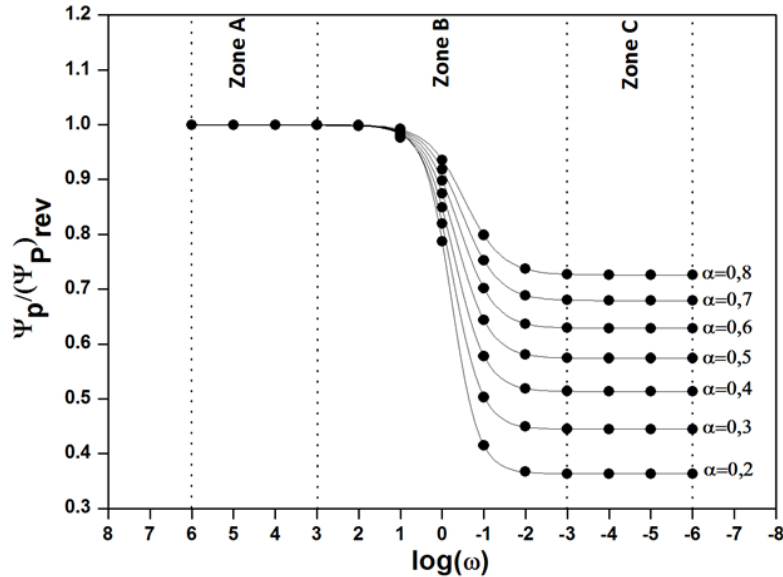
Fig. 3.1. Variation of the peak current ratio, $\Psi_p / (\Psi_p)_{rev}$, as the function of the dimensionless rate constant for several values of α. Solid lines are best fits to the sigmoidal Boltzmann functions with a correlation coefficient of 0.99. Zones A, B, C denote the reversible, quasi-reversible and totally irreversible zones, respectively.[6]
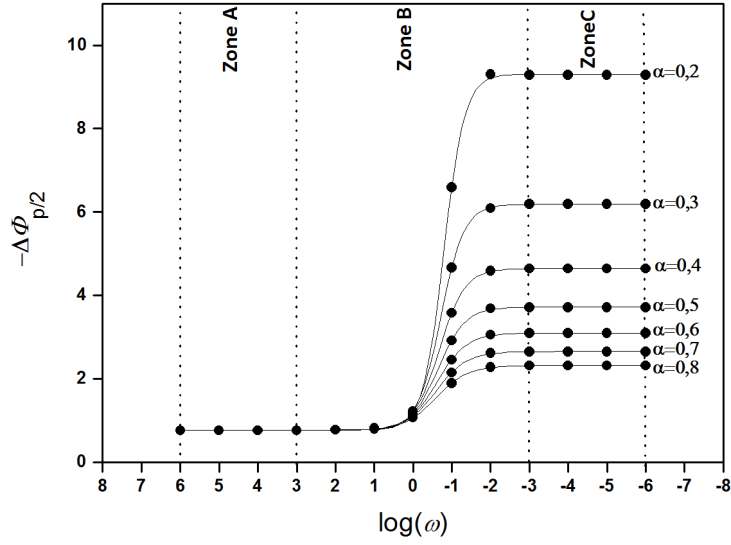
Fig. 3.2. Dependence of the half peak width of linear sweep voltammograms ($\Delta \Phi_{p/2}$) on the logarithm of the kinetic parameter ω for various α values. Solid lines are best fits to the sigmoidal Boltzmann functions with a correlation coefficient of 0.98.[6]
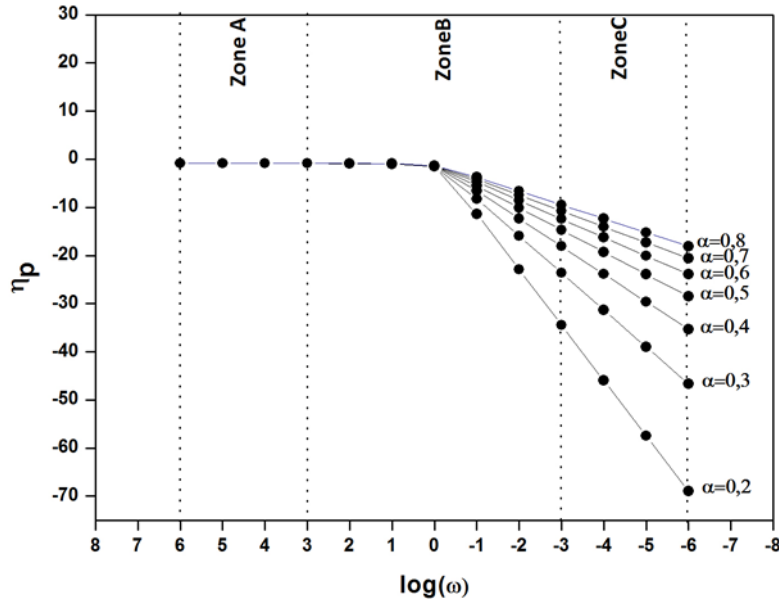
Fig. 3.3. Plots of the reduction peak position (η_p) against $\log(\omega)$ for various α values.[6]

The curves in Fig. 3.1 and 3.2 can be fitted with the following sigmoidal Boltzmann functions:

$$\frac{\Psi_p}{\left(\Psi_p\right)_{rev}} = 1 + \frac{\left(0.811\alpha^{0.5} - 1\right)}{1 + \exp\left[\dfrac{X - \left(-0.528\alpha - 0.099\right)}{0.477\alpha^{0.248}}\right]} \tag{3.12}$$

$$-\Delta\Phi_{p/2} = 0.770 + \frac{\left(1.857\alpha^{-1} - 0.770\right)}{1 + \exp\left[\dfrac{X + (0.557\alpha^{-0.216})}{0.445\alpha^{0.316}}\right]} \qquad (3.13)$$

where: $X = \log(\omega)$. From Fig. 3.3 it can be also established that the magnitude of η_p depends linearly on the logarithm of the kinetic parameter ω. Therefore, by using linear regression approximations, the dependency of η_p on ω and α could be expressed as follows:

$$\alpha\eta_p = 2.303X - \left[0.115\log(\alpha) + 0.78\right] \qquad (3.14)$$

This equation coincides with that established by Krulic for α =0.5 [5], and is valid in the region when $\log \omega \leq -1$. Each of these fit models enables voltammetric quantification of the electrode kinetics from simple peak current and peak potential measurements of the experimental linear sweep voltammograms for either reversible, quasi reversible or totally irreversible electron transfer process, provided that the value of α is known or can be estimated accurately.

Based on the work of Atek et al, three categories of reactivity can be determined, defined by the dimensionless heterogeneous rate constant:

Reversible: $\log \omega \geq 3$

Quasi-reversible: $-3 \leq \log \omega \leq 3$

Irreversible: $\log \omega \leq -3$

2. Evaluation of the kinetics for Cu(I)/Cu couple in acetonitrile

For understanding the limitations of the all-copper battery, it is crucial to evaluate the kinetics of the Cu(I)/Cu couple. This interest arises if the plating of copper on the negative side of the Cu RFB is used when the battery is charged electrochemically. In the case of the electrodeposition of Cu from a non-aqueous solution with ACN, only a one electron transfer step is expected. Indeed, by comparison with aqueous baths for electrochemical plating of Cu, the Cu cation present in solution is already Cu(I) and not Cu(II). Therefore, the first step for the reduction of Cu(II) to Cu(I) that is usually admitted to be the rate determining step in Cu plating with aqueous solution[7–10] is avoided in the studied ACN electrolyte.

$$Cu^+ + e^- \;\Longleftrightarrow\; Cu \qquad (1)$$

$$Cu^{2+} + e^- \;\Longleftrightarrow\; Cu^+ \qquad (2)$$
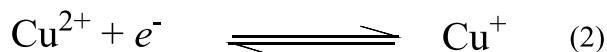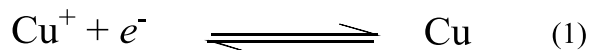
Furthermore, the deposition process analysed here involves the utilization of an electrode of Cu. As the plating of the metal is done on the same material, an instantaneous nucleation process is considered where the metallic copper is formed at the start of the current pulse during a chronoamperometric measurement.[11,12]

In this work, LSV and CV measurements were performed by using one-compartment three-electrode cell where the reference electrode and auxiliary electrode were coils of 1 mm diameter copper wire and with a copper disk serving as a working electrode. The working electrode was prepared by heat-sealing 1 mm diameter copper wire in 2 mm diameter glass tube, followed by polishing with consecutively finer abrasive papers followed by different sizes of alumina, down to 0.05μm particles, on polishing cloths. The electrolyte consisted of a mixture of given concentrations of [Cu(CH$_3$CN)$_4$]BF$_4$, 100 mM TEABF$_4$ as a supporting electrolyte, and acetonitrile as a solvent. All potentials are expressed *vs.* the Cu wire in the solution of the given concentration of [Cu(CH$_3$CN)$_4$]BF$_4$. Hence, the potential of the Cu reference in equilibrium with 10 mM Cu$^+$ solution in acetonitrile on the "non-aqueous standard copper electrode" scale (SCuE), *i.e. vs.* Cu$^+$ solution with the activity of 1 in equilibrium with Cu in acetonitrile is assumed to follow the Nernst equation considering the $\gamma_{Cu^+} = 1$, *i.e.* the potential of the reference is –0.118 V *vs.* SCuE in acetonitrile. To establish the relation with the ferrocene (Fc) scale recommended by IUPAC, the potential of the Fc$^+$/Fc couple *vs.* Cu/10 mM Cu$^+$ in ACN was measured as 0.69 ± 0.01 V, *i.e.* the potential of our reference electrode is –0.69 V *vs.* Fc$^+$/Fc. LSV data for the reduction of copper (I) in acetonitrile were recorded with an Autolab model PGSTAT302N potentiostat equipped with the SCAN250 analog scan generator module. We point out that, all experimental steps (solution preparation, LSV measurement) were performed at ambient temperature (25 °C) under anaerobic conditions using a nitrogen filled glove box. The results are shown in Fig. 3.4.
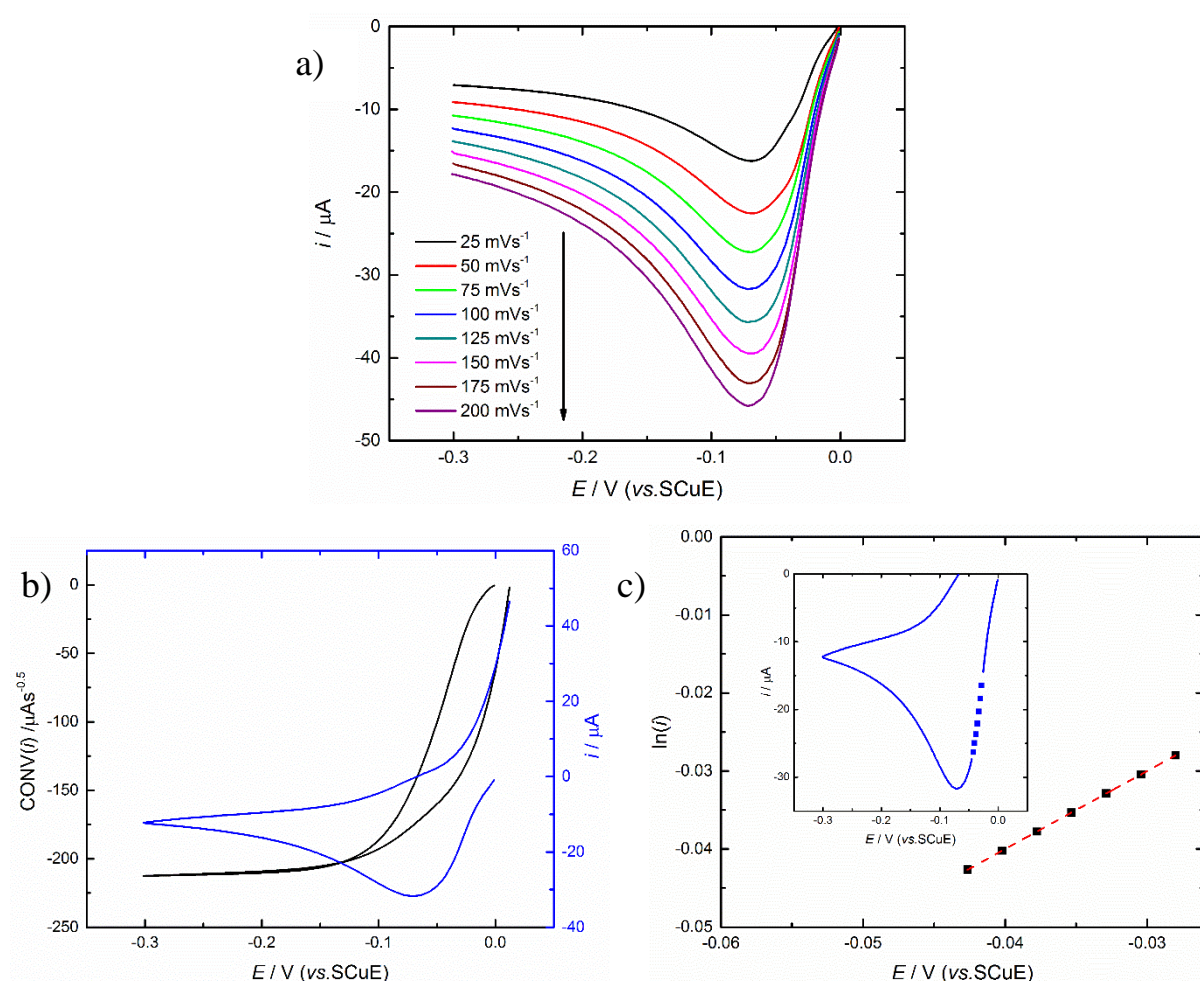
Figure 3.4. a) LSV curves for the deposition of Cu on a Cu electrode from a solution of 10 mM of tetrakis(acetonitrile)copper(I) tetrafluoroborate in acetonitrile. Scan rates from 25 fo 200 mV·s^{-1}. b) Semi-integrative CV in blue from the CV in black with scan rate at 100 mV·s^{-1}. c) Tafel plot for the reduction of Cu(I) to Cu from the kinetically limited part of the CV with scan rate at 100 mV·s^{-1}.

Firstly, the semi-integrative voltammetry was used for the calculation of Cu(I) diffusion coefficient and a direct Tafel analysis was used for the evaluation of the transfer coefficient α. Fig. 3.4b shows a sigmoidal curve (black) obtained from semi-integration of typical voltammetric current recorded at 100 mV·s^{-1}. The $D_{Cu(I)}$ is determined experimentally by the semi-integrative voltammetry with the method of Saila.[13] As shown in Fig. 3.4b and as per principle of semi-integration technique, the semi-integration of the voltammetric current responses with respect to time yields to the sigmoidal-type curve with a plateau. This plateau level represents the limiting semi-integral current, of height m* :

$$m^{*} = nFAC^{*}_{M^{n+}}D^{1/2}_{M^{n+}} \tag{3.15}$$

and the diffusion coefficient of Cu(I) in acetonitrile at 25°C was calculated utilizing this equation (as shown in Table 3.1) by considering the following experimental values: $n = 1$,

$C^*_{Cu^+} = 10.25 \text{mM}$. Fig. 3.4c depicts the representation of the Tafel plot obtained from experimental CV data, at a scan rate of 100 mV/s. Using the slope calculated from Fig. 3.4c and the Tafel equation, the value of α was calculated and the result is reported in Table 3.1.

In the next step, a more detailed examination of the voltammetric peaks allowed us to quantify the standard rate constant (k^0 in cm^2/s) for the Cu(I)/Cu(0) redox couple according to the models presented in this section 1. The results are listed in Table 3.1. With these values, Eqs. 3.12, 3.13 and 3.14 were used to obtain the final value for the k^0. In the work of Atek *et al*, the parameters $D_{Cu(I)}$, α and k^0 were also obtained by comparison of theoretical and the experimental linear scan voltammograms by using the LSV model algorithm with a series of adjustments in the input values, and are reported in the Table 3.1.

Table 3.1. Kinetic-mass transport parameters for Cu(I)/Cu(0) redox couple.

$D_{Cu(I)}$ [10^9m^2·s^{-1}]		α		k^0 [10^5 cm·s^{-1}]			
SI	Fit	Tafel	Fit	Working curves			Fit
				Eq. 3.12	Eq. 3.13	Eq. 3.14	
1.75	1.70	0.82	0.80	3.84	4.99	7.73	5.12

In the Table 3.1, the results for the diffusion coefficient, charge transfer coefficient and standard rate constant are given in the case of the Cu(I) deposition on Cu support from a electrolyte composed of ACN as solvent and TEABF$_4$ as supporting electrolyte. The diffusion parameter is comparable with the Cu(I) diffusion coefficient found in Chapter 2 ($1.56 \cdot 10^{-5}$ cm^2·s^{-1}). The charge transfer coefficient is here given for a reduction reaction ($\alpha = 0.8$) and in the previous chapter α was applied for the oxidation reaction of Cu(I) to Cu(II). So, to compare correctly the transfer coefficients, the effect of α on redox reactions has to be explained and described. The α parameter is defined as a measure of the symmetry of the energy barrier[14] and Fig. 3.5 illustrates schematically the three main cases for $\alpha = 0.5$, $\alpha < 0.5$ and $\alpha > 0.5$. In chapter 3, $\alpha_{Cu^+/Cu}$ equals 0.8 for the reduction of Cu(I) and, in Chapter 2, α_{Cu^{2+}/Cu^+} equals 0.7 for the oxidation of Cu(I). It is difficult to get straightforward conclusions about the transition state with α, however, it is possible to suggest a geometry for it with the symmetry of the energy barrier. In the case of $\alpha = 0.5$, the energy barrier is symmetric between the oxidized and reduced species and the reaction coordinates of transition state indicates that its geometry is an

intermediate between the both oxidation states. For the Cu deposition in ACN with $\alpha > 0.5$, the symmetry is lost and the transition state reaction coordinate suggests a geometry closer to the Cu(I) oxidation state during the electron transfer (Fig. 3.5). This observation reinforces the assumption that the solvation modification of the Cu centre does not need significant energy for the rearrangement of the solvation shell previously to the nucleation. This supports the assumption not to take into account the change of the environment around the metal centre for the reduction of Cu(I). The high value for α also indicates that the reaction happens in the inner part of the double layer.[15,16] Considering the Cu(I) oxidation in ACN, the symmetry of the energy barrier is similar ($\alpha > 0.5$) and the transition state reaction coordinates are again closer to the oxidized species containing more coordinating ACN ligands (Cu(II) for the oxidation of Cu(I) and Cu(I) during the deposition process).
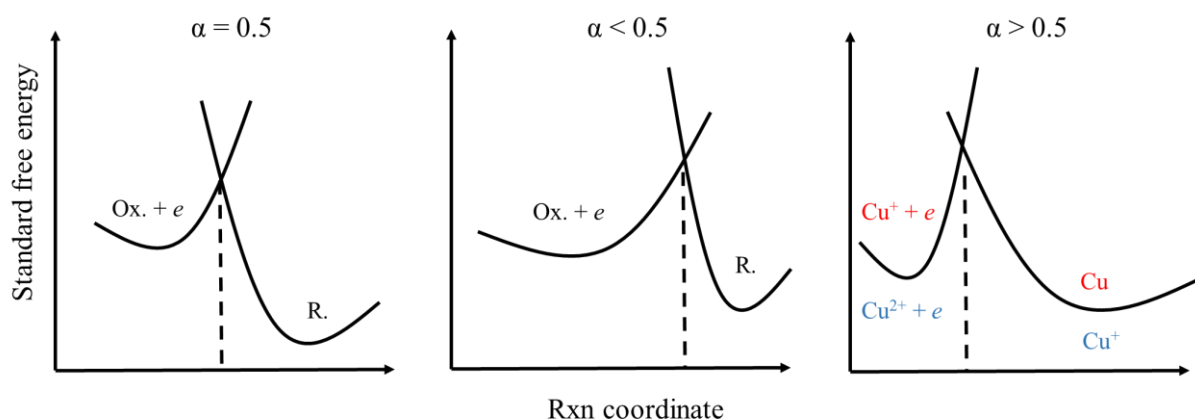
Figure 3.5. Schematic representation of the effect of the transfer coefficient on the symmetry of the transition state for the electron transfer of Cu(I)/Cu (in red) and Cu(II)/Cu(I) (in blue). Inspired by the textbook of A. Bard.[14]

Regarding the standard rate constant in Table 3.1, the kinetic parameter is calculated with the three working functions (Eq.3.12-3.14) and by fitting. The obtained results for k^0 shows a quasi-reversible process for the Cu deposition in ACN solution and is smaller than for the nucleation of Cu on mercury, which means than it is more difficult to plate Cu on itself than on mercury.[15,16] The k^0 calculated by the working curve for the reduction peak potential (η_p) (Eq. 3.14) has a value that deviates more than the other working function. This difference comes from the limitation of the linear regression in Eq. 3.4 that can be applied for $\omega < 0.1$. As the dimensionless heterogeneous rate constant is determined at 0.15 in the electrochemical reaction of the Cu plating, the kinetics does not fulfil the good criteria to be determined by the Eq. 3.4.

3.   Conclusion

The simulations and fittings of the LSV during Cu deposition from an ACN solution on a Cu electrode are in good agreement with the experimental LSV curves when the algorithm develop by Atek *et al.* is applied. The mass transport and kinetic parameters are accurately calculated with the Eqs. 3.12-3.13. The algorithm and working functions can be applied to deposition with instantaneous and one electron transfer process.

The standard heterogeneous rate constant is 200 times slower for the deposition of Cu(I) than for the Cu(I) oxidation (6.22 cm·s^{-1}). This implies that the discharge of the Cu RFB will be kinetically limited by the negative side of the cell during the electrochemical charge of the cell.

4.   References

1.   Krulic, D., Fatouros, N. & Liu, D. A complementary survey of staircase voltammetry with metal ion deposition on macroelectrodes. *Journal of Electroanalytical Chemistry* **754**, 30–39 (2015).

2.   Liu, D., Krulic, D., Groult, H. & Fatouros, N. Silver ion deposition on gold and silver disc electrodes from aqueous solutions and from dry or wet [EMIM][NTf2] room-temperature ionic liquid. *Journal of Electroanalytical Chemistry* **775**, 91–104 (2016).

3.   Berzins, T. & Delahay, P. Oscillographic Polarographic Waves for the Reversible Deposition of Metals on Solid Electrodes. *J. Am. Chem. Soc.* **75**, 555–559 (1953).

4.   Fatouros, N., Krulic, D. & Groult, H. Linear sweep and staircase voltammetries for reversible deposition of metal ions on the same metal and on foreign substrates. *Journal of Electroanalytical Chemistry* **625**, 1–6 (2009).

5.   Krulic, D., Fatouros, N. & Liu, D. A complementary survey of staircase voltammetry with metal ion deposition on macroelectrodes. *Journal of Electroanalytical Chemistry* **754**, 30–39 (2015).

6.   Atek, I., Maye, S., Girault, H. H., Affoune, A. M. & Peljo, P. Semi-analytical modelling of linear scan voltammetric responses for soluble-insoluble system: The case of metal deposition. *Journal of Electroanalytical Chemistry* **818**, 35–43 (2018).

7.   Chassaing, E. & Wiart, R. Epitaxial growth and electrode impedance of copper electrodeposits. *Electrochimica Acta* **29**, 649–660 (1984).

8.   Bockris, J. O. & Enyo, M. Mechanism of electrodeposition and dissolution processes of copper in aqueous solutions. *Trans. Faraday Soc.* **58**, 1187–1202 (1962).

9.   Chao, F. & Costa, M. Mechanism of copper deposition in a sulphate bath containing chlorides. *Bull. Soc., Chim. Fr* **10**, 4015 (1968).

10.   Mattsson, E. & Bockris, J. O. Galvanostatic studies of the kinetics of deposition and dissolution in the copper + copper sulphate system. *Trans. Faraday Soc.* **55**, 1586–1601 (1959).

11.   Bewick, A., Fleischmann, M. & Thirsk, H. R. Kinetics of the electrocrystallization of thin films of calomel. *Transactions of the Faraday Society* **58**, 2200–2216 (1962).

12.   Bijani, S. *et al.* Study of the Nucleation and Growth Mechanisms in the Electrodeposition of Micro- and Nanostructured Cu2O Thin Films. *J. Phys. Chem. C* **115**, 21373–21382 (2011).

13.   Saila, A. Etude des systemes electrochimiques quasi-reversibles par voltamperometrie a balayage lineaire et semi-integration. Applications aux comportements de rhenium et dysprosium en milieux de sels fondus. *Univ. Badji Mokhtar, Annaba,* 122 (2010).

14.   Allen J. Bard & Larry R. Faulkner. *Electrochemical Methods: Fundamentals and Applications, 2nd Edition - Allen J. Bard, Larry R. Faulkner.*

15.   Fawcett, W. R. & Foss, C. A. Role of the solvent in the kinetics of heterogeneous electron and ion transfer reactions. *Electrochimica Acta* **36**, 1767–1774 (1991).

16.   Fawcett, W. R. & Foss, C. A. On the nature of the transfer coefficient for ion transfer reactions. *Journal of Electroanalytical Chemistry and Interfacial Electrochemistry* **250**, 225–230 (1988).

Chapter IV

Thermodynamics of Cu^+, acetonitrile and propylene carbonate

1.   Introduction

In this Chapter IV, the thermodynamics of the Cu-ACN-PC system is studied to have a better characterization of the different properties of the heat to power Cu-RFB. During the charge-discharge cycling process of the Cu-RFB, the heat can induce the disproportionation of the Cu^+ to Cu and Cu^{2+} and replace electric power during the charging step of the battery. Consequently, the different phenomena induced by heat for the Cu-ACN-PC system should be analysed for an appropriate description of the thermal charge.

Many thermal analysis techniques are available to study the influence of temperature on materials properties[1]: thermogravimetry (TG)[2], derivative thermogravimetry (DTG)[3], differential thermal analysis (DTA)[4], differential scanning calorimetry (DSC)[5], thermomechanical analysis (dilatometry)[6], dynamic mechanical analysis (DMA)[7] and evolved gas detection (EGD)[8]. In this work, the chosen thermoanalytical method is DSC.

The differential scanning calorimetry is a well-known analysis that is close to DTA and is linked to the development of the thermocouples, which allows the measurement of a large range of temperatures. Since the beginning of the 20th century, DTA/DSC type of characterization was applied to material science. Roberts-Austen developed what seems to be the first differential temperature technique for alloy analysis in metallurgy application in 1899.[9] Saladin improved the data recording by photography in 1904 [10] and since then, the DTA was extend to mineralogy, geology, inorganic and organic chemistry. The denomination, differential scanning calorimetry (DSC), comes from a Perkin-Elmer team of researchers that modified DTA to have the output data as a direct calorimetric information and not simply as a temperature difference between the sample and reference.[11–13] After the sixties, the DSC continues to expand in the field of analytical chemistry, especially for the thermodynamic characterization of polymers (melting point, glass transition, degradation, polymerization, oxidation reaction).[1] Nowadays, DSC is used in many different domains of chemistry (biological samples, explosives, pharmaceuticals. metals, lubricants, polymers, organic compounds).[14]

The DSC samples are most generally in the solid state (metals, alloys, purified and dried chemicals, polymers …). As the physical state of the ACN-PC electrolyte is a liquid containing solubilized Cu⁺ salts, the interest of this work is to observe the thermal properties of the samples at higher temperatures. This implies that the liquid/gas equilibrium should not be a restriction for the utilization of DSC equipment. Fortunately, it is also possible to study liquids and their heat of vaporization. The availability of the DSC machine and the possibility to target liquid/gas transitions [15–19] are the main reasons for the selection of the DSC technique. However, three main factors have to be considered when gas are produced during the DSC measurements:

- If the sample is vaporized, the gas needs to be evacuated from the crucible (or pan) to avoid overpressure and to keep a constant pressure in the sample. Consequently, either the lid of the sample holder is pierced (pin hole)[15], or the lid is already perforated with a defined hole size.[19]

- As the vapours are removed from the crucible and from the furnace chamber by a flow of purging gas, the loss of the volatile compound is irreversible and the scanning back to lower temperatures doesn't allow to get the exothermic peak for the condensation of the gas. Then, no multiple cyclic scans can be measured on volatile samples.

- Dealing with volatile compounds implies unknown loss of the liquid by evaporation during the weighting of the sample and its introduction in the DSC machine. The cleaning step with the stream of purging gas can also increase this effect. Considering the presence of ACN with a relatively low boiling point in the samples, their preparation is particularly important.

The DSC is used to quantify thermodynamic constants such as the heat capacity and the enthalpy for some state transitions or reactions. For the Cu-ACN-PC system, the thermal energy, which is needed for the different changes of state during the heat treatment for the charge of the heat to power Cu-RFB, is investigated; the enthalpy for the vaporization of ACN and PC is determined and the enthalpy for the Cu^+ disproportionation is evaluated. The heat capacity is also analysed with DSC for different solutions regarding their concentrations of PC and $[Cu(CH_3CN)_4]BF_4$. With these different data, a calculation of the final theoretical Cu-RFB cycling efficiency with heat charge is given and analysed with the Carnot cycle.

2. Materials and methods

2.1. Chemicals

All solvents and chemicals were used as received without further purification and were stored in a glove box under nitrogen. The solvents were acetonitrile (ACN, CH_3CN, extra dry over molecular sieves, 99.9%, from Acros) and propylene carbonate (PC, $C_4H_6O_3$, anhydrous, 99.7%, from Sigma-Aldrich). The thermally active species tetrakis(acetonitrile)copper(I) tetrafluoroborate was either commercial, ($[Cu(CH_3CN)_4]BF_4$, > 98%, from TCi), or prepared by comproportionation reactions.[20,21] For the synthesis of $[Cu(CH_3CN)_4]BF_4$, copper(II) tetrafluoroborate hydrate ($Cu(BF_4)_2 \cdot xH_2O$, from Sigma-Aldrich), acetonitrile (ACN, CH_3CN, from Merck) and copper wire (dia. 1 mm, ≥ 99.99%, from GoodFellow) were of analytical grade and were used as received. The comproportionation reaction was performed in a Schlenk line filled with nitrogen. The Cu^+ complex with ACN is dried overnight under vacuum and stored in a nitrogen-filled glove box.

2.2. Differential scanning calorimetry

Thermal analysis data were recorded by differential scanning calorimetry with a Mettler Toledo DSC 821e. Calculation and data treatment were handled with the STARe thermal analysis software from Mettler Toledo. When air sensitive compounds were targeted, samples were prepared under inert atmosphere inside a glove box. DSC crucibles avoid contamination of the DSC oven by the sample and have a pin for contact with the thermocouple wires (standard aluminum crucible with pin and 40 μL volume, model n° 00027331). As liquid samples are investigated, the lids of the pan need to be pierced for the evacuation of the gas after evaporation (aluminum lid pierced with 50 μm hole, model n° 51140832). Solid or liquid samples usually have a mass between 10 and 35 mg for a volume of 25 μL.

The heat flow of the sample is determined *versus* an empty Al reference crucible with a heating rate (v) of 5, 10 or 20°C·min^{-1}. The DSC machine is composed of an outer chamber into which a flow of air is applied at 80 mL/min around the furnace to keep a constant environment and an inner chamber into which N_2 is introduced at 200 mL/min to protect the furnace from accumulation of oxygen and moisture, which may damage the cell. N_2 is also applied because it provides homogenous heat and heat transfer to the crucibles. Before measurements (especially for heat capacity), the sample chamber is cleaned at a temperature of 500°C for 5 min with a stream of purging gas in order to remove dust and other contaminants.
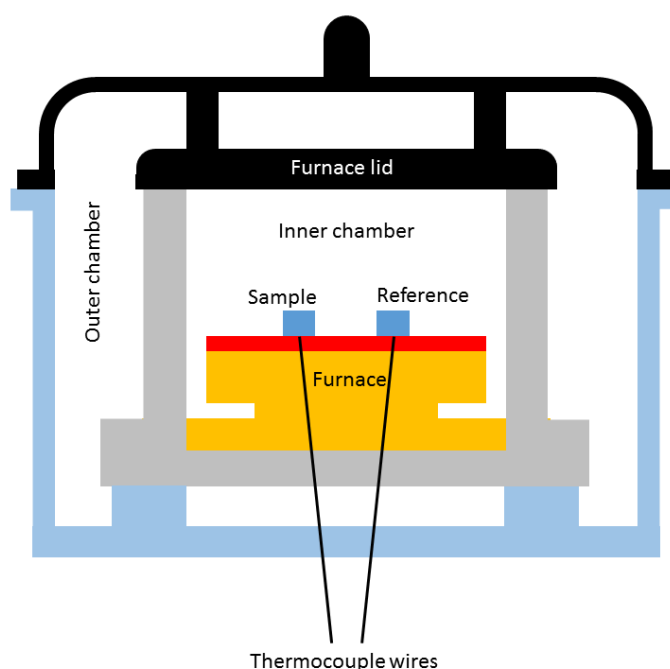
Figure 4.1. Illustration of the DSC oven with the different parts of the calorimetric chamber.

3.   Theory : DSC and thermodynamics

The differential scanning calorimetry is a method, which allows the measurement of the heat flow exchanged by a sample to reach selected temperatures. As the sample is confined in a metallic crucible, usually aluminium, the heat flow is recorded against a reference, which is commonly an empty crucible of the same composition. Another way to picture the thermoanalytic process is to describe the heat flow of the sample as the required heat to obtain the same temperature as the reference. The sample and reference are heated inside an isolated oven with a controlled temperature program. The scanning rate of temperature is defined in Eq. 4.1 and describes the temperature of the furnace in function of time, $T(t)$ (Eq. 4.2). [4]

$$v = \frac{dT}{dt} \tag{4.1}$$

$$T(t) = T_0 + vt \tag{4.2}$$

When the heat flow rate at the sample, $\dot{Q}_s$, changes, it means that the temperature T of the source (furnace, oven) is evolving with time (Eq. 4.2) and induces a variation of T_s (the sample temperature). However, the relationship between T_s and $\dot{Q}_s$ is not perfectly linear and is illustrated in Eq. 4.3. From this equation, two factors are responsible for the non-linearity. The first one is the signal thermal resistance between the sample holder and the environment of the oven chamber R. At the sample holder interface, some irreversible loss happens with the transfer of energy to the surrounding volume through convection, radiation and conduction (Fig. 4.2). Another source of deviation from the linear evolution of T_s vs $\dot{Q}_s$ is C, the heat capacity of the sample holder itself. As the temperatures are controlled and measured by a voltage with thermocouples, equivalent electrical circuit can be built to describe schematically the heat transfer processes (for more details see ref. [11]). Eq. 4.3 defines the response of the sample temperature linked with a modification of the heat flow in the sample:

$$\Delta T_s(t) = \Delta \dot{Q}_s * R \left[1 - e^{\frac{-t}{RC}} \right] \tag{4.3}$$

The function 4.3 has the characteristics of a low-pass filter, but is not convenient to use, because the temperature T_s can differ significantly from the applied T , which is more

practical to use as it is the main parameter under control during the experiment. To bypass this, T_s is compared with T, the temperature of the furnace. Then, the variation of the signal between the two temperatures can be amplified and allows a smooth control of $\dot{Q}_s$, the input heat flow to the sample from the source created by temperature control in Eq. 4.2. This relation 4.3 can be simplified by using a transfer function k, which is a parameter of the signal amplifier for $\dot{Q}$.

$$\frac{\mathrm{d}T_s}{\mathrm{d}\dot{Q}_s} = \frac{R}{1 + kR} \tag{4.4}$$

In Eq. 4.4, the case of steady-state response is considered, and then the evolution of T_s with $\dot{Q}_s$ is linear (t tends to 0). Additionally Eq. 4.4 can be modified by replacing $\mathrm{d}T_s$ by $\mathrm{d}\dot{Q}$ which depends on $T(t)$. The advantage of Eq. 4.5 is that the T can be used instead of T_s to show the results of the DSC measurement. The parameter K in Eq. 4.5 is called the calibration factor and it should be determined before a set of DSC data with a known sample (like metallic indium, In).

$$\frac{\mathrm{d}\dot{Q}}{\mathrm{d}\dot{Q}_s} = \frac{kR}{1 + kR} = K \tag{4.5}$$
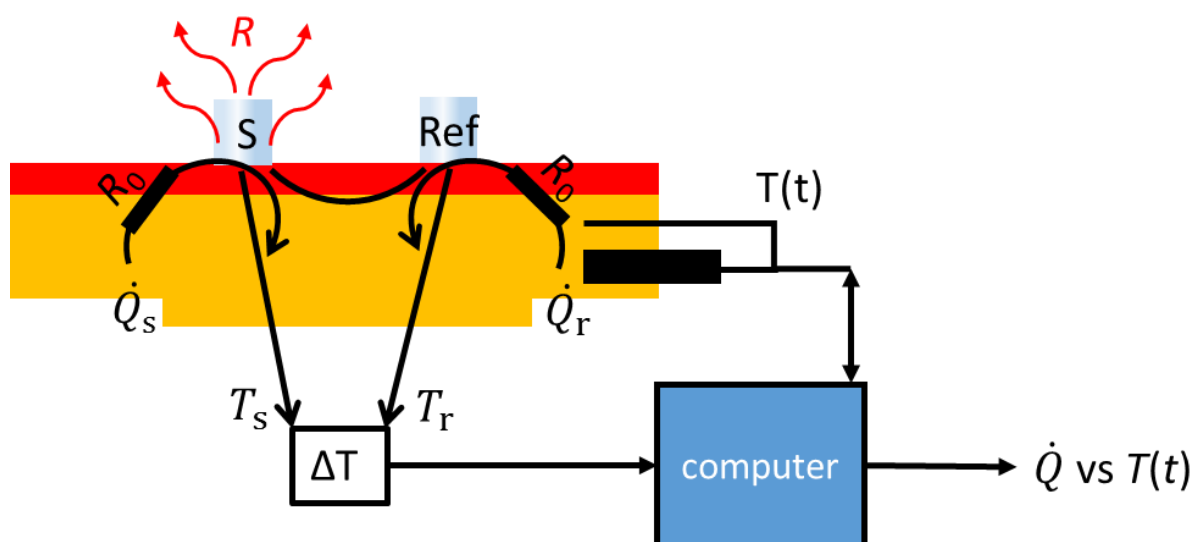
Figure 4.2. Scheme of the DSC temperature controlled thermoanalysis representing the heat flows with the main thermal resistances influencing the recorded signal.

In the next section, the focus will be the physics and thermodynamic parameters that can be obtained with the DSC thermoanalysis. The typical DSC curves are plotted with the heat flow, which is corresponding to a power (P or $\dot{Q}$, defined in Equation 4.1) *versus* the temperature of the furnace evolving with time (Eq. 4.2). This heat flow or power is usually given in the range of the μW or mW. A general description of the heat flow is given here:

$$P(T,t) = \dot{Q}(T,t) = \dot{Q}_0(T) + \dot{Q}_{Cp}(T) + \dot{Q}_{rxn}(T) \tag{4.6}$$

The measured heat is composed of three terms: $\dot{Q}_0(T)$ for the influence of the internal thermal resistance asymmetry and losses in the system, $\dot{Q}_{Cp}(T)$ for the heating of the sample that has a different heat capacity than the reference and $\dot{Q}_{rxn}(T)$ for the heat, which is needed in any transformation that can occur during the temperature scan (glass transition, state transition and diverse reactions).

As it was already mentioned, this $\dot{Q}$ represents the difference of heat, which is required for the sample to keep the same temperature as the reference. In Eq. 4.7, the measured signal $\dot{Q}$ is described as the difference between the heat flow given by the furnace to the sample $\dot{Q}_s$ (Eq. 4.8) and that from the furnace to the reference $\dot{Q}_r$ (Eq. 4.9). In the DSC instrument, the $\dot{Q}$ is measured by the deviation of the sample temperature T_s from the reference T_r. (Eq. 4.10). The temperature difference ΔT is recorded with thermocouples as an electric voltage (e.m.f.) corresponding to $\dot{Q}$ between the sample and reference. To link the temperature difference directly with the temperature, the thermal resistance between the sample (or reference) and the sample holder R_0 is defined in Eq. 4.10 and is specific for each DSC machine.

$$\dot{Q} = \frac{dQ}{dt} = \dot{Q}_s - \dot{Q}_r \tag{4.7}$$

$$\dot{Q}_s = \frac{T_s - T}{R_0} \tag{4.8}$$

$$\dot{Q}_r = \frac{T_r - T}{R_0} \qquad\qquad T = temperature\ of\ furnace \tag{4.9}$$

$$\dot{Q} = \frac{(T_s - T_r)}{R_0} = \frac{\Delta T}{R_0} \tag{4.10}$$

For a change of the sample physical state (melting/crystallization, evaporation, glass transition, decomposition (oxidation)), the heat flow curve is modified because more or less heat is provided to the sample for the physical/chemical transition. The transformation inside the sample is easily detected with a change of the heat slope (glass transition) or with a sharp peak (physical state transition). From the integration of the exo- or endothermic peak induced by the phase modification, the enthalpy of the process can be calculated if the mass (m) of the sample is known (Eq. 4.11-4.13). The mass obviously plays a major role for the enthalpy determination, as this thermodynamic property is extensive.

$$\dot{Q} = \frac{dH}{dT} * \frac{dT}{dt} = \frac{dH}{dt} \tag{4.11}$$

$$\Delta H = \frac{W * \Delta T}{m} = \int \frac{\dot{Q}}{m}\, dt - \int C_p dT \tag{4.12}$$

$$\Delta H = \int \frac{\dot{Q}}{m}\, dt \tag{4.13}$$

Here, Eq. 4.13 is slightly simplified and does not take into account the part of the heat coming from the heat capacity of the sample. For the enthalpy calculation with DSC data, this assumption is not critical as the integration of the peak can be done in different ways to remove the contribution of the sample thermal capacity by using an appropriate baseline (tangential, horizontal, spline baseline functions).

Another intensive thermodynamics property that can be calculated with DSC, is the thermal capacity. The easiest way to determine the heat capacity is at constant pressure and it is the reason why C_p is shown in Eq. 4.14-4.17, instead of C_v. With Eq. 4.14 and 4.11, Eq. 4.15 explains that C_p will change with time and with temperature. With the evolution of the DSC curve at a known temperature scan rate, it should be straightforward to obtain values for C_p according to Eq. 4.15. However, in this work, C_p is not directly obtained from Eq. 4.15. The reason is purely experimental as the slope of the baseline Q *vs. T* can fluctuate considerably between different sets of data.

$$C_p = \left(\frac{\partial H}{\partial T}\right)_p = T\left(\frac{\partial S}{\partial T}\right)_p \tag{4.14}$$

$$\dot{Q}_{Cp} = Cp * \frac{\mathrm{d}T}{\mathrm{d}t} \tag{4.15}$$

To determine the heat capacity of the sample, the so-called direct method is applied.[22] The sequence starts with an isothermal step (at 25°C in Fig. 4.3a) and is followed by a dynamic temperature period with a heating rate of 5°C·min⁻¹. The difference of heat flow between the two steps ($\Delta\dot{Q}_s$) depends on the C_p of the sample. In Eq. 4.16, the specific heat capacity is described and correspond to the amount of heat required to increase the temperature one degree higher for one gram of the compound. The advantage of this method is the use of a blank to define the proper baseline of the measurement. The signal of the blank is removed from $\Delta\dot{Q}_s$ to obtain an accurate value of the thermal capacity (Eq. 4.16). Before each measurement, several blank curves have to be recorded with an empty crucible against another to subtract more precisely the signal of the Al pan ($\Delta\dot{Q}_b$). In Fig. 4.3a, a typical measurement with the direct method is presented with the various parameters of Eq. 4.16 that are needed for the determination of the specific heat capacity. This figure also highlights the importance of the blank; indeed $\Delta\dot{Q}_b$ is not negligible on the final calculation of the specific heat capacity. In Fig. 4.3.b, the temperature profile is explained for the direct method with an initial isothermal step at 25°C followed by the linear *T* evolution controlled by *T* scan rate (5 °C/min).

$$C_p = \frac{\dot{Q}}{m} * \frac{1}{\mathrm{d}T/\mathrm{d}t} = \frac{\Delta\dot{Q}_s - \Delta\dot{Q}_b}{m \cdot v} = \frac{\Delta\dot{Q}}{m \cdot v} \tag{4.16}$$
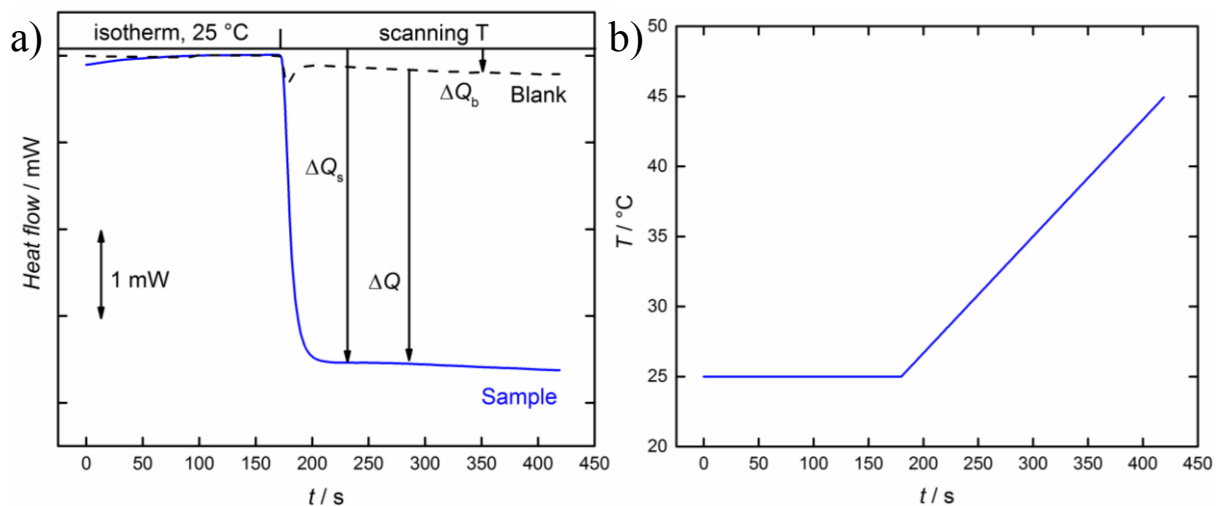
Figure 4.3. a) DSC measurement with the direct method sequence at 5 °C/min with the ideal flat baseline, the signal of the blank and of the sample. b) The temperature profile with time of the direct method with an initial isothermal step followed by the linear *T* evolution controlled by *T* scan rate.

With the C_p values of a mixture, containing *n* chemical species, and the C_p^* value for the pure compounds, the excess heat capacity C_p^E can be calculated with Eq. 4.17. In the case of interest, a binary mixture with two solvents (ACN and PC) is studied and the final Eq. 4.17 is shown below with x_i for the molar fraction of the chemical i:

$$C_p^E = C_p - \sum_{i=1}^{n} x_i C_{pi}^* = C_p - (x_{ACN} C_{p(ACN)}^* + x_{PC} C_{p(PC)}^*) \tag{4.17}$$

4.   Results and discussion

4.1.   Enthalpy of vaporization and disproportionation

The first set of data that are presented are linked with a change due to a chemical reaction or to a physical transition of the samples. In the DSC measurements, these transformations lead to a peak (Eq. 4.13) and they are easily detected from the heat flow diagram *versus* the temperature. In Fig. 4.4a, the three expected transformations for the Cu-ACN-PC system are observed. The first peak at 81°C appears with the vaporization of ACN. In all figures of this work, the endothermic peak are represented with a peak going down the *y*-axis of the heat flow. From the integration of the endothermic phase transition, the enthalpy of vaporization is calculated at $32.4 \, \text{kJ} \cdot \text{mol}^{-1}$ from several measurements similar than the one from Fig. 4.4a. The second peak at 161°C comes from the chemical reaction of the Cu(I) complex containing ACN ($Cu(CH_3CN)_4BF_4$) and is assigned to the disproportion reaction of Cu(I) to Cu and Cu(II) at higher temperatures than the ACN liquefaction temperature. The enthalpy of reaction of the thermal reaction is determined at $106.8 \, \text{kJ} \cdot \text{mol}^{-1}$. An image of the sample after the disproportionation reaction induced by heat is shown in Fig. 4.4b. and the particular color in the crucible can be assigned to final combination of metallic Cu and Cu(II) cation. In the same picture, a small hole piercing the lid of the crucible is visible. As mentioned in the experimental part, this hole allows the gas to leave the sample and to avoid interference for the remaining transitions at high temperatures. The last endothermic property at 242°C corresponds to the liquid to gas evolution of the PC with $\Delta H_{\text{vap}} = 54 \, \text{kJ} \cdot \text{mol}^{-1}$. After the measurement of the pure liquid ACN and PC, a plateau with no signal is detected in Fig. 4.4a. The appearance of this flat part of DSC curve is representing the measurement of the Al crucible *versus* another one and consequently does not show any deviation. It can happen that some noise is detected even after the transition if some impurities/dusts are present in the sample.
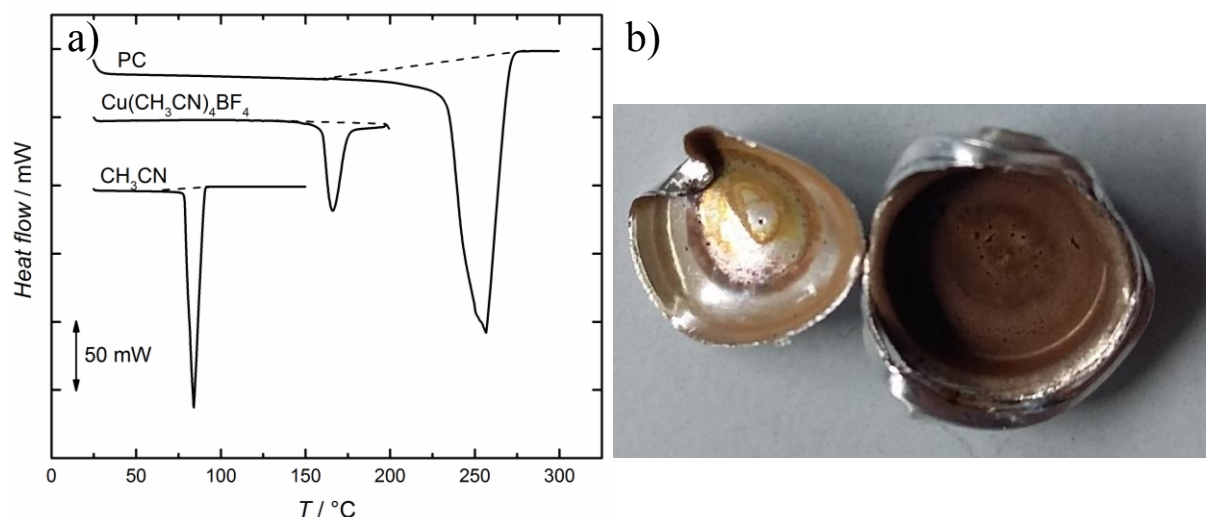
Figure 4.4. a) DSC of acetonitrile at 5 K·min⁻¹, propylene carbonate and solid [Cu(CH₃CN)₄]BF₄ at 20 K·min⁻¹. b) Image of the crucible initially loaded with Cu(I) powder after the DSC measurement until 300°C.

Table 4.1. Enthalpies and temperatures of vaporization/decomposition for acetonitrile, propylene carbonate and [Cu(CH₃CN)₄]BF₄ from DSC data peak integration.

Molecule	This work		Literature	
	ΔH / kJ·mol⁻¹	T / °C	ΔH / kJ·mol⁻¹	T / °C
acetonitrile	32.4 ± 1.6	81 ± 1	29.8-34.8 [a]	81-82 [b]
propylene carbonate	54.0 ± 1.8	242 ± 2	50.9-56.3 [c]	241-242 [d]
Cu(CH₃CN)₄BF₄	106.8 ± 4.4	161 ± 1	-	159-161 [e]

a[23,24]   b[23,25]   c[26,27]   d[23,28]   e[29]

In Table 4.1, the enthalpies and the temperatures of the different phenomena characterized before are summarised and compared with the literature. All of the results are in good agreement with the previous reported values and are not showing too much deviation from the averaged quantities. Here, the only data that is not found in other works is the enthalpy of reaction for the disproportionation of Cu(I) (ΔH_{rxn} = 106.8 kJ·mol⁻¹). For this sample, the crucible is filled with a solid, the white powder of Cu(I). This crucible is sealed and compressed to remove nitrogen/air from the sample and to have a better contact between the solid and the Al pan. The enthalpy for the Cu(I) powder is in the same range as the exothermic enthalpy for the cell reaction in Chap. 2 describing the Cu-Cu(II) electrochemical comproportionation to Cu(I) (ΔH_{rxn} = − 97.2 kJ·mol⁻¹).
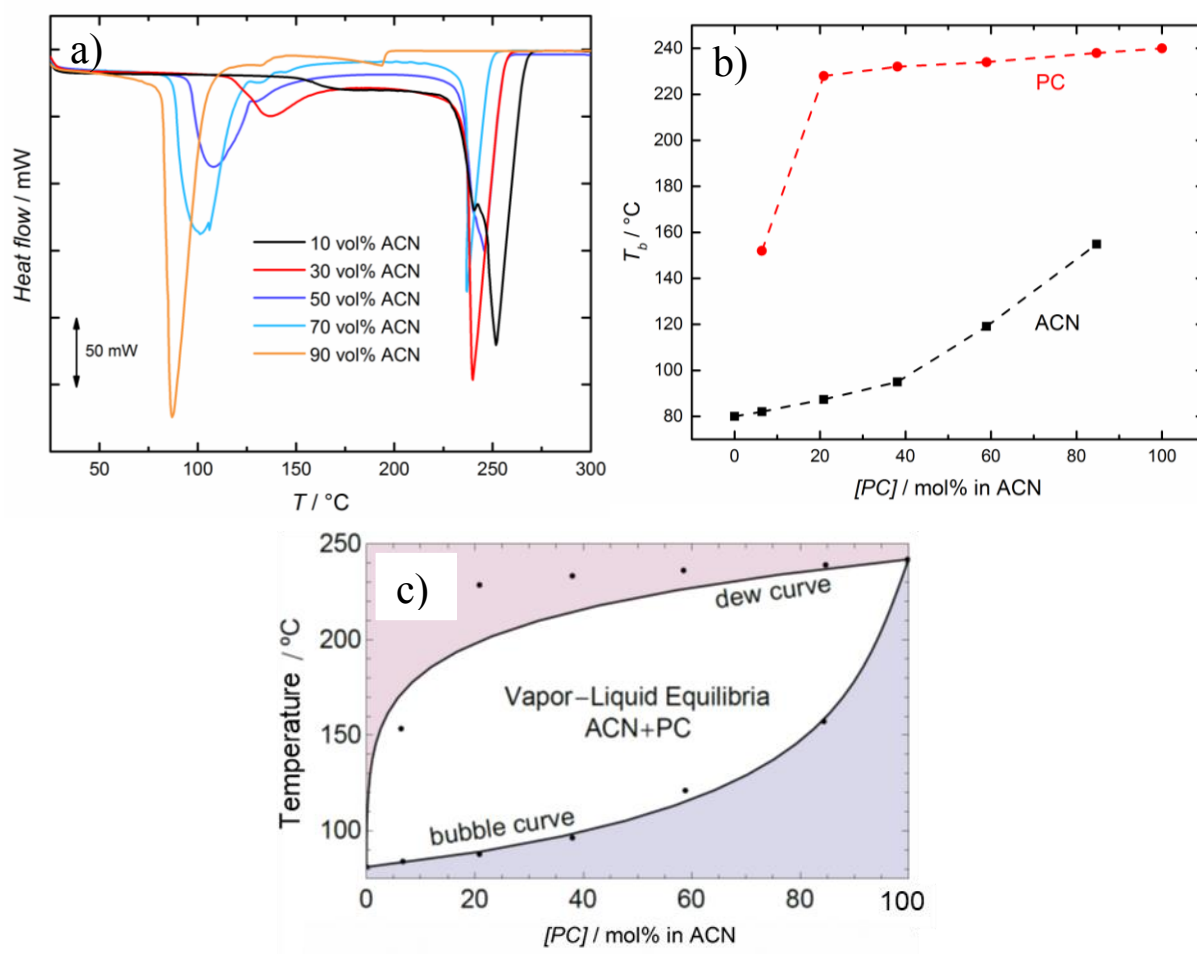
Figure 4.5. a) DSCs of acetonitrile-propylene carbonate mixture with 10 to 90 vol% acetonitrile, b) temperatures of vaporization of acetonitrile and propylene carbonate in the acetonitrile-propylene carbonate mixtures. c) Estimated vapour-liquid equilibrium curves for ACN+PC system.

The influence of the solvent composition on the temperature of vaporization is visible with DSC curves in Fig. 4.5a. The boiling point of ACN is evolving to higher temperature, T_b, when more PC is present in solution. Until 50 mol% of PC in the solvent content, the ACN-T_b is still under 100°C before to increase rapidly to higher T and reaches 154-155°C for the solution containing 90 vol% of PC (85 mol%). The modification of the PC-T_b is less important with changes in the ACN ratios and the PC-T_b is still at 228-230°C for a sample with only 30 mol% of PC. In Fig. 4.5a, the mixture content can also be identified by the decreasing peak area of the chemical compound, which is proportional to the molar concentration of the compound. The shape of the peak is also changing; it becomes broader and even starts to merge with the peak of the other molecule. The ACN peak in the 90 vol% PC solution looks more like a glass transition curve with the shape of a shoulder resulting from the overlapping of the PC and ACN

signal. From the general trend of these DSC curves, the stabilization effect of the PC on the vaporization of ACN is observed.

In Fig. 4.5b, the T_b are plotted as a function of the PC concentration in ACN to have a more detailed picture of the T_b trends for ACN and PC. It can be noticed that the temperatures, which are plotted in the graph, are not corresponding to the temperature of the peak itself. The onset T at the beginning of the endothermic peak is chosen because it is more representative for T_b than the peak T.[18] An example of the onset T calculation is presented in the Annexes. The onset T is determined by the intercept of the baseline before the peak with the tangent line from the following slope of the peak.

With the different temperatures of vaporization, a type of phase diagram for the vapour-liquid states of ACN and PC is estimated in Fig. 4.5c. The following equations 4.18-4.20 are applied to fit the boiling temperature curve of PC and ACN according to the PC content. Equations 4.18 and 4.19 for ACN or PC describe the molar fraction in the gas phase (x^G_{ACN}, x^G_{PC}) in function of the molar fraction in the liquid state (x^L_{ACN}, x^L_{PC}) and with the temperature and enthalpy of vaporization (ΔH^{ACN}_{vap}, ΔH^{PC}_{vap}). The additional fraction in the exponential is used to quantify the deviation from the ideal behaviour with Ω, the interaction parameter between ACN and PC. Microscopically, Ω is proportional to the exchange energy, that represents, the energy cost of exchanging one molecule of ACN from the bulk liquid of pure ACN into the bulk liquid of pure PC and one molecule of PC from the bulk liquid of pure PC into the bulk liquid of pure ACN.

$$x^G_{ACN} = x^L_{ACN} \exp\left[\frac{\Delta H^{ACN}_{vap}}{R}\left(\frac{1}{T^{ACN}_{vap}} - \frac{1}{T}\right) + \frac{\Omega\,(x^L_{PC})^2}{RT}\right] \tag{4.18}$$

$$x^G_{PC} = x^L_{PC} \exp\left[\frac{\Delta H^{PC}_{vap}}{R}\left(\frac{1}{T^{PC}_{vap}} - \frac{1}{T}\right) + \frac{\Omega\,(x^L_{ACN})^2}{RT}\right] \tag{4.19}$$

$$1 = \left(1 - x^L_{PC}\right) \exp\left[\frac{\Delta H^{ACN}_{vap}}{R}\left(\frac{1}{T^{ACN}_{vap}} - \frac{1}{T}\right) + \frac{\Omega(x^L_{PC})^2}{RT}\right]$$

$$+ x^L_{PC} \exp\left[\frac{\Delta H^{PC}_{vap}}{R}\left(\frac{1}{T^{PC}_{vap}} - \frac{1}{T}\right) + \frac{\Omega\,(1 - x^L_{PC})^2}{RT}\right] \tag{4.20}$$

The Equation 4.20 is finally obtained due to the relation: $x_{ACN}^L + x_{PC}^L = 1 = x_{ACN}^G + x_{PC}^G$. This equation can be used to fit the vapour-liquid equilibria of ACN-PC binary system.

As the pressure is constant at the atmospheric one, the gas escape from the sample when they are produced. The white area over the bubbling curve in Fig. 4.5c corresponds to the conditions where the ACN is in gaseous state and PC in the liquid form. It is in this window of *T* and PC concentrations that the PC can play the role of the working liquid when the ACN is evaporated to induce the chemical disproportionation of Cu(I). Consequently, higher *T* will lead to a totally dry electrolyte that is not useful anymore for a redox flow battery. The limit for the highest temperatures that can be reached for a redox flow battery application is defined by the dew curve in Fig. 4.5c.

In the following Fig. 4.6, the Cu(I) compound is added in the ACN-PC mixtures to characterize the behaviour the complex in the targeted media for the thermal reaction producing Cu and Cu(II). The 70 vol% ACN solution (solid line) clearly shows three nice peaks for each of the chemical species present in the sample: ACN vaporization (near 90°C), Cu(I) reaction (near 160°C) and the PC signal (near 230°C). In the same Fig. 4.6a, a dashed line shows the DSC curves for the 30 vol% ACN. The signals for ACN and Cu(I) are very close and are difficult to distinguish clearly. However, the first sharp peak is assigned to the ACN state transition and the following noisy one to the Cu(I). From this type of DSC, it is difficult to be quantitative as peaks and baselines are complicated to define. However, with the good choice of parameters for the baseline of the integration, some data have been used to confirmed the values reported in Table 4.1 (for example of different types of baselines for the integration see Annexes). During recording of the Cu(I) signal, it is not rare to have some noise. Some impurities in the synthesised complex is maybe a possible reason. Also, it could indicate that sometimes more than one step is induced by heat during the reaction and that the ACN removing from the Cu(I) complex is the first step before redox reaction induced by heat. Another explanation could be the bad sealing of the crucible and consequently the presence of oxygen could introduced Cu oxide species with heat.
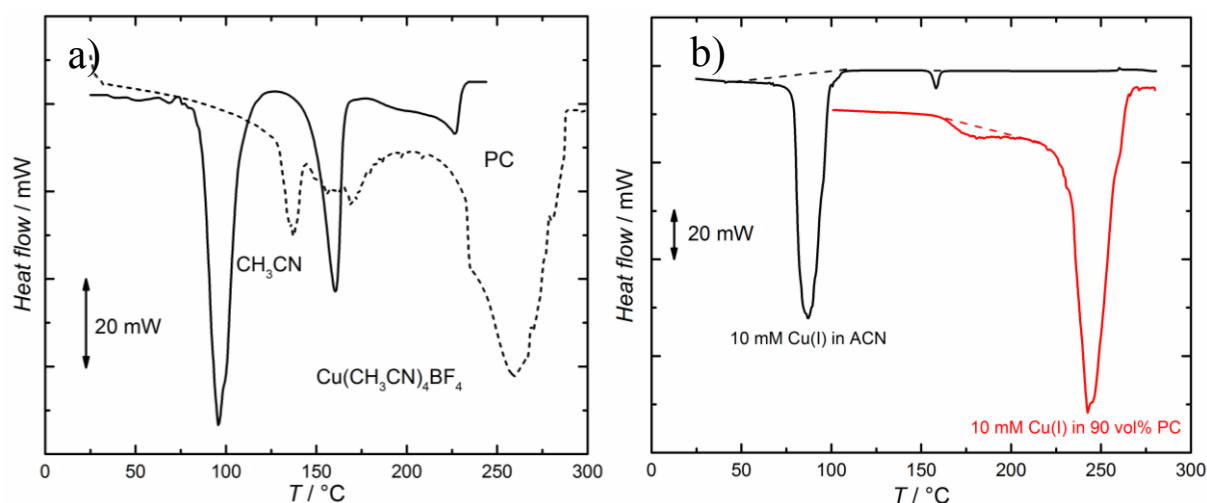
Figure 4.6. a) DSC for acetonitrile-propylene carbonate mixture of saturated [Cu(CH$_3$CN)$_4$]BF$_4$ at 20 K min^{-1} with 90 vol% acetonitrile (solid line) and the dashed line for Cu(I) in 30 vol% ACN. b) DSC curves for 10 mM Cu(I) in ACN (black line) and 10 vol% ACN (red line).

Smaller Cu(I) concentration are also tested to have a less noisy signal (Fig. 4.6b). In the pure ACN solution, the two peaks are straightforward to determine according to the temperature and peak area. For the red curve with only 10 vol% ACN, the signal for ACN and Cu(I) are totally combined together in a small peak just before the PC transition to gas.

4.2.   Heat capacity

The heat capacities are determined by the direct method explained in the theory and the different curves showing the isothermal and scanning steps are included in the Annexes. The values for the C_p according to the PC and Cu(I) content are summarized in Fig. 4.7a. The C_p without Cu(I) evolves monotonically from 92.7 J·mol^{-1}·K^{-1} for the pure ACN to 173.5 J·mol^{-1}·K^{-1} for the PC. From this set of data, the excess thermal capacity, C_p^E (Eq. 4.17) is plotted in Fig. 4.7b. The negative C_p^E explains that less heat is needed to heat the mixtures of ACN and PC than a standard solution expected from the pure solvent combinations. This negative deviation from additivity is an indication of an interaction between ACN and PC that allows a better thermal effect on the mixtures. In the case of $C_p^E \geq 0$, the absence of interactions isolate thermally the molecules from each other and they need more heat to rise their temperature.

The obtained results are relatively similar to those reported in literature for ACN [30–34] and PC [33,35–38]. A detailed data set with more ratios of ACN regarding PC is given for the heat capacity of ACN-PC mixtures by Piekarski *et al.*[33] Their results are relatively similar to those obtained here. They also calculated a negative C_p^E and the C_p increase from 92.36 to 166.98 $J\cdot mol^{-1}\cdot K^{-1}$. However, the intensity of C_p^E has less negative values in their case and the absolute intensity is one order lower than the results obtained in this work with DSC method. In this Chapter, stronger interactions are predicted from the obtained C_p^E value . The major factor, which is influencing the difference in the C_p^E is the C_p of the pure PC which is slightly higher in this work compared to Piekarski *et al.*
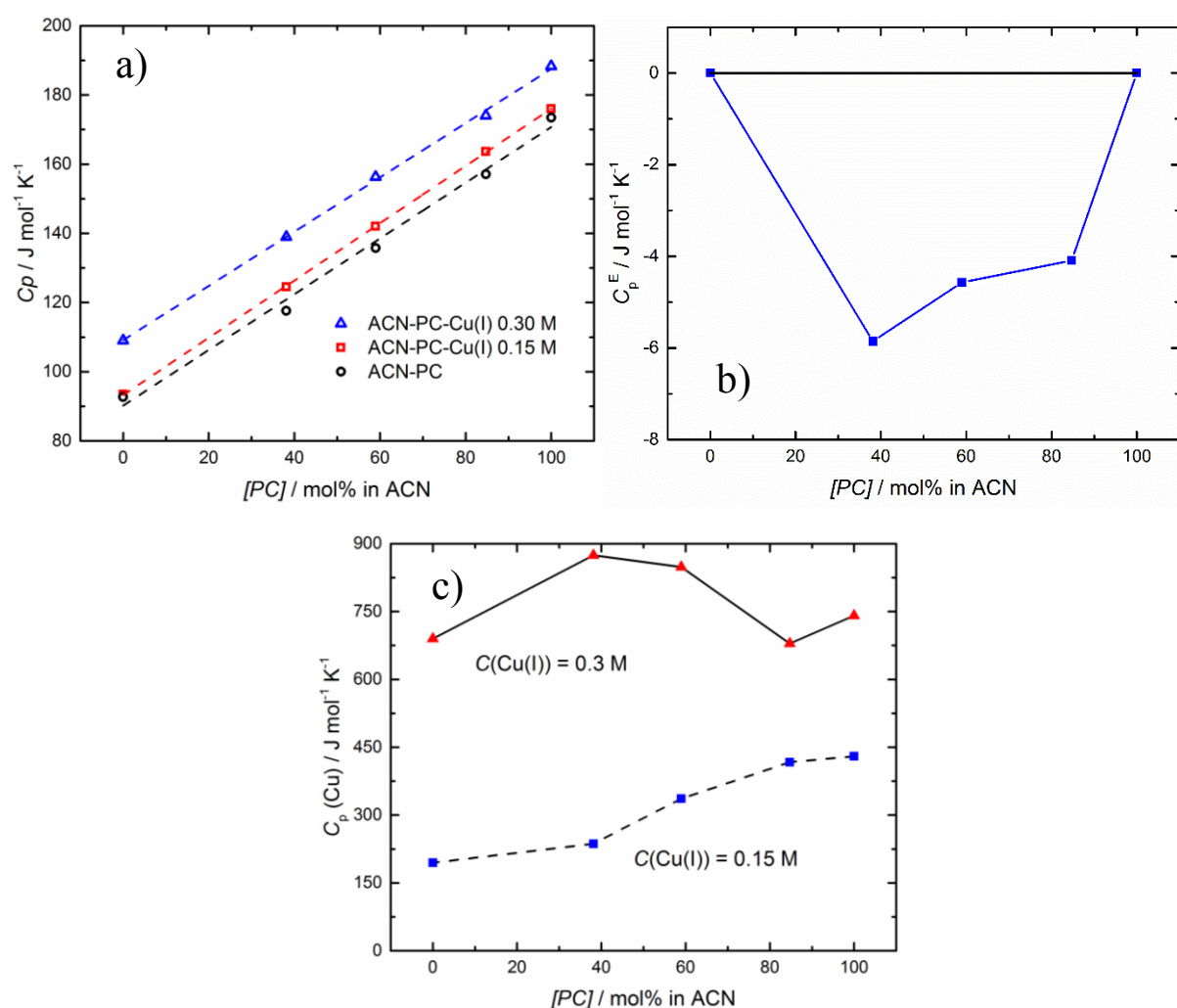
Figure 4.7. a) C_p evolution of acetonitrile-propylene carbonate mixtures containing [Cu(CH₃CN)₄]BF₄ according to the propylene carbonate content. b) C_p^E, excess heat capacity, for the binary mixture of ACN-PC. c) $C_{p,Cu}$, apparent heat capacity of Cu(I) at 0.15 and 0.3 M in the ACN-PC systems.

The same monotonic evolution of the C_p is noticed with the addition of the Cu(I) in solution. The effect of the Cu(I) salt on the C_p is to increase the thermal capacity for all the

different ratios of ACN-PC mixtures. The apparent C_p of the solubilized $[Cu(CH_3CN)_4]BF_4$ is approximated by Eq. 4.21. In this calculation, the excess heat capacity determined before is not taken into account and the assumption of the additivity is directly applied to quantify the Cu(I) C_p. For the 0.15 M Cu(I) solution, the average value for $C_{p,Cu}$ from the measurements in the different PC concentrations is 323 J·mol⁻¹·K⁻¹ and 767 J·mol⁻¹·K⁻¹ for the 0.3 M solutions. As the specific molar heat capacity is used in this work, it is surprising to detect a factor of 2.4 for this quantity between the two $C_{p,Cu}$. It means that the specific heat capacity for the Cu(I) complex depends also on the concentration of the salt. Consequently, the thermal behaviour with more concentrated Cu(I) solution consumes more energy to be heated and the $C_{p,Cu}$ evolves like a colligative property.

$$n_{Cu}C_{p,Cu} = n_{tot}C_{p,tot} - (n_{ACN}C_{p,ACN} + n_{PC}C_{p,PC}) \qquad (4.21)$$

By comparison, the C_p of the Cu(I) solid powder is determined with the direct method at 382.6 J·mol⁻¹·K⁻¹ and is close to the value for 0.15 M Cu(I) in solution. Also, the heat capacity of different salts in ACN and PC has been reported by G. Perron *et al.* and they noticed that the solvent influences the apparent C_p of the salt. [39] Here, in Fig. 4.7c, the same effect is observed with the 0.15 M Cu(I) solution with lower apparent $C_{p,Cu}$ with a higher ACN content. As ACN is the ligand and solvent, the interactions between the Cu centre of the organic molecules are more responsive with thermal energy to increase temperature of the solution.

4.3. Thermodynamic efficiencies

The efficiency of the heat-to-power conversion can be estimated based on the thermodynamic data obtained by the DSC analysis, as shown in equation 4.22-4.23. The factor 2 in the denominator is required because the electrolytes from both sides of the battery need to be regenerated (cf Cu-RFB scheme in Chapter 2). Here, only evaporation of acetonitrile is considered, although some extra energy will be required to also evaporate some PC, as shown by the vapour-liquid equilibrium curves in Fig. 4.5c.

$$\eta = \frac{W_{elec}}{2Q_{tot}} = \frac{nFE_{cell}c_{[Cu(I)(ACN)_4]^+}}{2(Q_{sol} + Q_{vap} + Q_{rxn})} \tag{4.22}$$

$$\eta = \frac{nFE_{cell}c_{[Cu(I)(ACN)_4]^+}}{2(\Delta T * C_p * c_{tot} + \Delta H_{vap}^{ACN} * c_{ACN} + \Delta H_{rxn}^{Cu(I)} * c_{[Cu(I)(ACN)_4]^+})} \tag{4.23}$$

The table 4.2 shows the contribution of each term considering 0.3 M [Cu(CH₃CN)₄]BF₄ solution in different solvents, considering a temperature difference from 70 to 160 °C.

Table 4.2. Estimation of the heat to power conversion according to Eq. 4.23 for a solution of [Cu(CH₃CN)₄]BF₄ (0.3 M).

	acetonitrile 10%(V/V)	acetonitrile 30%(V/V)	acetonitrile 50%(V/V)	acetonitrile 70%(V/V)	acetonitrile 100%(V/V)
E_{cell} / V	1.05	1.15	1.25	1.30	1.36
W_{clec} / kJ L⁻¹	30.4	33.3	36.2	37.6	39.4
Q_{rxn}(**Cu(I)**) / kJ L⁻¹	32.0	32.0	32.0	32.0	32.0
Q_{vap}(**CH₃CN**) / kJ L⁻¹	62.1	186.3	310.6	434.8	621.1
Q_{sol} / kJ L⁻¹	201	202	198	194	191
$\eta_{ther.\ regen.}$ / %	**5.1**	**4.0**	**3.3**	**2.8**	**2.3**

The electrical output that can be extracted for the heat-regenerated electrolyte is higher for solution with higher acetonitrile content because of the higher electrochemical window of Cu⁺ (see Chapter 2). Regarding the energy input, which is needed to drive the thermal disproportionation of the Cu⁺, the heat of vaporization for acetonitrile, as well as the heat required to heat the solution to 160°C are the two most important factors. The heat required for

the vaporization of acetonitrile increases significantly for solutions containing higher acetonitrile concentration. Consequently, the energy conversion efficiency is better for solutions with low acetonitrile content even if the final cell voltage is smaller. 5.1% theoretical efficiency could be improved for example by increasing the concentration of copper electrolyte to 1.5 M, as shown in the calculations in Table 4.3. The apparent molar heat capacity of the electrolyte estimated from the data shown in Fig. 4.7a using $C_{p,Cu}$ of 767 J·mol^{-1}K^{-1} is used to estimate Q_{sol}. More accurate estimations would require measurements of the heat capacity of 1.5 M copper solutions. This system would be able to obtain a theoretical efficiency of 13 %. The efficiencies for different temperature ranges (from low temperature until 80 °C as starting temperatures) are shown in Figure 4.8.

Table 4.3. Estimation of the heat to power conversion according to Eq. 4.23 for a solution of [Cu(CH$_3$CN)$_4$]BF$_4$ (1.5 M).

	acetonitrile 10%(V/V)	acetonitrile 30%(V/V)	acetonitrile 50%(V/V)	acetonitrile 70%(V/V)	acetonitrile 100%(V/V)
E_{cell} / V	1.05	1.15	1.25	1.30	1.36
W_{elec} / kJ L^{-1}	152	166	181	188	197
Q_{rxn}(**Cu(I)**) / kJ L^{-1}	160	160	160	160	160
Q_{vap}(**CH$_3$CN**) / kJ L^{-1}	62.1	186	311	435	621
Q_{sol} / kJ L^{-1}	349	403	454	457	514
$\eta_{ther. regen.}$ / %	**13.3**	**11.1**	**9.8**	**8.9**	**7.6**

The heat for the disproportionation (Q_{rxn}(Cu$^+$)) is approximated to be equal for all the solvent mixtures because the same concentration of Cu$^+$ is considered (0.3 M or 1.5 M).

For the heat capacities (Cp) of the different solutions, used to calculated the heat needed to warm the solution, the trend is to heat more for high propylene carbonate content to reach a given temperature (Fig. 4.7a). This can be explained by the thermal properties of propylene carbonate, which has to receive more thermal energy than acetonitrile to be heated. This behaviour explains why the energy to warm the solution is more important for the propylene carbonate rich solutions. However, another effect also influencing the Q_{sol} value is the changing temperature of the ACN vaporization within the different mixtures with propylene carbonate. Acetonitrile is thermally stabilized in the liquid state by the presence of propylene carbonate. This trend can be observed in Fig. 4.5a-c. This effect on acetonitrile vaporization

leads to an increase of thermal energy for the heating of the solution before the acetonitrile vaporization and Cu^+ disproportionation occur.
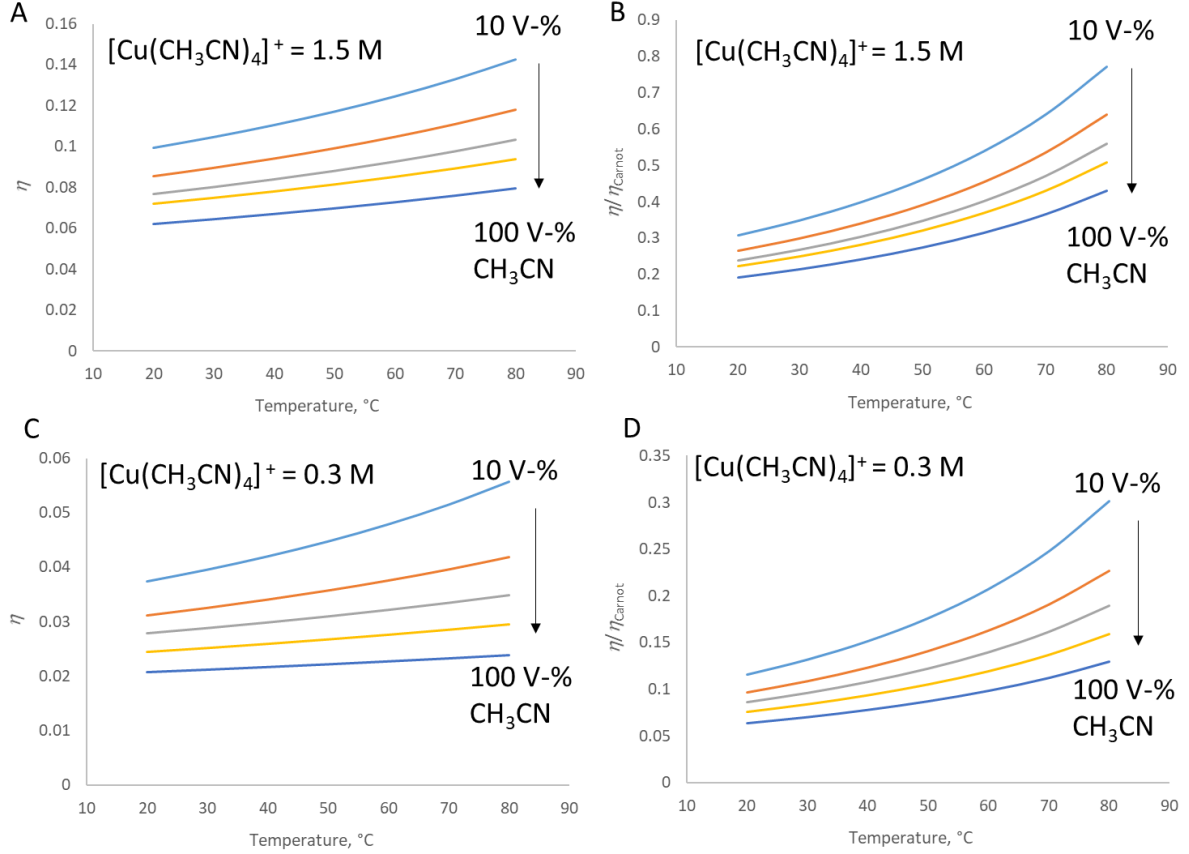
Figure 4.8. Dependence of the efficiency *versus* the lower temperature for different volume ratios of CH_3CN and PC, considering 1.5 M (a, b) and 0.3 M (c, d) Cu(I) salts. Efficiencies are shown on the left (a,c), while efficiencies in relation to the Carnot cycle efficiency are shown on the right (b, d).

$$\eta_{Carnot} = \frac{-W}{Q} = 1 - \frac{T_l}{T_h}$$

(4.24)

With the thermodynamics properties of Cu-ACN-PC systems and the calculation of the efficiencies with different starting temperatures (T_l) for the thermal charge, a full description of the efficiencies expected from the heat-to-power Cu-RFB can be given in Figs. 4.8. Considering the Carnot efficiency in Eq. 4.24, the Cu-RFB efficiencies can be compared in Fig. 4.8b-4.8d. These results confirm that the RFB final system is limited by classical thermodynamics according to the difference of temperatures required for the heat energy

transition during the charging step. However, efficiencies approaching the Carnot efficiencies can be obtained when using highly concentrated Cu-solutions with starting temperatures (T_1) of 70 to 80 °C.

Table 4.4. Estimation of the heat to power conversion according to Eq. 4.23 for a solution of [Cu(CH$_3$CN)$_4$]BF$_4$ (0.3 or 1.5 M) and considering a possible disproportionation without ACN vaporization.

	acetonitrile 10%(V/V)	acetonitrile 30%(V/V)	acetonitrile 50%(V/V)	acetonitrile 70%(V/V)	acetonitrile 100%(V/V)
$\eta_{ther.\ regen.}$ / % 0.3 M Cu(I)	6.5	7.1	7.9	8.3	8.8
$\eta_{ther.\ regen.}$ / % 1.5 M Cu(I)	14.9	14.8	14.7	15.2	14.6

As the ACN vaporization is one of the process, which is consuming the more energy during the thermal charge of the RFB, a system could be imagined to avoid the phase transition of ACN and consequently to reduce the heat uptake. However, if such a system is considered, an assumption needs to be done for the disproportionation of Cu(I): the reaction should be induced only by the high temperature at 160°C and not by the distillation (or removal) of ACN. With this hypothesis, Cu(II) and Cu could be produced in a ACN solution with Cu(I) at 160°C. For this decomposition reaction of Cu(I), the system has to be under high pressure to avoid the vaporization of ACN ($T_b = 81$°C at 1 atm). In Table 4.4, the final efficiencies of the pressurized process are given and all of them increase due to the absence of the heat for the ACN distillation. Obviously, the solutions containing more ACN have a better improvement of their efficiencies because now the ACN does not consume heat for the modification of its physical state.

5.   Conclusion

In this Chapter 4, the thermodynamics of the different endothermic steps during the thermal charge of the Cu-RFB are studied and quantified by the DSC technique. The enthalpy of vaporization of ACN and PC are calculated respectively as 32.4 and 54.0 kJ·mol^{-1}. The enthalpy of the disproportion reaction induced by heat is determined as 106.8 kJ·mol^{-1}. The evolution of the boiling temperature of ACN and PC according to their concentrations in the solvent composition allows representing the vapour-liquid equilibrium curves at constant pressure *versus* the temperature. For the heating of the solution without physical or chemical modification, the apparent specific thermal capacities of the Cu-ACN-PC mixtures are quantified by DSC with the direct method and this highlights the influence of the Cu$^+$ and PC concentrations on the increase of the C_p. Relatively strong interactions between ACN and PC are characterised with a negative excess heat capacity C_p^E.

The efficiencies of the thermal charge of the Cu-RFB followed by electrochemical discharge are described for different low temperatures and compared with the theoretical Carnot efficiency. The main limitations in the heat to power RFB are the concentration of the Cu$^+$ complex, which increase the efficiencies for high values, and the amount of ACN in solution, which influence negatively the performance of the battery when large quantities need to be evaporated. The efficiency of the heat-to-power conversion could also be improved by utilizing a co-solvent with lower heat capacity than PC.

6.   References

1. Turi, E. *Thermal Characterization of Polymeric Materials*. (Elsevier, 2012).

2. Bottom, R. Thermogravimetric analysis. *Principles and applications of thermal analysis* **3**, 87–118 (2008).

3. Gabbott, P. *Principles and Applications of Thermal Analysis*. (John Wiley & Sons, 2008).

4. Höhne, G., Hemminger, W. F. & Flammersheim, H.-J. *Differential Scanning Calorimetry*. (Springer Science & Business Media, 2013).

5. Lukas, K. & LeMaire, P. K. Differential scanning calorimetry: Fundamental overview. *Resonance* **14**, 807–817 (2009).

6. Beekedahl, N. Volume dilatometry. *Journal of research of the National Bureau of Standards* **43**, 145 (1949).

7. Menard, K. P. & Menard, N. Dynamic Mechanical Analysis. *Encyclopedia of Analytical Chemistry* 1–25 (American Cancer Society, 2017).

8. Kett, V., Gaisford, S. & Haines, P. *Principles of Thermal Analysis and Calorimetry*. (Royal Society of Chemistry, 2019).

9. Roberts-Austen, W. C. Fifth Alloy Research Report. *Proceedings of the Institution of Mechanical Engineers* **1**, 35–102 (1899).

10. Saladin, E. Iron Steel Metatlurg. *Metallogr.* **7**, 237–252 (1904).

11. O'Neill, M. J. The Analysis of a Temperature-Controlled Scanning Calorimeter. *Analytical Chemistry* **36**, 1238–1245 (1964).

12. Watson, E. S., O'Neill, M. J., Justin, Joshua. & Brenner, Nathaniel. A Differential Scanning Calorimeter for Quantitative Differential Thermal Analysis. *Anal. Chem.* **36**, 1233–1238 (1964).

13. Watson, E. S. & O'neill, M. J. *Differential microcalorimeter.* (1966).

14. Wendlandt, W. W. *Thermal methods of analysis*. (1974).

15. Farritor, R. E. & Tao, L. C. An improved method of measurement of vaporization heat of volatile liquids with a differential scanning calorimeter. *Thermochimica Acta* **1**, 297–304 (1970).

16. Mita, I., Imai, I. & Kambe, H. Determination of heat of mixing and heat of vaporization with a differential scanning calorimeter. *Thermochimica Acta* **2**, 337–344 (1971).

17. Olson, E. A. *et al.* Scanning calorimeter for nanoliter-scale liquid samples. *Appl. Phys. Lett.* **77**, 2671–2673 (2000).

18. Cassel, B. Determining Vapor Pressur by Pressure DSC. *Perkin Elmer, Application Note, Thermal Analysis* (2012).

19. Perkin-Elmer. Guide to Selection of Differential Scanning Calorimetry (DSC) Sample pans. *Technical Note, Thermal Analysis* (2013).

20. Morgan, H. H. CCCXLII.—Preparation and stability of cuprous nitrate and other cuprous salts in presence of nitriles. *J. Chem. Soc., Trans.* **123**, 2901–2907 (1923).

21. Kubas, G. J., Monzyk, B. & Crumbliss, A. L. Tetrakis(Acetonitrile)Copper(I) Hexafluorophosphate. in *Inorganic Syntheses* (ed. Shriver, D. F.) 90–92 (John Wiley & Sons, Inc., 1979).

22. Mettler-Toledo International Inc all rights. Measuring specific heat capacity. *Mettler Toledo Thermal Analysis* **UserCom No. 7.**, (2010).

23. Haynes, W. M. *CRC Handbook of Chemistry and Physics, 95th Edition*. (CRC Press, 2014).

24. Vladimír Majer & Vaclav Svoboda. *Enthalpies of vaporization of organic compounds: a critical review and data compilation*. (Blackwell Scientific Publications, 1985).

25. Di Cave, S. & Mazzarotta, B. Isobaric vapor-liquid equilibria for the binary systems formed by acetonitrile and aromatic hydrocarbons. *J. Chem. Eng. Data* **36**, 293–297 (1991).

26. Hong, C. S., Wakslak, R., Finston, H. & Fried, V. Some thermodynamic properties of systems containing propylene carbonate and ethylene carbonate. *Journal of Chemical and Engineering Data* **27**, 146–148 (1982).

27. Stephenson, R. M. & Malanowski, S. Properties of Organic Compounds. in *Handbook of the Thermodynamics of Organic Compounds* 1–471 (Springer Netherlands, 1987). doi:10.1007/978-94-009-3173-2_1

28. Rajapakse, N., Finston, H. L. & Fried, V. Liquid-liquid phase equilibria in the propylene carbonate+ methyl isobutyl ketone+ water system. *Journal of Chemical and Engineering Data* **31**, 408–410 (1986).

29. Hathaway, B. J., Holah, D. G. & Postlethwaite, J. D. 630. The preparation and properties of some tetrakis(methylcyanide)copper(I) complexes. *J. Chem. Soc.* 3215–3218 (1961).

30. de Visser, C. & Somsen, G. Thermochemical behavior of mixtures ofN,N-dimethylformamide with dimethylsulfoxide, acetonitrile, andN-methylformamide: Volumes and heat capacities. *J Solution Chem* **8**, 593–600 (1979).

31. Kolker, A. M., Kulikov, M. V. & Krestov, Al. G. Volumes and heat capacities of binary non-aqueous mixtures. Part 1. The systems acetonitrile—formamide and acetonitrile—N-methylformamide. *Thermochimica Acta* **211**, 61–72 (1992).

32. Kolker, A. M., Kulikov, M. V. & Krestov, Al. G. Volumes and heat capacities of binary non-aqueous mixtures. Part 2. The systems acetonitrile-N,N-dimethylformamide and acetonitrile-hexamethylphosphoric triamide. *Thermochimica Acta* **211**, 73–84 (1992).

33. Piekarski, H., Kubalczyk, K. & Wasiak, M. Volumes, Heat Capacities, and Compressibilities of the Mixtures of Acetonitrile with N,N-Dimethylacetamide and Propylene Carbonate. *J. Chem. Eng. Data* **55**, 5435–5440 (2010).

34. Piekarski, H. & Somsen, G. Heat Capacities and Volumes of Metanol + Acetonitrile Mixtures at 5 and 25 °C. *J. Solution Chem.* **21**, (1992).

35. Marcus, Y. Ion solvation. *Wiley* (1985).

36. Masood, A. K. M., Pethrick, R. A. & Swinton, F. L. Physicochemical studies of super-cooled liquids. Cyclic carbonates and α,β-unsaturated aldehydes. *J. Chem. Soc., Faraday Trans. 1* **72**, 20–28 (1976).

37. Vasil'ev, I.A. & Korkhov, A.D. Thermodynamic properties of alkylene carbonates at low temperatures. *Tr. Khim. Khim. Tekhnol.* (1974).

38. Peppel, W. J. Preparation and Properties of the Alkylene Carbonates. *Ind. Eng. Chem.* **50**, 767–770 (1958).

39. Perron, G., Trudeau, G. & Desnoyers, J. E. Heat capacities and isentropic compressibilities of electrolytes in propylene carbonate at 25 °C. *Can. J. Chem.* **65**, 1402–1406 (1987).

7. Annexes

7.1. Onset temperature determination on ACN peak with DSC.
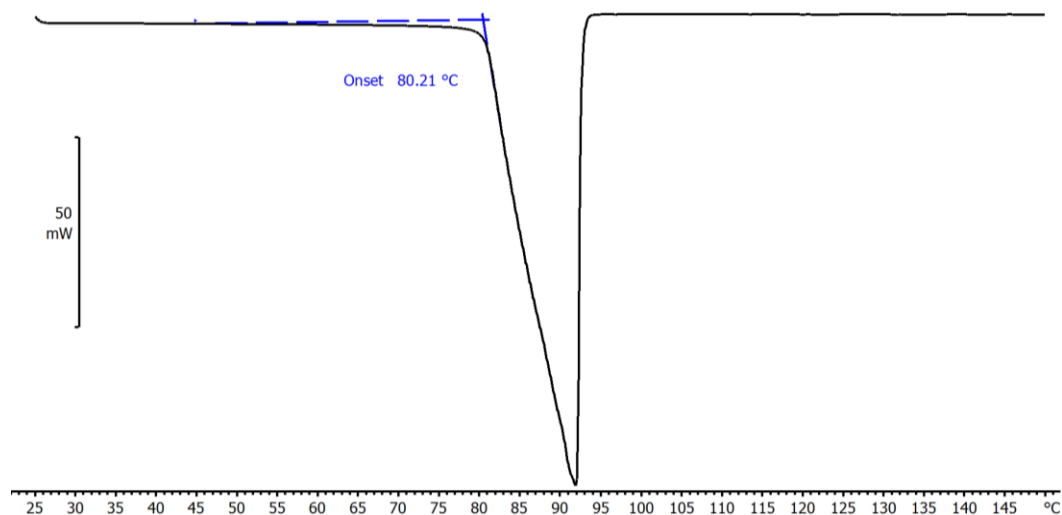
7.2. Baseline, horizontal and tangential from left side on PC peak with DSC.
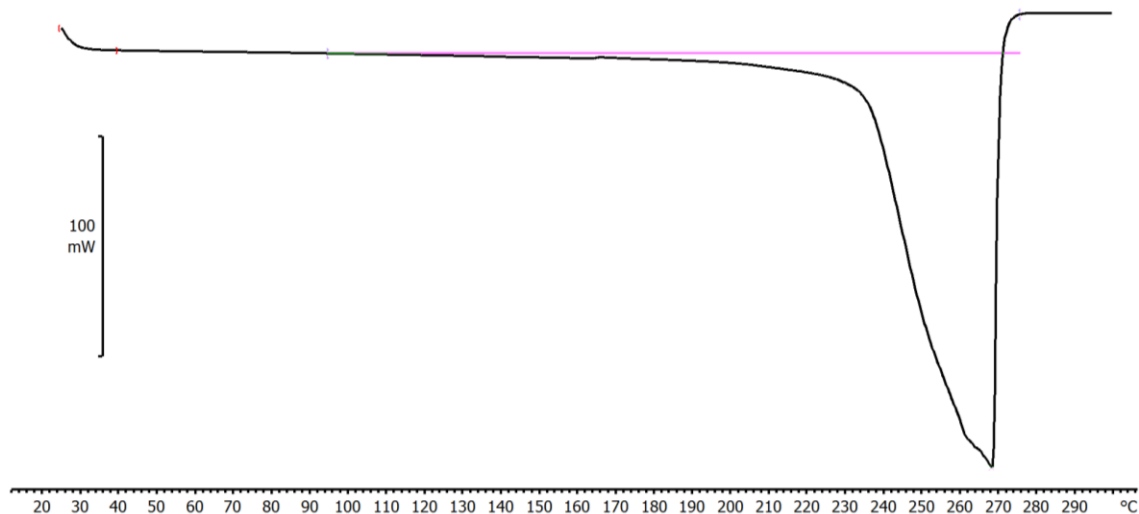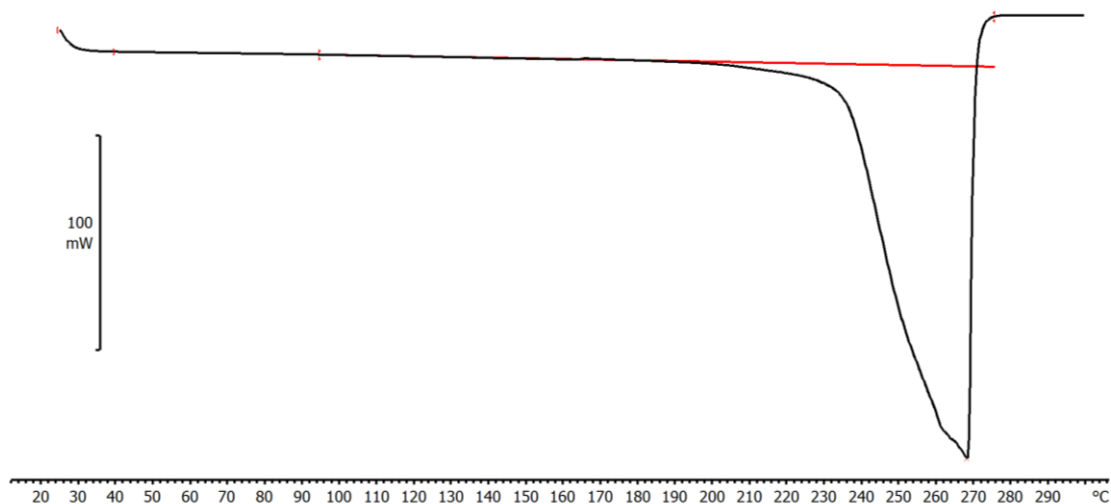
7.3. Baseline for integration on PC peak with DSC (line, spline, horizontal and tangential).

straight line

spline line
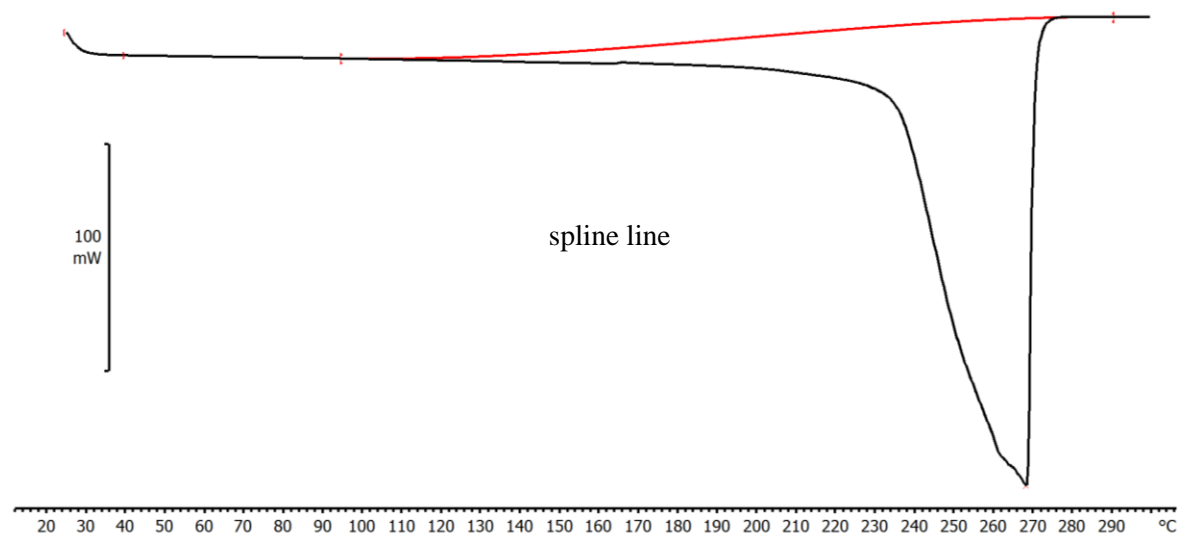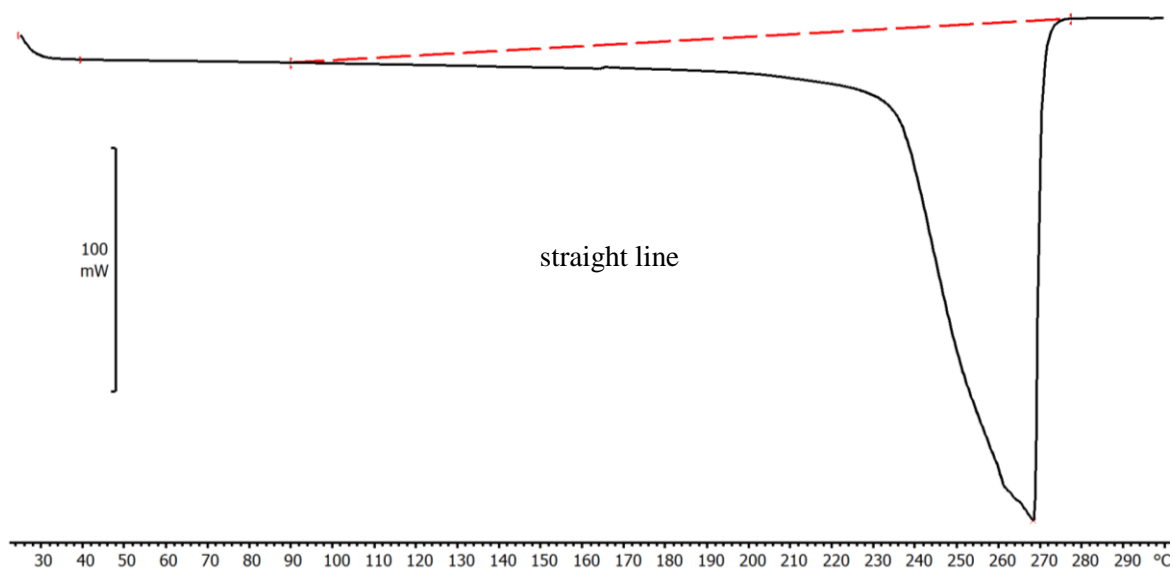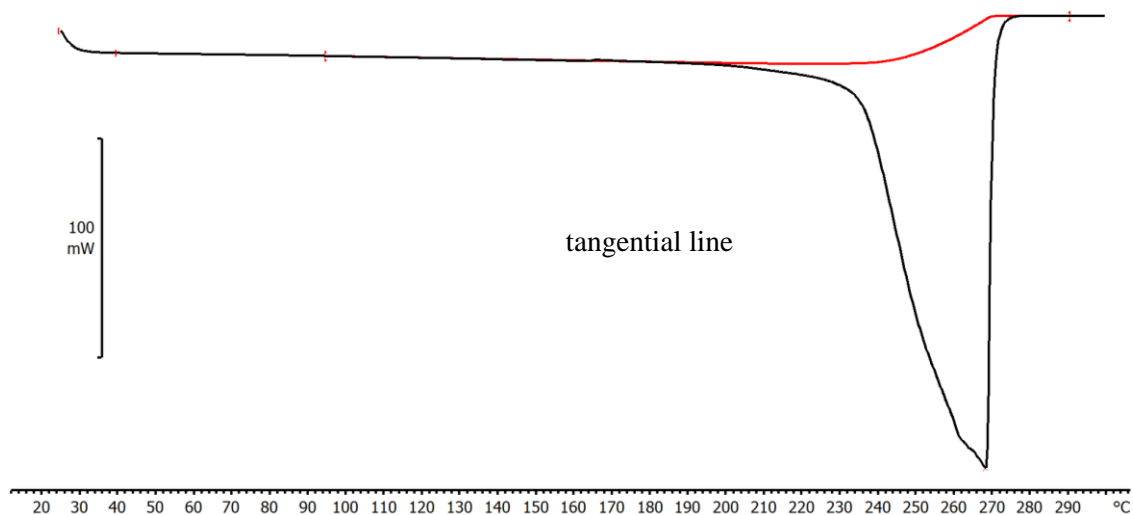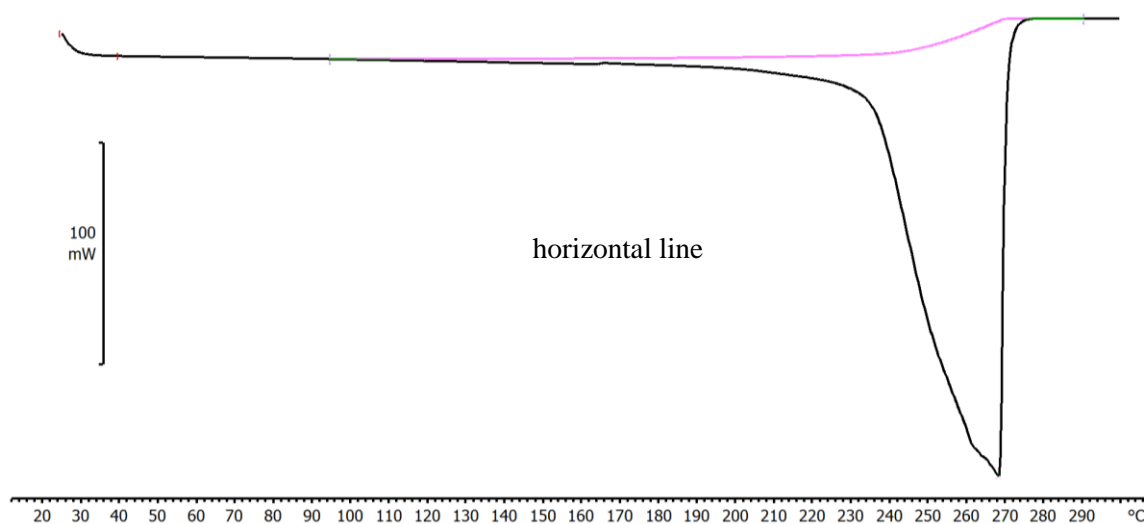
7.4. The direct method sequence with an isothermal step (at 25°C) followed by a dynamic temperature period with a heating rate of 5 °C·min⁻¹.

ACN 100 vol%, Cu(I) 0.15 M

ACN 50 vol%

ACN 50 vol%, Cu(I) 0.15 M

ACN 50 vol%, Cu(I) 0.3 M

ACN 30 vol%

ACN 30 vol%, Cu(I) 0.15 M

ACN 30 vol%, Cu(I) 0.3 M

ACN 10 vol%

ACN 10 vol%, Cu(I) 0.15 M
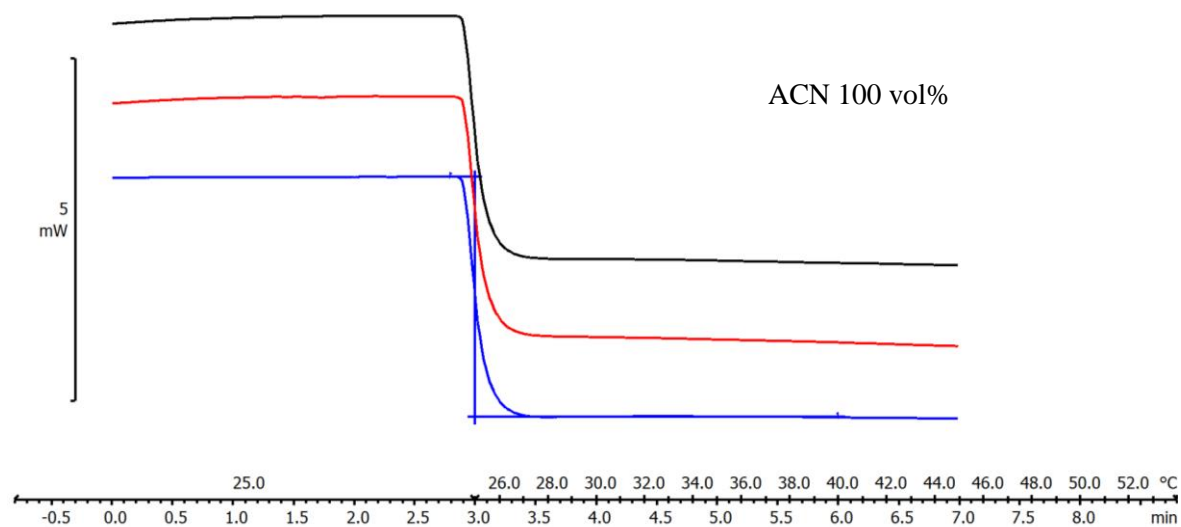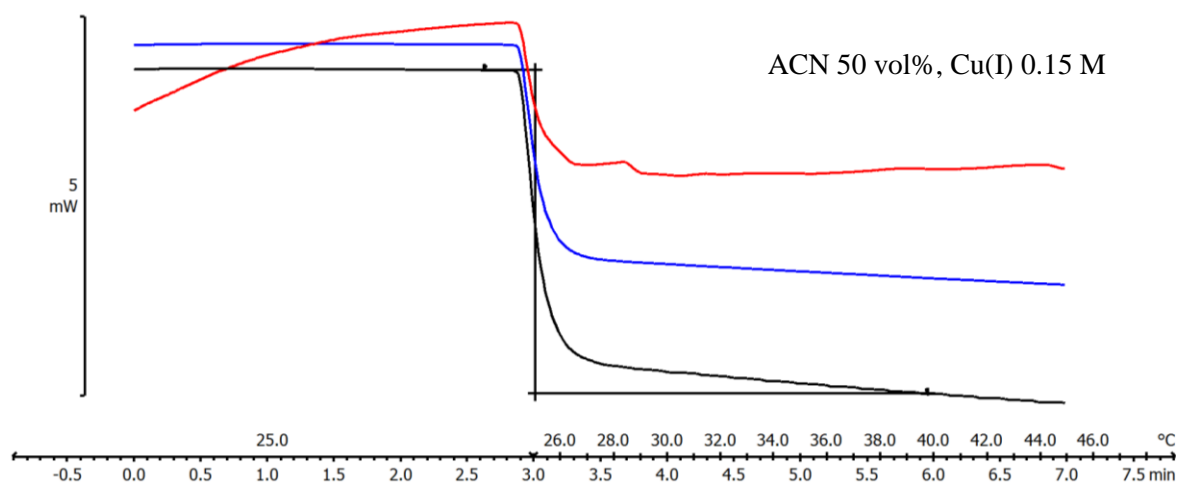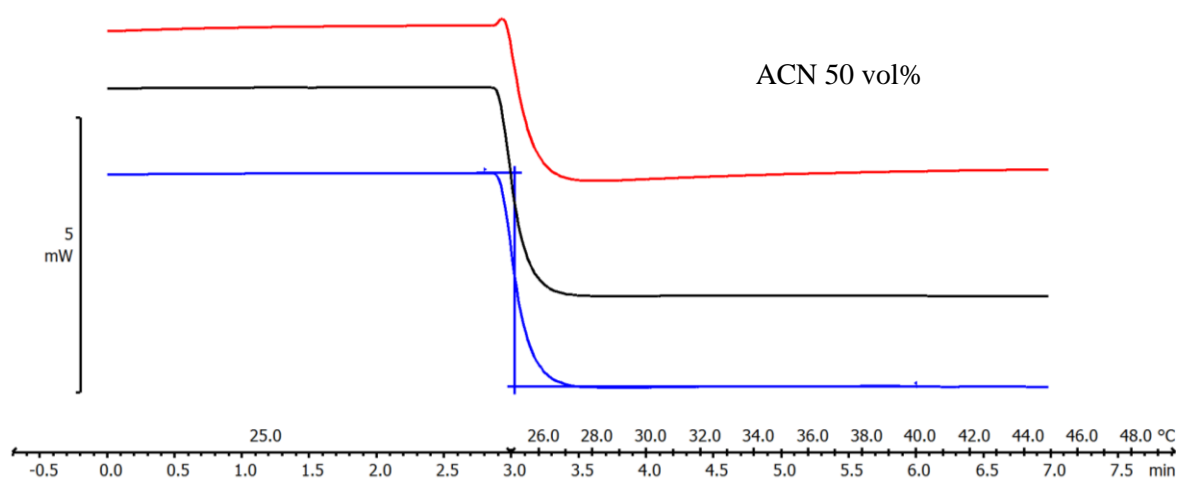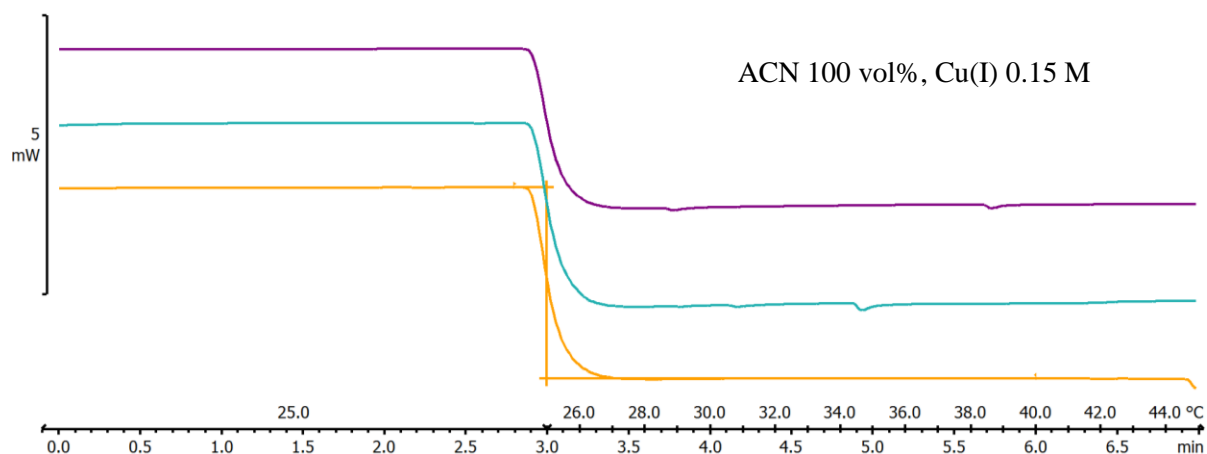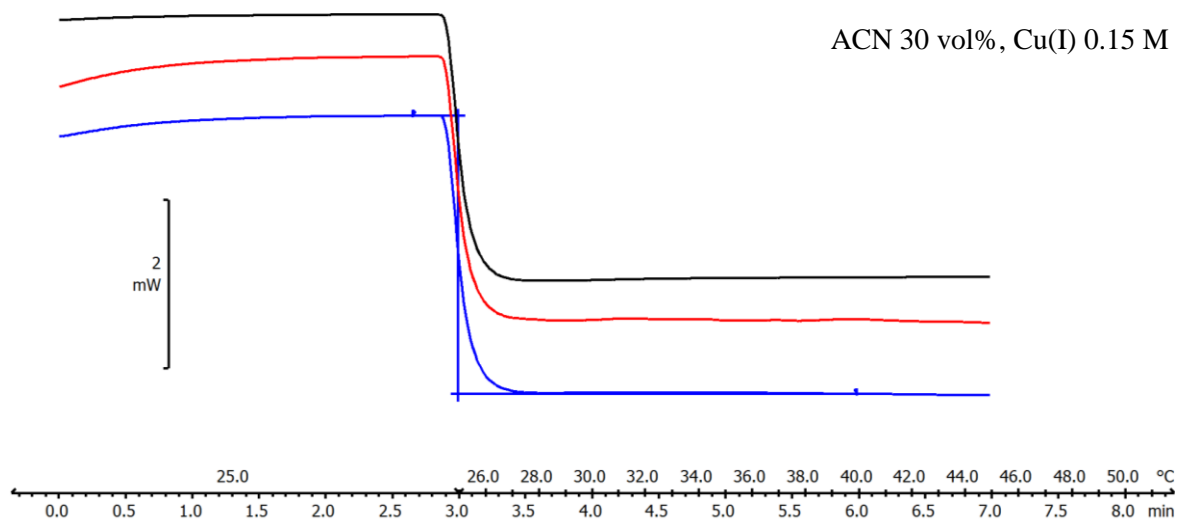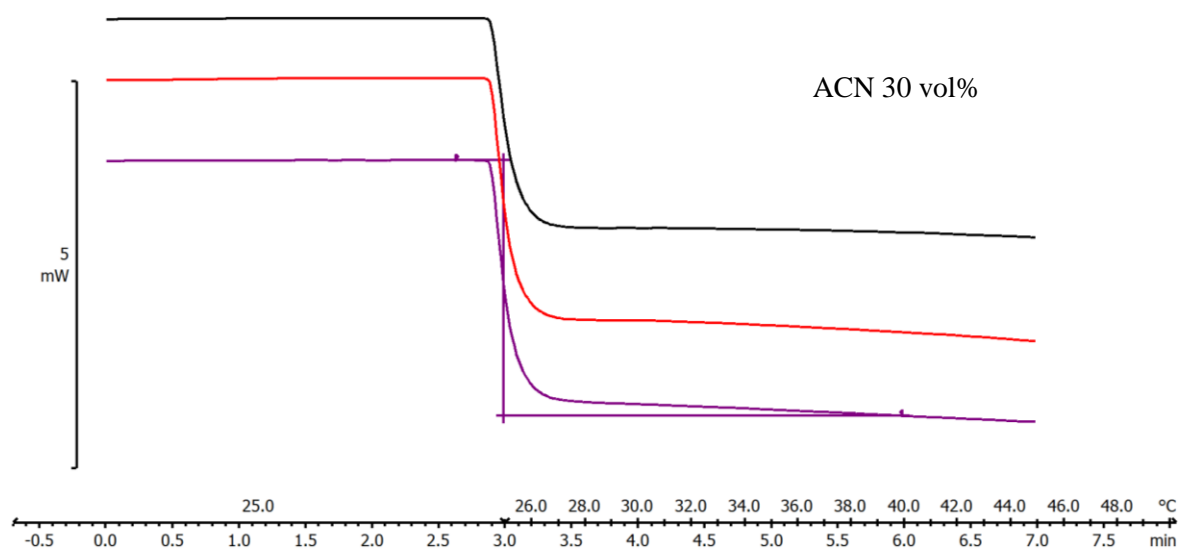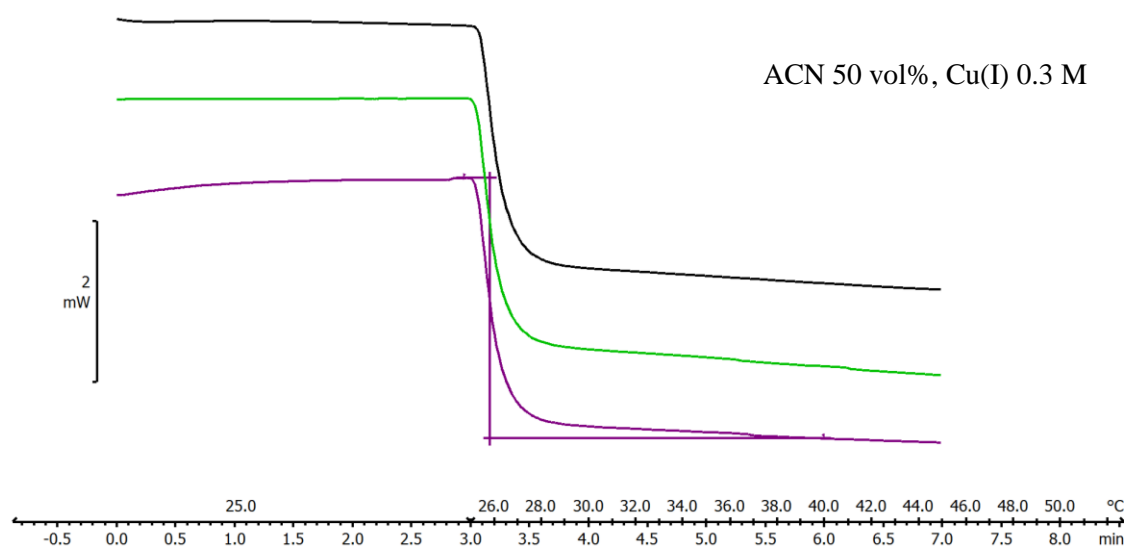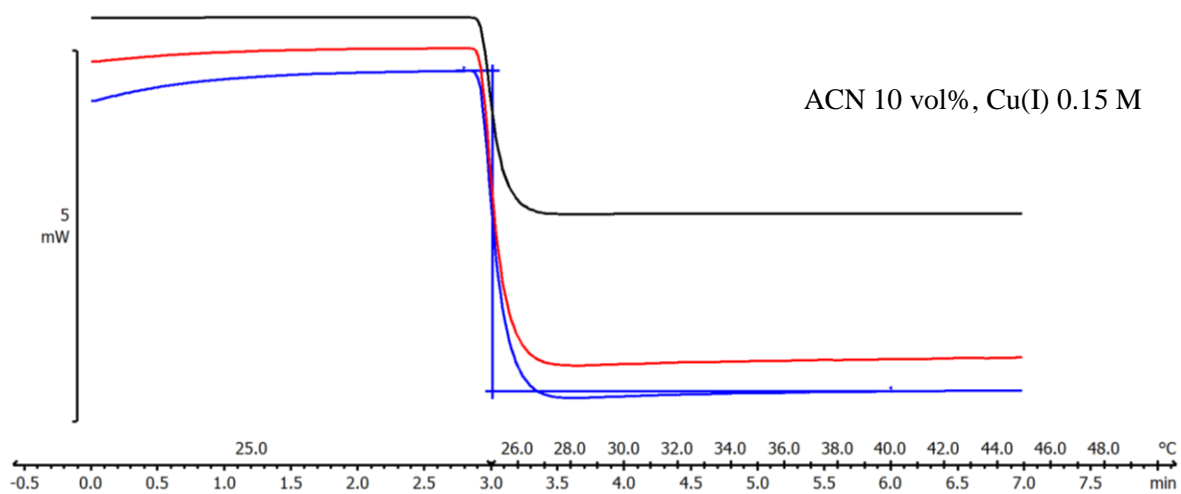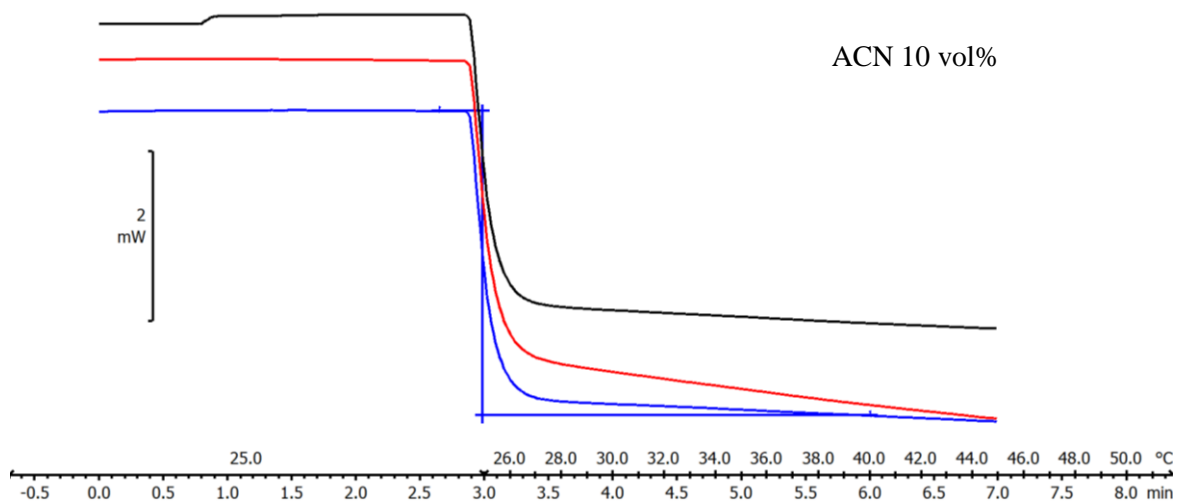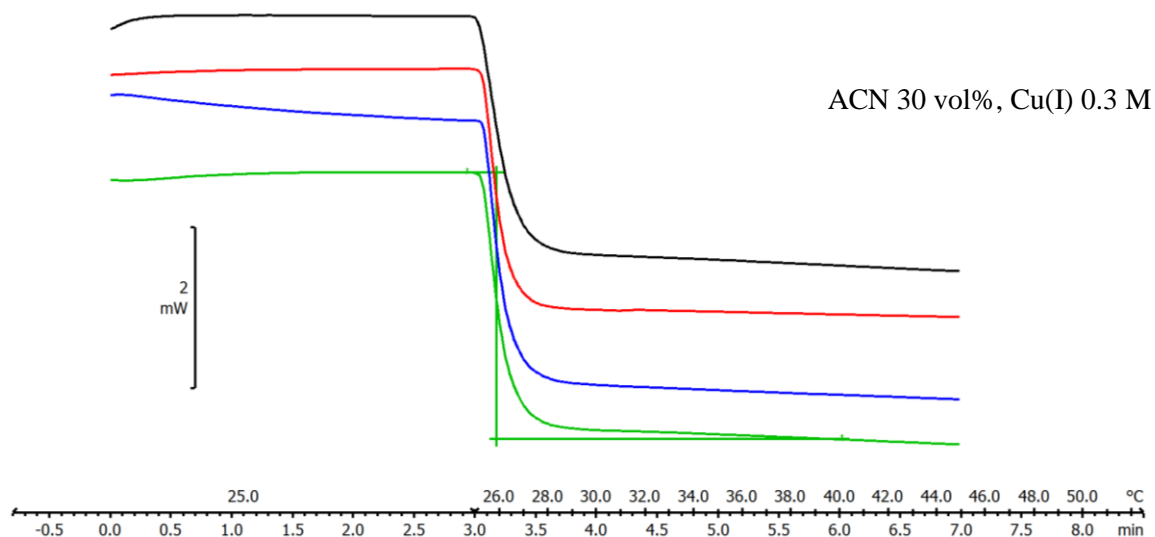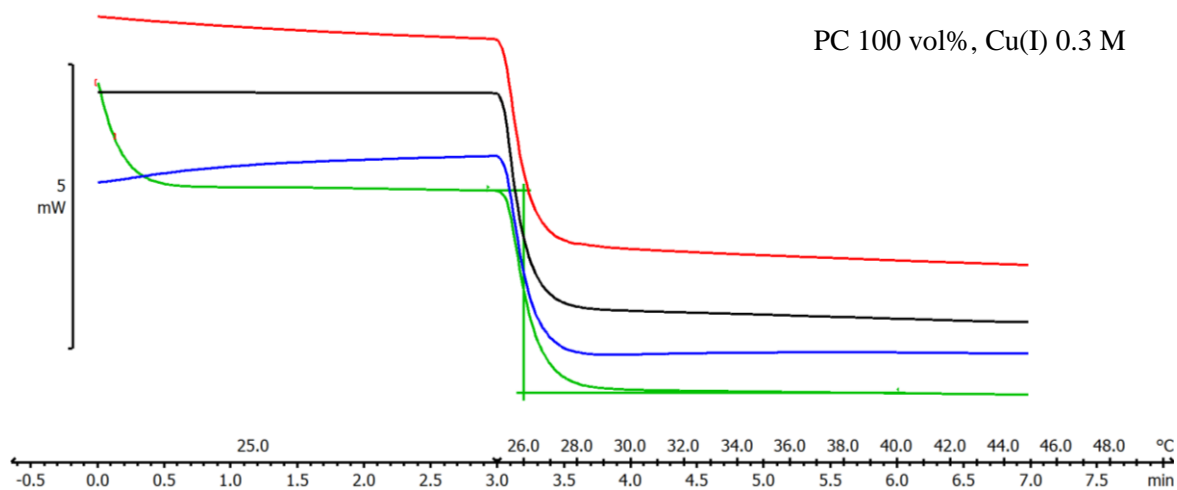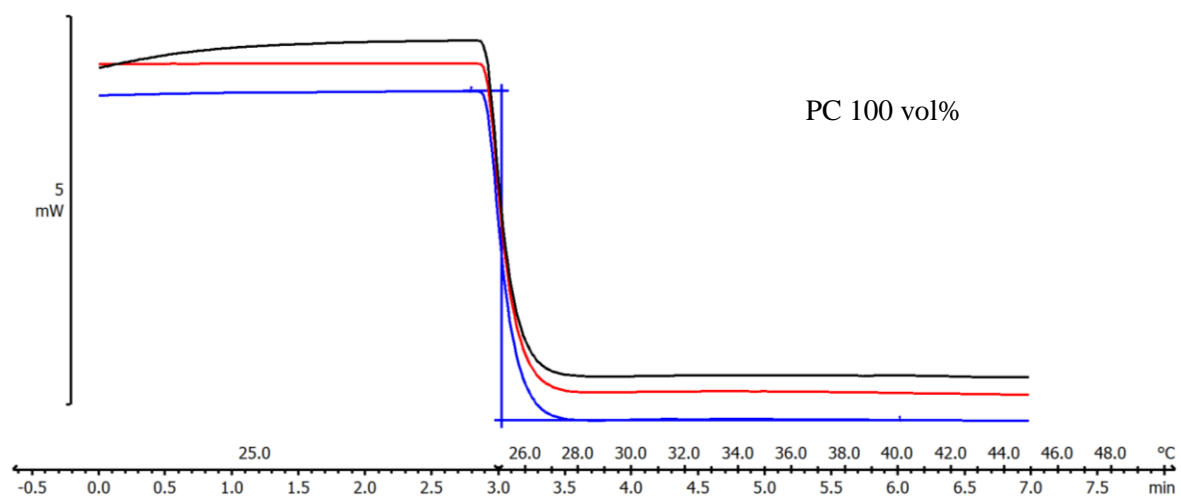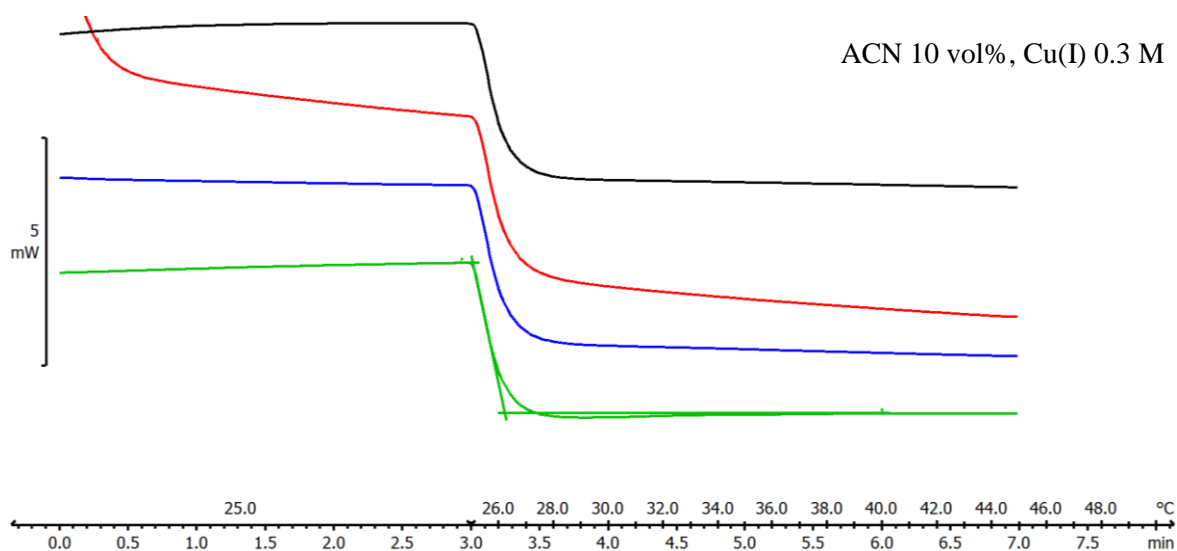
Chapter V

Development of the redox flow battery system

1.   Introduction

In this Chapter V, the optimization of the redox flow battery system with Cu(I) electrolyte is presented. The transition from a simple H-cell to a flow cell configuration is described and a comparison between both battery designs is provided. The original flow cell is significantly modified to develop a lab-scale testing system specifically for the redox flow batteries with electrolyte composed of organic solvents. The different components of the electrochemical cells are examined to be able to resist to the chemical, physical and mechanical conditions encountered in the Cu-RFB at elevated operating temperatures.

A specific attention is given to the choice of the membranes, which is one of the most important part inside the RFB; several types of membrane are tested to obtain the best idea of what criteria should be fulfilled by the separator for the Cu electrolyte. The importance of the negative electrode is also highlighted as the deposition/stripping process is one of the limiting factors of the battery. Cu plating and Cu slurry electrodes are investigated for the Cu(I)/Cu side for economical purposes or for the improvement of the efficiency, power output and thermal conversion.

2.   Battery efficiency calculations

The Coulombic efficiency is defined as the ratio of the charge, which is given by the battery during the discharge ($Q_{discharge}$), over the charge, which is accumulated during the previous charging process (Q_{charge}):

$$\eta_Q = \frac{Q_{discharge}}{Q_{charge}} \tag{5.1}$$

The energy efficiency is given by Equation 5.2 as the ratio between the charge (I_{charge}) and discharge ($I_{discharge}$) current. As the cell induced an Ohmic resistance, it is more useful to calculate the theoretical efficiency of a system with a minimal Ohmic drop. This allows a more accurate comparison of different systems. To be able to obtain this efficiency, the charge/discharge curves need to be corrected with Ohmic compensation. For that purpose, the resistance inside the cell is evaluated after each charging and discharging steps by chronopotentiometry. From these corrected potentials, the energy efficiency can be calculated with:

$$\eta_E = \frac{\left| I_{discharge} \int_{t_s}^{t_f} E \, dt \right|}{\left| I_{charge} \int_{t_0}^{t_s} E \, dt \right|} \tag{5.2}$$

3.   Materials and methods

3.1.   Chemicals

All solvents and chemicals were used as received without further purification and were stored in a glove box under nitrogen. The solvents were acetonitrile (CH$_3$CN, extra dry over molecular sieves, 99.9%, Acros) and propylene carbonate (C$_4$H$_6$O$_3$, anhydrous, 99.7%, Sigma-Aldrich). The supporting electrolytes were tetraethylammonuim tetrafluoroborate (TEABF$_4$, 99%, ABCR) or lithium hexafluorophosphate (LiPF$_6$, Battery Grade, Fluorochem). Tetrakis(acetonitrile)copper(I) hexafluorophosphate ([Cu(CH$_3$CN)$_4$]PF$_6$, 98%, ABCR) was used as received as a redox active molecule in the RFB. The electroactive species tetrakis(acetonitrile)copper(I) tetrafluoroborate was either commercial, ([Cu(CH$_3$CN)$_4$]BF$_4$, >

98%, TCi), or prepared by comproportionation reactions. The reducing ability of metallic Cu on Cu^{2+} has been known since 1923, when Morgan used this method for the preparation of cuprous chloride or bromide-mono(acetonitrile) complexes[1]. Therefore the synthesis of Cu^+ can be easily made in acetonitrile by comproportionation [2–4]. For this synthesis of $[Cu(CH_3CN)_4]BF_4$, copper(II) tetrafluoroborate hydrate ($Cu(BF_4)_2 \cdot xH_2O$, Sigma-Aldrich), acetonitrile (Merck) and copper wire (dia. 1 mm, $\geq$ 99.99%, GoodFellow) were of analytical grade and were used as received. The comproportionation reaction occurs in a Schlenk line with nitrogen. The Cu^+ complex with acetonitrile is dried overnight under vacuum and stored in a nitrogen-filled glove box.

Regarding the Cu particles synthesis by the cathodic corrosion method, the Cu wires (dia. 0.2mm and 1 mm, purity 99.9%, Advent) were placed in the aqueous bath (MilliQ water, 18.2 MΩ cm) of PVP (polyvinylpyrrolidone, MW ≈ 10'000, Sigma-Aldrich) and sulphuric acid (H_2SO_4, 95-97% for analysis, Merk).

3.2.   RFB components

Two different set-ups are assembled to test the charge-discharge cycling of the battery. Both cells were filled with a acetonitrile-propylene carbonate solution containing 0.15-0.3 M $TEABF_4$ and 0.15-0.3 M $[Cu(CH_3CN)_4]BF_4$. Here, $TEABF_4$ was utilized to improve the conductivity of the electrolytes. The anion-exchange membrane (FAB-PK-130, Fumatech) is either directly included under its dry state or soaked in acetonitrile with 0.15 M $TEABF_4$ during 24 hours before utilization. All gaskets, seals and tubing need to be chemically resistant to acetonitrile. H-cell type redox flow battery is constructed utilizing two jacketed half-cells of 3.4 mL (PermeGear Horizontal Cell from SES GmgH). The cell is filled up inside the glovebox to avoid the presence of oxygen and water. For the negative side, a copper wire is used as an electrode and a platinum wire was used for the positive side. The area available for the ionic transport is 1.13 cm^2 with an opening diameter of 12 mm. For the other flow cell, the usual stack is constructed with the membrane, current collectors and carbon-felt electrodes ((compressible with thickness 3.2 or 6.5 mm, C content $\geq$ 95 %, FuelCellStore) or Cu foam (thickness 6.35 mm, 99.9%, GoodFellow) electrodes (8 or 10 cm^2) from a hardware cell from Fuel Cell Technologies, Inc. The calculations of the Coulombic and energy efficiencies are

illustrated in the section 2. Electrochemical impedance spectroscopy was utilized to evaluate the ohmic resistance of the cell. The anions exchange membranes are either directly included under its dry state or soaked in acetonitrile with 0.15 M TEABF$_4$ during 24 hours before utilisation. All gaskets (24SH-ePTFE gasket sheets, 1mm, from TEADIT), seals and tubing (Masterflex Solve-Flex, from Cole-Parmer) need to be chemically resistant to acetonitrile.

3.3. XPS, XRD and SEM

X-ray diffraction (XRD) data were collected in Bragg Brentano geometry on a D8 Bruker Discover diffractometer equipped with a non-monochromated Cu-source and a LynxEye XE detector. Rietveld refinement was done with Topas.[5] The instrumental resolution was collected on the SRM1976b standard, the data of which were profile-fitted to obtain the empirical resolution function, which was then used to obtain domain sizes from integral breadths on sample data.

The images are recorded with a scanning electron microscope (SEM). The SEM is a Teneo SEM (FEI, USA) equipped with a Schottky field emission gun. Secondary electron detection was achieved with an Everhart-Thornley detector and an in-lens detector. For composition characterisation, X-rays are detected by energy-dispersive X-ray spectroscopy (EDX) (XFlash Silicon drift detector) inside the SEM.

The XPS measurements are carried out on a VersaProbe II (Physical Electronics Inc) using the monochromated Kα X-ray line of an aluminium anode. The pass energy is set to 46.95 eV with a step size of 0.2 eV. The samples are electrically isolated from the sample holder and charges are compensated. The spectra are referenced at 284.8 eV using the C-C bound component of the C1s transition.

4.   Hardware and current collectors

At the beginning of the Cu battery project, the first cyclings were applied with a potentiostat during the charge and the electrical output was recorded during the discharge. At that time, no consideration was given to try an electrical discharge from the thermally regenerated Cu-Cu(II) solution. The primary goal was to confirm that the electrolyte based on Cu(I) in ACN and PC can be utilised as a simple redox system for energy storage. For that purpose, a rather basic H-cell set-up was built with an anionic membrane between two half-cells. The glassware set-up can be observed in Fig. 5.1.
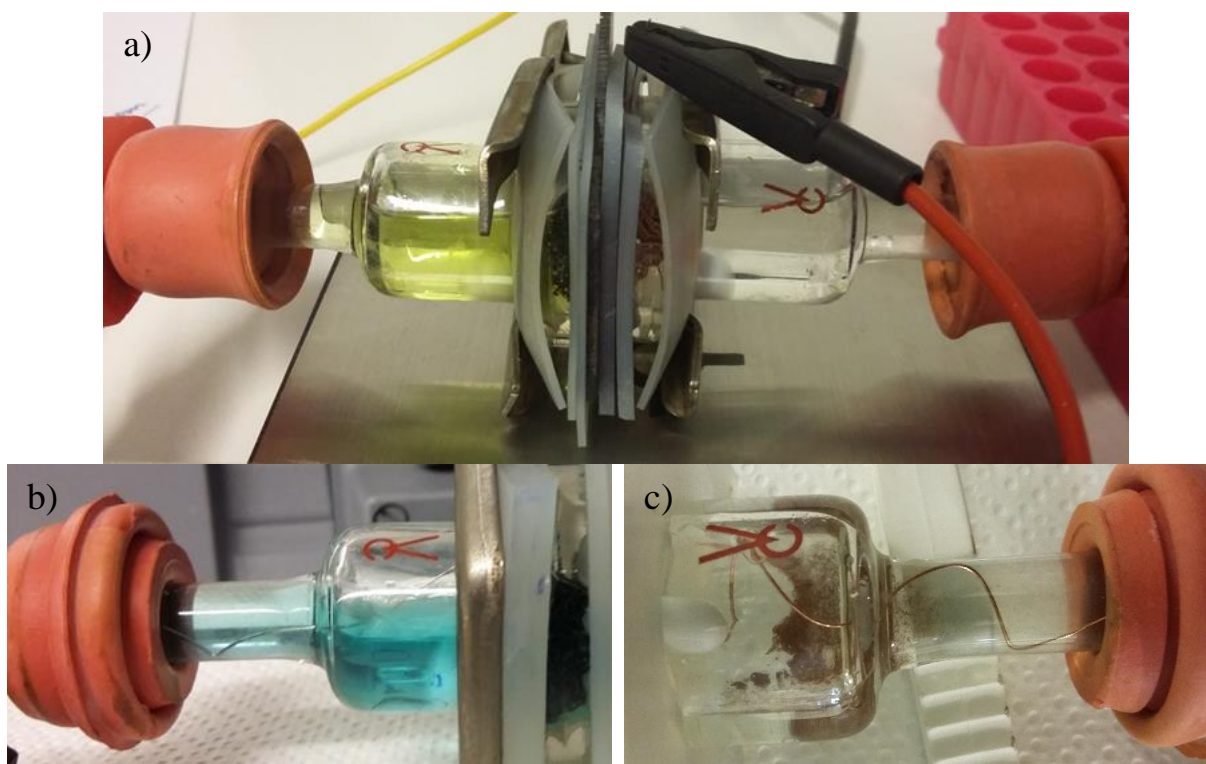
Figure 5.1. a) Picture of the Cu cell with glassware for the two half cells. On the left, RVC electrode for the Cu(II)/Cu(I) couple and, on the right, Cu wire electrode for the Cu deposition and stripping. Both sides are separated by an anionic membrane, FAB-PK-130. b) The positive side colour transition with water diffusion. c) Cu particles at the bottom of the positive side after several cycles of copper deposition and stripping on the Cu wire .

In Fig. 5.1, the miniaturized cell is used to record the voltage between the anode and cathode with time and according to the applied current. A set of data are shown here in Fig. 5.2 and confirms the ability to build potential with Cu(I) electrolyte by applying a current between both electrodes. From the potential curves in Fig. 5.2a, a large difference of voltage is observed between the charge and the discharge. This effect is mainly assigned to the long distance between both electrodes in this cell configuration, resulting in a cell resistance of around 40-48 Ω. In Fig. 5.2a, the *iR* compensation is not applied to highlight the increasing difference of the voltage between the charge and discharge curves with increasing currents. With decreasing charge-discharge current density, the gap of potential is reduced as expected from the Ohm's law. According to Fig. 5.2, the H-cell configuration is limited to low current densities. However, the efficiencies obtained with the *iR*-corrected potential curves allows predicting a better behaviour if the set-up is improved to minimize the internal resistance. Regarding the energy efficiency between 40 and 60%, the current density plays an important role, even if the *iR*-compensation is applied, and with lower current, a lower voltage difference is observed between the charging and discharging plateau. Likewise, low current densities allow reaching higher capacities of the cell both during the charging and discharging steps.
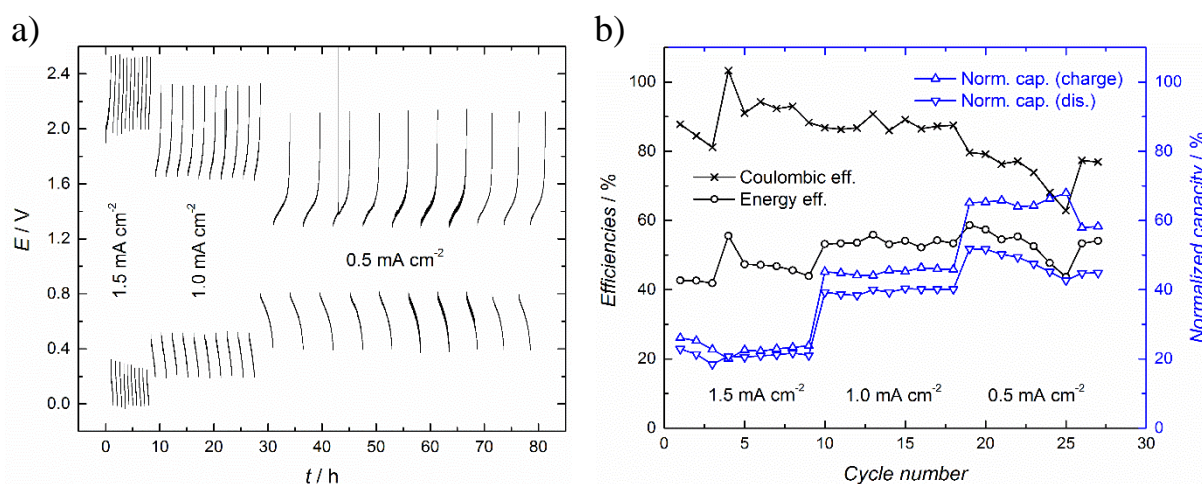
Figure 5.2. H-cell experiment with non-corrected charge/discharge curves at 1.5, 1.0 and 0.5 mA·cm^{-2}. The electrolyte is made with [Cu(CH$_3$CN)$_4$]BF$_4$ (0.15 mM) and 0.15 M (TEABF$_4$) in acetonitrile-propylene carbonate solvent (90 vol% of propylene carbonate). a) This graph shows the recorded voltage during the 10 cycles for the different current densities applied. b) The Coulombic and energy efficiencies for each cycles, the energy efficiency is calculated with *iR* corrected curves. In blue, the normalized capacity of the charges and discharges are indicated.

The Coulombic efficiency is more or less stable at the beginning for 1.5 and 1.0 mA·cm^{-2} and stays in the interval 80-90%. Although the charges and discharges reach higher capacities at 0.5 mA·cm^{-2}, smaller ratios of the charged capacities can be recovered back and lower Coulombic efficiencies are obtained for the last cycles. Two key observations could explain this lowering of the discharge capacity during the last cycles. In Fig. 5.1a, a solution colour transition from green to blue is detected by eye in the positive half-cell and is assigned to the slow diffusion of water and oxygen from the surrounding atmosphere into the electrolyte. This water intake makes the oxidation of Cu$^+$ to Cu^{2+} more irreversible and stabilizes some Cu ion in the 2+ oxidation state. However, the ACN content is large enough to ensure a certain reversibility of the Cu(II)/Cu(I) couple. Furthermore, if the water concentration is significantly influencing the electrochemistry of the cell, a shift to lower voltage should be detected for the cell voltage and no such effect is clearly observed. In parallel to the water diffusion, oxygen can also pass through the gaskets and sealing to induce the formation of Cu oxides. Furthermore, significant changes in the shape of the Cu electrode occur during the cycling. With this cell design, the Cu nucleation on the Cu wire is growing in a preferential orientation to the direction of the membrane in a way to minimize the distance/resistance between the two electrodes. This non-homogenous plating on the Cu wire surface is expected, but has the disadvantage that some of the Cu nodules can break off during discharge, leading to irreversible losses of metallic Cu. In Fig. 5.1c, Cu particles detached from the electrode are visible in the bottom of the cell after cycling of the battery, with no possibility to be oxidized back to Cu(I).

To improve the cycling performance of the battery, a redox flow architecture is adapted for the single cell. Compared to the previous system, this set-up allows the control of the distance between the electrodes and to reduce significantly the cell resistance to few ohms (1-3 Ω). Consequently, higher current densities can be utilized and higher normalized capacities are obtained with the flow of electrolyte induced by the pumps through the porous electrodes. The high active surface area of the C-felt and Cu foam electrodes coupled with the flow of the solutions allows cycling the battery to reach any targeted state of charge (SOC). Furthermore, the usual advantages of the RFB are accessible (decoupling power production and capacity), and especially the flexibility of this system design that can be applied to build a cell capable to use the Cu electrochemistry in organic solvents.

Starting from the commercial fuel cell from Fuel Cell Technologies, several modifications have to be done to allow testing of the Cu chemistry in non-aqueous solvents. The schematic representation optimized system is shown in Fig. 5.3 with the different parts of

the set-up. A particular focus is on the current collector, which is the most deeply modified component among the hardware.
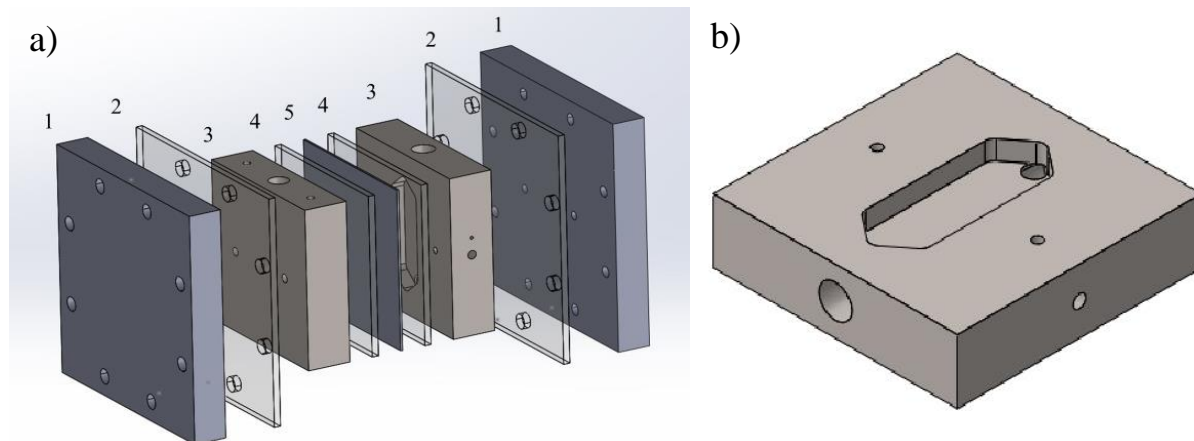
Figure 5.3. Illustration of the flow cell hardware with 1) the external parts for compression of the different pieces 2) gaskets for sealing, 3) current collectors 4) gaskets for sealing and separation of the positive and negative side, 5) ion selective or porous membrane as a separator. On the right, a scheme of the current collector design.

The end plates used to compress and maintain the structure of the RFB are made of stainless steel to distribute the mechanical force applied when screwing the cell. As stainless steel can conduct electricity, these pieces of the cell are isolated from the current collectors and electrodes with a gasket made of PTFE (polytetrafluoroethylene). The current collectors are made of titanium to be chemically resistant to the electrolytes, with a chamber for the insertion of the porous electrode. The original material of the current collector was based on carbon material; however, degradation of the carbon support was noticed with the ACN and PC solvents. It is known that PC is reactive with graphite inside Li battery and the degradation of PC and graphite can occur.[6–9] Consequently, titanium is chosen for the current collector for its chemical resistivity, but also to facilitate the mechanical cleaning of a more robust current collector (for example with sandblasting). The design of the current collector is made to have the flow of electrolyte coming directly through it without crossing any other components of the cell. The initial flow of the liquid inside the cell was constructed with tubing going through both external parts and current collectors. In a way to avoid possible leakages, the tubing are directly connected to the current collector to wet the electrode in the defined chamber. The separation and electrical isolation between the current collectors is ensured by the ionic membrane and expanded PTFE gasket (24SH-ePTFE gasket sheets, 1 mm, from TEADIT).

In Fig. 5.4b and 5.5, the full RFB is represented with the connections between the electrolyte tanks and cell, and pumping by the peristaltic pumps. The tubing (Masterflex Solve-Flex, from Cole-Parmer), gaskets and connectors for the tubing that are in contact with the electrolyte need to be chemically resistant to the solution, particularly to the ACN. From different chemical resistance tables for ACN, fluoropolymers and olefin polymers are the most suitable choice for the material of the plastic parts of the battery.[10–12] Three main types of polymers are used in the final set-up: PTFE, PE (polyethylene) and EPDM (ethylene propylene diene monomer). Conversely, PS (polystyrene), PSF (polysulfone), PC (polycarbonate) and silicone need to be avoided for the Cu-ACN-PC system.

In Fig. 5.5a, The Ti current collectors are presented with their respective electrode: Cu foam for the side of the copper deposition and C-felt for the Cu(I) oxidation during the charge (Fig. 5.4a). The single cell is shown when compressed by the endplates in Fig. 5.5b. Additionally, the temperature of the cell can be managed with cartridge heaters, which are implemented in each side of the end plate and controlled by a PID controller that records the temperature in the endplates with a thermocouple.
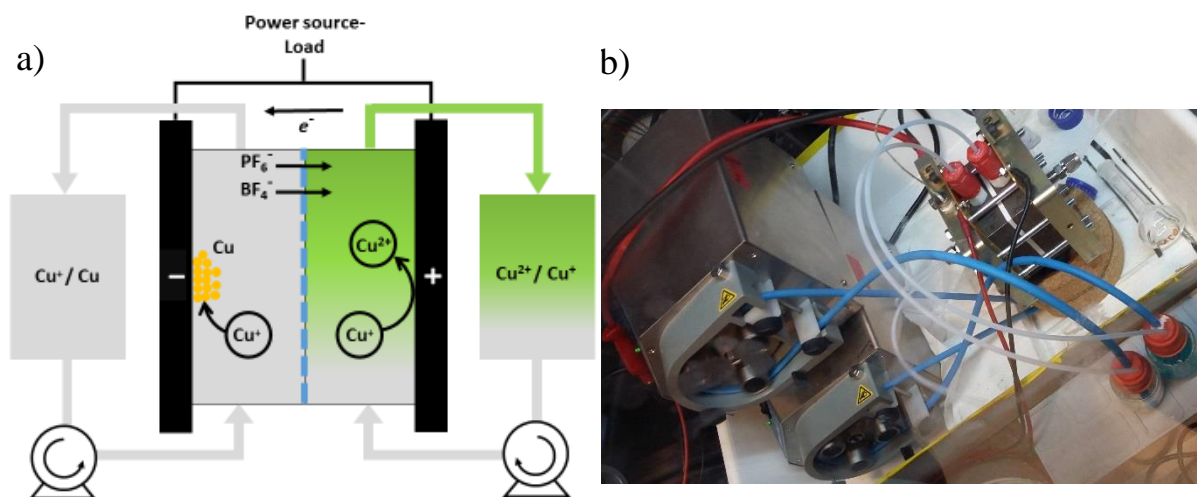
Figure 5.4. a) Scheme of the Cu-RFB during the electrical charging process, b) the real Cu-RFB system in the controlled inert atmosphere of a glovebox: two peristaltic pumps, cell and electrolyte tanks.
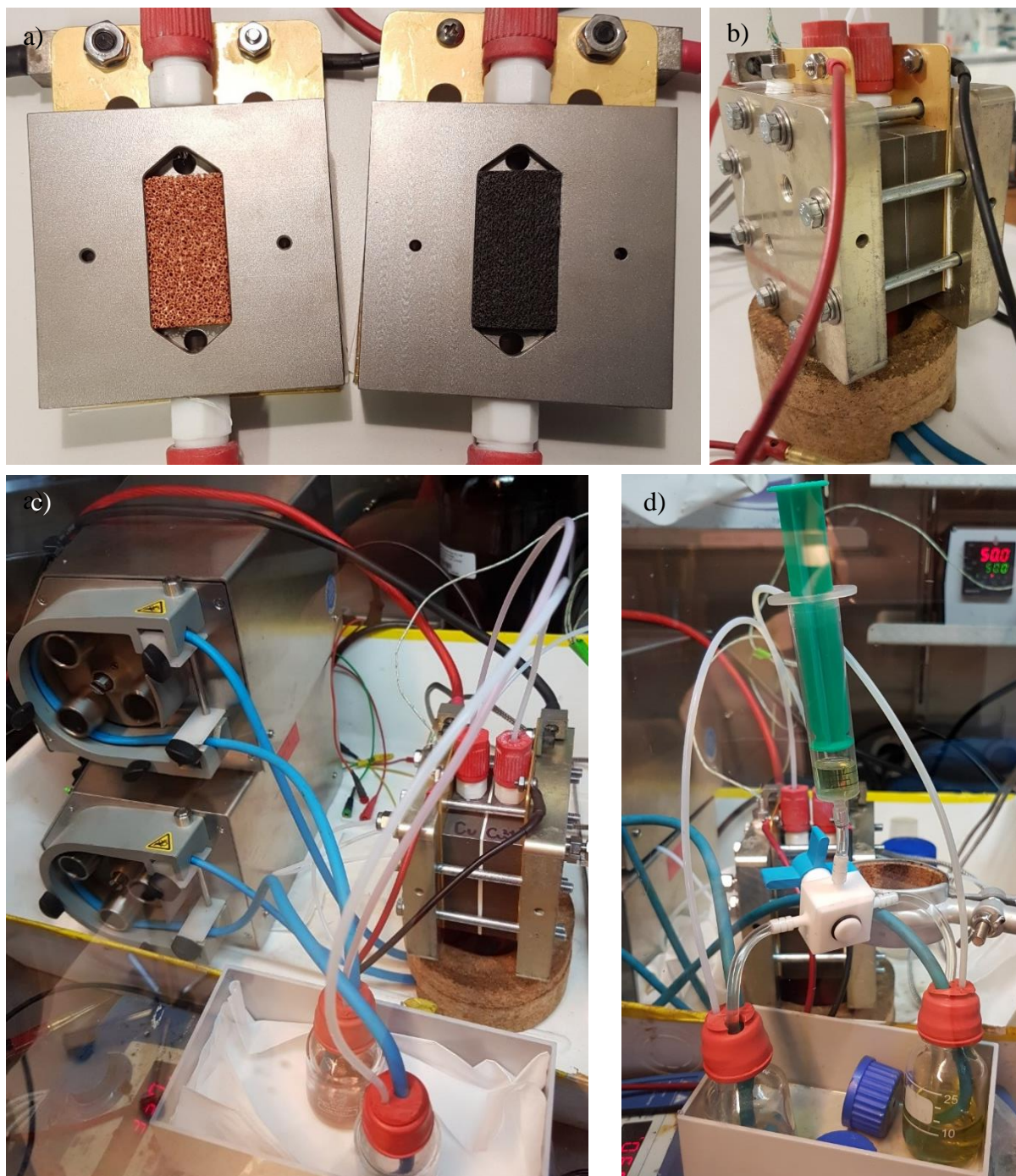
Figure 5.5. a) The Ti negative current collector with metallic Cu foam electrode and the Ti positive current collector with the C-felt electrode have been designed especially for the testing of the Cu-RFB. b) The compressed electrochemical cell is used for the flow experiment with an anionic membrane between the two electrodes. c) The complete set-up includes peristaltic pumps for the flowing of the electrolyte, typical flow rate are between 40-45 mL·min⁻¹. Tubing, O-ring and gaskets are made from polymers that can resist chemically to the organic solvent of the electrolyte like EPDM or expanded PTFE (Masterflex Solve-Flex from Cole-Parmer and 24SH-ePTFE gasket sheets from TEADIT). d) Connection between the (−) and (+) tank with a bridge of electrolyte.

5.   Membranes

The membranes are one of the most important layer in the assembly of the flow cell and are categorised here by their thickness, porosity, ion selectivity and composition. An effective membrane should satisfy two major criteria. First, it should play the role of a separator between the (−) and (+) side to avoid any short circuit. If both electrodes are connected by direct contact, no charge can be store in the system and no accumulation of Cu and Cu(II) is possible. Furtermore, any short circuit would create hot points and represent a safety hazard. Thus, the membrane should isolate both sides of the battery. However in the same time, it should also act as a salt bridge and should allow equilibrating the charges between the − and + side during the charge/discharge steps. Secondly, it should minimize the cross-over of Cu^{2+} into the negative side, as this reaction leads to self-discharge of the battery. In consequence, the membranes separate physically the electrodes and are permeable to ions to compensate the electron migration from one side of the cell to the other (Fig. 5.4a).[13]

5.1. Porous membranes

The tested membranes are listed in Tables 5.1 and 5.2 with their main characteristics and suitability for the Cu-ACN-PC system. In the optimized single flow cell, the main contribution to the cell resistance is assigned to the membrane between the positive and negative side. Among all the porous membranes listed in Table 5.1, almost none of them are satisfactory for the Cu RFB, if they are simply used as received. The nice advantage with these types of membranes could have been to reduce the price of the separator comparing to the ion selective ones[14,15] and to decrease the resistance of the cell for this non-aqueous RFB. However, the porosity and pore sizes in these membranes is too high, allowing uncontrolled and undesired crossover of Cu ions and fast self-dicharge.

An attempt to modify the porosity of the separator is done by deposition of PVC polymer on the PTFE filter membrane (Omnipore membrane filter from Millipore, Merck). With this technique, a layer of PVC is doctor bladed from a solution of 50 mg/mL in THF (tetrahydrofuran) on the PTFE support. The membrane is dried overnight at ambient

temperature and inserted in the RFB without pre-treatment. In Fig. 5.6a, two charge/discharge steps are shown for the Cu-RFB with this PVC-PTFE membrane. *iR*-corrected data is shown because the resistance between the cycles decreases significantly from 6.6 to 3.0 Ω. After these two cycles, no charge storage is possible and the resistance is even lower, corresponding to those of the bare PTFE filter (Table 5.1). The reason of the resistance diminution is assigned to the dissolution of the PVC layer by ACN and consequently, by the recovery of the initial pore size of the PTFE filter, leading to the crossover of Cu ion through the membrane and preventing the efficient changing of the cell. This effect is also visible between both charge/discharge operations with the decrease of the capacity that is recovered during the discharge (Fig.5.6a). The Coulombic efficiency is significantly lowered with the higher cross-over of Cu ions. However, the energy efficiency with no *iR*-compensation is better for the second cycle with weak capacity because the resistance of the modified separator has a better ionic conductivity. Even if the chosen treatment is not chemically stable and does not allow long-term battery cycling, it gives an indication that it should be possible to produce a membrane for organic RFB with a rather simple procedure. To improve the performance of the porous membrane, the deposition technique and the pore-filling polymer have to be developed further. Better control of the pore size, thickness of the additional layer and resistance of the final membrane could be obtained with an ink-jet printing method if an ink can be formulated.[16,17] For the chemicals, PVA (poly(vinyl alcohol)), PE, PP (polypropylene) or fluoropolymers should be targeted for more stability with ACN. Another possibility could be to transform the PTFE support into an ion selective membrane by filling the pores with ion exchange resins and a crosslinkers.[18–20]
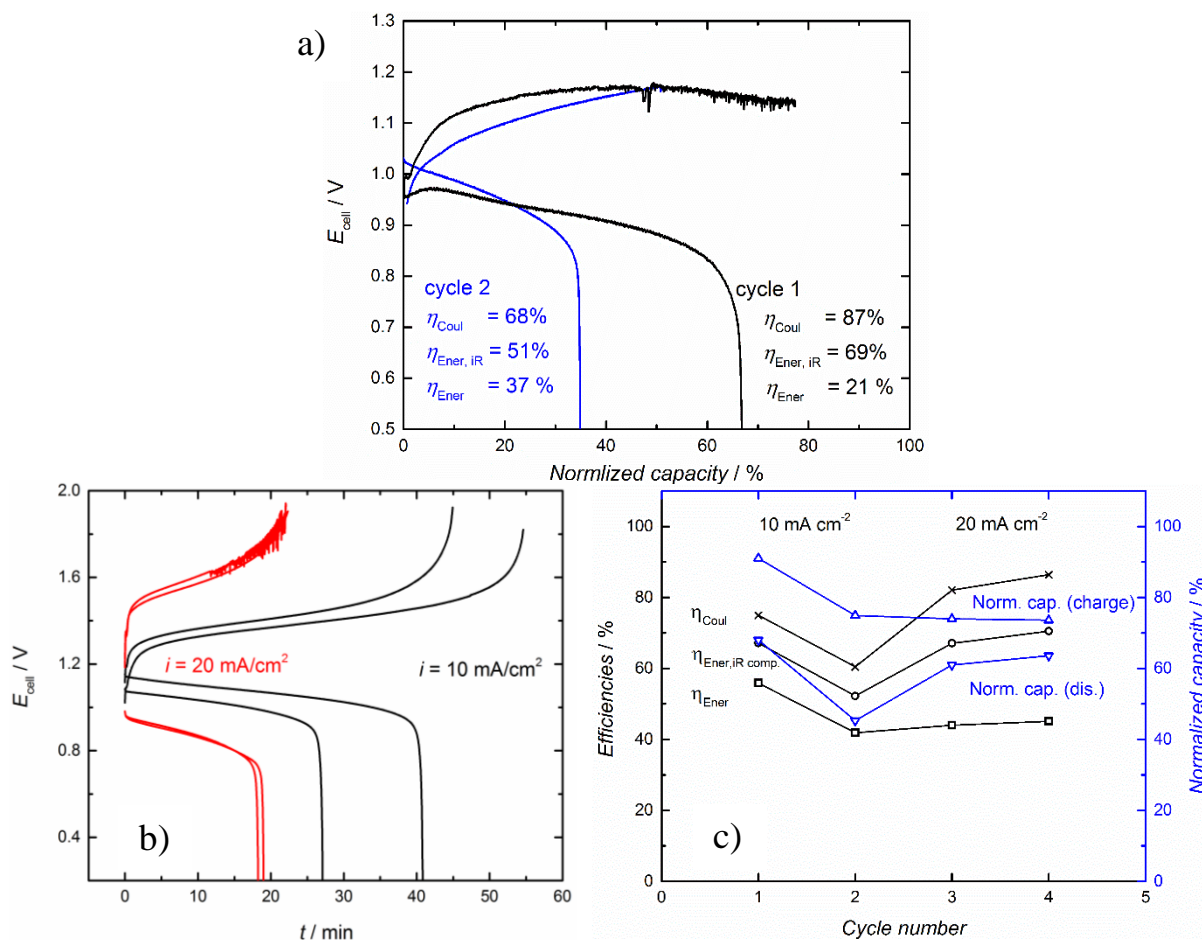
Figure 5.6. Cu-RFB with [Cu(CH$_3$CN)$_4$]BF$_4$ (0.15 mM) and 0.3 M (TEABF$_4$) in acetonitrile-propylene carbonate solvent (50 vol% of propylene carbonate). a) *iR*-corrected potential curves for i = 10 mA·cm^{-2} with modified Omnipore filter, b) potential curves without *iR*-correction at i = 20 and 10 mA·cm^{-2} with Zirfon membrane. c) Efficiencies and normalized capacities for the RFB with Zirfon membrane.

Another type of porous membranes has a potential applicability for the Cu-RFB: the Zirfon Perl membrane (from Agfa) that is composed of a PSU type (polysulfone) organic mesh with an inorganic coating of zinc oxide and ZrO$_2$. These membranes are typically applied as separators for the alkaline water electrolysis.[21–23] With this membrane, few cycles are possible and are presented in Fig. 5.6b with no *iR*-correction to show the nice behaviour of the membrane regarding the resistance of the system (1.3-1.8 Ω). Two different current densities are used to perform the cycling; a clear difference is observable with a faster charge and a larger potential gap between charge and discharge curve for the high current density. Following the Ohm's law, the loss of potential during high current discharge implies losses for the energy efficiencies and should result in lower energy efficiencies. However, the energy efficiencies are quite comparable at 10 and 20 mA·cm^{-2} because the loss of capacity of the RFB is more significant when lower current is applied (Fig. 5.6c). The low Coulombic efficiency observed at 10

mA·cm^{-2} is attributed to the crossover of Cu ions, which have more time to diffuse through the membrane during the longer cycling process with a smaller electric current. These losses also affect the capacity.

Even if the cycling of the Cu-RFB is acceptable with the Zirfon membrane, the stability of the membrane is again an issue and does not allow long-term cycling of the Cu system. The last noisy charging step in Fig. 5.6b is showing the difficulty to accumulate Cu and Cu(II) on each side of the cell. After this process, the RFB was not able to charge the electrolyte anymore. To prevent the diffusion of Cu species, a Cu-RFB with two layers of Zirfon was tested. The disadvantage of adding more layers is the increased resistance of the whole cell. Indeed, it will be more difficult to cross the physical barrier also for the supporting electrolyte. By impedance spectroscopy and chrono-potentiometry, the resistance of the cell was approximated around 1.0-1.7 Ω for one layer of the Zirfon membrane. For the doubled one, this resistance is around 2.0-4.0 Ω. The typical resistances during the cycling are 3.5 to 3.9 Ω, resulting in *ca.* 0.3 V of *iR* losses for 10 mA·cm^{-2}, which is already larger than what was obtained with anionic membranes (see below). Nevertheless, this time, the cycling of the RFB can be done for a long time with a porous membrane (Fig. 5.7).

From the different cycling tests, the set-up with two membranes looks quiet promising because around 50 cycles are characterized with two different current densities (5 and 10 mA·cm^{-2}). With 20 mA·cm^{-2}, the voltage difference between the charge and discharge was too large to be considered as a good cycling. In Fig. 5.7a, the 10 first cycles at 5 mA·cm^{-2} (Fig. 5.7b) exhibit high Coulombic and energy efficiencies when the *iR* drop is corrected (*CE* = 94-96 % and *EE* = 81-84 %). The solvent crossover can already be observed and is relatively important already after the ninth cycle with a normalized discharge capacity decreasing from 90% to 65%. By balancing the volume of the tanks, the capacity of the RFB can be recovered easily as it is shown in the 10th cycle in Fig. 5.7a-b. This possibility to access again to a high state of charge (SOC) after the rebalancing is a good sign regarding the Cu migration through the membrane, because if the SOC close to 100% can be reached, no relevant loss of Cu is present. In the case of the doubled Zirfon membrane, the crossover is different than for the other porous membrane that are not able to store chemical energy (permeable to Cu ions) and arises for the slower diffusion of the ACN with multiple cycles. The volume imbalance is happening in the opposite way as with anionic membrane and the volume of the (−) tank is larger after charging than the positive one.

With higher current (10 mA·cm^{-2}), the energy efficiency is lower than before (*EE* = 70-75) which is expected with a larger gap of voltage for the charge/discharges curves (Fig. 5.7c). However, the *iR* compensation keeps the *EE* in a good range for the Cu RFB. The SOC is a bit lower than expected probably due to an imprecise balancing of the volume of the tanks after the previous measurements. In Fig. 5.7c, the capacity decreased down to 45% of the maximal capacity of the cell after the 38th cycle.

For the last 13 cycles, a bridge between the two tanks is implemented to decrease the solvent crossover through the membrane and to have a better equilibrium of the osmotic pressure (image of the set-up with connection between in Fig. 5.5d). A specific attention needs to be taken when the bridge is filled with the electrolyte and gas bubbles that will insulate the system have to be avoided. In Fig. 5.7d, the bridge between the two sides of cell tanks works. The capacity is more stable than before and less charge is lost because of the crossover with time. Here the real capacity is higher than before, because the volume of electrolyte had to be increased to make a good bridge. Several observations indicates that the connection worked:

- Capacity stability,

- Resistance of the cell is lowered due to the contact between the two sides (R = 3.2-3.5 Ω with the tank connection),

- Charging steps are noisy probably because a gradient of concentration needs to be built through the junction,

- Coulombic efficiency is smaller than before because some Cu ions can flow through the bridge between the tanks.
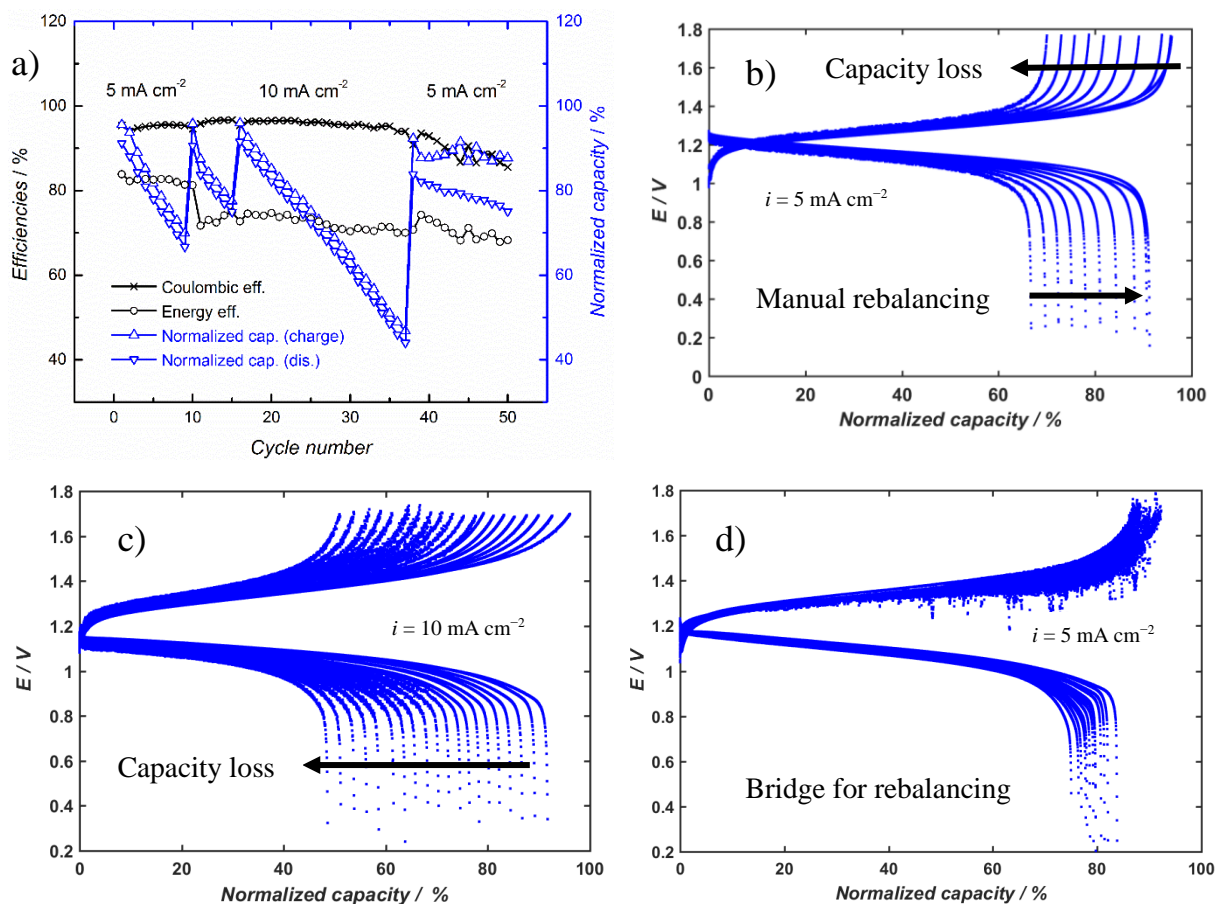
Figure 5.7. Cu RFB with 0.15 M [Cu(ACN)$_4$]BF$_4$ and 0.3 M supporting electrolyte (TEABF$_4$). Membrane is composed of two Zirfon Perl layers (Agfa). a) Efficiencies and normalized capacities for the RFB. b) First 10 cycles (*iR* corrected curves) with manual balance of the tanks volume for the last charge, at constant current, $i = \pm 40$ mA (5 mA·cm^{-2}). c) 20 cycles (16th-48th) (*iR* corrected curves) at constant current, $i = \pm 80$ mA (10 mA·cm^{-2}). d) Last 13 cycles (*iR* corrected curves) at constant current, $i = \pm 40$ mA (5 mA·cm^{-2}), with connection between + and − tank to decrease the losses of capacity.

Table 5.1. Porous membranes tested for Cu-RFB. Information for the porosity, material and thickness are taken from the supplier product description.

Name	Material	Pore diam./ nm	Porosity / %	Thickness/ μm	Cell R/ Ω	Suitable for Cu-RFB	Remarks
Celgard 2400	PP monolayer	43	41	25	0.4-0.8	NO	porosity too high
Celgard 2500	PP monolayer	64	55	25	0.4-0.8	NO	porosity too high
Celgard 3401	PP + surfactant coated	43	41	25	0.4-0.8	NO	porosity too high
Celgard 3501	PP + surfactant coated	64	55	25	0.4-0.8	NO	porosity too high
Zirfon Perl (Agfa)	PSU + coating (ZrO$_2$ +polymers)	150 [23]	55	500	1.0-1.8	YES	up to 130°C, only few cycles possible
Zirfon Perl 2 layers	PSU + coating (ZrO$_2$ +polymers)	-	55	1000	3.0-4.0	YES	up to 130°C
Omnipore membrane filter	PTFE (Merck Millipore)	100	-	30-85	0.2-0.8	NO	up to 130°C
modified Omnipore filter	PTFE + PVC	<100	-	<500	1.2-35	More tests needed	deposition technique with more control

Table 5.2. Ion selective membranes tested for Cu-RFB. Information for the type, material and thickness are taken from the supplier product description.

Membrane	Type	Material	Thickness/ μm	Cell R/ Ω	Suitable for Cu-RFB	Remarks
FAB-PK-130 (Fumatech)	anionic	polymer + PEEK reinforced	110-130	2.0-3.0	YES	not produced any more by supplier
FAA-PK-130 (Fumatech)	anionic	polymer + PEEK reinforced	110-130	2.0-3.0	YES	seems more sensitive to elevated temperatures
FAPQ-3100-PF (Fumatech)	anionic	polymer + PTFE reinforced	90-110	2.0-3.0	YES	
FAP-330-PE (Fumatech)	anionic	polymer + PE reinforced	24-32	1.0-1.7	YES	
VANADion 20 (Ion Power)	cationic	Nafion	225-275	0.5-1.0	NO	permeable to Cu ions

5.2. Ion-selective membranes

In Table 5.2, all the tested anionic membranes are shown to be suitable for the Cu-RFB in organic solvents. Theses separators need to be reinforced with a polymer, which can resist chemically to ACN. For the long-term cycling procedure (Fig. 5.8), the Cu RFB is built with the FAP-330-PE anionic membrane reinforced with PE, due to its availability, resistance to temperature and slightly lower cell resistance with its thinner thickness. The cationic perfluorosulfonic Nafion type membranes are not appropriate for the Cu electrolyte containing no proton in solution. If an aqueous and acidic environment is wetting the cationic membrane, the proton hopping is driving the diffusion from one sulfonated group to the other.[24–30] However, in the organic environment of the ACN-PC system, the separator is not specific enough to the cation of the supporting electrolyte and Cu cations can freely diffuse in both tanks of the RFB.
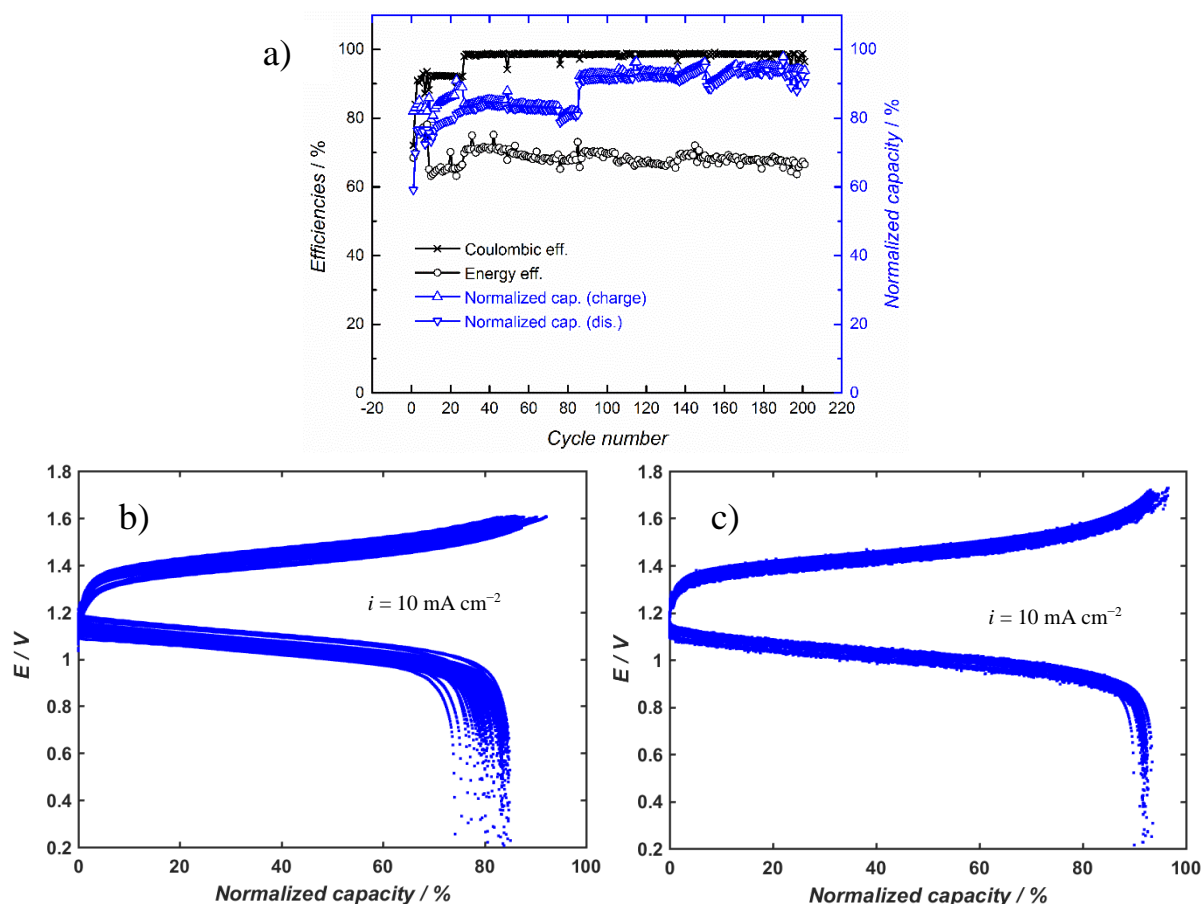
Figure 5.8. Cu RFB with 0.15 M [Cu(ACN)$_4$]BF$_4$ and 0.3 M supporting electrolyte (TEABF$_4$) with FAP-330-PE anionic membrane and connection between tank, $i = \pm 80$ mA (10 mA·cm^{-2}). a) Efficiencies and normalized capacities for the RFB. b) Charge/discharge cycles (*iR* corrected curves) with targeted SOC of 80-85%. c) Charge/discharge cycles (*iR* corrected curves) with targeted SOC of 90-95%.

The test for long-term cycling process of the Cu RFB is done with the optimized set-up and the FAP-330-PE anionic membrane. The charging process is applied electrochemically at a constant current (10 mA·cm^{-2}) with two different SOC of 80-85% for the first 80 cycles (Fig. 5.8b) and 90-95% for the last ones (Fig. 5.8c). In Fig. 5.8a, the stability of the cell efficiencies and capacities is reached by the addition of the connection between both tanks. The energy efficiency is stable during the 200 *iR*-corrected cycles with an averaged value of 68%. No specific modification of the resistance is noticed during the long-term test of the cell within the interval of 1.2-1.7 Ω. After the 26th discharge, the coulombic efficiency is slightly improved because the bridge for the equilibration of the ACN migration is purged due to the presence of interfering bubbles in the tubing. Regarding the SOC, the capacity of the cell is increased by targeting a higher cut-off voltage before the switch from the charge to the discharge step. This effect is visible in Fig. 5.8a after 80 cycles when the SOC is around 90% with an increase of the cut-off potential of 0.1 V.

After the 200 cycles, the C-felt electrode and Ti current collector at the positive side of the cell seems to not have suffered any damages. Oppositely, a strong modification of the shape and morphology of the Cu foam electrode is observed. The Cu negative electrode lost 19% of its initial weight after more than 200 cycles (Fig. 5.9). The part of the electrode which is the most damaged is in the middle of the side next to the membrane where the distance between the two electrodes is the smallest (Fig. 5.9a-b). The repetition of the deposition and stripping on the negative side during the charge and discharge, promotes the degradation of Cu structure and the irreversible detachment of Cu particles (Fig. 5.9a-b). Comparing to the initial treated Cu area (Fig. 5.9d), the surface is either relatively homogenous with the stripping/deposition on the whole surface (Fig. 5.9e), or the nucleation takes place on a specific place of the electrode surface (Fig. 5.9f). Consequently, as the Cu is growing on a defined area, Cu crystallites are formed on the surface of the copper in a specific direction (Fig. 5.9f). With the flow of electrolyte and the stripping to recover the Cu(I), the crystallites can break and an irreversible loss of material appears with some detached Cu particles in the negative tank. Another side effect of the orientated Cu crystal growth is the possibility to connect the negative side with the positive side, leading to a short circuit where no charge can be accumulated and only a current is flowing is the system.
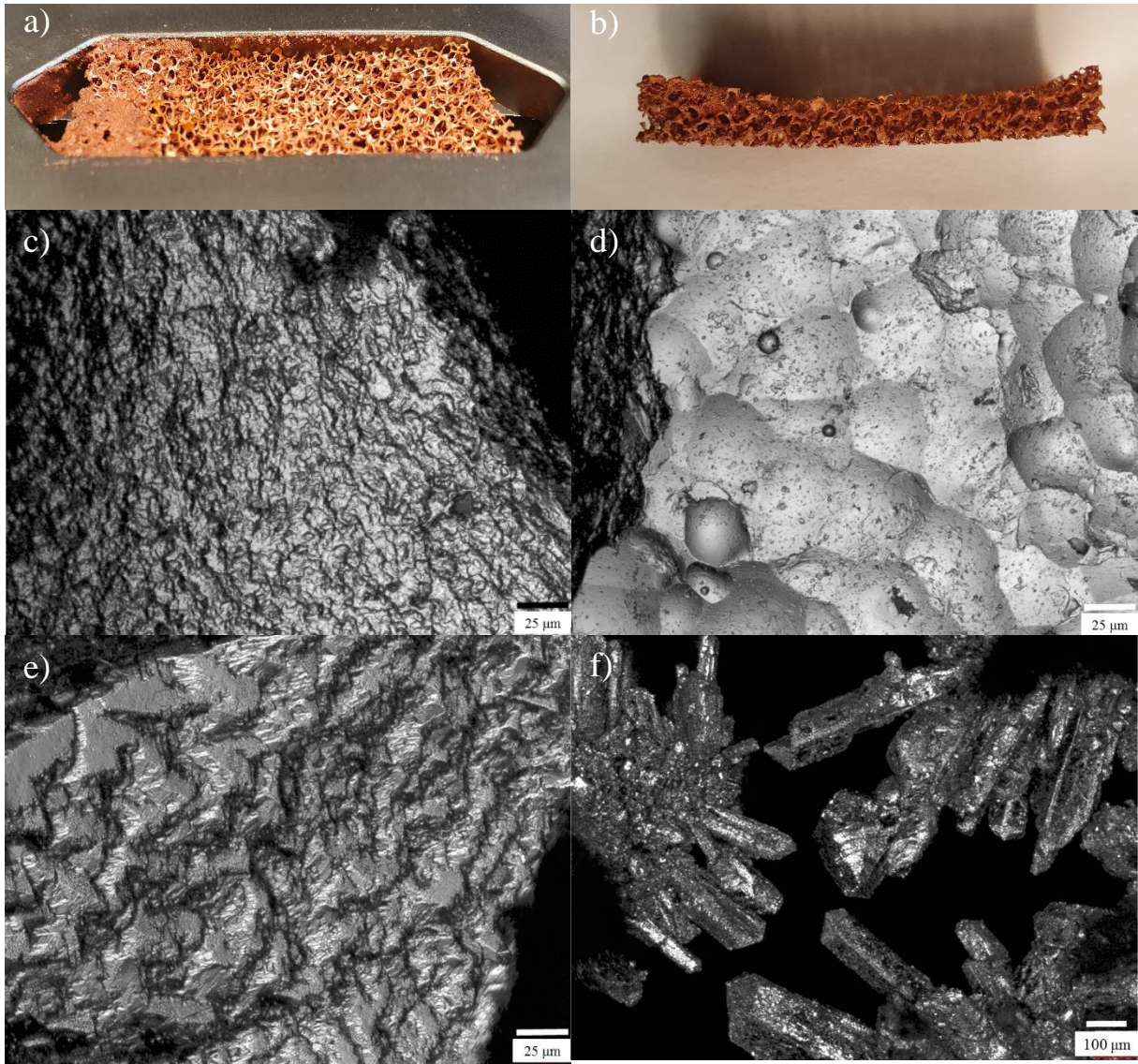
Figure 5.9. Images of the negative Cu foam electrode after 200 cycles. a) Directly after the disassembly of the cell in the Ti current collector. b) Degradation particularly in the middle of the electrode. c) Laser microscopy image of the raw Cu foam surface. d) Laser microscopy image of the pre-treated Cu foam surface with sandblasting technique to remove the oxide layer. e) Laser microscopy image of the Cu foam surface after 200 cycles in the centre of the electrode and f) on the side of the electrode with preferential nucleation direction.

6. Negative side

From the different Cu RFB tests, the key element of the cell is the Cu(I)/Cu side. The deposition/stripping reaction is the electrochemical process, which limits kinetically the charging process with the standard heterogeneous rate constant of $0.05 \cdot 10^{-5}$ cm·s^{-1} *vs.* $6.4 \cdot 10^{-5}$ cm·s^{-1} for the Cu(I) oxidation. Furthermore, the constant degradation of the porous Cu electrode is an issue for the cost and stability of the battery cycling. The ideal component for the negative electrode of the battery seems obviously to be metallic Cu for a fast and instantaneous deposition from the Cu(I) solution as developed in Chapter III. Here, two alternatives for mitigation of the corrosion of the negative electrode are proposed: a porous reticulated vitreous carbon (RVC) electrode with a Cu plated layer and a Cu slurry electrode.

6.1. Cu plated RVC electrode

The electrochemical deposition of Cu on a conductive surface by the reduction of a Cu salt is commonly done in acidic aqueous solution. The bath, which is used for the plating of the RVC network, is composed of sulphuric acid (H_2SO_4, 2.2 mol·dm^{-3}), copper sulphate ($CuSO_4$, 0.3 mol·dm^{-3}), sodium chloride (NaCl, 1.4 mmol·dm^{-3}), polyethylene glycol (PEG, 1.0 g·dm^{-3}) and a sulfonated thio-compound ($NaSCH_2CH_2CH_2SO_3H$, $3.8 \cdot 10^{-6}$ mol·dm^{-3}). This bath formulation was previously described by E. Thompson and M. Goodenough *et al*.[31–35] $CuSO_4$ is the source of Cu(II) cations that will be reduced to metallic Cu on the C support; the acidic conditions with H_2SO_4 should prevent the presence of too much Cu oxides on the deposited surface and plays the role of the conductive supporting electrolyte.

In Fig. 5.10a-b, the deposition/stripping of Cu(II)/Cu is characterized electrochemically by a three electrode set-up with the RVC support as WE and a self-made RE (Cu wire, $CuSO_4$ (0.3 mol·dm^{-3}) NaCl (1.4 mmol·dm^{-3}) and H_2SO_4 (2.2 mol·dm^{-3})). During the deposition process, if a homogenous deposition of the Cu on the WE is needed, the CE electrode has to surround the WE to avoid a preferential direction and a specific area of the Cu growth. The CE is made of a bended Cu plate in cylindrical shape (height = 3 cm and diameter = 4 cm) and is immersed in the bath around the WE and RE. The hysteresis of the deposition

current curve starting at 0.01 V (*vs.* Cu(II)/Cu) is a characteristic of the Cu(II) reduction with Cl⁻ in the electrolyte (Fig. 5.10a). Cl⁻ can also form Cu(I) complexes and, when Cl⁻ is added alone to the acidic Cu(II) bath, the deposition of Cu is promoted.[36] However, Cl⁻ and PEG together in solution are two additives that are known to inhibit the Cu deposition on a conductive surface with the formation of an adsorbed layer on the electrode.[31,35,37,38] The advantage to add both PEG and chloride is to obtain a uniform deposition of the Cu layer, avoiding dendrites or other 3D structures formation.
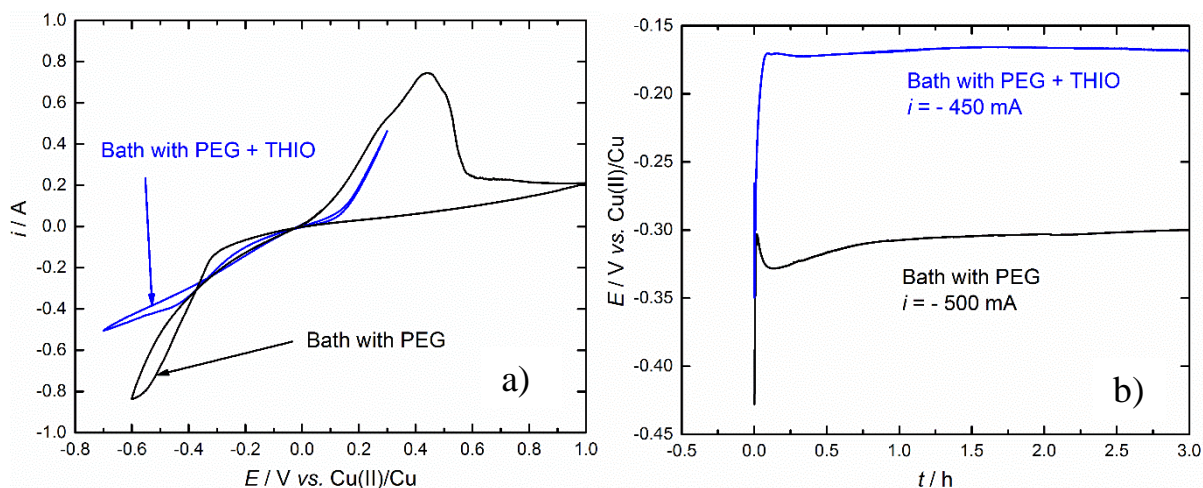
Figure 5.10. a) CV for the deposition/stripping on the RVC WE with the bath without and with the thio sulfonated additives. b) Chronopotentiometry for the Cu deposition during 3 hours with the same baths.

In the complete electroplating bath, the 3-mercaptopropylsulphoinc acid reacts with Cu(II) and oxygen in solution to form, respectively a Cu(I) complex with the thiolate compound (Cu(I) $SCH_2CH_2CH_2SO_3H$) and $(SCH_2CH_2CH_2SO_3H)_2$.[32] The thiolate molecule is considered as a brightener because the stabilization of the Cu(I) thiolate complex is important intermediate for the good aspect of the plating.[33] In Fig. 5.10b, three steps can be observed during the deposition of copper at constant current. The deposition of the first layer of Cu occurs almost directly when the current is applied.[39,40] Thus, after few seconds, the overpotential decreases rapidly because the plating of Cu on itself is facilitated compared on RVC. For the full bath with the thiolate brightener, a constant plateau for the overpotential is reached during the continuous plating of Cu. Regarding the bath without this additive, the plateau for the deposition at constant overpotential happens later (Fig. 5.10b). After the deposition of the first layer, additional negative overvoltage is required to maintain the Cu plating at the same current. This probably highlights the difficulty to nucleate some specific areas of the WE, which need higher

potential to be plated. Even if specific functions and chemistry are given for the different additives, it is strongly believed that they interact all together in a way to optimise the levelling effect for a homogenous initial Cu plating of the RVC followed by constant growth of the layer.

Different SEM images are recorded for the plating of Cu on RVC with various bath formulations and secondary electron detection is applied for the visualization of the topography of the deposition (Fig. 5.11). The Fig. 5.11a-b with only $CuSO_4$ and sulfuric acid as a bath show a non-uniform plating with preferential nucleation sites and orientation. In Fig 5.11b, small nucleation sites are visible with a size around 100-300 nm. Addition of PEG alone still produces some dendrites on some edge of the electrode (Fig. 5.11c); however, the plating in the centre of the RVC WE is slightly smoother (Fig. 5.11d). When PEG and NaCl are included in the electroplating bath, crystallites with a preferential orientation are detected instead of dendrites and the Cu layer is more homogenous (Fig. 5.11e-f). The levelling effect with the film formation of the PEG + NaCl can be observed in these two images. The final deposition with all additives is shown in Fig. 5.11g-h and shows no preferential nucleation orientation even on the edge of the RVC structure (Fig. 5.11g). Furthermore, no nucleation sites are detected in Fig. 5.11h compared to the simple acidic Cu(II) bath.

The RVC structure with an electrodeposition treatment for the addition of a Cu layer is used as the negative electrode in the Cu RFB (Fig. 5.12b). The efficiencies and stability of the RFB with these types of electrode have lower performance than the optimized cell design with the Cu foam electrode. In Fig 5.12a, the decay of the Coulombic and energy efficiency is attributed to the degradation of the Cu layer with time. As it is shown previously with the long-term cycling, the pure Cu electrode already suffers a lot of degradation after more than 200 cycles. The Cu on the RVC network is more affected to the repetition of the deposition/stripping steps and as less Cu is contained in the RVC than in a pure Cu electrode, the deterioration of the cycling is faster. However, the cycling of the cell is possible with this set-up and allows considering the C support with plated Cu as an alternative for the negative electrode. If the electrode is further developed and becomes more stable, it could be economically advantageous to use Cu plated C-based electrode in the RFB.
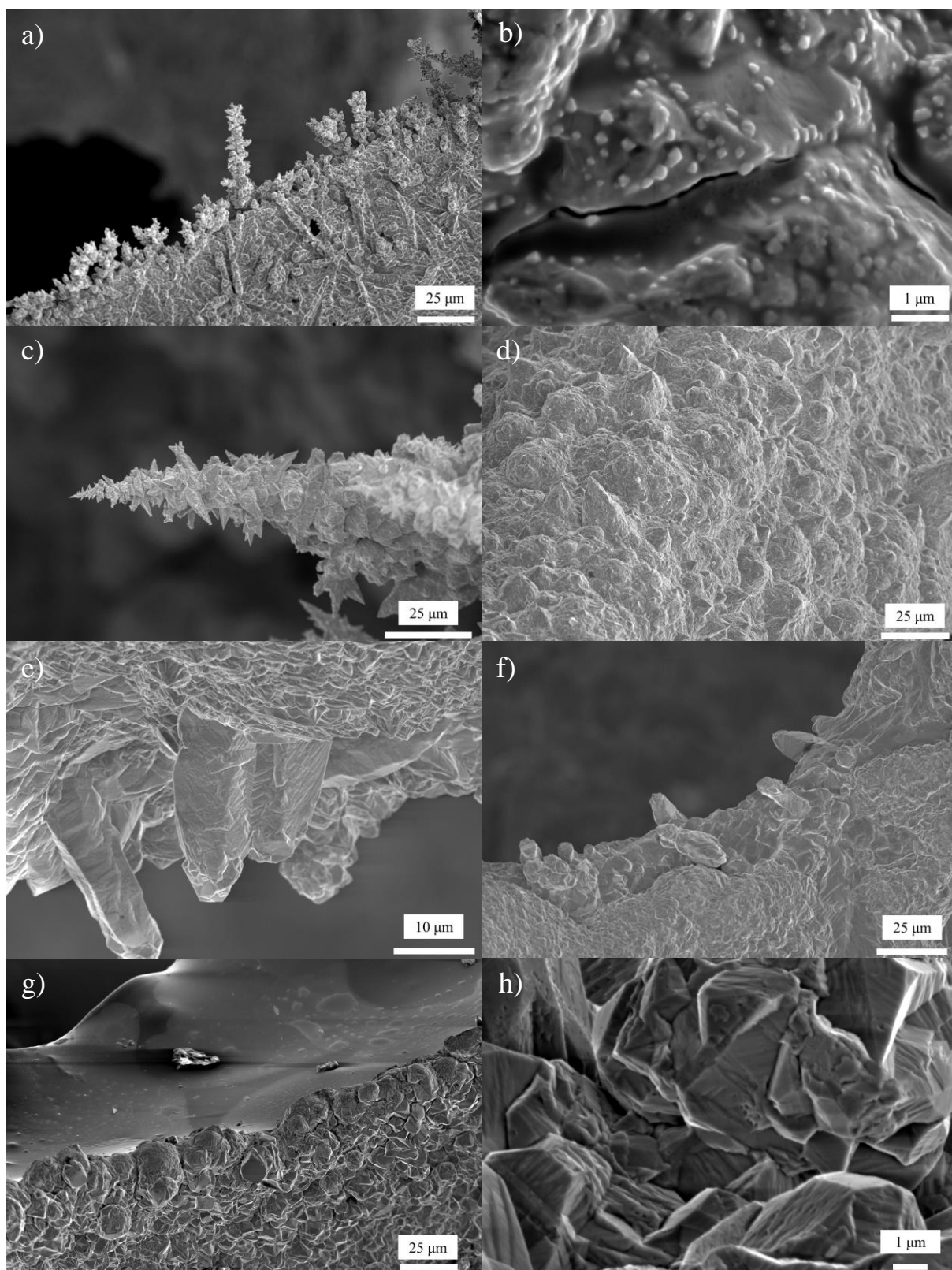
Figure 5.11. SEM images of the RVC electrode after Cu plating on the surface, SE detection at 0.8 nA and 8kV, with acidic Cu(II) bath (a-b) without additives, (c-d) with PEG, (e-f) with PEG and NaCl, (g-h) with all additives. For image g, the upper part is bare RVC and Cu layer in the lower part of the picture.
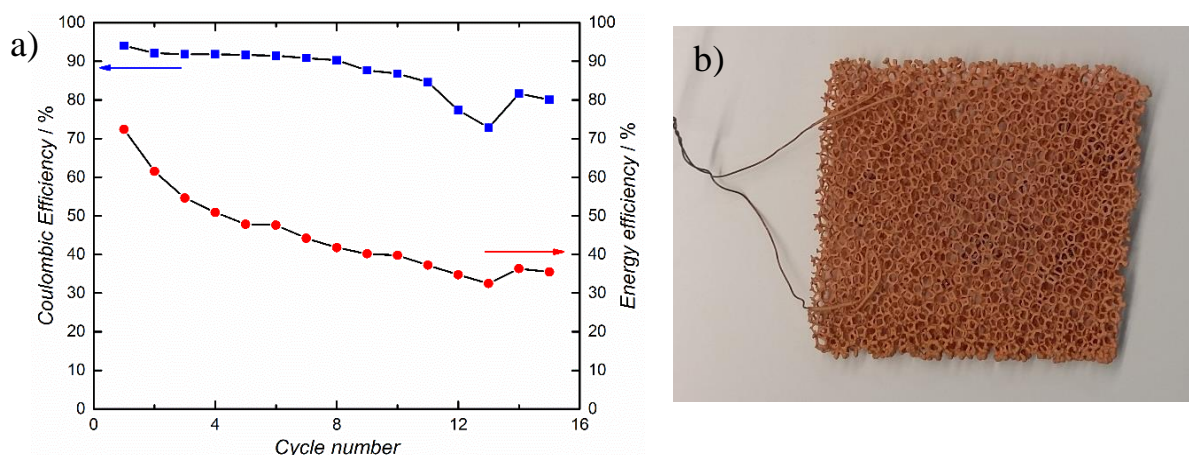
Figure 5.12. Cu RFB with 0.15 M [Cu(ACN)$_4$]PF$_6$ and 0.5 M supporting electrolyte (LiPF$_6$) with FAB-PK-130 anionic membrane, $i = \pm100$ mA (10 mA·cm^{-2}). a) Efficiencies for the RFB. b) Image of the Cu-RVC electrode made by electrodeposition.

6.2.   Slurry electrode

Another option for the modification of the negative electrode of the RFB is to use a slurry electrode. Slurry electrodes are defined as particle suspensions in the electrolyte, which are electronically conductive and able to form an electrically conductive network in the solution if a high enough volume percentage of particles is reached.[41] In the Cu RFB, the slurry flows on the negative side and will be in electrical contact with the current collector. The size and concentration of the particles in the electrolyte are important to control its viscosity and conductivity. The interest for the Cu cell is obviously to deal with the Cu plating. With the Cu slurry, the metallic Cu can be deposited electrochemically on the Cu surface of the particles from the reduction of Cu(I). This type of electrode allows decoupling of the storage capacity from the power, as they can be stored in the negative tank.[42] Previously with solid electrode, the Cu was kept deposited on the electrode, which could be a disadvantage if massive quantity of Cu is produced during the charging of the cell.

6.2.1. Synthesis of the Cu particles

For Cu particles synthesis, a large choice of techniques can be applied depending of the targeted size, morphology and oxidation state of the particles.[43] In this work, the Cu powder is produced by the so-called cathodic corrosion method, which is described by M. Koper *and al.*[44,45] This process is classified under the wet chemistry method for nanoparticles production, because the metal synthesis occurs in solution. During the corrosion technique, a high voltage (± 10 V) is applied between two Cu wires, which are immersed in a conductive bath, and the polarization of the DC current at each electrode is switched from (+) to (−) at high frequency (100 Hz). The violent electrical conditions at the Cu wire induces its corrosion and the formation Cu NPs in solution.

The destruction of the wires to NPs is relatively fast but requires a constant manual insertion of both wires in solution to continuously produce Cu suspension. As the slurry electrode needs high content of Cu particles, the focus of this work is to have a system, which is able to synthesise the metallic particles at constant rate. In Fig. 5.13a-b, the automatised metal corrosion set-up is represented with a motor that induces the smooth and steady immersion of a thin Cu wire in the electrolyte. The speed of insertion of the thin Cu wire can be tuned in the range of 2-8 mm·min^{-1}. In the motorised corrosion machine, only one wire is treated to give NPs, the second electrode is a larger Cu electrode that is simply present to act as a CE. The thin Cu wire is connected to the electrical circuit by one of the rollers, which is linked to the power supply and, in the same time, is pushing down the wire in the bath for corrosion. During the synthesis, a stream of nitrogen is provided to avoid the oxide formation and the bath is cooled with water due the heat generation during the wire corrosion. Furthermore, addition of PVP (polyvinylpyrrolidone) and constant stirring of the solution are required to mitigate the Cu particles agglomeration. Several failures happened during the optimization of the set-up: bad electrical contact of the conductive roller produces formation of electric arcs, or the Cu wire goes out of the expected path and damages some plastic parts of the machine. However, the installation was modified to give a stable Cu corrosion and, in Fig. 5.13c, the Cu NPs suspension is shown with the brown colour of the solid Cu in the bath. In the same picture, bubbles of O_2 and H_2 are visible on the Cu due to high potential difference between both wires.

Various baths were tested for the Cu NPs production in aqueous and organic solvents. As the Cu battery is working with an electrolyte based on an organic solvent composition, water

should be avoided in the system for the stability of Cu(I) ions. Therefore, baths with TEABF$_4$ 0.5M in ACN and TEABF$_4$ 0.2M in methanol can produce Cu particles that have a low water content. However, the corrosion was very slow and the Cu NPs amount that can be collected was not sufficient for the formulation of a slurry electrode. The final bath composition is made of 1M H$_2$SO$_4$ and 1 wt% PVP in water. Consequently, before to implement the Cu particles in the RFB, they need to be cleaned to remove water. For this purpose, the final Cu suspension is centrifuged and washed with ACN several times before to be dried under vacuum.
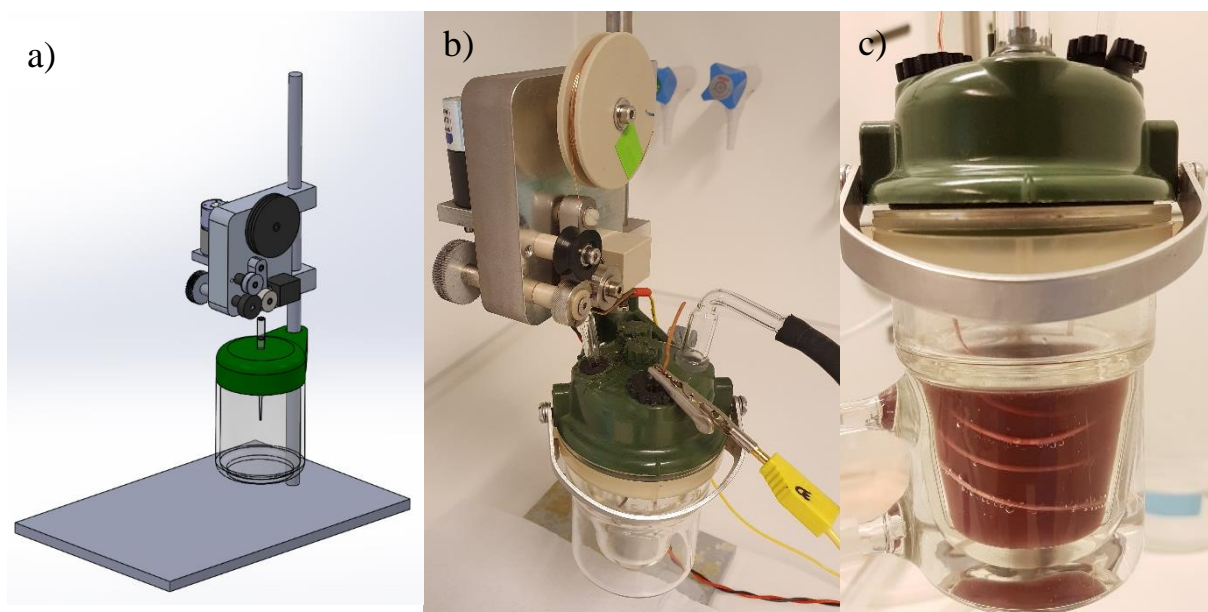
Figure 5.13. a) Scheme of the motorized set-up for Cu NPs synthesis by corrosion method. b) Image of the same system. c) Image of the Cu NPs suspension in the bath for Cu corrosion (1M H$_2$SO$_4$ in water).
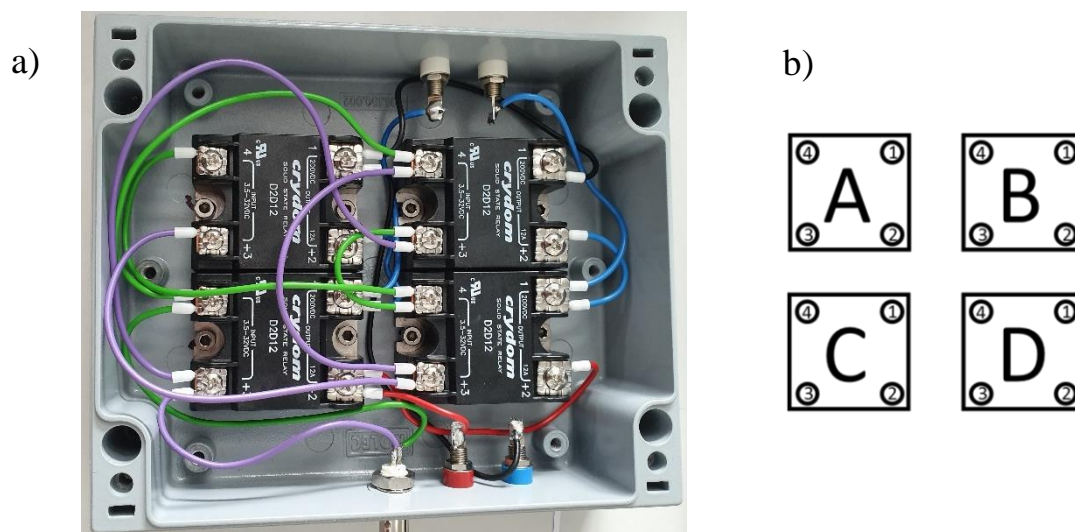
Figure 5.14. a) Image of the 4 relays for the switch of polarization between the corroded wire and the counter electrode. b) Schematic representation of the 4 relays.

The electronic circuit is the key part of the set-up and is briefly explained in this paragraph. The electronic system is composed of one power supply, one function generator for the tuning of the DC current and 4 relays (Fig. 5.14). The function generator module gives the frequency of the polarization modification at the Cu wire and the square wave shape for the DC current. The circuit presented in the Fig. 5.15 imitates an AC current with the utilization of a DC source. When the function generator activates the relay A and D (red path in Fig. 5.15a), the current from the power supply can cross these relays and the left output connection is negatively polarized and the right is positively polarized (red sign in Fig. 5.15b). In the opposite way, the activation of the relay C and B (black path in Fig. 5.15a) induces the other polarization at the Cu wires. This system produces the modification of the polarization at both Cu wire and with the high frequency for the Cu corrosion in the electrolyte.
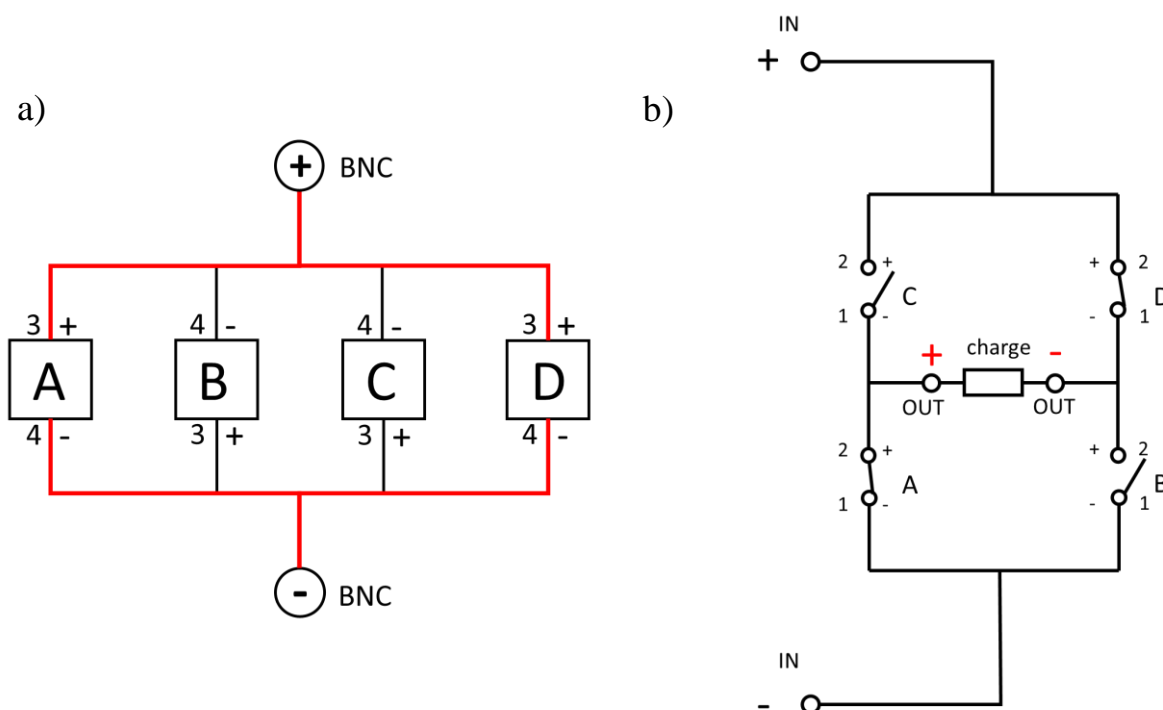
Figure 5.15. a) Electrical scheme for the opening of the gates in the relays A and D. b) Electrical scheme for the output of the DC current with a square wave function.

6.2.2. Characterization of the Cu particles

The solid Cu powder was imaged with SEM and a range of NPs going from 15-250 nm is detected in Fig. 5.16a-b. The smallest size of the NPs analysed by SEM corresponds to the predicated size domain of the crystallites with a single phase determined by XRD. Comparing to M. Koper *and al*., the size of the NPs is larger than their average value of 5.2 nm.[44,45] The difference arises from the different choice of corrosion bath for the Cu NPs synthesis. Here the bath used is acidified with H_2SO_4 to protect the Cu particles from oxidation. In Fig. 5.16c, the remaining PVP stabilizer is not totally washed and some impurities of the polymer appears as a dark film in the upper part on the right side of the SEM image in Fig. 5.16c. Another important aspect of the NPs is highlighted with the SEM imaging; the agglomeration of the NPs is important during the cleaning process of the particles with particles sizes reaching 4-10 µm. The centrifugation of the NPs to remove water is obviously influencing the formation of larger particles with their accumulation at the bottom of the vial.
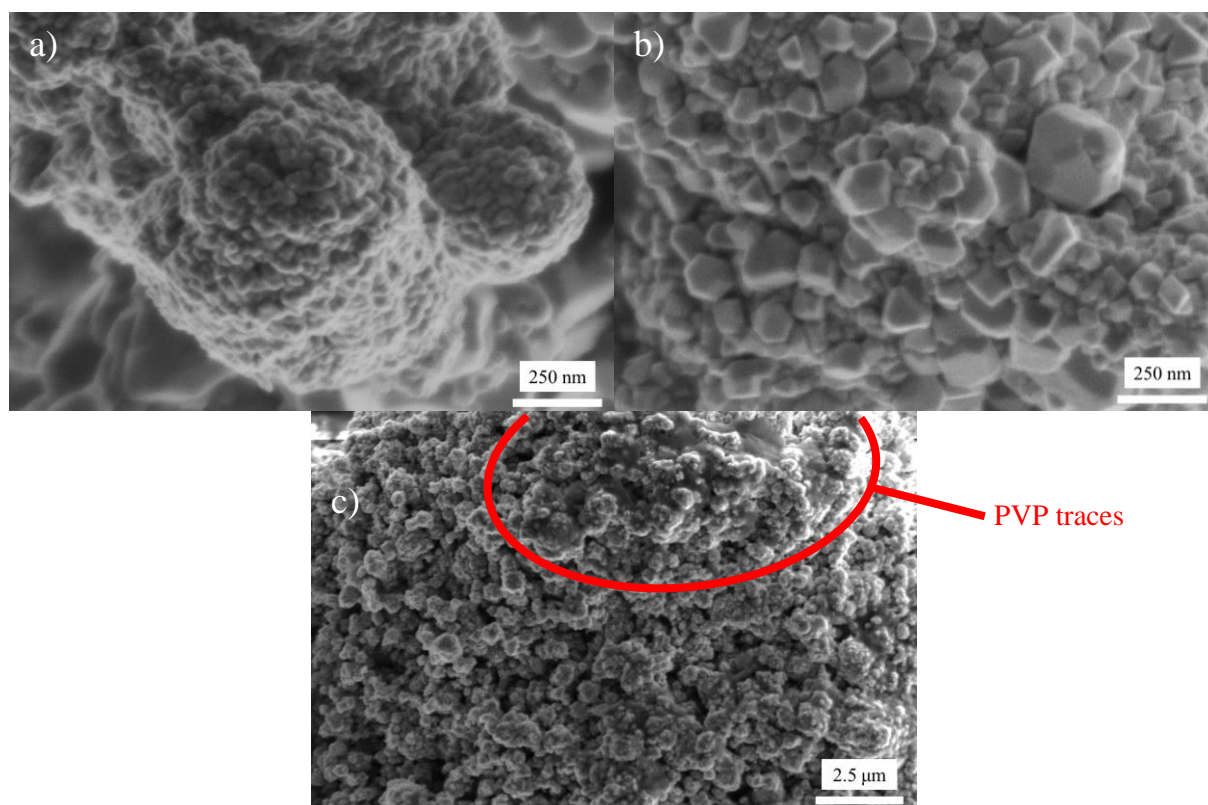
Figure 5.16. SEM images of the Cu particles produced by the wire corrosion method. SE detection at 6.3 pA and 1.0 kV. Corrosion bath: 1M H_2SO_4 and 1 wt% PVP in water. a) Aggregation of Cu NPs (15-40 nm) in the final Cu particle. b) Cu NPs (50-250 nm). c) Image of the remaining PVP film on the Cu particles.

In Table 5.3, the surface and bulk composition of the particle surface and bulk is given respectively by the XPS and XRD analysis for the three tested corrosion baths. The Cu oxidation is present on the particles as the cleaning of the particles is done at ambient atmosphere and it seems non-avoidable to have totally pure Cu particles without further treatment to remove the oxide or by doing the complete synthesis in an oxygen free environment. However, with the corrosion set-up, the washing process applied and the need to have a relatively large production for the slurry electrode, it was not possible to work during the all procedure under protected conditions. In addition, the chemical treatment in acidic condition for the oxide removal used mainly acid in aqueous solution, which is not ideal, as water will be introduced again. A plasma treatment with H_2 or O_2 seems to be a good option if better control of the oxide content is targeted.[46]

Table 5.3. XPS and XRD characterization of the final Cu particles synthesis.

Corrosion bath	XPS composition (surface)	XPS mol%	XRD composition (bulk)	XRD *wt*%	XRD size domain (nm)
NaOH, 1 M	Cu	trace	Cu	20	29
	Cu_2O	~ 30	Cu_2O	37	27
	CuO	~ 70	CuO	43	25
H_2SO_4, 1 M	Cu	trace			
	Cu_2O	~ 45	Cu	65	64
	CuO	~ 55	Cu_2O	35	7
PVP, 1 %(w/w)	Cu	~ 10	Cu	65	30
+ H_2SO_4, 1 M	Cu_2O	~ 90	Cu_2O	35	18

The basic conditions for the corrosion bath are not ideal for the Cu production with a low content of Cu(0) in the core of the particles. Inversely, the acidic conditions are more favourable to stabilize metallic Cu and are more appropriate for the slurry synthesis. Addition of PVP has two positive effects: it protects the surface from oxidation (10% Cu on the surface) and allows conserving a smaller size domain of the crystallite during the detachment of the Cu particles from the wire (Table 5.3).
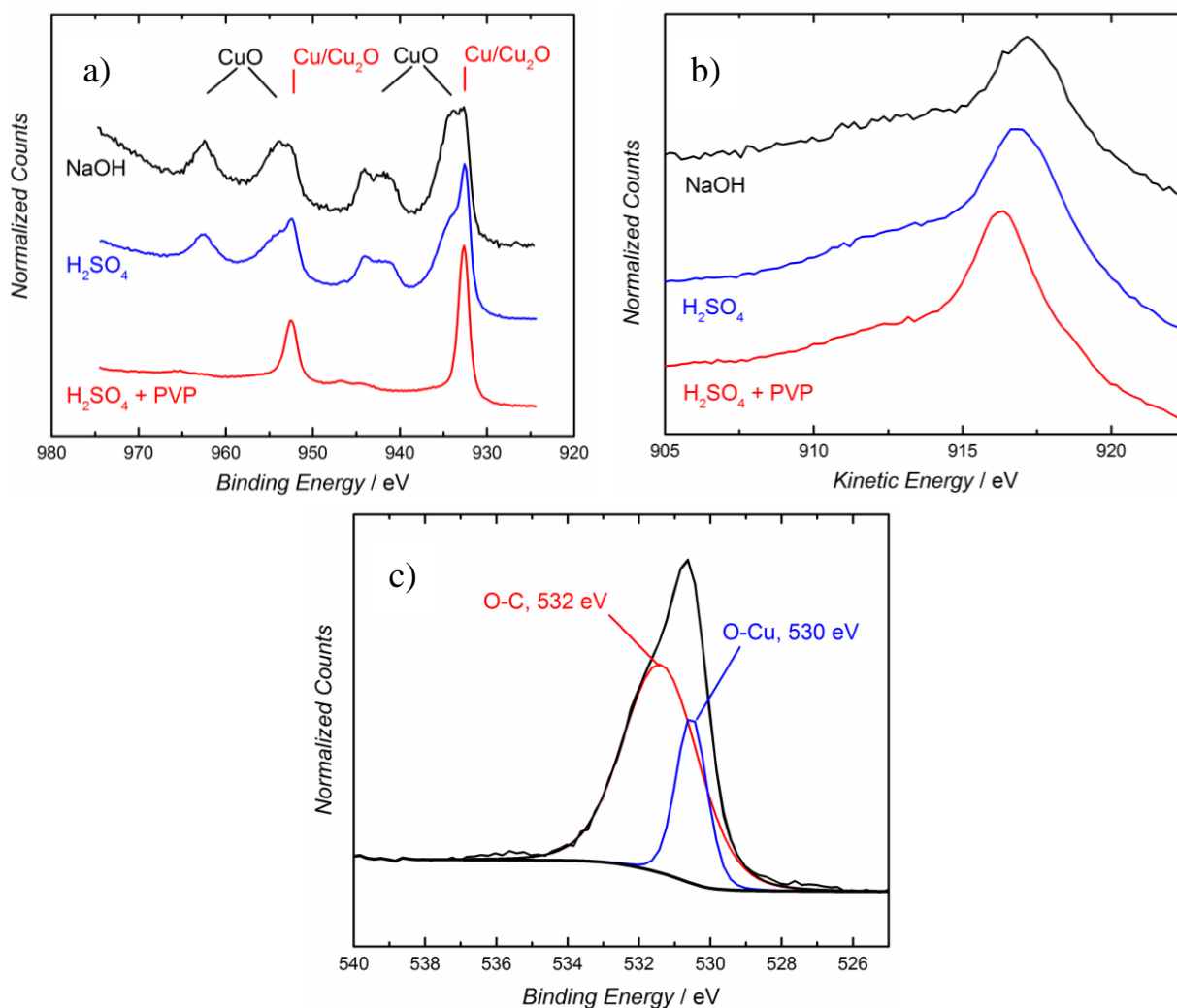
Figure 5.17. XPS spectra of the Cu particles produced by the wire corrosion method in three different baths (1M H₂SO₄, 1M NaOH, and 1M H₂SO₄ + 1 wt% PVP in water). a) Cu 2p spectra, b) Cu LMM Auger peaks, c) O 1s spectra for the Cu powder after cleaning for water removal.

The determination of the surface composition by XPS is not particularly straightforward. Indeed, the signal for the binding energies of photo-emitted electron are very similar for the Cu(0) and CuO oxide, especially if the electron configuration 2p is considered. The main peaks for Cu, Cu_2O and CuO are respectively at 932.6, 932.2 and 933.8 eV according to literature.[47–49] The presence of Cu(II) oxide is clear for the Cu particles from the corrosion bath with NaOH and H_2SO_4, because the strong satellite peaks of CuO are present in the range of 940-945 eV (Fig. 5.17a). The main peak of these two solid powders have the contributions of the Cu(II) oxide at 932.6 eV and Cu(I) or Cu at 933.8 eV. For the XPS signal of the Cu from the PVP + H_2SO_4 bath, the peak appears at 932.6 eV and seems closer to Cu(0). However, as the difference of binding energy with the Cu(I) oxide peak is so small, it is recommended to

check the Auger spectral lines-shapes of the Cu sample to determine more precisely the oxidation state.[47,48] Cu, Cu_2O and CuO Auger peaks for the Cu LMM spectrum are respectively at 918.6, 916.8 and 917.7 eV.[50] In Fig 5.17b, the Auger LMM peak are at 917.2, 916.8 and 916.4 eV for the basic, acidic and PVP corrosion bath. In the three cases, the peak, which was previously assigned to Cu(0) is more probably arising from the Cu(I) oxide or a mix of Cu(I) and metallic Cu. A clear confirmation of the Cu(I) oxide presence is shown in Fig. 5.17c with the peak at 530.4 eV, which is assigned to the photo-emitted electron binding energy of an oxygen metal bond. The second peak (931.4 eV) in the O 1s spectrum line comes from C-O bond contained in contaminants and most probably PVP.

6.2.3.   Cu slurry in the RFB

Utilization of the copper slurry is considered as promising way to facilitate the coupling of the heat charge with electrical discharge as discussed in Chapter 6. The conductive particles suspensions act as an anode and can flow through the cell with the electrolyte. Consecutively to the implementation of slurries, several technical modifications are applied to the cell. Indeed, a large pressure drop was noticed inside the system between the anodic cavity and the compressed C-felt of the cathodic side. The pressure difference across the membrane could lead to the rupture of the membrane (Fig. 5.18a-b). Consequently, different types of membrane supports were inserted inside the cavity of the negative current collector to compensate the pressure difference through the separator. Among the additional support for the membrane, the more appropriate choices are the porous and conductive structures (RVC, porous metal structure like INOX). The main advantage of these membrane supports is the ability to induce a turbulent flow of the slurry and to conduct the current from the particles to the current collector. RVC is chosen because of the nice porosity and cheaper prize.

In Chapter 6, the polarization curves and power outputs of the Cu slurry are compared with the Cu foam electrode (Fig.5.5c) and can reach equivalent performance than the ideal porous electrode if the concentration of 15 *wt*% Cu NPs is reached inside the negative electrolyte. Few cycling of the RFB with the slurry electrode is presented in Fig. 5.18c-d. The Coulombic efficiencies are slightly lower than with the solid negative electrodes (95%) with an averaged value of 85%. This decrease of performance is attributed to a lack of reversibility

during the stripping of the deposited Cu on the slurry electrode, consequently the Cu from the electrical charge is not fully converted to Cu(I) during the discharge. The cut-off voltage during charge is targeted to reach 90% of the maximal capacity and the relatively fast decay of the normalized capacity indicates that probably shorter times for the charge should be set to observe less effects on the capacity fade. However, these experiments were done without a connecting tube between the two tanks to balance the osmotic pressure, so some of the capacity fade could be attributed to the solvent cross-over.
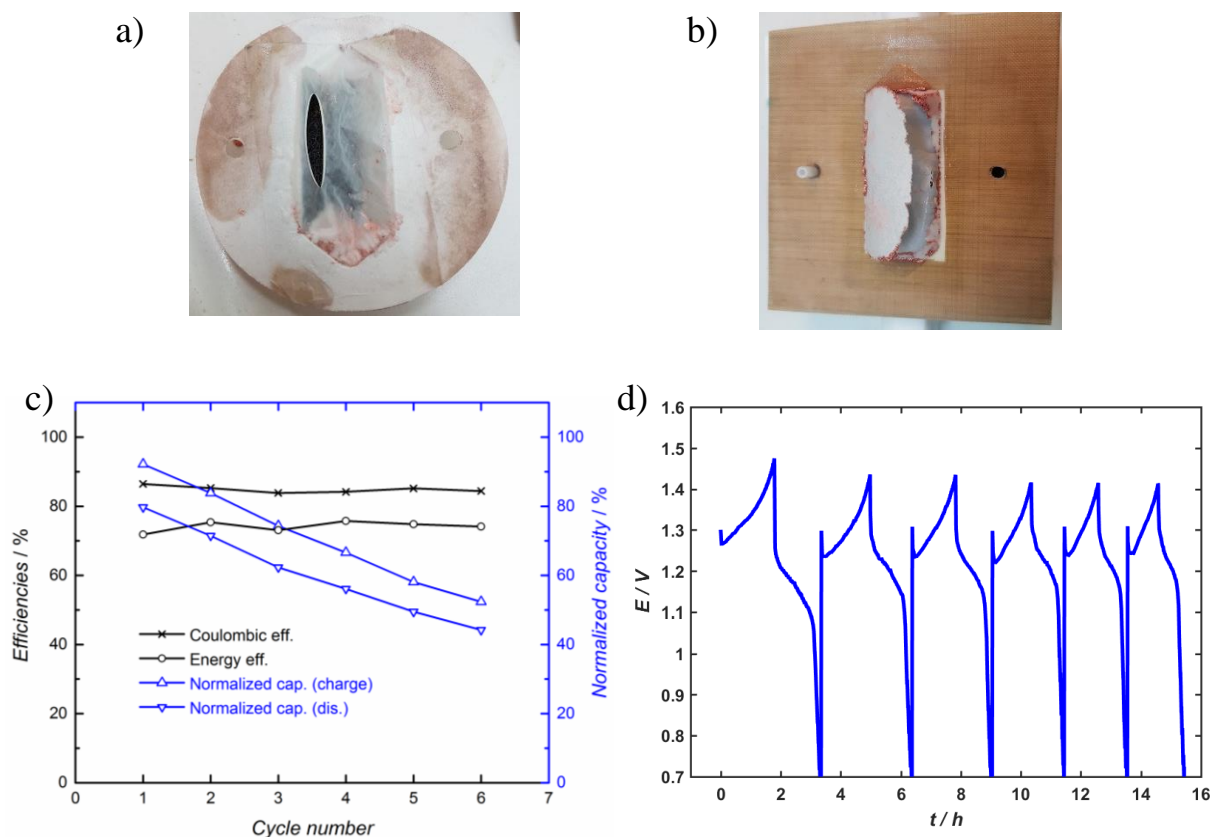
Figure 5.18. Cu-RFB battery with slurry Cu electrode, RVC membrane support in the current collector, 0.15 M [Cu(ACN)$_4$]BF$_4$ and 0.3 M supporting electrolyte (TEABF$_4$) with FAB-PK-130 anionic membrane, $i = \pm80$ mA (10 mA·cm^{-2}). a-b) Images of the broken membrane without support in the current collector cavity. c) Efficiencies and normalized capacities of the Cu RFB with slurry electrode. d) *iR*-corrected curves of the charge discharge cycles.

The energy efficiencies in Fig. 5.18c are calculated from the *iR*-corrected curves of voltage with time plotted in Fig. 5.18d and have an averaged value of 74%. If this efficiency is determined without compensation of the voltage losses by the resistance of the cell, the energy efficiency has a mean value of 47%. With the optimized Cu-RFB showing 200 cycles, these

parameters are 69% and 56%. The resistance with the slurry electrode is slightly increasing in the cell with $R = 2.6$ Ω *versus* $R = 1.5$ Ω when the Cu foam electrode is inserted in the battery. The slurry Cu negative electrode is showing performances that are inferior, but still acceptable and promising. Even with the different challenges linked with the synthesis and the implementations in the RFB, the slurry system have better results for the energy storage than the Cu plated RVC electrode.

7.   Conclusion

In this chapter, an optimized flow cell is developed for the energy storage in the non-aqueous Cu battery. This Cu-RFB shows good stability over time with more than 200 charge/discharge cycles. A particular attention is given to two key elements of the set-up, which are the membrane and the negative electrode. Regarding the membrane choice for the organic Cu system, the anion selective separators are the most suitable for a suitable management of the Cu ions crossover. The Zirfon membrane is also interesting for the system, as it is the only commercial porous separator that is able to maintain a slow diffusion of the Cu ions between both sides of the battery. Membrane production from polymers, which are chemically resistant to ACN (PTFE, PE), should lead to a porous layer that can be appropriate for the application of the Cu RFB with organic solvents. In this chapter, the deposition of PVC on PTFE filter can be considered as a potential alternative for a porous membrane, if PVC is changed for another polymer (like PVA, PE) and if the deposition process is better controlled. The cationic type of separators are not appropriate for the Cu-RFB, because the membrane is not selective enough to the cations from the supporting electrolyte and allows the crossover of the positively charged electroactive species. Furthermore, low cross-over of Cu across the membrane is not sufficient to complete a long term cycling procedure; the migration of the solvent (ACN) through the membrane induces non-negligible losses of capacity with time. Therefore, the salt bridge type connection is added to the single cell set-up to equilibrate the volume and osmotic pressure between the tanks.

Two modifications for the negative electrode are investigated and show new possibilities for battery constructions to store energy in Cu-RFB. The carbon-based structures

plated with Cu have lower performance than Cu-based electrodes, but are still able to act as a conductive electrode. Cu slurry electrode is the most promising alternative with a comparable power output as the Cu foam electrode. To improve the performance of the slurry, the synthesis of NPs should be modified to preserve a high content of metallic Cu and mitigate the formation of oxides. The separation and washing steps of the NPs could be followed by other treatments to lower the particles agglomeration and decrease the oxide content: a more violent sonication between centrifugation during the washing steps, a plasma treatment of the particles and a protective environment are possible options for an improved NPs synthesis. In addition, a corrosion bath based on non-aqueous solvents might be interesting to use if the corrosion is fast enough to have a significant production of particles.

With the single cell Cu-RFB set-up based on the ACN-PC solvent composition, the limitation comes from the negative side mainly because the electrochemical reaction implies the change of state from the solubilized Cu(I) to the solid Cu with a relatively slow kinetics.

8. References

1.   Morgan, H. H. CCCXLII.—Preparation and stability of cuprous nitrate and other cuprous salts in presence of nitriles. *J. Chem. Soc., Trans.* **123**, 2901–2907 (1923).

2.   Hathaway, B. J., Holah, D. G. & Postlethwaite, J. D. 630. The preparation and properties of some tetrakis(methylcyanide)copper(I) complexes. *J. Chem. Soc.* 3215–3218 (1961).

3.   Hathaway, B. J., Holah, D. G. & Underhill, A. E. 468. The preparation and properties of some bivalent transition-metal tetrafluoroborate–methyl cyanide complexes. *J. Chem. Soc.* 2444–2448 (1962).

4.   Kubas, G. J., Monzyk, B. & Crumbliss, A. L. Tetrakis(Acetonitrile)Copper(I) Hexafluorophosphate. *Inorganic Syntheses* (ed. Shriver, D. F.) 90–92 (John Wiley & Sons, Inc., 1979).

5.   Coelho, A. A. Whole-profile structure solution from powder diffraction data using simulated annealing. *J Appl Cryst* **33**, 899–908 (2000).

6.   Wagner, M. R. *et al.* Electrolyte Decomposition Reactions on Tin- and Graphite-Based Anodes are Different. *Electrochem. Solid-State Lett.* **7**, A201–A205 (2004).

7.   Eichinger, G. Cathodic decomposition reactions of propylene carbonate. *Journal of Electroanalytical Chemistry and Interfacial Electrochemistry* **74**, 183–193 (1976).

8.   Arakawa, M. & Yamaki, J.-I. The cathodic decomposition of propylene carbonate in lithium batteries. *Journal of Electroanalytical Chemistry and Interfacial Electrochemistry* **219**, 273–280 (1987).

9.   Nakamura, H., Komatsu, H. & Yoshio, M. Suppression of electrochemical decomposition of propylene carbonate at a graphite anode in lithium-ion cells. *Journal of Power Sources* **62**, 219–222 (1996).

10.   Chemical Resistance | Hose and Fittings Source. https://www.hoseandfittings.com/technical-info/rubber-chemical-resistance/.

11.   Thermo Fisher Scientific. Labware Chemical Resistance Table.

12.   EMD Milipore Corporation. Chemical Compatibility of Filter Components. (2015).

13.   Wang, W. *et al.* Recent Progress in Redox Flow Battery Research and Development. *Adv. Funct. Mater.* **23**, 970–986 (2013).

14.   Wang, W. *et al.* A New Fe/V Redox Flow Battery Using a Sulfuric/Chloric Mixed-Acid Supporting Electrolyte. *Advanced Energy Materials* **2**, 487–493 (2012).

15.   H. Kamath, S. Rajagopalan & M. Zwillenberg. Vanadium Redox Flow Batteries: An In-Depth Analysis. 102 (2007).

16.   Gao, P. *et al.* Template Synthesis of Nanostructured Polymeric Membranes by Inkjet Printing. *ACS Appl. Mater. Interfaces* **8**, 3386–3395 (2016).

17. T. Delaney, J., R. Liberski, A., Perelaer, J. & S. Schubert, U. Reactive inkjet printing of calcium alginate hydrogel porogens—a new strategy to open- pore structured matrices with controlled geometry. *Soft Matter* **6**, 866–869 (2010).

18. Shin, S.-H., Yun, S.-H. & Moon, S.-H. A review of current developments in non-aqueous redox flow batteries: characterization of their membranes for design perspective. *RSC Advances* **3**, 9095–9116 (2013).

19. Mohammadi, T. & Skyllas-Kazacos, M. Characterisation of novel composite membrane for redox flow battery applications. *Journal of Membrane Science* **98**, 77–87 (1995).

20. Haddadi-asl, V. & Mohammadi, T. Effect of Processing Methods and Conditions on Properties of Conductive Carbon-Polyolefins Composite. *Iranian Polymer Journal* **5**, 153–164 (1996).

21. Lee, N., Duong, D. T. & Kim, D. Cyclic ammonium grafted poly (arylene ether ketone) hydroxide ion exchange membranes for alkaline water electrolysis with high chemical stability and cell efficiency. *Electrochimica Acta* **271**, 150–157 (2018).

22. Schalenbach, M., Lueke, W. & Stolten, D. Hydrogen Diffusivity and Electrolyte Permeability of the Zirfon PERL Separator for Alkaline Water Electrolysis. *J. Electrochem. Soc.* **163**, F1480–F1488 (2016).

23. Rodríguez, J. *et al.* Simple and Precise Approach for Determination of Ohmic Contribution of Diaphragms in Alkaline Water Electrolysis. *Membranes* **9**, 129 (2019).

24. Peighambardoust, S. J., Rowshanzamir, S. & Amjadi, M. Review of the proton exchange membranes for fuel cell applications. *International Journal of Hydrogen Energy* **35**, 9349–9384 (2010).

25. Li, Z. *et al.* Enhanced proton conductivity of proton exchange membranes by incorporating sulfonated metal-organic frameworks. *Journal of Power Sources* **262**, 372–379 (2014).

26. Zhang, B. *et al.* Enhanced proton conductivity of Nafion nanohybrid membrane incorporated with phosphonic acid functionalized graphene oxide at elevated temperature and low humidity. *Journal of Membrane Science* **518**, 243–253 (2016).

27. Devanathan, R. *et al.* Atomistic Simulation of Water Percolation and Proton Hopping in Nafion Fuel Cell Membrane. *J. Phys. Chem. B* **114**, 13681–13690 (2010).

28. Yan, L., Zhu, S., Ji, X. & Lu, W. Proton Hopping in Phosphoric Acid Solvated Nafion Membrane: A Molecular Simulation Study. *J. Phys. Chem. B* **111**, 6357–6363 (2007).

29. Miyake, N., Wainright, J. S. & Savinell, R. F. Evaluation of a Sol-Gel Derived Nafion/Silica Hybrid Membrane for Proton Electrolyte Membrane Fuel Cell Applications: I. Proton Conductivity and Water Content. *J. Electrochem. Soc.* **148**, A898–A904 (2001).

30. Mahreni, A., Mohamad, A. B., Kadhum, A. A. H., Daud, W. R. W. & Iyuke, S. E. Nafion/silicon oxide/phosphotungstic acid nanocomposite membrane with enhanced proton conductivity. *Journal of Membrane Science* **327**, 32–40 (2009).

31. Healy, J. P., Pletcher, D. & Goodenough, M. The chemistry of the additives in an acid copper electroplating bath: Part I. Polyethylene glycol and chloride ion. *Journal of Electroanalytical Chemistry* **338**, 155–165 (1992).

32. Healy, J. P., Pletcher, D. & Goodenough, M. The chemistry of the additives in an acid copper electroplating bath: Part II. The instability 4,5-dithiaoctane-1,8-disulphonic acid in the bath on open circuit. *Journal of Electroanalytical Chemistry* **338**, 167–177 (1992).

33. Healy, J. P., Pletcher, D. & Goodenough, M. The chemistry of the additives in an acid copper electroplating bath: Part III. The mechanism of brightening by 4,5-dithia-octane-1, 8-disulphonic acid. *Journal of Electroanalytical Chemistry* **338**, 179–187 (1992).

34. Thompson, E. W. Acid Copper Plating for Electronics. *Transactions of the IMF* **59**, 30–32 (1981).

35. Goodenough, M. & Whitlaw, K. J. Studies of copper deposition for high aspect ratio printed circuit boards. *Transactions of the IMF* **67**, 57–62 (1989).

36. Chao, F. & Costa, M. Mechanism of copper deposition in a sulphate bath containing chlorides. *Bull. Soc., Chim. Fr* **10**, 4015 (1968).

37. Hill, M. R. H. & Rogers, G. T. Polyethylene glycol in copper electrodeposition onto a rotating disk electrode. *Journal of Electroanalytical Chemistry and Interfacial Electrochemistry* **86**, 179–188 (1978).

38. Yokoi, M., Konishi, S. & Hayashi, T. Adsorption Behavior of Polyoxyethyleneglycole on the Copper Surface in an Acid Copper Sulfate Bath. *Electrochemical Society of Japan* **52**, 218–223 (1984).

39. Scharifker, B. & Hills, G. Theoretical and experimental studies of multiple nucleation. *Electrochimica Acta* **28**, 879–889 (1983).

40. Gunawardena, G., Hills, G., Montenegro, I. & Scharifker, B. Electrochemical nucleation: Part I. General considerations. *Journal of Electroanalytical Chemistry and Interfacial Electrochemistry* **138**, 225–239 (1982).

41. Petek, T. J., Hoyt, N. C., Savinell, R. F. & Wainright, J. S. Characterizing slurry electrodes using electrochemical impedance spectroscopy. *Journal of the Electrochemical Society* **163**, A5001–A5009 (2016).

42. Petek, T. J., Hoyt, N. C., Savinell, R. F. & Wainright, J. S. Slurry electrodes for iron plating in an all-iron flow battery. *Journal of Power Sources* **294**, 620–626 (2015).

43. Gawande, M. B. *et al.* Cu and Cu-Based Nanoparticles: Synthesis and Applications in Catalysis. *Chemical Reviews* **116**, 3722–3811 (2016).

44. Yanson, A. I. *et al.* Cathodic Corrosion: A Quick, Clean, and Versatile Method for the Synthesis of Metallic Nanoparticles. *Angewandte Chemie International Edition* **50**, 6346–6350 (2011).

45. Feng, J. *et al.* Cathodic Corrosion of a Bulk Wire to Nonaggregated Functional Nanocrystals and Nanoalloys. *ACS Appl. Mater. Interfaces* **10**, 9532–9540 (2018).

46. Mistry, H. *et al.* Highly selective plasma-activated copper catalysts for carbon dioxide reduction to ethylene. *Nat Commun* **7**, 1–9 (2016).

47. Biesinger, M. C. Advanced analysis of copper X-ray photoelectron spectra: Advanced analysis of copper X-ray photoelectron spectra. *Surface and Interface Analysis* **49**, 1325–1334 (2017).

48. Biesinger, M. C., Lau, L. W. M., Gerson, A. R. & Smart, R. St. C. Resolving surface chemical states in XPS analysis of first row transition metals, oxides and hydroxides: Sc, Ti, V, Cu and Zn. *Applied Surface Science* **257**, 887–898 (2010).

49. A.V. Naumkin, A. Kraut-Vass, S. W. Gaarenstroom & C.J. Powell. NIST Standard Reference Database 20, Version 4.1. https://srdata.nist.gov/xps/.

50. Thermo Scientific XPS. XPS Interpretation of Copper. https://xpssimplified.com/elements/copper.php.

Chapter VI

Cu redox flow battery for heat to power conversion and energy storage

Based on the submitted paper,

Thermally regenerative nanoslurry based copper redox-flow battery for heat-to-power conversion with low-grade thermal energy

S. Maye, H. H. Girault & P. Peljo,

Abstract

In this Chapter VI, the thermal charge of the non-aqueous Cu battery is demonstrated in an optimized flow cell. The electrochemistry studies of Chapter 2 and 3 is coupled with the thermodynamics that was exposed in Chapter 4 about the heat conversion to chemical energy for energy storage application.

Low-grade heat (below 200 °C) is available in vast quantities from industry, or from standard roof-top solar thermal collectors. However, production of electric power from these heat sources is challenging with existing technologies. Thermally regenerative batteries allow both the conversion and the storage of thermal energy into electric power, but they suffer from low operation voltages and low output power. Here, we propose a thermally regenerative flow battery based on copper complexation with acetonitrile in non-aqueous solutions operating at

voltages above 1 V. Cu(I) complex can be destabilized by removal of acetonitrile by distillation, leading to production of solid copper and Cu(II) in solution, thereby charging the battery. We demonstrate the electricity production at power densities up to 200 $W \cdot m^{-2}$, and estimate the theoretical efficiency of the full system between 5-13%. The results demonstrate a proof-of-concept for producing and storing electricity from low-quality heat.

1.   Introduction

Low-grade thermal energy (< 200 °C) generated by industry, but also increasingly available from geothermal energy sources and rooftop solar thermal collectors, is an enormous underutilized resource. For example, as much as 20 to 50 % of the energy consumed in the industrial manufacturing processes is lost as waste heat. Although waste heat recovery offers significant energy savings and improved energy efficiency, it is still not industrially exploited. This shows that the technical challenges for utilizing this energy are higher than for converting wind or solar energy into electricity. In this work, we have doubled the cell voltage of a thermally regenerative flow battery to 1.2 V. Although thermo-electrochemical systems have been demonstrated earlier, achieving a cell voltage larger than 1V opens the way to practical electrochemical heat recovery systems. As this work describes a major leap forward in terms of theoretical thermal conversion efficiency, cell voltage, and energy storage density, these improvements could make this technology industrially relevant.

Environmental concerns about the use of natural resources drive us to improve the energy efficiency of existing processes. In this context, the large availability of low-grade heat (temperatures < 200 ℃) mainly from industry, but also from geothermal sources and solar thermal collectors, has drawn increasing attention for heat-to-power generation.[1–5] Thermoelectric devices (solid-state semiconductor-based systems) have been extensively investigated for these purposes, but remain expensive and require an additional battery to realize energy storage.[6–8] While conventional approaches to heat-to-power conversion, such as steam turbines, are limited to cold temperatures above 100 ℃ to avoid condensation of water, the organic Rankine cycle or the Kalina cycle circumvent this problem by replacing water with lower boiling point organic solvents or ammonia, but such systems require large scale installations and cannot store energy.[9–13]

Thermoelectrochemical systems for heat-to-power conversion have been reviewed recently.[5,14,15] Liquid-based thermoelectric systems, where a cell voltage is produced by a temperature gradient between the two electrodes[16,17], and salinity gradient energy systems, utilizing different salt concentrations obtained by evaporation to generate cell voltages[18], are only able to produce modest cell voltages (< 300 mV) and output powers. On the other hand, higher cell voltages can be achieved with thermally regenerative batteries, where thermal reactions induce a chemical reaction to charge the battery. Most thermally regenerative batteries are based on copper[19–21] or silver[22] complexation with ammonia or acetonitrile[23,24] in aqueous solutions. The removal or addition of the complexing agent is used to change or even inverse the cell voltage,[19–21] or to induce disproportionation of a Cu(I) complex to produce Cu and Cu(II) as described *vide infra*.[23,24] Cu and Cu(II) can then be discharged in a battery to produce electricity. The advantage of these systems is that in addition to heat-to-power conversion, they are also able to store energy.[23] However, almost all the concepts proposed in literature show cell voltages below *ca*. 0.65 V, resulting in low output power. One exception is a Zn and Cu based system using ammonia to change the voltage of the positive Cu-electrode, enabling operation at high power densities but low thermal efficiencies of < 1 %.[25] The comparison of the ammonia system and the present concept is illustrated in Scheme 6.1.

These recent reports show that exploitation of low-temperature heat sources by means of unconventional technologies is attracting significant interest from the scientific community. The main difficulty has been to reach a reasonable efficiency, of the order of 10%. Currently, only one technique reaches this goal[26] while the others are limited to 1% or less[5].

One approach to increase the cell voltage is to remove water. Indeed, an all-copper battery in water-free acetonitrile has a cell voltage of 1.3 V[27] in comparison to an aqueous system cell voltage of 0.62 V.[23] It is important to note that the all-copper battery in non-aqueous acetonitrile cannot be charged with heat, as removal of all the solvent would result in a mixture of solid copper powder and Cu(II) salt precipitate. Additionally, as acetonitrile forms an azeotrope with water meaning that distillation results in removal of both water and acetonitrile[24], replacement of water with another high boiling point co-solvent allows reducing the energy demand for the thermal regeneration step. While thermally regenerative copper battery employing 30 % aqueous acetonitrile solution has a maximum theoretical efficiency of *ca*. 6 % mainly due to the low cell voltage and the energy demand to evaporate water, non-aqueous systems described here show much higher theoretical efficiencies of up to 13 %.

In this work, we demonstrate unpreceded cell voltage and high output power for a thermo-electrochemical battery, by utilizing a copper-acetonitrile system with propylene carbonate as a co-solvent due to its high boiling point (242 °C) and stability. The co-solvent is essential to solubilize the Cu(II) salt, allowing separation of solid copper from the Cu(II) electrolyte. We characterize all the thermodynamic parameters of the system to evaluate the theoretical full cycle efficiency, and demonstrate the heat-to-power production and storage with this system.

Here, we demonstrate that the theoretical efficiency can reach up to 13%, with a volumetric energy density of 26 Wh·L^{-1}. These values are considerably higher than reported previously (0.5 % and 0.65 Wh·L^{-1})[19] whilst keeping a similar power density. This significant enhancement in comparison with previous works on thermally regenerable systems is obtained because of increased cell voltage, from 0.5 V[19] up to 1.2 V in the present work.

The remaining challenge of this type of systems has been the question of how to re-introduce the heat-charged electrolytes into the electrochemical cell. Here, we solve this issue by utilizing nanoslurry based copper electrolyte. Slurry-based flow batteries have been demonstrated before, but they require careful control of the particle size.[28–30] In this work, nanosized copper slurry is used to promote nucleation of the copper recovered by the thermal regeneration. This allows separation of copper from the thermally regenerated solution by, for example, centrifugation. Addition of acetonitrile into the copper nanoparticles allow recirculation of the copper through the electrochemical cell as a slurry without compromising the power density or energy storage capacity, as demonstrated below.

2.   Material and methods

2.1.   Chemicals

All solvents and chemicals were used as received without further purification and were stored in a glove box under nitrogen. The solvents were acetonitrile (CH_3CN, extra dry over molecular sieves, 99.9%, Acros) and propylene carbonate ($C_4H_6O_3$, anhydrous, 99.7%, Sigma-Aldrich). The supporting electrolytes were tetraethylammonuim tetrafluoroborate ($TEABF_4$, 99%, ABCR) or lithium hexafluorophosphate ($LiPF_6$, Battery Grade, Fluorochem). Tetrakis(acetonitrile)copper(I) hexafluorophosphate ($[Cu(CH_3CN)_4]PF_6$, 98%, ABCR) was used as received as a redox active molecule in the RFB. The electroactive species tetrakis(acetonitrile)copper(I) tetrafluoroborate was either commercial, ($[Cu(CH_3CN)_4]BF_4$, > 98%, TCi), or prepared by comproportionation reactions. The reducing ability of metallic Cu on Cu^{2+} has been known since 1923, when Morgan used this method for the preparation of cuprous chloride or bromide-mono(acetonitrile) complexes[31]. Therefore the synthesis of Cu^+ can be easily made in acetonitrile by comproportionation (cf ESI)[32–34]. For the synthesis of $[Cu(CH_3CN)_4]BF_4$, copper(II) tetrafluoroborate hydrate ($Cu(BF_4)_2·xH_2O$, Sigma-Aldrich), acetonitrile (Merck) and copper wire (dia. 1 mm, ≥ 99.99%, GoodFellow) were of analytical grade and were used as received. The comproportionation reaction occurs in a Schlenk line with nitrogen. The Cu^+ complex with acetonitrile is dried overnight under vacuum and stored in a nitrogen-filled glove box. Regarding the Cu particles synthesis by the cathodic corrosion method, the Cu wires (dia. 0.2mm and 1 mm, purity 99.9%, Advent) were placed in the aqueous bath (MiliQ water, 18.2 MΩ cm) of PVP (polyvinylpyrrolidone, MW ≈ 10'000, Sigma-Aldrich) and sulphuric acid (H_2SO_4, 95-97% for analysis, Merk).

2.2.   Electrochemical analysis

Electrochemical analyses were obtained with a Metrohm Autolab potentiostat. Cyclic voltammetry (CV) and chronopotentiometry (CP) were performed inside a three-electrode set-up with a Pt wire as counter electrode (CE) and a Pt disk working electrode (WE, dia. 2mm). The RE was made with a Cu wire (dia. 1mm, $\geq$ 99.99%, GoodFellow) inside the solution containing 0.1 M TEABF$_4$ as a supporting electrolyte and 0.01 M [Cu(CH$_3$CN)$_4$]BF$_4$ in acetonitrile-propylene carbonate mixtures.

All experiments were performed under an anaerobic atmosphere with a flow of nitrogen or argon.

Two different set-ups are assembled to test the charge-discharge cycling of the battery. Both cells were filled with a acetonitrile-propylene carbonate solution containing 0.15-0.3 M TEABF$_4$ and 0.15-0.3 M [Cu(CH$_3$CN)$_4$]BF$_4$. Here, TEABF$_4$ was utilized to improve the conductivity of the electrolytes. The anion-exchange membrane (FAB-PK-130, Fumatech) is either directly included under its dry state or soaked in acetonitrile with 0.15 M TEABF$_4$ during 24 hours before utilization. All gaskets, seals and tubing need to be chemically resistant to acetonitrile. H-cell type redox flow battery is constructed utilizing two jacketed half-cells of 3.4 mL (PermeGear Horizontal Cell from SES GmgH). The cell is filled up inside the glovebox to avoid the presence of oxygen and water. For the negative side, a copper wire is used as an electrode and a platinum wire was used for the positive side. The area available for the ionic transport is 1.13 cm^2 with an opening diameter of 12 mm. For the other flow cell, the usual stack is constructed with the anionic membrane, current collectors and carbon-felt electrodes (10 cm^2) from a cell hardware from Fuel Cell Technologies, INC. The calculations of the Coulombic and energy efficiencies are illustrated in the section 2 of Chapter 5. Electrochemical impedance spectroscopy was utilized to evaluate the Ohmic resistance of the cell.

2.3. Cu particles synthesis

The production of the Cu particles for the slurry electrode is done *via* the cathodic corrosion method, which is inspired from Koper *et al.*[35,36] An automatized set-up for Cu corrosion is developed for a continuous production. The motorized equipment drives a thin Cu wire (dia. 0.2mm, purity 99.9%, Advent) in an aqueous acidic bath (1M H_2SO_4) with a stabilizing agent (1 *wt*% PVP). The speed of the descending wire can be tuned between 2 and 8 mm·min^{-1}. The corrosion of the Cu wire is generated when the electrified wire is introduced in the conductive bath solution, in which a second Cu wire is used as a counter electrode. The electrical circuit generates a square-wave signal with a frequency of 100 Hz (programmable function generator, HM8 150, Rohde & Schwarz Hameg) and with a polarization from a DC current switching between ± 10 V (DC power supply, RND 320-K3005D, RND Lab). The fast change of polarization is the driving force for the electrical corrosion of the thin wire when it is immerged in the bath. To remove water from the Cu particles, the bath for corrosion is centrifuged and particles washed several times with ACN, before to be finally dried under vacuum.

2.4. Analytical techniques

UV-vis spectroscopy was carried out with a ChemStation for UV-visible spectroscopy (Agilent Technologies, USA). Cu^{2+} samples from the thermal regeneration are filtered and centrifuged to remove the metallic Cu which is produced during the same reaction.

The images are recorded with a scanning electron microscope (SEM) and a transmission electron microscope (TEM). The SEM is a Teneo SEM (FEI, USA) equipped with a Schottky field emission gun. Secondary electron detection was achieved with an Everhart-Thornley detector and an in-lens detector. The TEM is a Tecnai G2 Spirit Twin (FEI, USA) equipped with a LaB6 electron gun. For composition characterisation, X-rays are detected by energy-dispersive X-ray spectroscopy (EDX) (XFlash Silicon drift detector) inside the SEM.

2.5.   Thermal regeneration

Two consecutive charge processes with a thermal treatment are done to characterize the voltage, power and discharge that can be obtained during the discharge of the electrolyte in a RFB. During the first charge, the electrolyte (50%(vol/vol) ACN and PC, 0.3 M TEABF$_4$, 0.15 M [Cu(CH$_3$CH)$_4$]BF$_4$) containing a Cu slurry (15%(w/w)) is heated overnight between 120 and 140°C to distillate the ACN from the solution and to disproportionate the Cu(I) to Cu and Cu(II). After this process, the resulting Cu-Cu(II)-PC solution is centrifuged to separate the solid Cu slurry from the Cu(II) solution. The ACN is introduced back in the Cu(II) solution to have at least 10 vol% ACN in the positive tank and the main fraction of ACN is kept to fluidize the Cu slurry and to allow the future oxidation of Cu to the Cu(I) complex [Cu(CH$_3$CH)$_4$]BF$_4$. The Cu suspension and the Cu(II) solution are flown through the RFB with a RVC electrode and Ti current collector on the negative side and with a Ti current collector coupled with a C-felt electrode on the positive one. The discharge current is set to 10 mA cm^{-2}. When the electrolyte is discharged, both sides are mixed together in one tank and another heat treatment is applied. By following the same procedure than before, the electrolyte is again discharged in the RFB.

3. Results and discussion

3.1. Thermally regenerative copper battery

The operation of the copper battery is based on three oxidation states of copper, as illustrated in Scheme 5.1. Upon discharge, metallic copper is oxidized to Cu(I) on the negative electrode and Cu(II) is reduced to Cu(I) on the positive electrode.[27,37–40] Copper complexing agents such as acetonitrile, ammonia, or chloride are required to stabilize the Cu(I) oxidation state.[41–45] With acetonitrile or ammonia, this property can be used advantageously to realize a thermally regenerative battery, as destabilization of the Cu(I) can be achieved in a thermal reaction simply by removing the acetonitrile into the gas phase upon distillation. Once the complexing agent is removed, Cu(I) disproportionates according to the following reaction:

$2\,Cu(I) \rightarrow Cu + Cu(II)$, *i.e.* nucleation of Cu particles and generation of Cu(II) species dissolved in solution takes place. Obviously, a co-solvent such as water or propylene carbonate used in this work is required to avoid precipitation of Cu(II) salts. Solid Cu and the Cu(II) containing solution can be separated and introduced back into the battery after the addition of the recovered acetonitrile, finishing the thermal regeneration step. Now, the energy is stored in the battery, and can be converted into electricity upon demand. Additionally, the battery can be charged with electricity (as described *vide infra*) instead of the thermal charge.

This concept is drastically different from the other typical systems, as illustrated in Scheme 6.1. In the ammonia based thermally regenerative battery with copper electrodes and copper salts there is ammonia only in the negative electrolyte. Upon discharge, Cu is deposited on the positive side and dissolving in the negative side, but the presence of ammonia in the negative side results in the cell voltage of ca. 0.5 V. During discharge the concentration of copper decreases on the positive side, and increases in the negative side. After the cell discharge at room temperature, ammonia is separated from the negative electrolyte using a conventional distillation process, and then added into the Cu-poor positive electrolyte of the previous step. Now this electrolyte becomes the negative electrolyte for the sequel discharge cycle. (Figure reprinted with permission from ref. 5).
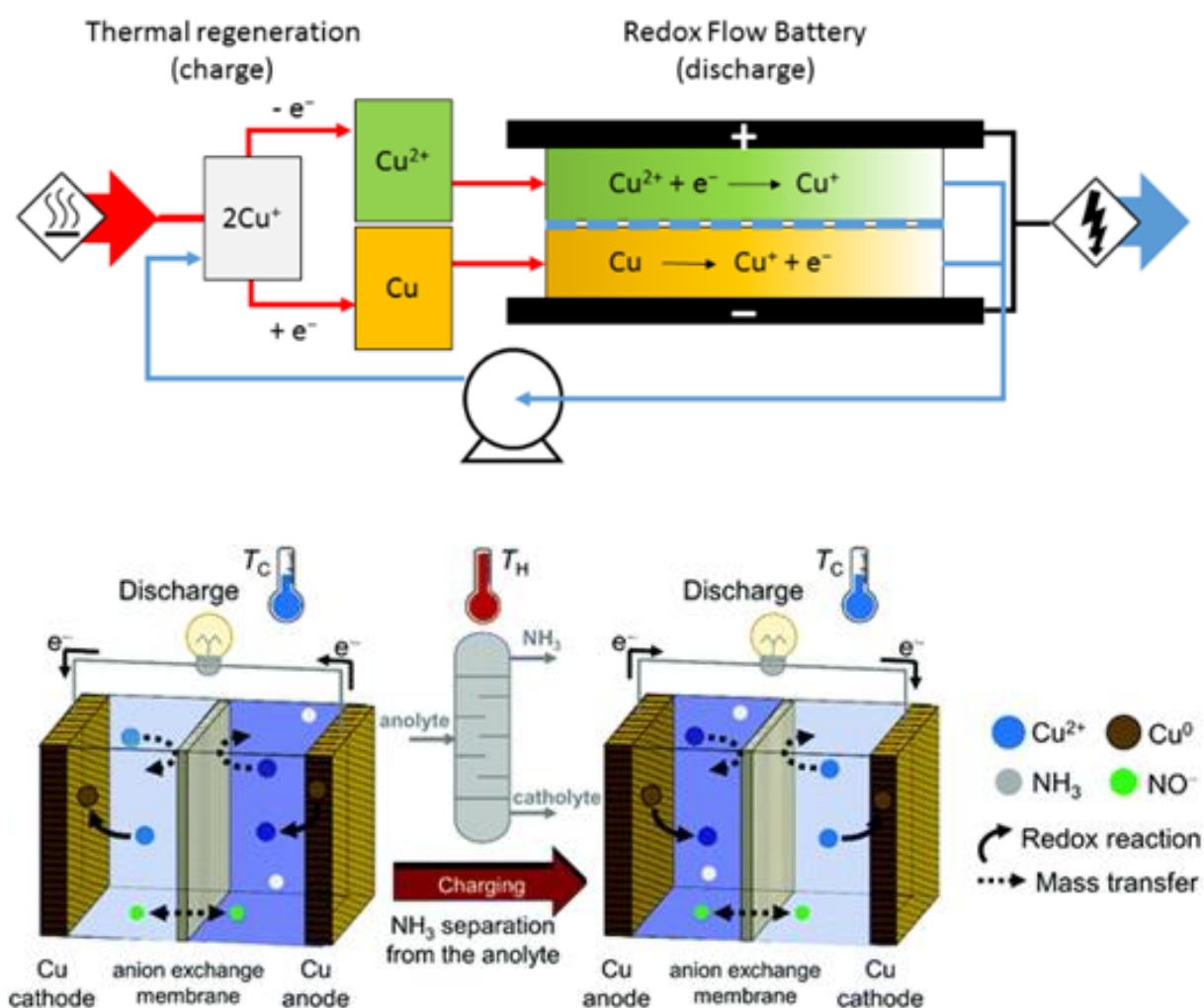
Scheme 6.1. (Up) Scheme of the cycle process of the Cu redox flow battery for heat to power conversion. (Down) Schematic of an ammonia based thermally regenerative battery with copper electrodes and copper salts as well as ammonia only in the anolyte. Two chambers are separated by an anion exchange membrane. After the cell discharges at room temperature, ammonia is separated from the anolyte using a conventional distillation process, and then added to the other electrolyte for the sequel discharge cycle. (Figure reprinted with permission from ref. 5)

3.2. All copper redox flow battery

To understand how efficiently the chemical energy produced in the thermal step can be converted into electricity, experiments with the all-copper battery are required. The charge and discharge reactions of such a battery are shown below.

Negative electrode (Cu):

$$Cu^+ + e^- \underset{discharge}{\overset{charge}{\rightleftharpoons}} Cu$$
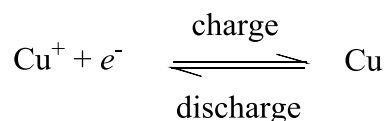
Positive electrode (carbon felt):

$$Cu^+ \underset{discharge}{\overset{charge}{\rightleftharpoons}} Cu^{2+} + e^-$$
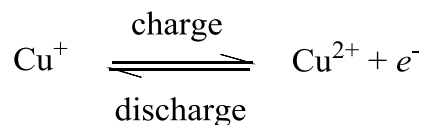
The electrochemical kinetics of the negative and positive electrode reactions have been investigated earlier (in Chapters 2 and 3).[46] In short, both reactions have reasonably facile kinetics, with much higher reaction rates than obtained in the state-of-the-art vanadium flow batteries. Figures 6.1a and 6.1b show 44 charge-discharge cycles measured with an H-cell as shown in Chapter 5. At the beginning of the experiment, the device is fully discharged and both positive and negative electrolytes consist of 0.15 M [Cu(CH$_3$CN)$_4$]BF$_4$ (copper acetonitrile tetrafluoroborate) and 0.15 M TEABF$_4$ (tetraethylammonium tetrafluoroborate) as the supporting electrolyte. The first 40 charge/discharge periods were performed with a current density of 10 mA·cm^{-2} and the last four steps were done with a current density of 1 mA·cm^{-2}.

As mentioned above, the potentials are corrected for the ohmic resistance induced by the membrane and electrolyte (Figure 6.1a). For the performance of the battery in Figure 6.1b, the efficiencies are calculated with all 44 cycles as detailed in the Equations 5.1 and 5.2. The Coulombic and energy efficiencies are stable during 33 cycles after which they slightly decrease, and on average are around 95% and 51%. These efficiencies are comparable to other all Cu redox flow cells[23,27,47]. When lower current densities are applied, a better energy efficiency is obtained, as overpotential losses for the electrochemical reactions decrease. Indeed, an overpotential of approximately 50 mV is calculated at 10 mA·cm^{-2} *versus ca.* 10 mV

at 1 mA·cm^{-2}. These values can be determined from the potential drop when switching the current on, when *iR* correction is taken into account.

Charging and discharging at 10 mA·cm^{-2} allow the utilization of ca. 45 % of the total capacity, while a lower current density of 1 mA·cm^{-2} allows access to 84 % of the whole capacity during the cell charging. Relatively low current densities are employed to avoid high ohmic losses, as it is typical for systems employing non-aqueous electrolytes. By looking at the evolution of the Coulombic charge in Figure 6.1b, a loss of capacity is noticed. Almost 50% capacity loss is observed between the first and 40th charging step. Some of this capacity fade can be attributed to slow diffusion of oxygen and water into solution, leading to side reactions with oxygen. However, the major cause of the capacity fade is most likely the formation of dendrites on the Cu electrode upon charging, followed by detachment of the dendrites upon discharge. Some particles of Cu are then deposited at the bottom of the cell, and this behaviour could most likely be mitigated by common industrial copper plating additives.[48–51]
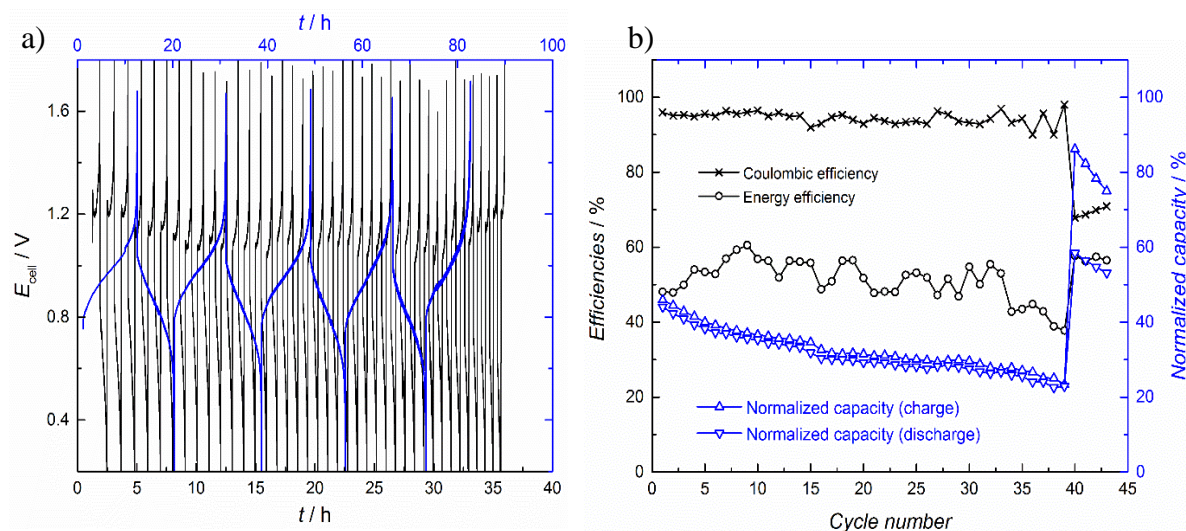
Figure 6.1 Cu redox battery with [Cu(CH$_3$CN)$_4$]BF$_4$ (0.15 M) and TEABF$_4$ (0.15 M) and *i* = 10 and 1 mA·cm^{-2}, respectively the black and blue curve, a) *iR* corrected potential cycling with time and b) efficiencies and normalized capacities of the battery for all cycles.

With the optimization of the cell (Chapter 5), resistances between 0.5-3.0 Ω are reached with a typical flow cell. Considering the *iR* losses, the redox flow battery (RFB) is much more suitable than a miniaturized H-cell with more than ten times higher the resistance (10-25 Ω). The critical parameters are the distance between the electrodes, and the conductivities of the electrolyte and the membrane. The distance is much smaller and easier to control inside the RFB. Another important factor is the concentration of supporting electrolyte in acetonitrile and it can be increased by using more soluble species, like LiPF$_6$ (lithium hexafluorophosphate) or LiTFSI (lithium bis(trifluoromethanesulfonyl)imide). In Figure 6.2, charge-discharge cycles of the RFB with 0.5 M LiPF$_6$ supporting electrolyte are shown, with improved efficiencies in comparison with the H-cell. The Coulombic efficiency is stable during the battery test and its averaged value is 98% (Fig. 6.2b). However, the energy efficiency decreases with time, starting from 81% and reducing to 44% after 50 cycles (Fig. 6.2b). A similar trend is also observed for the state of charge (Fig. 6.2b) and is assigned to solvent crossover through the anionic membrane, which is observed as a significant change of the volume in both tanks (at the end of the cycling test: $V_- < V_+$). However, the state of charge and energy efficiency can be easily recovered if the discharge solutions (mainly Cu(I) species on both sides) are mixed and equally separated back between the positive and negative tanks (Fig. 6.3). This behaviour is also observed in typical vanadium redox flow batteries, and electrolyte rebalancing systems have been developed to deal with this problem[52–55].

The energy storage density of the described system is 2.6 Wh·L^{-1} (0.15 M Cu(I)-species), but it can be increased to 26 Wh·L^{-1} by utilizing TFSI-anion as a counter ion.[32]

Another approach is to replace the copper electrode with carbon foam and flow a slurry composed of copper nanoparticles on the negative side. This transforms the system to a true flow battery, where the capacity of the system is independent of the electrode mass and depends only on the volume of the electrolyte. Polarization curves with 5 w-% and 15 w-% nanoslurry electrolytes are shown in Fig. 6.2c, displaying even higher power densities than could be obtained with copper foam.
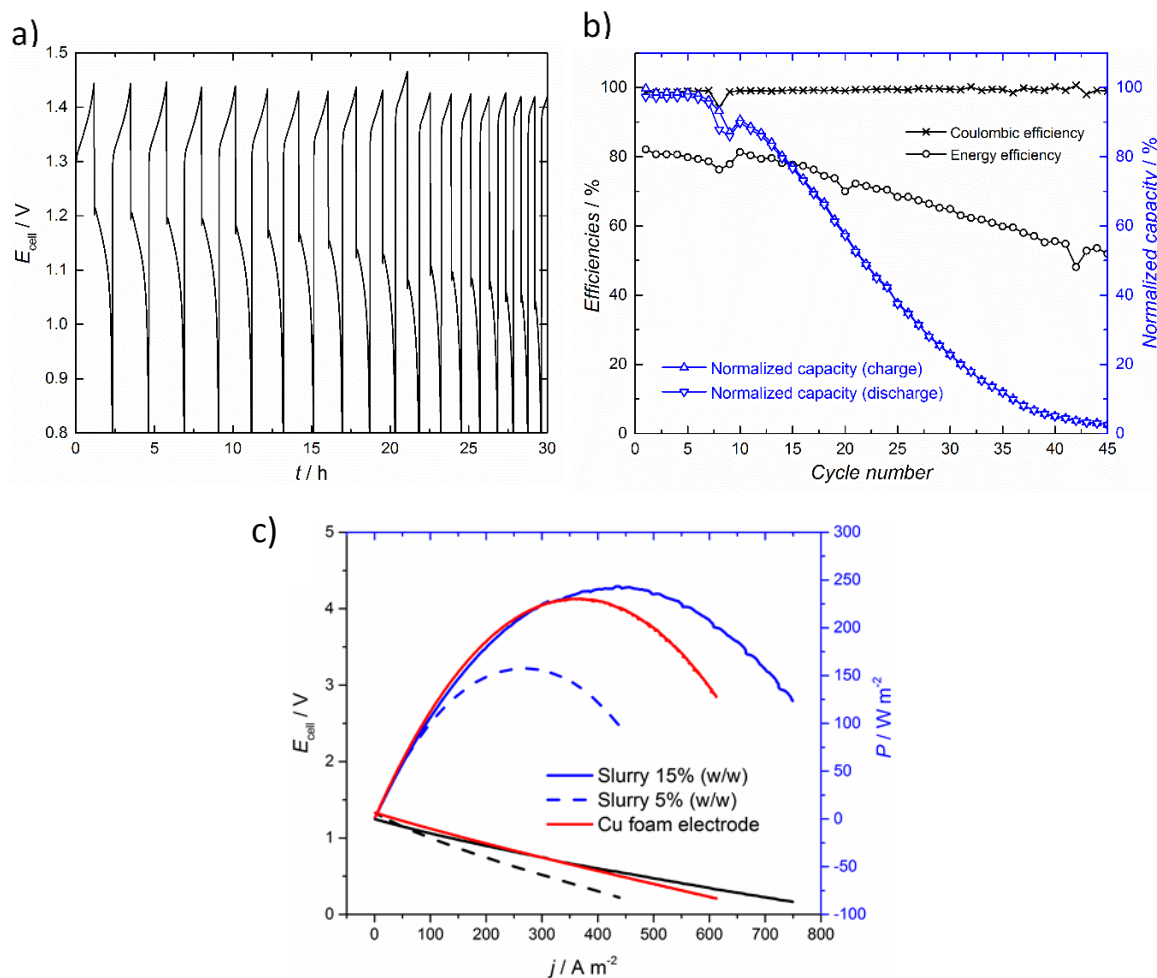
Figure 6.2. Cu redox flow battery with $[Cu(CH_3CN)_4]PF_6$ (0.15 M) and $LiPF_6$ (0.5 M) and $i = 10$ mA·cm^{-2}, a) *iR* corrected potential cycling with time and b) efficiencies and normalized capacities of the battery for all cycles. c) Power output with Cu foam and nanoslurry electrolytes with a composition of 50 vol% ACN containing 0.15 M $[Cu(CH_3CN)_4]BF_4$.
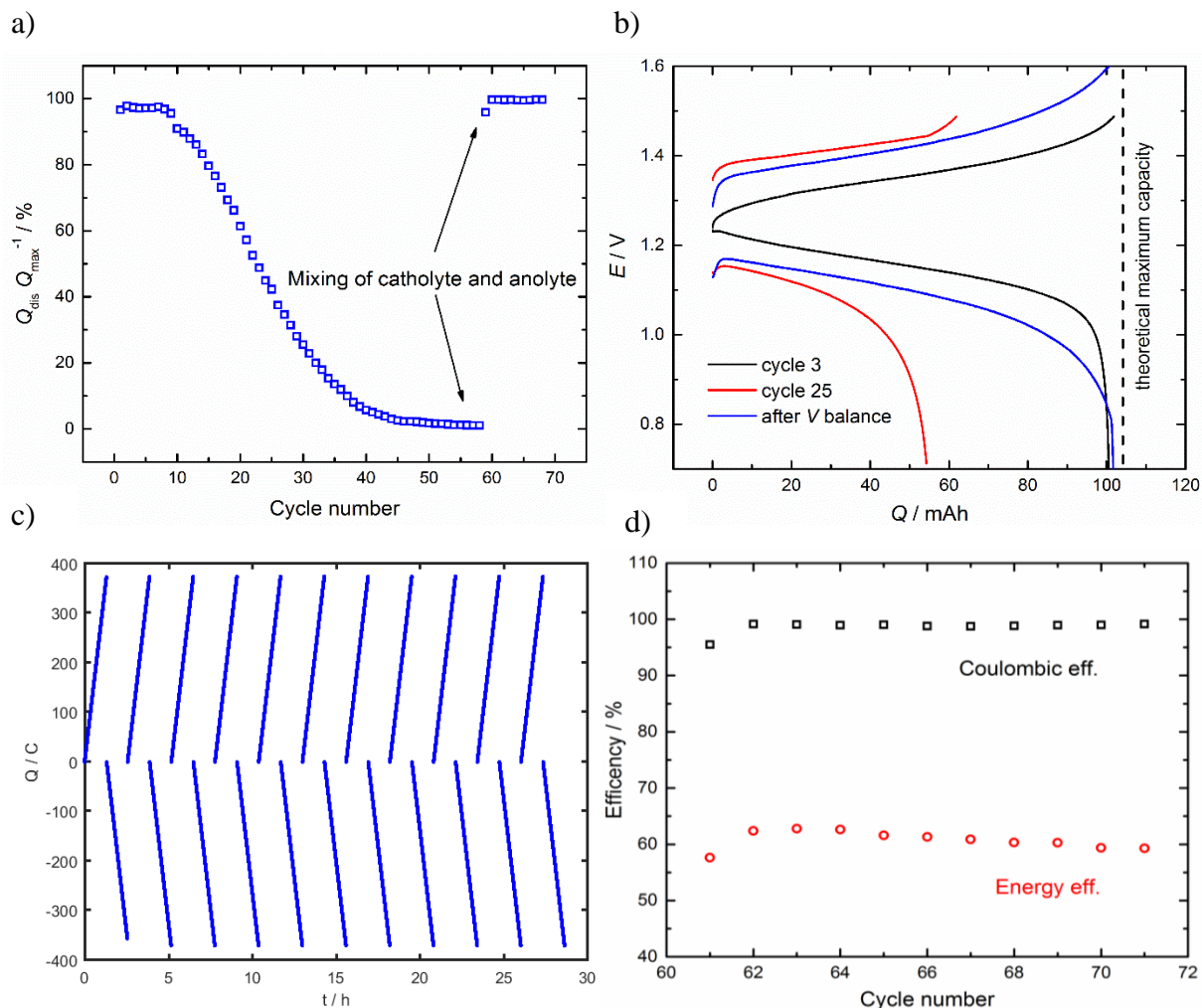
a)

b)

c)

d)

Figure 6.3. Crossover phenomena between the positive and negative side during the cycling of the flow cell. The electrolyte solution is made with $[Cu(CH_3CN)_4]PF_6$ (0.15 M) and $LiPF_6$ (0.5 M). The applied current density is $i = 10$ mA·cm^{-2}. a) Evolution of the electrical capacity during the discharge. After 30 cycles, 20% of the maximum theoretical capacity is still discharged. After mixing of the totally discharge electrolyte containing mainly Cu^+ cation, the volume in both tanks is equilibrated and the full capacity is available again. b) The *iR*-corrected cycles 3, 25 and 61of the RFB experiment shows again the recovering of the capacity by mixing the electrolyte. Furthermore, the evolution of the voltage illustrates a modification of the internal resistance of the cell and explains the decreasing of energy efficiency with time. c) The capacity in *C* are plotted to observe the stability of the cycling after the 11 cycles following the volume balance. d) The energy efficiency is not totally recovered but is back to 60% after the volume balance.

3.3.   Thermal regeneration and heat-to-power conversion

The reaction leading to the formation of Cu(II) and Cu from Cu(I) is a disproportionation. The description of this process is given when Cu(I) complexes with acetonitrile are destabilized by heat:

$$2 \text{ Cu(CH}_3\text{CN)}_4^+ \; \underset{\text{Under N}_2}{\overset{\text{120-160 °C}}{\rightleftharpoons}} \; \text{Cu} + \text{Cu}^{2+} + 8 \text{ CH}_3\text{CN}$$
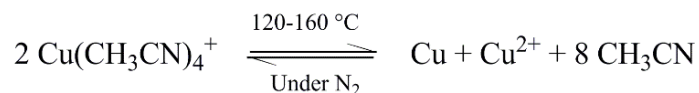
Differential scanning calorimetry (DSC) measurements shown in Chapter 4 demonstrate that the disproportionation step can be distinguished from the acetonitrile vaporization at 82 °C, taking place at *ca.* 160 °C for solid $\text{Cu(CH}_3\text{CN)}_4\text{BF}_4$. This indicates that the disproportionation reaction cannot simply be induced by the distillation of the acetonitrile solvent close to 81 °C, but a surplus of heat is required to destabilize the Cu(I) complex. Further investigations indicate that Cu(I) disproportionation could be realized at temperatures near 120°C for a 30% acetonitrile- 70% propylene carbonate solution. The thermodynamic parameters including enthalpies of vaporization and heat capacities for various ratios of Cu(I) containing acetonitrile-propylene carbonate mixtures have been measured with DSC, and are reported in Chapter 4. These results also confirm that it is necessary to consider the excess energy of destabilizing the complex, as it is clearly not correct to consider simple evaporation of the complexing agent as suggested previously[20]. This issue was also highlighted recently[21].

The Cu(I) solution was heated under nitrogen between 140-160°C to induce thermal regeneration. In order to keep a solution after the disproportionation, the solvent is partially composed of propylene carbonate, which remains mostly in the liquid state (b.p. = 242°C). The completion of the reaction and the formation of Cu particles and Cu(II) solution was confirmed by the colour transition from the transparent Cu(I) solution to the Cu(II) and with the appearance of some metallic Cu particles (Fig. 6.4d). The acetonitrile condensate removed during thermal regeneration is collected to be introduced back in the system for the electrochemical discharge.

We analysed the resulting solution with different techniques to verify and describe the presence of Cu(II) and metallic Cu. The UV-vis spectra for Cu^+ and Cu^{2+} in ACN, PC and water are shown in Fig. 6.4a. The conversion of Cu^+ during the disproportionation is observed by UV-vis spectroscopy of the final Cu^{2+} solution in propylene carbonate. The spectrum of $\text{Cu(BF}_4)_2$ in water shows the characteristic peak of Cu^{2+} with a maximum of absorbance around 810 nm.[56]

In acetonitrile and propylene carbonate, this peak is shifted to smaller wavelength and appears around 760 and 785 nm. This confirms the presence of Cu^{2+} in the final thermally generated solution. The comparison of the UV-vis spectra of Cu^+ and Cu^{2+} is easy and fast, because Cu^+ electronic configuration $[Ar]4s^03d^{10}$ cannot absorb light in the UV-vis range. Indeed, Cu^+ d orbital, which is completely full with 10 electrons, is not able to promote an electron with UV-vis light. In consequence, regardless the ligand and symmetry of the complex, no peak should be recorded for any Cu^+ solution. The bulk electrolysis to reduce all the generated Cu^{2+} is was performed at 0.9 V (vs. Cu/Cu^+) to quantify the amount of Cu^{2+} ions (Fig. 6.4b). From the initial concentration of Cu^+, the efficiency of the Cu^+ thermal disproportionation is determined around 98% regarding the Coulombic efficiency of the reaction. This indicates that a complete conversion of the Cu(I) can be achieved by heat. By eye, Cu^{2+} cation looks blue in water or green/turquoise in acetonitrile-propylene carbonate mixtures due to the absence of water. As expected in the case of a pure Cu^+, no trace of Cu^{2+} appears and the solution is transparent (Fig. 6.4c). Nice shiny Cu particles are visible in the Cu^{2+} electrolyte after the thermal treatment (Fig. 6.4d).
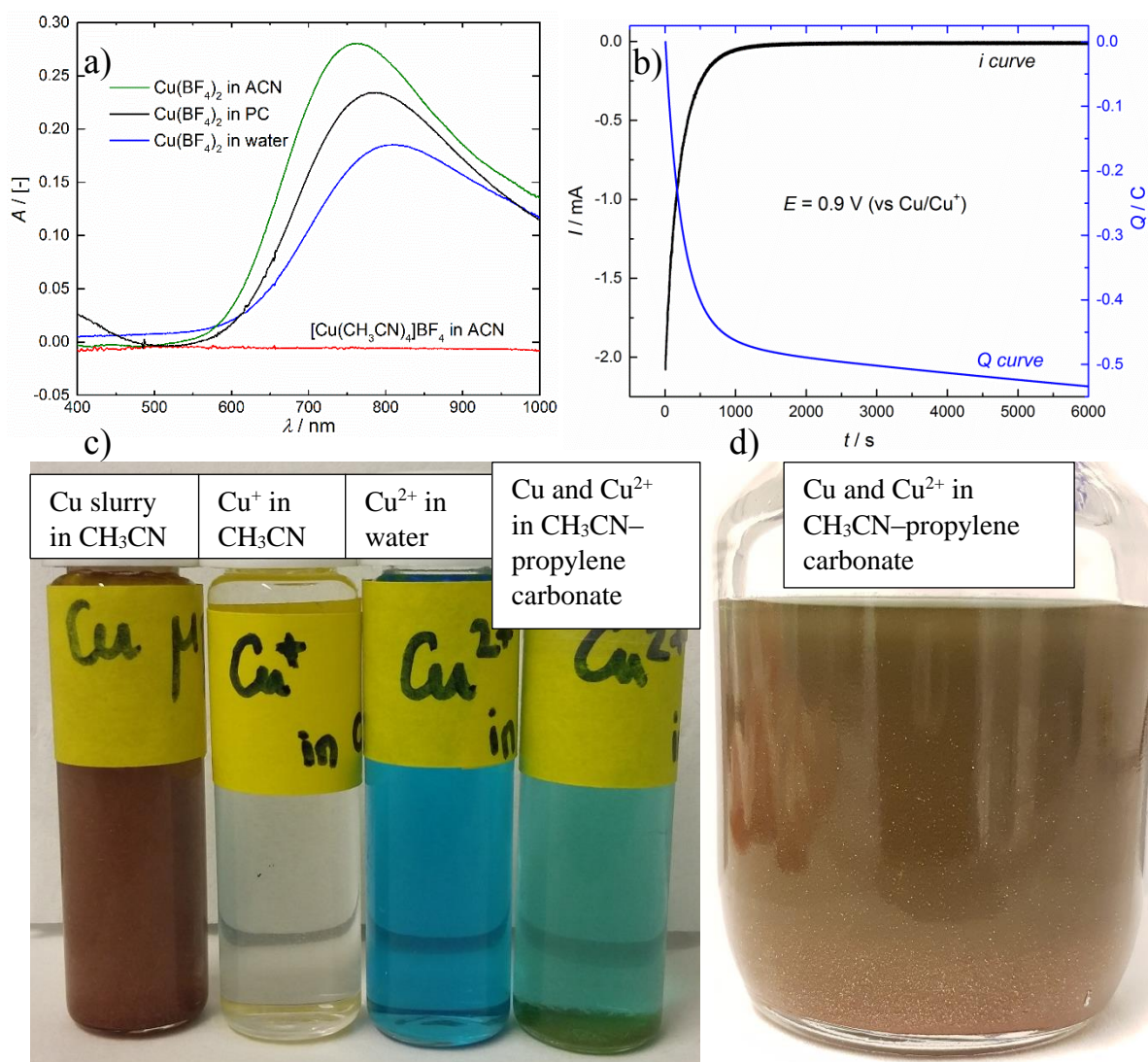
Figure 6.4. Analysis of the thermal regeneration of the Cu^{2+}. a) UV-vis spectra for Cu^+ and Cu^{2+} in acetonitrile, propylene carbonate and water. b) The bulk electrolysis of the generated Cu^{2+} at 0.9 V (vs. Cu/Cu^+). c) Cu^{2+} cation looks blue in water or green/turquoise in acetonitrile-propylene carbonate mixtures due to the absence of water. As expected in the case of a pure Cu^+, no trace of Cu^{2+} appears and the solution is transparent. d) Cu-Cu^{2+} solution after thermal treatment of a $[Cu(CH_3CN)_4]BF_4$ (0.15 mM) and $TEABF_4$ (0.3 M) in acetonitrile-propylene carbonate solvent (90%(V/V) of propylene carbonate.
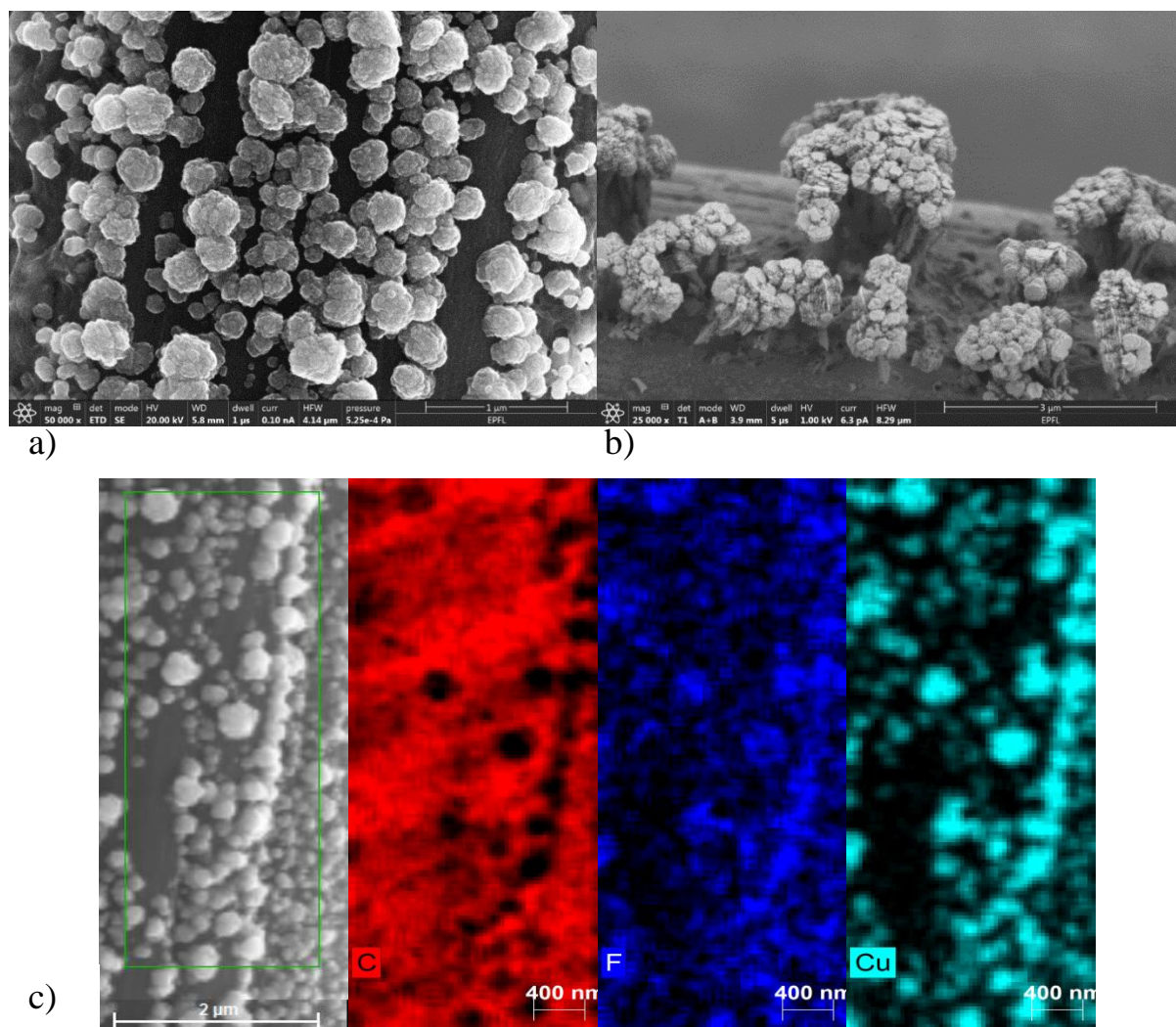
Figure 6.5. SEM images of thermally regenerated Cu on carbon fibre with electron beam at a) 20 kV and b) 1 kV, c) EDX scans of regenerated Cu on carbon fibre.

When thermal regenration step was performed in the presence of carbon fibers, copper nucleated preferentially on the fibers as shown in the SEM images in Figure 6.5. The secondary electron (SE) detection clearly shows Cu particles of more or less spherical shape on the surface of the carbon fibres. Also, some edge effects appear with brighter contours of some Cu clusters. This means that more SE can escape from the side of the particles and this confirms that Cu clusters are not simply recovering the carbon fibre like a flat homogenous layer. To improve the topographical contrast and to have a better idea of the shape of the regenerated Cu, the electron accelerating voltage has been decreased to 1 kV and the detection is done in-lens (Fig. 6.5b). With a lower voltage, the volume of interaction inside the sample will be smaller and less backscattered electron (BSE) will reach the detector. Consequently, in Figure 6.5b, there

is less contrast between the carbon fibre and Cu, which appears brighter at high voltage with more BSE. However, by analysing carefully the topology, the thermal regeneration seems to form spherical Cu clusters made of nanoparticles and gives a shape similar to a cauliflower when it is nucleated on carbon fibre. In addition to the electron microscopy imaging, chemical characterisation is carried out in Figure 6.5c. The goal of this is to confirm the presence of the Cu and also to check if some other chemicals appear in the sample. With a silicon drift detector, energy dispersive X-ray (EDX) mapping has been recorded at 15 keV. Carbon coming from the support is observed in red and the particles containing Cu in light blue. Beside of that, the EDX analysis revealed fluorine in the sample. This can be explained by the composition of the solution, that is heated for the thermal regeneration, and contains BF_4^- counter anion of $[Cu(CH_3CN)_4]^+$. Therefore it is not surprising to detect fluorine.

Dynamic light scattering (DLS) was used to analyse the size distribution of the thermally regenerated Cu particles in the absence of carbon fibers, found to be between 70 and 460 nm in diameter, as shown in Fig. 6.6a. The average value for the diameter of the synthesised Cu particles is 187 ± 1 nm with a peak of population around 122 nm. TEM analysis shown in Figure 6.6b indicates that smaller Cu particles down to 5 nm in diameter are also present. This implies that many different sizes of metallic Cu are produced during the thermal treatment of Cu(I). The complete conversion of Cu(I) to Cu and Cu(II) was confirmed by UV/Vis spectroscopy and bulk electrolysis, as shown in Fig. 6.4a-b.
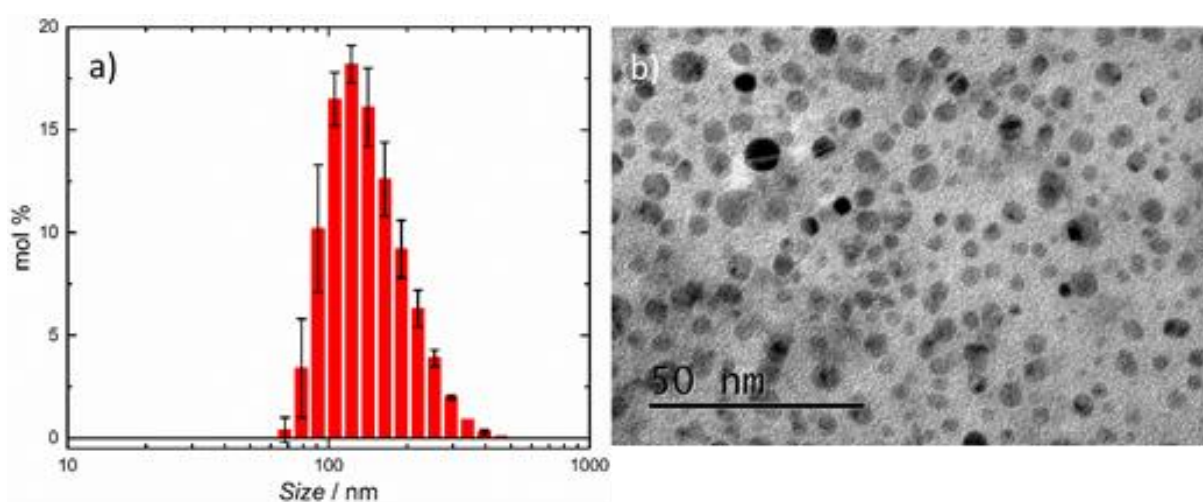

Figure 6.6. After thermal regeneration from [Cu(CH3CN)4]BF4, a) Cu NPs size distribution from DLS measurement and b) TEM images of Cu particles produced upon thermal regeneration.

A flow cell was assembled to demonstrate that the system can be used to realize heat-to-power conversion. Three different methods were tested: 1) discharge of the positive side only, 2) discharge of the full cell, with Cu particles filtered off and added into the cell, and 3) discharge of the full cell with a nanoslurry electrolyte. In the first case, copper particles were separated from the solution by filtration, and the recovered Cu(II) electrolyte was introduced into the positive side of the cell. A fraction of the distilled acetonitrile was introduced back in the Cu(II) solution to obtain the positive electrolyte, and a copper foam was used as the negative electrode. In the second case, the filter with Cu particles was introduced between the carbon foam current collector and the anionic membrane. In the last case, copper nanoslurry particles were used as seeds for nucleating copper during the disproportionation reaction and separated from the resulting Cu^{2+} solution by centrifugation. Large fraction (*ca.* 15 mL) of the recovered acetonitrile was added into the slurry, resulting in *ca.* 90% CH_3CN solution, and *ca.* 10 mL was added into the positive electrolyte (30% V/V CH_3CN).

The electrochemical discharge of the thermally charged battery at a constant current is shown in Figure 6.7, and polarization curves in Figure 6.8. When a heat-regenerated solution was used on the positive side, with Cu foam as the negative electrode, the cell voltage is around 1.1 V and the capacity of the discharge corresponds to 85-90 % of the theoretical capacity of the battery. This difference might come from the loss of some Cu(II) solution during the thermal regeneration process, but it could be also due to an incomplete thermal treatment of the initial Cu(I) solution. In this case, the cell was limited by the Cu(II)/Cu(I) couple, with the excess of Cu present on the negative side. For the second case, much lower discharge voltages and capacities are obtained, because the negative electrode reaction limits also the cell performance, and, at some point, contact between the Cu-particles and the electrode is lost. Higher discharge voltage and capacity is reached when a 15 w-% Cu nanoslurry electrolyte is used. The first cycle allowed to utilize 80% of the nominal capacity, while this number was reduced to 70% for the second discharge. Further cycling is required to evaluate the long-term stability of the system, but the use of the nanoslurry electrode allows envisaging a full process based on this concept. These curves also prove that heat storage is possible inside a Cu RFB through a chemical energy conversion.
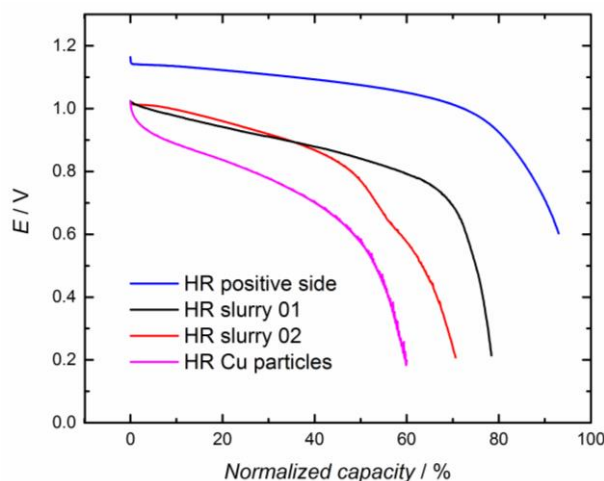
Figure 6.7. Typical *iR*-corrrected curves in a RFB at 10 mA cm^{-2}. The positive electrolyte is composed of heat-regenerated $Cu(BF_4)_2$ (0.15 M) and $TEABF_4$ (0.15 M) in acetonitrile-propylene carbonate mixture and the negative electrolyte of $TEABF_4$ (0.15 M) in acetonitrile-propylene carbonate mixture. The acetonitrile is collected from the distilled fraction during the thermal disproportionation of the Cu(I). Additionally, on the negative side, the filter with the Cu particles is added in parallel to the membrane.

The performance of the Cu-RFB is described in Figure 6.8b by the power production for the three different cases. Highest power density of 210 W·m^{-2} is achieved with Cu-foam electrode, but nanoslurry system is able to show power densities of *ca.* 150 W·m^{-2}. These values compare favourably with the earlier report of 136 W·m^{-2} for aqueous ammonia based Cu-system,[20] and of 236 W·m^{-2} for the aqueous ammonia based Cu system at elevated temperatures.[19] According to these results, the power that can be produced from a thermal treatment is promising and allows considering this Cu-RFB as potentially efficient tool to convert heat into stored electricity. Furthermore, if the resistance of the system could be decreased, much better performance could be obtained (see *iR*-corrected polarization and power curves in Fig. 6.10b, showing significant increase in power density). Such improvements are expected in the future, considering that the membranes developed for non-aqueous systems are inferior in comparison to the membranes used for aqueous systems.[52]
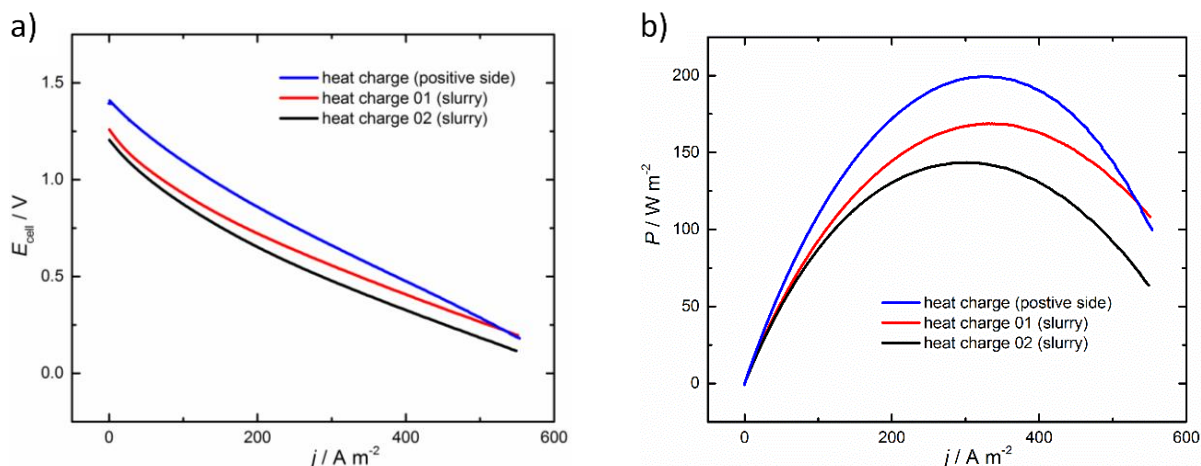
Figure. 6.8 a) Polarization curves (no iR correction) and b) corresponding power production of the Cu-RFB in different conditions. The starting solution for the thermal treatment of Cu(I) (0.3 M) to Cu-Cu(II) has a solvent composition of 50% acetonitrile in propylene carbonate. The polarization curves are done inside the cell with Cu foam electrode, named heat charge positive side (blue curve), inside a cell with Cu slurry electrode showing the first discharge (red curve) and second discharge (black curve) after two consecutive heat charge processes.
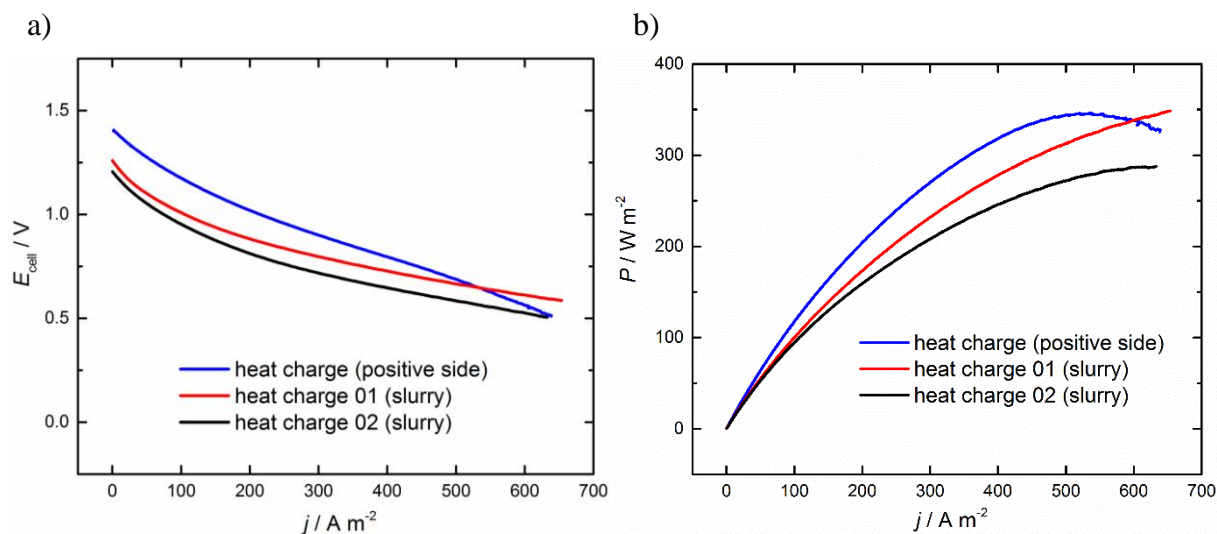
Figure 6.9. a) Polarization curves (with *iR* correction, *R* = 0.9-3 Ω) and b) corresponding power production of the Cu-RFB after heat regeneration. The starting solution for the thermal treatment of Cu(I) (0.3 M) to Cu-Cu(II) has a solvent composition of 50% acetonitrile in propylene carbonate. The polarization curves are done inside the cell with Cu foam electrode, named heat charge positive side (blue curve), inside a cell with Cu slurry electrode showing the first discharge (red curve) and second discharge (black curve) after two consecutive heat charge processes. With the compensation of the cell resistance, the expected power production increases compared to the experimental data. This indicates that if the conductivity of the RFB can be improved, the final power production would be more efficient.

3.4. Thermodynamic analysis

When considering the thermal charging of the battery, disproportionation of Cu(I) requires higher temperatures of around 140-160°C than the simple evaporation of acetonitrile, depending slightly on the acetonitrile-propylene carbonate ratios. We can determine the theoretical efficiency of the battery based on the values of the vaporization and reaction enthalpies and the heat capacity, as illustrated below and in Chapter 4. The efficiency is defined by the ratio of the output energy (electrical work) and the input heat, which is required for the vaporisation of acetonitrile, destabilization of Cu(I) and heating of the solution:

$$\eta = \frac{W_{elec}}{2Q_{tot}} = \frac{nFE_{cell}c_{[Cu(I)(ACN)_4]^+}}{2(Q_{sol} + Q_{vap} + Q_{rxn})}$$

$$= \frac{nFE_{cell}c_{[Cu(I)(ACN)_4]^+}}{2(\Delta T * C_p * c_{tot} + \Delta H_{vap}^{ACN} * c_{ACN} + \Delta H_{rxn}^{Cu(I)} * c_{[Cu(I)(ACN)_4]^+})} \tag{6.1}$$

The maximum efficiency of a work production by heat conversion is that of a Carnot cycle. With T_{cold} at 343 K and T_{hot} between 433 K, the maximum efficiency is 21 %. As described in the Chapter 4, two main factors influencing the heat conversion efficiency are acetonitrile and Cu(I) concentrations in the electrolyte. With increasing amounts of acetonitrile, more heat is required for the distillation process and lower efficiencies are reached (2% for a 100% acetonitrile solution with 0.3 M [Cu(CH₃CN)₄]BF₄ against 5% for a 10% acetonitrile solution). An opposite effect is predicted according to the Cu(I) concentration with 13% for a 1.5 M solution and 5% for a 0.3 M solution both containing 10% acetonitrile. Hence, for a battery with an optimized thermal energy conversion, low acetonitrile ratio and high Cu(I) concentration are preferable. Nevertheless, it is important to highlight that the voltage potential and kinetics parameters will decrease with a small acetonitrile content. Additionally, significant amount of heat is required for heating up the solution. Therefore, a co-solvent with lower heat capacity would improve the efficient.

4.   Conclusion

In this chapter, we present thermally regenerative non-aqueous copper batteries as a means to convert low-grade thermal energy into electrical energy, stored in a battery. We have investigated the electrochemistry and the thermodynamic properties of the system, and show that heat with temperature between 140-160℃ can be converted into electricity. Replacement of water with a higher boiling point co-solvent, propylene carbonate, allows unprecedented cell voltages and a high output power for a thermo-electrochemical battery. Additionally, the theoretical efficiencies approaching 65% of the Carnot efficiency for heat to power conversion (up to 13 %) can be achieved with optimized solution compositions. Applicability of nanoslurry electrode for the negative side of the battery is also demonstrated, allowing multiple cycles of heat-to-power conversion.

Overall, this work opens the way to thermo-electrochemical electricity generation to exploit industrially waste heat and thereby provide new alternative routes of renewable energy.

5. References

1.   International Energy Agency (IEA). Combined heat and power: evaluating the benefits of greater global investment. (2008).

2.   Waske, A. *et al.* Energy harvesting near room temperature using a thermomagnetic generator with a pretzel-like magnetic flux topology. *Nature Energy* **4**, 68 (2019).

3.   Straub, A. P., Yip, N. Y., Lin, S., Lee, J. & Elimelech, M. Harvesting low-grade heat energy using thermo-osmotic vapour transport through nanoporous membranes. *Nature Energy* **1**, 16090 (2016).

4.   Rowe, A. M. A new twist. *Nature Energy* **4**, 12 (2019).

5.   Rahimi, M. *et al.* Emerging electrochemical and membrane-based systems to convert low-grade heat to electricity. *Energy Environ. Sci.* **11**, 276–285 (2018).

6.   Champier, D. Thermoelectric generators: A review of applications. *Energy Conversion and Management* **140**, 167–181 (2017).

7.   Hamid Elsheikh, M. *et al.* A review on thermoelectric renewable energy: Principle parameters that affect their performance. *Renewable and Sustainable Energy Reviews* **30**, 337–355 (2014).

8.   Zheng, X. F., Liu, C. X., Yan, Y. Y. & Wang, Q. A review of thermoelectrics research – Recent developments and potentials for sustainable and renewable energy applications. *Renewable and Sustainable Energy Reviews* **32**, 486–503 (2014).

9.   Goswami, D. Y. & Kreith, F. *Energy Conversion*. (CRC Press, 2007).

10.   Bao, J. & Zhao, L. A review of working fluid and expander selections for organic Rankine cycle. *Renewable and Sustainable Energy Reviews* **24**, 325–342 (2013).

11.   Little, A. B. & Garimella, S. Comparative assessment of alternative cycles for waste heat recovery and upgrade. *Energy* **36**, 4492–4504 (2011).

12.   Kalina, A. I. Combined-Cycle System With Novel Bottoming Cycle. *J. Eng. Gas Turbines Power* **106**, 737–742 (1984).

13.   Ogriseck, S. Integration of Kalina cycle in a combined heat and power plant, a case study. *Applied Thermal Engineering* **29**, 2843–2848 (2009).

14.   F. Dupont, M., R. MacFarlane, D. & M. Pringle, J. Thermo-electrochemical cells for waste heat harvesting – progress and perspectives. *Chemical Communications* **53**, 6288–6302 (2017).

15.   Jokinen, M., Manzanares, J. A., Kontturi, K. & Murtomäki, L. Thermal potential of ion-exchange membranes and its application to thermoelectric power generation. *Journal of Membrane Science* **499**, 234–244 (2016).

16.   Reynard, D., Dennison, C. R., Battistel, A. & Girault, H. H. Efficiency improvement of an all-vanadium redox flow battery by harvesting low-grade heat. *Journal of Power Sources* **390**, 30–37 (2018).

17. Gao, C., Lee, S. W. & Yang, Y. Thermally Regenerative Electrochemical Cycle for Low-Grade Heat Harvesting. *ACS Energy Lett.* **2**, 2326–2334 (2017).

18. Yip, N. Y., Brogioli, D., Hamelers, H. V. M. & Nijmeijer, K. Salinity Gradients for Sustainable Energy: Primer, Progress, and Prospects. *Environ. Sci. Technol.* **50**, 12072–12094 (2016).

19. Zhang, F., LaBarge, N., Yang, W., Liu, J. & Logan, B. E. Enhancing Low-Grade Thermal Energy Recovery in a Thermally Regenerative Ammonia Battery Using Elevated Temperatures. *ChemSusChem* **8**, 1043–1048 (2015).

20. Zhang, F., Liu, J., Yang, W. & E. Logan, B. A thermally regenerative ammonia-based battery for efficient harvesting of low-grade thermal energy as electrical power. *Energy & Environmental Science* **8**, 343–349 (2015).

21. Vicari, F. *et al.* On the regeneration of thermally regenerative ammonia batteries. *J Appl Electrochem* **48**, 1381–1388 (2018).

22. Rahimi, M., Kim, T., Gorski, C. A. & Logan, B. E. A thermally regenerative ammonia battery with carbon-silver electrodes for converting low-grade waste heat to electricity. *Journal of Power Sources* **373**, 95–102 (2018).

23. Peljo, P., Lloyd, D., Doan, N., Majaneva, M. & Kontturi, K. Towards a thermally regenerative all-copper redox flow battery. *Phys. Chem. Chem. Phys.* **16**, 2831–2835 (2014).

24. Parker, A. J., Muir, D. M., Smart, Y. C. & Avraamides, J. An application of acetonitrile leaching and disproportionation. *Hydrometallurgy* **7**, 213–233 (1981).

25. Wang, W. *et al.* A bimetallic thermally regenerative ammonia-based battery for high power density and efficiently harvesting low-grade thermal energy. *Journal of Materials Chemistry A* (2019).

26. Marino, M., Misuri, L., Carati, A. & Brogioli, D. Proof-of-Concept of a Zinc-Silver Battery for the Extraction of Energy from a Concentration Difference. *Energies* **7**, 3664–3683 (2014).

27. Kratochvil, B. & Betty, K. R. A Secondary Battery Based on the Copper(II)-(I) and (I)-(0) Couples in Acetonitrile. *J. Electrochem. Soc.* **121**, 851–854 (1974).

28. Petek, T. J., Hoyt, N. C., Savinell, R. F. & Wainright, J. S. Slurry electrodes for iron plating in an all-iron flow battery. *Journal of Power Sources* **294**, 620–626 (2015).

29. Yan, W. *et al.* All-polymer particulate slurry batteries. *Nat Commun* **10**, 1–11 (2019).

30. Qi, Z. & Koenig, G. M. Review Article: Flow battery systems with solid electroactive materials. *Journal of Vacuum Science & Technology B, Nanotechnology and Microelectronics: Materials, Processing, Measurement, and Phenomena* **35**, 040801 (2017).

31. Morgan, H. H. CCCXLII.—Preparation and stability of cuprous nitrate and other cuprous salts in presence of nitriles. *J. Chem. Soc., Trans.* **123**, 2901–2907 (1923).

32. Hathaway, B. J., Holah, D. G. & Postlethwaite, J. D. 630. The preparation and properties of some tetrakis(methylcyanide)copper(I) complexes. *J. Chem. Soc.* 3215–3218 (1961). doi:10.1039/JR9610003215

33. Hathaway, B. J., Holah, D. G. & Underhill, A. E. 468. The preparation and properties of some bivalent transition-metal tetrafluoroborate–methyl cyanide complexes. *J. Chem. Soc.* 2444–2448 (1962). doi:10.1039/JR9620002444

34. Kubas, G. J., Monzyk, B. & Crumbliss, A. L. Tetrakis(Acetonitrile)Copper(I) Hexafluorophosphate. in *Inorganic Syntheses* (ed. Shriver, D. F.) 90–92 (John Wiley & Sons, Inc., 1979).

35. Yanson, A. I. *et al.* Cathodic Corrosion: A Quick, Clean, and Versatile Method for the Synthesis of Metallic Nanoparticles. *Angewandte Chemie International Edition* **50**, 6346–6350 (2011).

36. Feng, J. *et al.* Cathodic Corrosion of a Bulk Wire to Nonaggregated Functional Nanocrystals and Nanoalloys. *ACS Appl. Mater. Interfaces* **10**, 9532–9540 (2018).

37. Stricker, E. A., Krueger, K. W., Savinell, R. F. & Wainright, J. S. Investigating a Bromide Supported Electrolyte for an All-Copper Flow Battery. *J. Electrochem. Soc.* **165**, A1797–A1804 (2018).

38. Li, Y. *et al.* A non-aqueous all-copper redox flow battery with highly soluble active species. *Electrochimica Acta* **236**, 116–121 (2017).

39. Sanz, L., Lloyd, D., Magdalena, E., Palma, J. & Kontturi, K. Description and performance of a novel aqueous all-copper redox flow battery. *Journal of Power Sources* **268**, 121–128 (2014).

40. Lloyd, D., Magdalena, E., Sanz, L., Murtomäki, L. & Kontturi, K. Preparation of a cost-effective, scalable and energy efficient all-copper redox flow battery. *Journal of Power Sources* **292**, 87–94 (2015).

41. Rizvi, M. A., Akhoon, S. A., Maqsood, S. R. & Peerzada, G. M. Synergistic effect of perchlorate ions and acetonitrile medium explored for extension in copper redoximetry. *J Anal Chem* **70**, 633–638 (2015).

42. Torras, J. & Alemán, C. Determination of New Cu+, Cu2+, and Zn2+ Lennard-Jones Ion Parameters in Acetonitrile. *J. Phys. Chem. B* **117**, 10513–10522 (2013).

43. Brugger, J. *et al.* An XAS study of the structure and thermodynamics of Cu(I) chloride complexes in brines up to high temperature (400°C, 600bar). *Geochimica et Cosmochimica Acta* **71**, 4920–4941 (2007).

44. Sanz, L., Palma, J., García-Quismondo, E. & Anderson, M. The effect of chloride ion complexation on reversibility and redox potential of the Cu(II)/Cu(I) couple for use in redox flow batteries. *Journal of Power Sources* **224**, 278–284 (2013).

45. Rorabacher, D. B. Electron Transfer by Copper Centers. *Chem. Rev.* **104**, 651–698 (2004).

46.   Atek, I., Maye, S., Girault, H. H., Affoune, A. M. & Peljo, P. Semi-analytical modelling of linear scan voltammetric responses for soluble-insoluble system: The case of metal deposition. *Journal of Electroanalytical Chemistry* **818**, 35–43 (2018).

47.   Leung, P. *et al.* Evaluation of electrode materials for all-copper hybrid flow batteries. *Journal of Power Sources* **310**, 1–11 (2016).

48.   Crousier, J. & Bimaghra, I. Electrodeposition of copper from sulphate and chloride solutions. *Electrochimica Acta* **34**, 1205–1211 (1989).

49.   Plieth, W. Additives in the electrocrystallization process. *Electrochimica Acta* **37**, 2115–2121 (1992).

50.   Healy, J. P., Pletcher, D. & Goodenough, M. The chemistry of the additives in an acid copper electroplating bath: Part II. The instability 4,5-dithiaoctane-1,8-disulphonic acid in the bath on open circuit. *Journal of Electroanalytical Chemistry* **338**, 167–177 (1992).

51.   Jovic, V. D. & Jovic, B. M. Copper electrodeposition from a copper acid baths in the presence of PEG and NaCl. *Journal of the Serbian Chemical Society* **66**, 935–952 (2001).

52.   Sekiguchi, S. *et al.* Redox flow battery. (2004).

53.   Corcuera, S. & Skyllas-Kazacos, M. State-of-Charge Monitoring and Electrolyte Rebalancing Methods for the Vanadium Redox Flow Battery. *European Chemical Bulletin* **1**, 511–519 (2012).

54.   Wang, K., Liu, L., Xi, J., Wu, Z. & Qiu, X. Reduction of capacity decay in vanadium flow batteries by an electrolyte-reflow method. *Journal of Power Sources* **338**, 17–25 (2017).

55.   Bhattarai, A. *et al.* Novel Approaches for Solving the Capacity Fade Problem during Operation of a Vanadium Redox Flow Battery. *Batteries* **4**, 48 (2018).

56.   Dodi, G., Hritcu, D., Lisa, G. & Popa, M. I. Core–shell magnetic chitosan particles functionalized by grafting: Synthesis and characterization. *Chemical Engineering Journal* **203**, 130–141 (2012).

Chapter VII

Conclusions and outlook

In this work, a copper redox flow battery for energy storage is described. We have also shown that the device is not only able to store electrical power but also thermal energy at relatively low temperatures that are usually considered as waste heat (140-160°C). The electrolyte, which is chosen for the heat conversion to chemical energy in the electrochemical cell, is composed of three main chemicals: Cu salts, acetonitrile (ACN) and propylene carbonate (PC). The research of A. Parker *et al.* demonstrates the ability of Cu(I) complexes with ACN to undergo a disproportionation reaction when the water-ACN solvent is evaporated.[1] This chemical reaction promoted by heat induces to formation of metallic Cu(0) and Cu(II). Therefore, the idea to apply this reaction to store heat as chemical energy based on the thermal treatment of the Cu-ACN complex has been proposed by P. Peljo *et al.*[2] To facilitate the transfer of the Cu and Cu(II) species in the energy storage device, the solubilized state of the final electroactive species needs to be preserved. The originality of the present research is to introduce the final liquid electrolyte, which is charged by heat, in a flow cell. For that purpose, PC is added to the solvent composition because this chemical will not evaporate during the ACN distillation (T_b = 242°C) and will conserve the Cu(II) salt in solution. Another advantage to replace water as the co-solvent by PC is the better stabilization of the Cu(I) complex in a pure organic phase, significantly improving the cell voltage. At the end, the final electrolyte is based only on the organic solvent composition of ACN and PC containing the Cu electroactive species.

By electrochemical analysis (Chapter 2 and 3), we confirmed the nice stabilization of the Cu(I) species in ACN and PC mixtures, even when low concentration of ACN are present in solvent composition. The effect of the PC on the potential of the cell is very weak comparing to water, as 90 vol% PC and 10 vol% ACN solution still shows a cell voltage of 1.0 V. The maximum cell voltage for standard conditions with pure ACN is determined at 1.24 V for the Cu-ACN battery. The main effects of PC is to decrease the quasi-reversible kinetics of the electron transfer (for 100% ACN, $k^0 = 6.25 \cdot 10^{-3}$ cm·s^{-1} and for 10% ACN, $k^0 = 1.12 \cdot 10^{-4}$ cm·s^{-1}), to increase the viscosity (for 100% ACN, $\eta = 0.38$ cP and for 10% ACN, $\eta = 1.91$ cP) and therefore lower diffusion coefficient of the Cu(I) and Cu(II) at the electrode (for Cu(I) and 100% ACN, $D = 1.48 \cdot 10^{-5}$ cm^2·s^{-1} and for 10% ACN, $D = 2.54 \cdot 10^{-6}$ cm^2·s^{-1}). The activation energies for the electron transfer and the diffusion at the electrode are also increased with higher PC contents.

The thermodynamics of the Cu-ACN-PC system is analysed in Chapter 4 mainly by differential scanning calorimetry (DSC). The heat capacities, temperatures and enthalpies of vaporization and reaction that are calculated from the DSC measurements to allow estimation of the energy efficiency of the thermal conversion to electricity. Equation 7.1 (or 4.23) describes the efficiency as the ratio of the electrical output that can be recovered from the thermal energy needed to heat the solution and to induce the disproportionation of Cu(I):

$$\eta = \frac{nFE_{cell}c_{[Cu(I)(ACN)_4]^+}}{2(\Delta T * C_p * c_{tot} + \Delta H_{vap}^{ACN} * c_{ACN} + \Delta H_{rxn}^{Cu(I)} * c_{[Cu(I)(ACN)_4]^+})} \tag{7.1}$$

Three main factors influencing the final efficiency of the thermal conversion are: the ACN concentration, the Cu(I) concentration and the starting temperature. According to Equation 7.1 and the data in Chapter 4, the maximum performance is reached when:

- Low ACN contents are present in solution because less heat is needed to evaporate it,
- Cu(I) is more concentrated and gives more products during the disproportionation reaction,
- The starting temperature is closer to the boiling point of the ACN.

The best theoretical efficiencies are determined between 10% ($T_0 = 20°C$) and 14% ($T_0 = 80°C$) for a solution with 1.5 M Cu(I) and 10 vol% ACN. The energy density of the system with 1.5M Cu(I) salt has an energy storage density of 25.8 Wh·L^{-1}. These performances can be obtained with a Cu(I) salt with Tf$_2$N$^-$ as counter anion, as [Cu(CH$_3$CN)$_4$]Tf$_2$N is known to be an ionic liquid, and very soluble Cu(I) species in ACN that can reach a concentration of ~3M and that can be used in a redox flow battery.[3,4] For an energy storage device using thermal energy as the input, these results are among the highest that can be reached for a thermodynamic process limited by Carnot. Even better efficiency can be expected from the system if the heat capacity of the electrolyte is modified by changing propylene carbonate by another solvent with high boiling point and lower C_p (*e.g.* ethylene carbonate).

The redox flow battery had been developed to deal with the resistance of the cell, the transport of chemicals and solvents through the separator, the deposition/stripping process of Cu on the negative side and the long-term cycling of the cell (Chapter 5). To achieve more than 200 cycles, a set-up for the long-term cycling was built with an anionic membrane reinforced with PE, a porous Cu negative electrode and a hydraulic shunt between the tanks to mitigate the ACN crossover and loss of capacity. With an electrical charge of the battery, the energy efficiency reaches 56 % in average at 10 mA·cm^{-2} (69% with *iR* correction) and highlights the need to develop and use a membrane with a low resistance. From the difference of performances between the thermal or electrical charges, it is obvious that the Cu-RFB is performing better in a purely electrical mode. However, the great opportunity here is the capacity of the battery to switch to a different type of energy input when heat is available. Even a third option is possible if energy lower than 140-160°C is present; the implementation of a thermally regenerative electrochemical cycle (TREC) could be done to heat the solution during the charge and to reduce the electrical energy input. Such system should increase the energy efficiency of around five additional percents.[5]

A particular attention was given to the electrode for the Cu(I)/Cu redox couple. The change of physical state for the Cu ion and the slower kinetic of the deposition are the main factors contributing to losses of capacity and performance during long-term cycling. The Cu slurry electrode was proposed as an alternative for the negative side of the battery. The advantage of the conductive particle suspension is that it keeps the property of the classical

RFB to decouple the capacity of the system regarding the mass of the electrode. As the slurry can be stored in the positive tank as a charged electrolyte, the capacity only depends on the volume of the solution. The cathodic corrosion method was investigated for the Cu nanoparticles (NPs) synthesis[6] and an automatized set up was built to have a production able to give enough quantity of powder for slurry integration in the RFB (Chapter 5). Even if the Cu NPs are oxidized partially during the synthesis, the slurry is still active enough to reach similar or slightly higher power and current density than the Cu foam electrode (with thermal charging and 0.3 M Cu(I), $P = 175$ W·m^{-2} at $j = 350$ A·m^{-2} and with electrical charging and 0.15 M Cu(I), $P = 240$ W·m^{-2} at $j = 450$ A·m^{-2}). A more exotic type of liquid electrodes could be imagined if eutectic metal alloys are added in the negative side (Hg, Galinstan (Ga-In-Sn) or Field's alloys (Bi-In-Sn) among others). The kinetics of deposition on these amalgams could be improved, as it is known that the kinetics is faster on mercury than on Cu surface.[7,8] Another idea could be to have two different Cu(II)/Cu(I) redox couples for each side of the Cu-RFB. Therefore, the problem of the deposition/stripping process can be avoided. However, the thermal conversion will be no more possible with such a system. A potential candidate for the negative Cu(I) complex is the N,N,N-tris-(2-(dimethylamino)ethyl)amine) complex or [Cu(Me$_6$tren)]. This Cu(II)/Cu(I) couple has a redox potential in ACN around -0.6 and -0.3V (vs. Ag/Ag$^+$),[9] which is lower than the deposition potential of Cu(I) in ACN (0.3V (*vs.* Ag/AgCl)). Consequently, a higher cell voltage could also be obtained ($E_{cell} = 1.5\text{-}1.8$V) with such Cu complex on the negative side and with the Cu-ACN complex on the positive one.

If we want to apply the heat to power Cu RFB to the industry, several drawbacks have to be pointed out. The economic study of the battery reveals that the cost of the kWh will be mainly influence by the price of the electrolyte and especially the supporting electrolyte (LiPF$_6$, TEABF$_4$ and Tf$_2$N) for the organic solvent composition. This parameter was highlighted by the cost studies of Li-ion battery.[10] Another disadvantage of the organic solvent composition is the relative toxicity of the acetonitrile and the possibility to produce cyanide when it is decomposing at high temperatures. However, this compound is already used in the chemical industry and its implementation in an industrial RFB should be possible without too many difficulties.

Finally, as this work describes a major leap forward in terms of theoretical thermal conversion efficiency, cell voltage, and energy storage density, these improvements could make this technology industrially relevant.

Overall, this work opens the way to thermo-electrochemical electricity generation to exploit industrially waste heat or solar thermal energy and thereby provide new alternative routes of renewable energy.
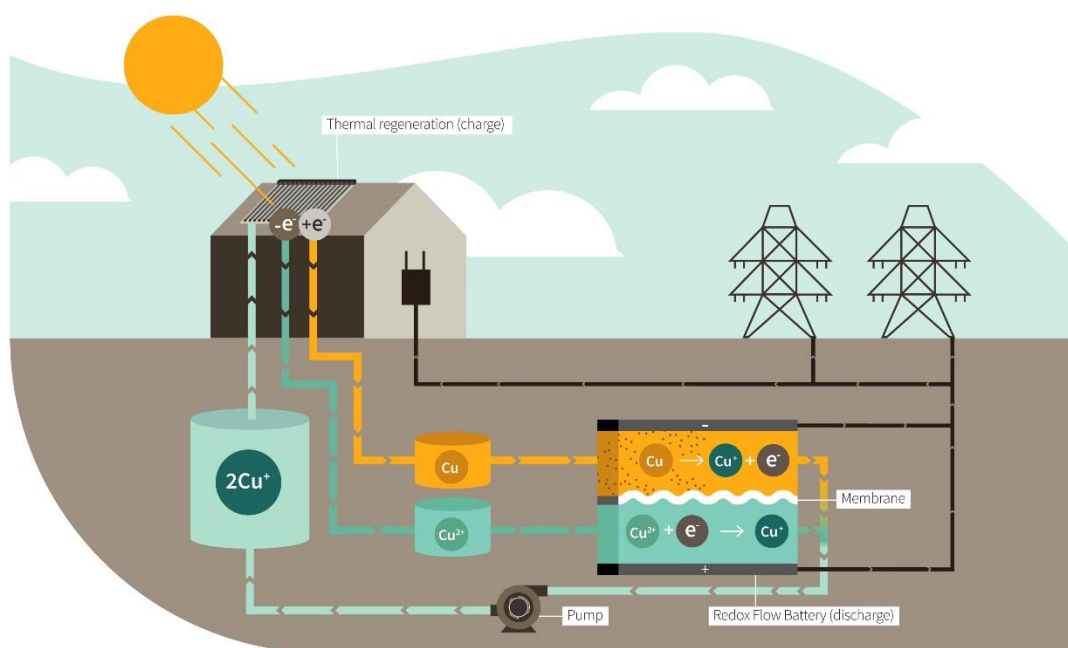
SCHEME OF THE HEAT REGENERATION SYSTEM

References

1. Parker, A. J., Muir, D. M., Smart, Y. C. & Avraamides, J. An application of acetonitrile leaching and disproportionation.: Refining segregated copper from roasted concentrates and ores. *Hydrometallurgy* **7**, 213–233 (1981).

2. Peljo, P., Lloyd, D., Doan, N., Majaneva, M. & Kontturi, K. Towards a thermally regenerative all-copper redox flow battery. *Phys. Chem. Chem. Phys.* **16**, 2831–2835 (2014).

3. Schaltin, S. *et al.* Towards an all-copper redox flow battery based on a copper-containing ionic liquid. *Chem. Commun.* **52**, 414–417 (2016).

4. Li, Y. *et al.* A non-aqueous all-copper redox flow battery with highly soluble active species. *Electrochimica Acta* **236**, 116–121 (2017).

5. Reynard, D., Dennison, C. R., Battistel, A. & Girault, H. H. Efficiency improvement of an all-vanadium redox flow battery by harvesting low-grade heat. *Journal of Power Sources* **390**, 30–37 (2018).

6. Feng, J. *et al.* Cathodic Corrosion of a Bulk Wire to Nonaggregated Functional Nanocrystals and Nanoalloys. *ACS Appl. Mater. Interfaces* **10**, 9532–9540 (2018).

7. Fawcett, W. R. & Foss, C. A. Role of the solvent in the kinetics of heterogeneous electron and ion transfer reactions. *Electrochimica Acta* **36**, 1767–1774 (1991).

8. Fawcett, W. R. & Foss, C. A. On the nature of the transfer coefficient for ion transfer reactions. *Journal of Electroanalytical Chemistry and Interfacial Electrochemistry* **250**, 225–230 (1988).

9. Bell, C. A., Bernhardt, P. V. & Monteiro, M. J. A Rapid Electrochemical Method for Determining Rate Coefficients for Copper-Catalyzed Polymerizations. *J. Am. Chem. Soc.* **133**, 11944–11947 (2011).

10. Wood, D. L., Li, J. & Daniel, C. Prospects for reducing the processing cost of lithium ion batteries. *Journal of Power Sources* **275**, 234–242 (2015).

Sunny MAYE

Espaces des Remparts 25
CH-1950 Sion
Tél. mobile : 079/960.41.05
E-mail : sunny.maye@epfl.ch

Né le 12 mai 1991
Célibataire
Suisse

MSc in biological and molecular chemistry EPFL

Formation

Sept. 2015 – en cours	**Thèse de doctorat, Assistant** "Copper battery for heat to power conversion and energy storage"**,** au Laboratoire d'Electrochimie Physique et Analytique (LEPA, EPFL), sous la supervision de Prof. Hubert H. Girault et du Dr. Pekka Peljo. Développement de batterie à flux redox pour la conversion d'énergie thermique à basses températures en électricité.
Sept. 2010 – fév. 2015	**Master of Science en Chimie Moléculaire et Biologique**, Chimiste diplômé EPF, Ecole Polytechnique Fédérale de Lausanne. Projet de Master (LEPA, EPFL): "Voltammetric monitoring of antioxidants in blood through the formulation and inkjet-printing of carbon nanotube dispersion"
Sept. 2010 – fév. 2013	**Bachelor of Science en Chimie et Génie Chimique,** Ecole Polytechnique Fédérale de Lausanne.
Août 2005-juin 2010	**Maturité gymnasiale :** option spécifique chimie-biologie, Lycée-Collège de la Planta, Sion.

Compétences

Chimie :
- Electrodéposition de métaux et caractérisation de matériaux.
- Formulation d'encres et impression 3D de conducteurs électriques.
- Synthèses organiques, inorganiques, de nanoparticules métalliques.
- Analyses électrochimiques, chimiques et optiques.

Ingénierie, développement et design de cellules électrochimiques, batteries et autre montages.

Langues

Français	Langue maternelle
Anglais	Bonne compréhension et expression professionnelles
Allemand	Connaissances de base, notions scolaire et gymnasiales

Autres activités, loisirs et centres d'intérêt

Soutien scolaire, Fondation Cité Printemps – centre d'accueil et de rééducation, Sion.
Joueur et moniteur de tennis, compétitions et interclubs au Tennis Club de Valère et Tennis Club des Iles, Sion.
Sports de montagne (ski, ski de randonnée, VTT, escalade).
Voyages, œnologie, théâtre.

Prix

Juillet 2018	**Metrohm Young Chemist Award 2018,** "Copper redox flow battery for heat to power conversion." délivré par Metrohm Schweiz AG.
Juin 2017	**Mention d'excellence en enseignement,** délivrée par la section de chimie et génie chimique de l'EPFL.
Juin 2016	**Prix du meilleur poster,** International Flow Battery Forum, Karlsruhe.

Publications

Juillet 2019	Rivier L., Peljo P., <u>Maye S.</u>, Méndez M.A., Vrubel H., Vannay L.A.C., Corminboeuf C., Scanlon M.D. and Girault H.H., Mechanistic study of the photogeneration of hydrogen by decamethylruthenocene, *Chemistry – A European Journal* **25**(55), pp. 12769–12779 (2019).
Juin 2018	Atek I., <u>Maye S.</u>, Girault H.H., Affoune A.M. and Peljo P., Semi-analytical modelling of linear scan voltammetric responses for soluble-insoluble system: The case of metal deposition, *Journal of Electroanalytical Chemistry* **818**, pp.35–43 (2018).
Août 2017	Bardyn M., <u>Maye S.</u>, Lesch A., Delobel J., Tissot J.-D., Cortés-Salazar F.,Tacchini P., Lion N., Girault H.H. and Prudent M., The antioxidant capacity of erythrocyte concentrates is increased during the first week of storage and correlated with the uric acid level, *Vox Sanguinis* **112**(7), pp. 638–647 (2017).